UNIVERSIDADE FEDERAL DO RIO GRANDE DO SUL

INSTITUTO DE PESQUISAS HIDRÁULICAS

PROGRAMA DE PÓS-GRADUAÇÃO EM RECURSOS HÍDRICOS E SANEAMENTO AMBIENTAL

ALICE CÉSAR FASSONI DE ANDRADE

MAPEAMENTO E CARACTERIZAÇÃO DO SISTEMA RIO-PLANÍCIE DA AMAZÔNIA CENTRAL VIA SENSORIAMENTO REMOTO E MODELAGEM HIDRÁULICA

PORTO ALEGRE

2020

ALICE CÉSAR FASSONI DE ANDRADE

MAPEAMENTO E CARACTERIZAÇÃO DO SISTEMA RIO-PLANÍCIE DA AMAZÔNIA CENTRAL VIA SENSORIAMENTO REMOTO E MODELAGEM HIDRÁULICA

Tese apresentada ao Programa de Pós-graduação em Recursos Hídricos e Saneamento Ambiental da Universidade Federal do Rio Grande do Sul, como requisito parcial à obtenção do grau de doutora.

Orientador: Rodrigo Cauduro Dias de Paiva

PORTO ALEGRE

2020

CIP - Catalogação na Publicação

Fassoni-Andrade, Alice

Mapeamento e caracterização do sistema rio-planície da Amazônia central via sensoriamento remoto e modelagem hidráulica / Alice Fassoni-Andrade. -- 2020.

167 f.

Orientador: Rodrigo Paiva.

Tese (Doutorado) -- Universidade Federal do Rio Grande do Sul, Instituto de Pesquisas Hidráulicas, Programa de Pós-Graduação em Recursos Hídricos e Saneamento Ambiental, Porto Alegre, BR-RS, 2020.

Elaborada pelo Sistema de Geração Automática de Ficha Catalográfica da UFRGS com os dados fornecidos pelo(a) autor(a).

ALICE CÉSAR FASSONI DE ANDRADE

MAPEAMENTO E CARACTERIZAÇÃO DO SISTEMA RIO-PLANÍCIE DA AMAZÔNIA CENTRAL VIA SENSORIAMENTO REMOTO E MODELAGEM HIDRÁULICA

Tese apresentada ao Programa de Pós-graduação em Recursos Hídricos e Saneamento Ambiental da Universidade Federal do Rio Grande do Sul, como requisito parcial à obtenção do grau de doutora.

Aprovado em: Porto Alegre, 2 de março de 2020.

_____

Prof. Dr. Rodrigo Cauduro Dias de Paiva – UFRGS
Orientador

_____

Prof. Dr. Walter Collischonn– UFRGS
Examinador

_____

Prof. Dr. Thiago Sanna Freire Silva – University of Stirling
Examinador

_____

Prof. Dr. Conrado de Moraes Rudorff – CEMADEN
Examinador

AGRADECIMENTOS

Apenas 0,2% da população brasileira possui doutorado[*] e apenas 26% dos pesquisadores com doutorado na área de engenharia são mulheres[**]. Portanto, me sinto privilegiada por finalizar esse doutorado. Agradeço aos contribuintes brasileiros que indiretamente pagaram a minha bolsa de estudos durante os quatro anos e espero que essa pesquisa contribua para o desenvolvimento científico do país.

Agradeço ao André pelo apoio e pelas diversas dificuldades e alegrias que passamos juntos. Agradeço aos meus pais pelas oportunidades de estudo e por sempre me apoiarem. Obrigada por acreditarem no meu potencial.

Sou grata a diversas pessoas que auxiliaram essa pesquisa. Agradeço ao Rodrigo pela confiança, orientação e amizade. Agradeço à diversos pesquisadores e amigos que contribuíram de forma essencial disponibilizando ou processando dados, revisando manuscritos, discutindo resultados e dando conselhos. Alguns deles: Adriana, Aline, Anderson, Artur, Ayan, Conrado, Cláudio, Daniel, Evlyn, Fernando, Hugo, Jean-François, João, Luna, Marie-Paule, Mino, Pedro, Sly, Vinícius e Walter. Também agradeço aos amigos de Porto Alegre pelas hospedagens: Gabriel, João, Luana, Nureyev e Renata.

Agradeço as seguintes instituições pelo suporte financeiro: Conselho Nacional de Desenvolvimento Científico e Tecnológico (CNPq), Coordenação de Aperfeiçoamento de Pessoal de Nível Superior (CAPES), Universidade Federal do Rio Grande do Sul (UFRGS) e Instituto de Pesquisas Hidráulicas (IPH). Em especial, agradeço aos professores do IPH e aos pesquisadores do grupo de pesquisa HGE pelo aprendizado e amizade. Também agradeço ao ex-coordenador Juan Martín e ao secretário Thiago por auxiliar em questões burocráticas.

Por último, gostaria de compartilhar que os momentos mais marcantes do doutorado podem ser agrupados em três: aqueles em que conheci os rios e lagos da Amazônia, aqueles em que recebi um feedback positivo de algum pesquisador que eu admirava, e aqueles em que consegui processar algum dado difícil ou ter uma boa ideia. Esses momentos foram tão espetaculares que agradeço a Deus por ter vivido tudo isso e por ter me dado saúde, inteligência e criatividade para desenvolver a pesquisa.

[*] Dado de 2019 da publicação *Education at a Glance*. *Organisation for Economic Co-operation and Development – OECD.*
[**] Dado de 2020 do programa Open Box.

Caro leitor,

Essa tese possui várias figuras bonitas.
Espero que te inspire para deixarmos a ciência mais atraente.

Boa leitura.

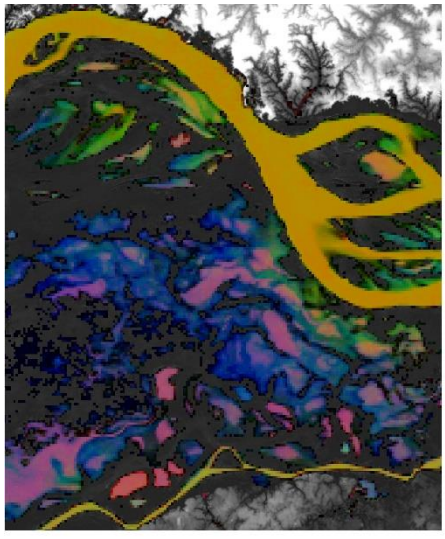

Sedimentos

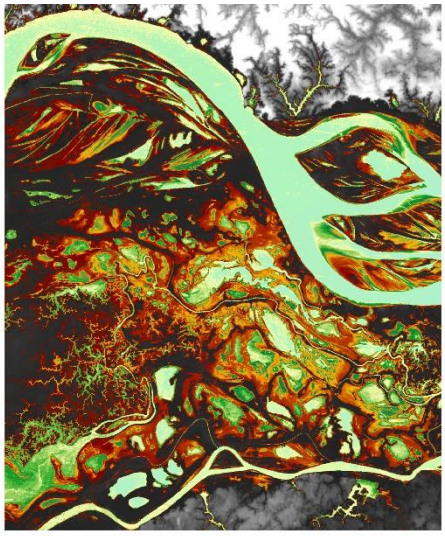

Topografia

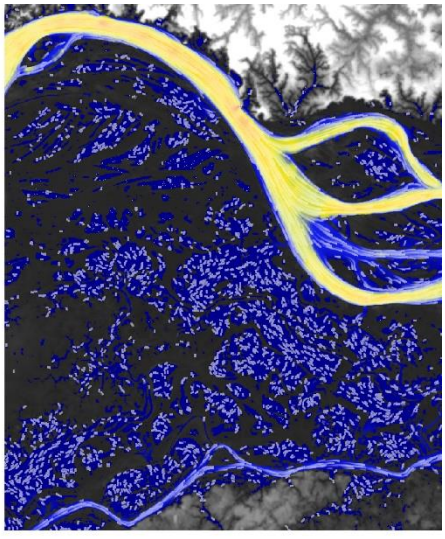

Hidrodinâmica

RESUMO

O rio Amazonas é o maior rio do mundo, e sua cheia anual promove uma inundação extensa, influenciando processos hidrológicos, o balanço de carbono e a distribuição e riquezas de espécies. No entanto, os processos relacionados à variação de sedimentos em suspensão nos lagos e rios, à topografia da planície de inundação e à troca de água entre o rio e a planície na região central da bacia ainda não são completamente compreendidos. O sensoriamento remoto e a simulação hidráulica são ferramentas que podem auxiliar esses estudos. O objetivo desta pesquisa é desenvolver técnicas de sensoriamento remoto e modelagem para mapear, compreender e caracterizar a dinâmica de sedimentos, a topografia e a hidrodinâmica do sistema rio-planície da Amazônia central. Foi desenvolvido um mapeamento da dinâmica de sedimentos nos rios e lagos dessa região considerando, pela primeira vez, águas com baixas concentrações de sedimentos e abrangendo uma área de 1900 x 600 km^2. A análise temporal de 15 anos de imagens permitiu avaliar a variação sazonal da concentração de sedimentos e a caracterização desse sistema. Por exemplo, lagos rasos aumentam a concentração de sedimentos no período de seca devido a ressuspensão promovida pelo vento, e recebem sedimentos do rio durante a cheia. Também foram desenvolvidos uma metodologia e um aplicativo para estimativa da elevação do terreno em áreas sazonalmente inundadas utilizando como dados de entrada séries temporais do nível da água e um mapa que representa a frequência de inundação. A nova técnica torna possível o mapeamento direto da topografia de lagos e a estimativa da curva cota-área-volume ativo de reservatórios utilizando dados de sensoriamento remoto. A partir desta metodologia, foi realizado de forma pioneira um mapeamento de alta resolução da topografia da planície de inundação da Amazônia abrangendo uma área de 837 x 266 km^2. Cerca de 50% dessa área permanece com profundidade menor que 2 m e 6 m nos períodos de água-baixa e água-alta, respectivamente. Esse mapeamento foi utilizado para a simulação hidráulica bidimensional do escoamento de água no rio Amazonas e na planície em uma área de 40 mil km^2. A simulação de três anos hidrológicos (2008 a 2010) permitiu a melhor compreensão de processos hidrológicos nesse sistema, como a troca de água entre o rio e a planície. A planície possui uma variação média anual de volume e de área inundada de 167,27 km^3 e 7,56 mil km^2, respectivamente. Os fluxos de água do rio para a planície são predominantes no início da enchente do rio e se tornam expressivos na cheia. Nesse período, também ocorre um fluxo expressivo de saída de água da planície para o rio. Na vazante predomina os fluxos para o rio e pode ocorrer entrada de água na planície por efeito de remanso. As técnicas desenvolvidas nessa pesquisa podem ser aplicadas a outros sistemas hidrológicos e com novos dados de satélites previstos para lançamento. Os mapeamentos desenvolvidos estão disponíveis para estudos hidrológicos, ecológicos e de gestão na região central da Amazônia.

Palavras-chave: Sedimentos em suspensão, topografia, cota-área-volume, lagos, planície de inundação, Flood2Topo app, fluxos de água, HEC-RAS.

ABSTRACT

Mapping and characterization of the central Amazon river-floodplain system by remote sensing and hydraulic modeling

The Amazon River is the largest river in the world, and the annual flood produces an extensive inundated area, influencing hydrological processes, carbon balance, and species diversity. However, the processes related to the variation of suspended sediments in lakes and rivers, the floodplain topography and the water exchange between river and floodplain in the central Amazon basin are not yet fully understood. Remote sensing and hydraulic simulation are tools that support these studies. The goal of this research is to develop remote sensing and modeling techniques to map, understand and characterize the sediment dynamics, topography and hydrodynamics of the central Amazon River-floodplain system. A mapping of sediment dynamics in rivers and lakes of this region was developed considering, for the first time, waters with low concentrations of sediments and covering an area of 1900 x 600 km^2. Temporal filtering of 15 years of images allowed to evaluate the seasonal variation of sediments concentration and to characterize this system. For example, in shallow lakes, the sediment concentration increases during dry seasons due to resuspension caused by wind, and during the flood due to the transport of sediments from the river. A methodology and an application for estimating terrain elevation in seasonally flooded areas were also developed using time series of water level and flood frequency map as input data. The new method allows to directly map topography of lakes and to estimate level-area-volume active relationship of reservoirs using remote sensing data. Based on this methodology, high-resolution mapping of the Amazon floodplain topography was performed covering an area of 837 x 266 km^2. About 50% of this area remains with depth less than 2 m and 6 m in low-water and high-water periods, respectively. This mapping was used for two-dimensional hydraulic simulation of water flow in the Amazon River and floodplain in an area of 40 thousand km^2. The simulation of three hydrological years (2008 to 2010) allowed a better understanding of hydrological processes in this system, such as the water exchange between the River and floodplain. The floodplain has an average annual variation in volume and flooded areas of 167.27 km^3 and 7.56 thousand km^2, respectively. Water flows from the River to floodplain are prevalent at the beginning of the river's flood and become expressive in the flood peak. During this period, there is also an expressive outflow from the floodplain to the River. In the falling period, flows to the River are predominant and water may enter the floodplain due to the backwater effect. The methods developed in this research can be applied to other hydrological systems and using new satellite data planned for launch. The mappings developed are available to hydrological, ecological and management studies in the central Amazon basin.

Keywords: Suspended sediments, topography, level-area-volume, lakes, floodplain, Flood2Topo app, water flows, HEC-RAS.

SUMÁRIO

CAPÍTULO 1. Introdução

1.1 Motivação desse estudo

A bacia do rio Amazonas é a maior do mundo, com uma área de drenagem de 6 milhões de km^2 e fluxo médio anual para o oceano de 200-220 mil $m^3.s^{-1}$. A região central da bacia possui cerca de 6500 lagos ao longo da planície de inundação adjacente ao rio Solimões-Amazonas (SIPPEL; HAMILTON; MELACK, 1992) e diversos canais que variam em forma, profundidade e conectividade (TRIGG et al., 2012). Essas planícies funcionam como reservatórios naturais e atenuam a onda de cheia (PAIVA et al., 2013). Possuem também grande importância nos fluxos de carbono, nutrientes e sedimentos, os quais sustentam ecossistemas diversos e criam condições favoráveis à pesca de subsistência de comunidades ribeirinhas (JUNK et al., 2012; MELACK et al., 2009). Além disso, os habitats de planície contribuem com a emissão de dióxido de carbono (210 ± 60 Tg C ano^{-1}, RICHEY et al., 2002) e metano (6,8 ± 1,3 Tg C ano^{-1}, MELACK et al., 2004) para a atmosfera. A bacia também possui grande importância na geração de energia hidrelétrica, sendo que os barramentos de usinas construídas podem afetar as planícies aluviais, a composição florística das florestas inundadas, e a pluma de sedimentos no estuário (DA ROCHA et al., 2019; FORSBERG et al., 2017; LATRUBESSE et al., 2017; RESENDE et al., 2019). Esses fatores, aliados à necessidade de avaliar o efeito das mudanças climáticas sobre o funcionamento do sistema rio-planície (SORRIBAS et al., 2016) e o desflorestamento (COE; COSTA; SOARES-FILHO, 2009; LEITE et al., 2012) ressaltam a importância do estudo da hidrologia superficial da bacia amazônica.

Nas últimas décadas, o desafio de estudar um sistema grande e complexo, como a bacia Amazônica, tem sido enfrentado com auxílio do sensoriamento remoto e a modelagem hidrodinâmica. Estudos utilizando dados de satélites mapearam áreas úmidas (ARNESEN et al., 2013; HESS et al., 2015), estimaram sedimentos em suspensão na superfície dos rios (LOBO; COSTA; NOVO, 2015; PARK; LATRUBESSE, 2014), avaliaram o nível da água no rio (SANTOS DA SILVA et al., 2012), os estoques de água (FRAPPART et al., 2011; TOURIAN; REAGER; SNEEUW, 2018) e a variação do nível da água na planície de inundação (ALSDORF et al., 2000; CAO et al., 2018). Modelos hidrológicos também permitiram ampliar a compreensão do funcionamento da hidrologia da Amazônia (PAIVA et al., 2013; WILSON et al., 2007). No entanto, ainda existem lacunas em relação à variação de sedimentos nos rios e nos lagos, à topografia da planície de inundação e à caracterização dos fluxos de água entre o rio e a planície de inundação.

A estimativa de sedimentos em suspensão na superfície dos rios foi realizada para diversos rios da Amazônia utilizando imagens orbitais (LOBO; COSTA; NOVO, 2015; MANGIAROTTI et al., 2012; MARTINEZ et al., 2009; MONTANHER et al., 2014; PARK; LATRUBESSE, 2014). No entanto, esses estudos são locais e, de forma geral, não consideraram rios com baixa concentração de sedimentos e lagos da planície. Em uma escala de bacia, ainda não foi realizado um mapeamento que facilite a compreensão da dinâmica espaço-temporal de sedimentos nesse ambiente. Esse mapeamento pode ser utilizado, por exemplo, para avaliar a relação entre a concentração de sedimentos e a riqueza de espécies de peixes, pássaros e plantas na Amazônia (JUNK et al., 2011, 2015; RODRIGUES, 2007, PARK & LATRUBESSE, 2015), auxiliar na classificação de tipologias de rios (RÍOS-VILLAMIZAR et al., 2020; SIOLI, 1984) e entender o sistema em termos de variação espaço-temporal de sedimentos e fluxos de água.

Muitos avanços também foram feitos para o mapeamento da topografia de corpos d'água utilizando o sensoriamento remoto. As abordagens atuais permitem a estimativa nas áreas temporariamente inundadas, e, de forma geral, necessitam da delimitação da área inundada de cada corpo d'agua individualmente (ARSEN et al., 2013; FENG et al., 2011; GETIRANA; CHUL; TSENG, 2018). Portanto, são abordagem dispendiosas em grandes regiões com lagos que podem ficar isolados e/ou conectados dependendo do nível da água. Assim, é necessário um avanço nas atuais metodologias para que a topografia seja estimada sistematicamente. Tal técnica permitiria criar bases de dados globais da topografia de lagos naturais e artificiais, como já existem para o volume de lagos (CRÉTAUX et al., 2011; SCHWATKE et al., 2015). Aplicada as áreas de água aberta da planície da Amazonas, o mapeamento poderia ser utilizado para estudos hidrológicos, ecológicos e geomorfológicos, como avaliar a profundidade da água na planície, avaliar o crescimento de espécies vegetais relacionadas a topografia da região sazonalmente inundada (JUNK; PIEDADE, 1997; SILVA; COSTA; MELACK, 2010) e entender a configuração dos canais, lagos e rios mapeados (LATRUBESSE, 2012).

As simulações hidráulicas representam o escoamento da água e fornecem informações importantes para a compreensão do sistema rio-planície, como extensão de área inundada, nível da água, velocidade e direção da água. Em escala regional, a modelagem hidráulica de um trecho do rio Solimões foi explorada por diferentes estudos (BAUGH et al., 2013; TRIGG et al., 2009; WILSON et al., 2007; YAMAZAKI et al., 2012). Em escala local, apenas três lagos da planície central do rio Amazonas foram estudados (BONNET et al., 2008, 2017; JI et al., 2019; PINEL et al., 2019; RUDORFF;

MELACK; BATES, 2014a). Apesar dos avanços no entendimento da troca de água rio-planície, os estudos regionais apontam algumas dificuldades ou limitações para a modelagem, como a falta de dados batimétricos, a correção dos dados topográficos e a limitação dos modelos. Por outro lado, os estudos locais detalhados não são capazes de fornecer um completo entendimento da troca de água rio-planície na bacia Amazônica. Assim, a utilização de um mapeamento topográfico sistemático e de alta resolução da planície de inundação permitiria a simulação hidráulica do escoamento da água de uma área extensa com boa representação da topografia. Essa simulação ampliaria a compreensão dos fluxos de água na planície de inundação, sua interação hidrodinâmica com o rio e seu efeito sobre o ecossistema.

1.2 Objetivo e perguntas científicas

O objetivo dessa pesquisa é desenvolver técnicas de sensoriamento remoto e modelagem para mapear, compreender e caracterizar a dinâmica de sedimentos, a topografia e a hidrodinâmica do sistema rio-planície da Amazônia central. Os artigos científicos abordam as seguintes perguntas específicas do objetivo geral da tese:

Como mapear a variação espaço temporal da concentração de sedimentos nos lagos e rios na Amazônia central? Qual é a variação sazonal da concentração de sedimentos nos lagos e rios? Quais os fatores que afetam essa variação da concentração de sedimentos?

É possível estimar sistematicamente a topografia de lagos com dados de satélites atualmente disponíveis? Quais as vantagens e limitações dessa técnica? Qual a aplicabilidade global do método?

Qual é a variação topográfica dos lagos e canais da planície de inundação do rio Amazonas? Qual é a profundidade e o volume da água nessa planície nos períodos de cheia e estiagem? Por que a profundidade da água na planície tem um padrão de decrescente de montante para jusante ao longo rio?

Qual é a extensão de área inundada, o volume armazenado e a profundidade da água na planície de inundação do rio Amazonas? Qual o fluxo de água do rio que vai para a planície e vice-versa? Qual é a circulação da água dentro da planície de inundação ao longo do ano? Como as variáveis hidrológicas são afetadas em anos de seca e cheia extremas?

1.3 Organização da tese

A tese está dividida em sete capítulos, sendo a estrutura geral e a área foco do estudo apresentadas na Figura 1.1. O primeiro capítulo é introdutório e o segundo aborda as características gerais da bacia amazônica, as técnicas e dados de sensoriamento remoto aplicados à hidrologia superficial da Amazônia e uma revisão dos modelos hidráulicos, bem como os estudos realizados para entender os fluxos de água no sistema rio-planície da Amazônia. Os quatro capítulos seguintes são elaborados em formato de artigos científicos. O capítulo 3 trata de um mapeamento espaço-temporal de sedimentos em suspensão nos rios e lagos da Amazônia. O capítulo 4 apresenta um novo método para estimativa da topografia de lagos utilizando dados de satélites. O capítulo 5 mostra a aplicação dessa técnica para mapear a topografia da planície de inundação do rio Amazonas. O último artigo (capítulo 6) utiliza a topografia da planície de inundação, estimada no capítulo 5, para aplicação de um modelo hidráulico bidimensional. Finalmente, no capítulo 7, as principais conclusões e observações da tese são destacadas em relação ao avanço na hidrologia do sistema rio-planície da Amazônia e as técnicas desenvolvidas.

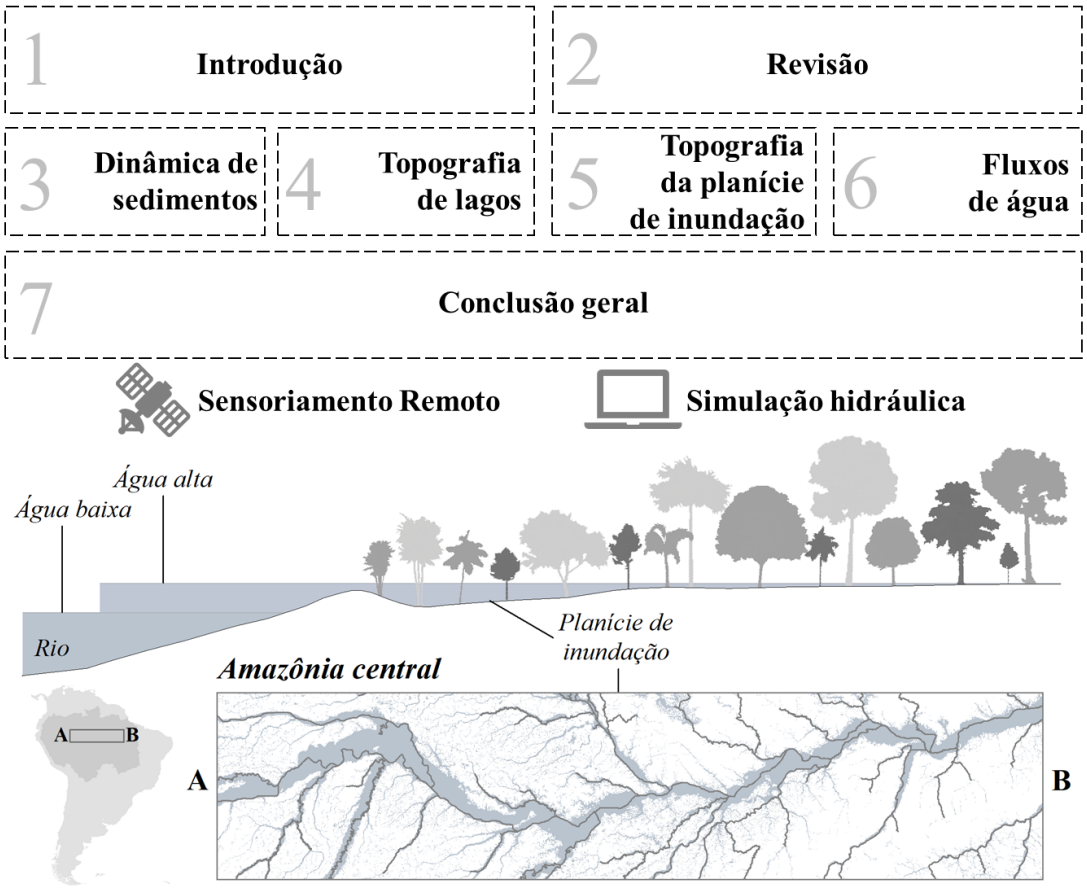

Figura 1.1. Esquema geral da estrutura da tese e área foco do estudo.

CAPÍTULO 2. Fundamentos teóricos

2.1 Bacia Amazônica

A bacia Amazônica representa a maior e a mais complexa rede de rios e de áreas úmidas do mundo com uma área de drenagem de 6 milhões de km^2 (LATRUBESSE et al., 2017). A bacia abrange seis países - Bolívia, Brasil, Colômbia, Equador, Guiana, Peru e Venezuela, sendo 63% de sua área localizada no Brasil, e inclui o primeiro, o quinto e o sexto maiores rios do mundo em vazão, os rios Amazonas, Negro e Madeira (Figura 2.1). O rio principal, denominado rio Solimões até a confluência com o rio Negro, e rio Amazonas deste ponto em diante, possui extensão de aproximadamente 6900 km sentido oeste-leste e desagua no Oceano Atlântico (Figura 2.1). O fluxo médio anual para o oceano é de 200-220 mil $m^3.s^{-1}$, o qual inclui os rios Amazonas e Tocantins (RICHEY et al., 1989) e representa entre 16% a 18% do fluxo de água doce global para o oceano (LATRUBESSE et al., 2017). Além disso, o rio Amazonas tem uma descarga média anual de sedimentos em suspensão de 1200 $Mt.ano^{-1}$ em Óbidos (MEADE et al., 1985).

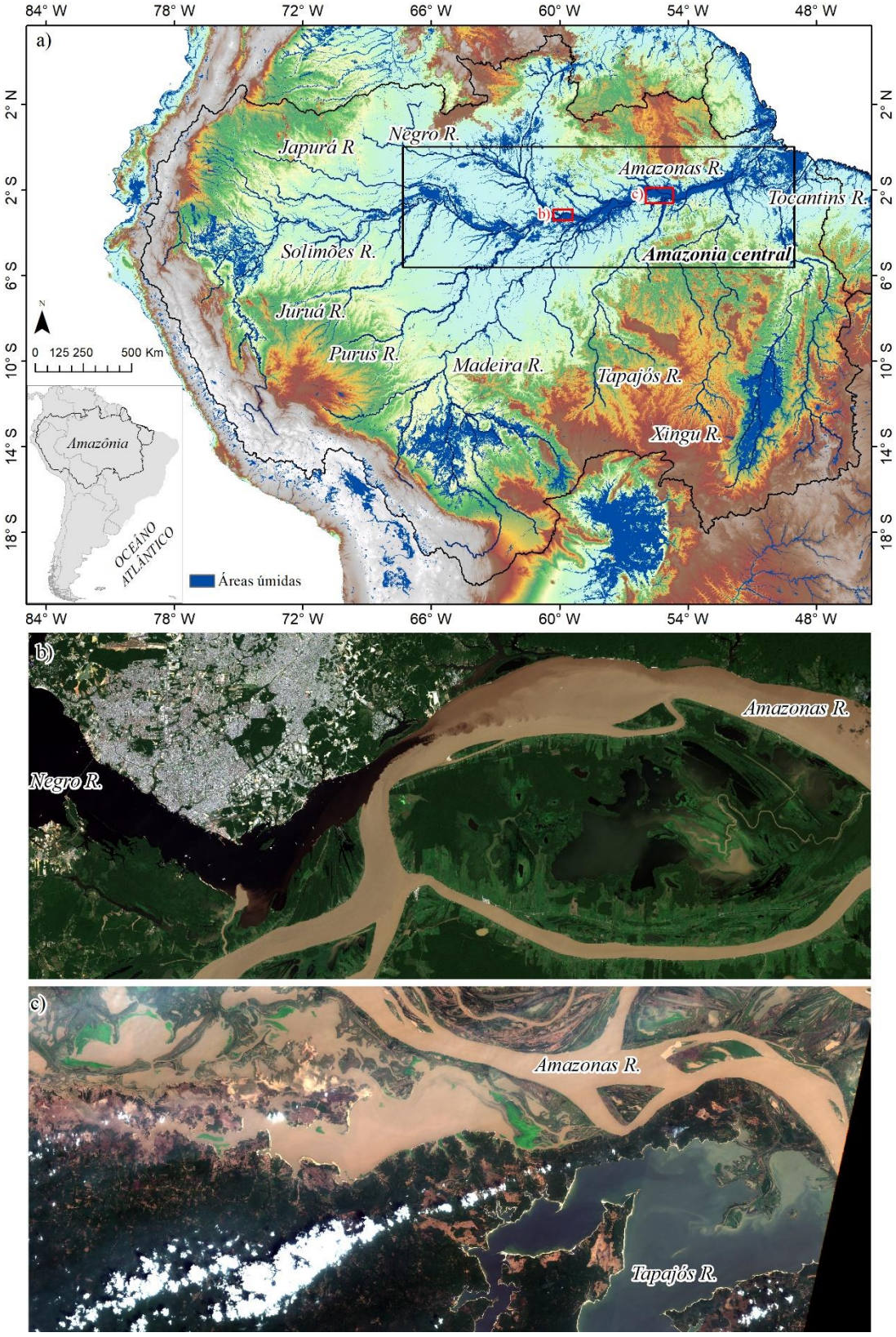

Figura 2.1 a) Localização da Bacia Amazônica. Imagens do satélite Sentinel-2 do encontro das águas b) do rio Negro com o rio Amazonas - 2/Jul/2018; Sentinel-2/MSI, tiles T21MTS e T20MRB; e c) do rio Amazonas com o rio Tapajós - 12/Jun/2017; Sentinel-2/MSI, tiles T21MXT e T21MYT.

Em grandes bacias hidrográficas tropicais, como a bacia amazônica, o hidrograma normalmente exibe um pico de inundação por ano (JUNK; BAYLEY; SPARKS, 1989). A cheia do rio Amazonas ocorre em Maio/Junho e o período de água baixa em outubro/novembro, com uma amplitude de variação do nível da água menor que 13 m (BIRKETT et al., 2002). A declividade da superfície da água entre a confluência com o rio Negro até o oceano é muito baixa e variável ao longo do ano, fazendo com que o efeito de remanso regule o escoamento nos principais tributários do rio Amazonas. Outro efeito identificado até 1000 km a montante da foz do rio Amazonas, é a influência da maré (KOSUTH et al., 2009). Grande parte do volume da água do rio é escoada para a planície de inundação e essa tem um importante papel no armazenamento da água do rio (PAIVA et al., 2013).

Os rios da bacia amazônica são classificados de acordo com parâmetros físicos e químicos da água em rios de água branca, preta ou clara (SIOLI, 1956). Rios de água branca que drenam a Cordilheira dos Andes, como os rios Solimões e Madeira, transportam grande quantidade de sedimentos ricos em nutrientes. Já os rios de água preta são ricos em ácidos húmicos, os quais são lixiviados de solos podzólicos em florestas do noroeste da bacia e que dão à água uma coloração marrom-avermelhada. Os rios de água clara, como o rio Tapajós, são transparentes e esverdeados com baixa concentração de sedimentos e sólidos dissolvidos. Como exemplo, as Figura 2.1b e c apresentam imagens de satélites dos rios de água preta, água branca e água clara onde as diferenças na cor da água são facilmente observadas. As diferentes características dos rios têm implicações no ecossistema local como diversidade de peixes, fertilidade do solo e abundância de mosquitos (JUNK et al., 2011).

O foco desse estudo é a planície aluvial do rio Solimões-Amazonas na região central da bacia Amazônica (quadro preto na Figura 2.1a), que corresponde às áreas permanentemente alagadas e/ou inundáveis na cheia anual. Ao longo da planície, as áreas de água aberta (vegetação inundada) aumentam (reduzem) de montante para jusante no sentido do escoamento do rio (HESS et al., 2015). Mertes et al. (1996) caracterizaram a planície de acordo com características geomorfológicas. No trecho a montante do rio Solimões, os lagos e canais tendem a ser estreitos e confinados por diques marginais e barras de deposição (*scroll bar*), enquanto no trecho médio, além dos lagos estreitos, a planície possui lagos maiores de formato circular. À jusante, entre a confluência do rio Madeira e do rio Tapajós, a planície é dominada por grandes lagos, rasos e irregulares

formados por deposição de material fino devido ao fluxo que extravasa o nível de margens planas e escoa por sobre as margens. Já a planície à jusante da confluência do rio Tapajós até o estuário possui poucos lagos.

A topografia da planície de inundação é um dos fatores que promove a variação espaço-temporal do fluxo da água na planície (ALSDORF et al., 2007; ALSDORF, 2003). No início da inundação, a superfície da água é variável e controlada pela topografia dos canais, lagos e depressões na planície, e durante a cheia, o fluxo da planície é mais parecido com o do rio (ALSDORF et al., 2007). Além de receber água do rio principal e dos tributários locais, a planície recebe água do escoamento local, da precipitação, e do lençol freático, contribuindo para a mistura de águas com diferentes características (MERTES, 1997; MERTES et al., 1995). Assim, o pulso de inundação anual do rio promove a troca de sedimentos e nutrientes com a planície e altera as condições ecológicas estabelecidas na planície durante o período de seca (JUNK; BAYLEY; SPARKS, 1989; MELACK et al., 2009). Portanto, estudos que busquem compreender os processos hidrológicos e ecológicos nas planícies de inundação da Amazônia são importantes para entender o papel global das planícies em relação ao funcionamento ecológico, uma vez que a planície possui ecossistemas próprios adaptados a inundação e têm contribuição para a geração de gases de efeito estufa.

2.2 Sensoriamento remoto aplicado a hidrologia superficial da Amazônia

O sensoriamento remoto tem sido utilizado como ferramenta em estudos de águas superficiais na bacia amazônica auxiliando na compreensão de processos hidrológicos e ecológicos nos rios e nas planícies de inundação. A Figura 2.2 exemplifica os parâmetros que foram mensurados por satélites na Amazônia, tais como a variação do armazenamento de água pelo satélite *Gravity Recovery and Climate Experiment* (GRACE), nível da água no rio e na planície por altímetros (ICESat, Jason, ENVISAT e TOPEX/Poseidon), a extensão de área inundada, o tipo de vegetação e a variação do nível da água na planície de inundação por radares (JERS-1, ALOS e Radarsat-2), estimativas de componentes da água, tais como sedimento e clorofila, nos rios e lagos (MODIS, Landsat e Sentinel) e também a elevação do terreno (SRTM DEM e MERIT DEM).

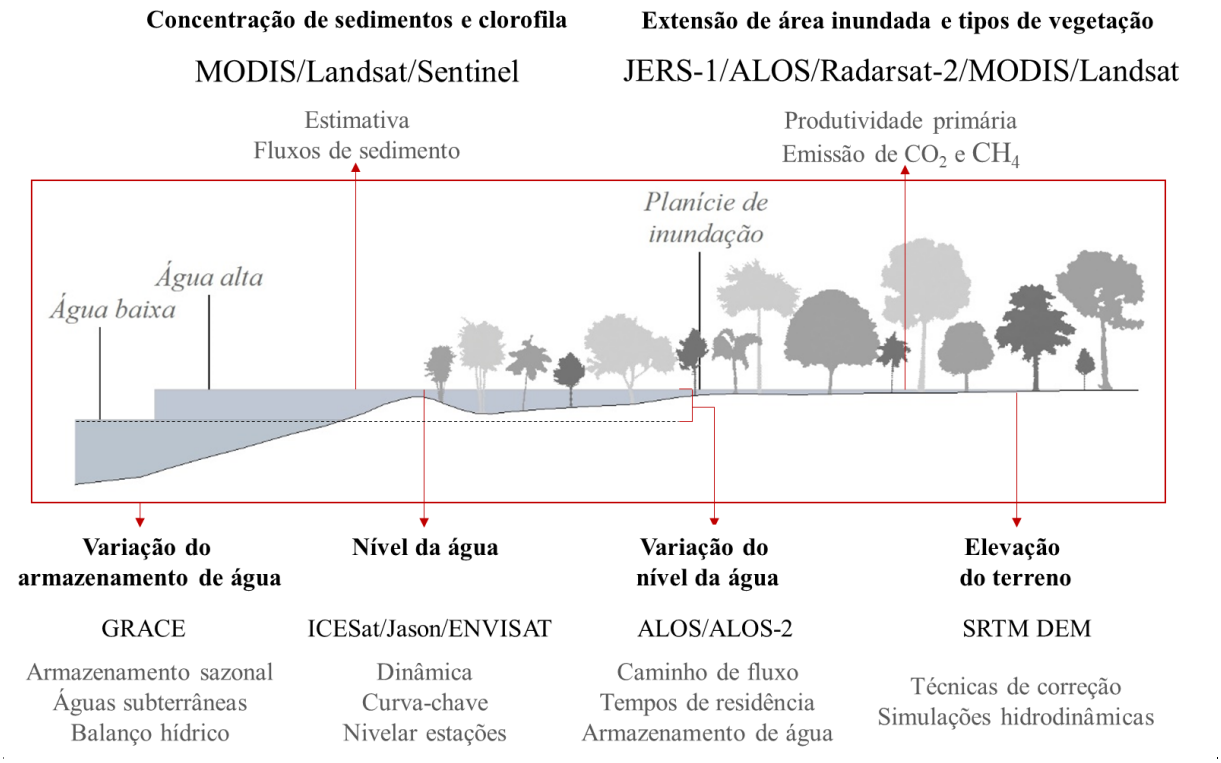

Figura 2.2 Exemplos de variáveis hidrológicas mensuradas por satélites e aplicações na Amazônia.

2.2.1 Extensão de área inundada

Hess et al. (2003, 2015) utilizaram imagens do *Japanese Earth Resources Satellite-1* (JERS-1, banda L) para mapear áreas úmidas e tipos de vegetação nos períodos de água baixa e alta (disponível em < https://daac.ornl.gov/cgi-bin/dsviewer.pl?ds_id=1284>). Sensores SAR na banda L são comumente utilizados para essa aplicação pois esse comprimento de onda é pouco ou nada afetado pela cobertura de nuvens e condições atmosféricas, e têm capacidade de penetrar o dossel da vegetação. Hess et al. (2015) estimaram que a área úmida representa 14% da área total da bacia sendo 77% de vegetação lenhosa, 14% macrófita aquática e 9% de água aberta no período da cheia. Esse mapeamento deu suporte para outros estudos, como estimativa de taxas regionais de emissão de metano (MELACK et al., 2004) e do balanço de carbono orgânico (RICHEY et al., 2002, 2013). Além disso, foi utilizado como dado de entrada e validação de modelos hidrológicos e hidráulicos (BONNET et al., 2017; PAIVA et al., 2013; RUDORFF et al., 2014; WILSON et al., 2007).

Outros estudos foram realizados para estimar a área de inundação na bacia Amazônica, como Arnesen et al. (2013), que utilizaram dados do satélite ALOS (sensor

PALSAR e banda L) para mapear a planície de inundação do Lago Grande de Curuai. Posteriormente, esse mapeamento foi feito com o mesmo sensor para toda a bacia (CHAPMAN et al., 2015, disponível em <https://wetlands.jpl.nasa.gov>). Além do mapeamento na Amazônia, Hamilton et al. (2002) compararam a área de inundação de grandes planícies de inundação da América do Sul, como a do rio Amazonas, Ilha do Bananal (rio Araguaía) e planícies do Pantanal (rio Paraguai), utilizando o sensor *Scanning Multichannel Microwave Radiometer* (SMMR, satélite Nimbus-7).

2.2.2 Tipos de vegetação em áreas úmidas

A vegetação da planície de inundação também foi mapeada em escala regional. Furtado, Silva e Novo (2016) analisaram a melhor configuração de polarização de imagens *Synthetic Aperture Radar* (SAR) do sensor Radarsat-2 (banda C) para mapeamento de tipos de vegetação na planície do Lago Grande de Curuai. Ferreira-Ferreira et al., (2014) mapearam o tipo de vegetação na reserva de desenvolvimento sustentável Mamirauá utilizando dados ALOS/PALSAR e mostraram que o tipo de vegetação está relacionado com o padrão de inundação combinando classes de duração de inundação e vegetação. A sazonalidade da cobertura de macrófitas aquáticas em várzeas também está relacionada com o pulso de inundação, uma vez que a variação do nível da água nos lagos afeta seu crescimento. Essa vegetação tem grande importância na fixação e ciclagem do carbono, com contribuição de 34% na produtividade primária estimada em áreas de inundação (MELACK et al., 2009). O mapeamento, a estimativa da produtividade primária e/ou o efeito do pulso de inundação sobre o crescimento horizontal e vertical da vegetação na planície de inundação foram caracterizados utilizando dados orbitais por diversos trabalhos (COSTA, 2005, 2004; MARTINEZ; LE TOAN, 2007; SARTORI et al., 2011; SILVA; COSTA; MELACK, 2009, 2010; SILVA; MELACK; NOVO, 2013). Técnicas de sensoriamento remoto também foram utilizadas para avaliar a mortandade da floresta de igapó após a construção do reservatório de Balbina, quando o pulso de inundação anual foi alterado (RESENDE et al., 2019).

2.2.3 Concentração de sedimentos em suspensão e clorofila

A estimativa da concentração de sedimentos em suspensão por sensoriamento remoto foi feita em vários rios da bacia Amazônia. Montanher et al. (2014) buscaram um modelo empírico global para a concentração de sedimentos de rios de água branca

utilizando dados do satélite Landsat 5. No entanto, os autores constataram que modelos locais possuem maior acurácia devido às diferenças das propriedades da água em cada local. Park e Latrubesse (2014) também estabeleceram modelos empíricos locais para três estações em rios de água branca utilizando o sensor MODIS. Os autores obtiveram baixos valores de RMSE da concentração de sedimentos em relação a um modelo considerando todas as estações, e mostraram também que os modelos regionais podem ser mais acurados quando avaliados de forma individualizada em períodos de vazante e de enchente do rio. Outros trabalhos foram realizados para compreender o fluxo de sedimentos nos rios de água branca da bacia utilizando dados MODIS, como para o rio Madeira (VAUCHEL et al., 2017; VILLAR et al., 2013), o rio Solimões (VILLAR et al., 2017) e o rio Amazonas (MANGIAROTTI et al., 2012; MARTINEZ et al., 2009). Nos rios de água preta e clara, devido à baixa concentração, apenas um estudo foi realizado para estimativa de sedimentos no rio Tapajós utilizando imagens Landsat (LOBO; COSTA; NOVO, 2015).

Os trabalhos apresentados possuem enfoque nos rios e mostram a dificuldade na criação de um único modelo acurado para a bacia. Nos lagos da planície de inundação a dificuldade é ainda maior devido a lacuna de dados de monitoramento. A estimativa de sedimentos em lagos da planície foi desenvolvida utilizando imagens de sensores orbitais para o Lago Grande de Curuai (ALCÂNTARA et al., 2010; BARBOSA et al., 2009; BOURGOIN et al., 2007). Com exceção dessa planície representativa do trecho baixo do rio Amazonas, poucos trabalhos locais ou regionais foram feitos para entender a dinâmica de sedimentos na planície utilizando imagens de satélite (PARK; LATRUBESSE, 2017). A clorofila também foi mapeada nos lagos da planície do trecho baixo do rio Amazonas, sendo que maiores concentrações foram observadas no início da vazante em setembro (NOVO et al., 2006).

2.2.4 Nível da água

A altimetria por satélite é uma ferramenta útil para estimar o nível da água em áreas de difícil acesso ou pouco monitoradas como a Amazônia. Diversos satélites foram utilizados nos rios e planícies da bacia (ex.: ICESat, Jason, ENVISAT e TOPEX/Poseidon). Calmant et al. (2012), Hall et al. (2012) e Moreira (2016) utilizaram a altimetria para nivelar estações fluviométricas de monitoramento do nível dos rios, uma vez que muitas das estações de monitoramento na bacia possuem uma referência arbitrária. A altimetria também foi utilizada nos rios para avaliar padrões espaciais e

temporais de variações de nível na água e os gradientes da superfície da água (BIRKETT et al., 2002), derivar curvas chaves (LEON et al., 2006; PARIS et al., 2016; ZAKHAROVA et al., 2006) e validar modelos hidrodinâmicos (PAIVA et al., 2013; WILSON et al., 2007; YAMAZAKI et al., 2012).

A utilização da altimetria na planície de inundação ainda foi pouco explorada. Assumindo que os níveis mínimos da águas superficiais coincidam com o nível de base do lençol freático, Pfeffer et al. (2014) forneceram mapas de baixa água do lençol freático na Amazônia central com base em dados de altimetria nos rios e na planície. Santos da Silva et al. (2012) avaliaram a dinâmica de variação do nível no rio e em algumas planícies da bacia. Na planície da bacia do rio Negro, a altimetria foi utilizada para avaliar variações espaço-temporais do volume de água, não tendo sido encontrada relação entre o volume de água e a área inundada (FRAPPART et al., 2005). De forma similar, a dinâmica de inundação da planície da bacia do alto rio Madeira foi caracterizada, observando uma variação de 10 km^3 a 94 km^3 no volume armazenado na planície (OVANDO et al., 2018).

2.2.5 Variação do nível da água

A técnica de interferometria diferencial de imagens SAR permite obter informações sobre as alterações em deslocamentos de alvos na superfície, como a variação do nível da água na planície de inundação (ALSDORF et al., 2000). O processamento interferométrico utilizando a banda L do satélite ALOS permitiu Alsdorf et al. (2007, 2005, 2000) detectarem pequenas mudanças da superfície da água em áreas de vegetação inundada da Amazônia. Os autores mostraram que as velocidades e direções de fluxo de água na planície podem mudar com a passagem da onda de cheia. Antes da cheia, os fluxos são controlados pela topografia local e durante a cheia o fluxo é mais parecido com o do rio Amazonas e, portanto, a superfície da água não é sempre equivalente ao nível do rio (ALSDORF et al., 2007). Cao et al. (2018) também mostraram a complexidade dos padrões das variações do nível da água na planície de inundação, localizada na confluência do rio Solimões com o rio Japurá, utilizando dados do ALOS-2.

2.2.6 Variação do armazenamento de água

O satélite GRACE permite avaliar a variação no armazenamento de água através de medidas das mudanças gravitacionais da Terra. Frappart et al. (2019) estimaram as

variações espaço-temporais da anomalia do armazenamento de águas subterrâneas entre 2003 e 2010 na bacia Amazônica a partir da decomposição do armazenamento total de água, obtido pelo GRACE, nas contribuições individuais (superfície, umidade do solo e subterrânea). Os autores mostraram que as variações sazonais do armazenamento de águas subterrâneas representam entre 20 e 35% das variações sazonais do volume total da bacia. Anteriormente, Frappart et al. (2011) avaliaram anomalias das águas subterrâneas na bacia do rio Negro, e Alsdorf et al. (2010) avaliaram o armazenamento sazonal da água nas planícies de inundação central da Amazônia. Também foram estimados o total de água drenada na bacia (1766 km^3) e o tempo de residência da água armazenada (2 meses), isto é, o tempo em que a água que entra na bacia por precipitação permanece antes de sair por escoamento ou evapotranspiração (TOURIAN; REAGER; SNEEUW, 2018). Além disso, os autores mostraram que, em média, 65% da água drenada é armazenada como água de superfície. Os dados GRACE também foram utilizados como suporte para análise de secas e cheias extremas na bacia Amazônica, mostrando como o armazenamento varia nesses eventos (CHEN et al., 2009a; CHEN; WILSON; TAPLEY, 2010; FRAPPART et al., 2012).

2.2.7 Elevação do terreno

A interferometria também foi utilizada para elaborar Modelos Digitais de Elevação – MDEs, como o *Shuttle Radar Topography Mission* – SRTM – banda C (FARR et al., 2007b). Esse modelo foi utilizado em várias simulações hidrodinâmicas na Amazônia (PAIVA et al., 2013; RUDORFF; MELACK; BATES, 2014b; TRIGG et al., 2009; WILSON et al., 2007; YAMAZAKI et al., 2012) mas é afetado pela cobertura de vegetação ou outros objetos na superfície e possuem erros como o viés absoluto, ruídos do tipo *speckle* (aspecto granulado na imagem devido à presença aleatória de pixels com valores extremos) e *stripe noise* (ruído em forma de listras). Dessa forma, métodos para correção desses erros foram aplicados para estudos locais na Amazônia (BAUGH et al., 2013; PINEL et al., 2015; RUDORFF; MELACK; BATES, 2014b; YAMAZAKI et al., 2012). Recentemente, modelos globais ou quase globais foram disponibilizados com a correção do viés provocado pela vegetação (O'LOUGHLIN et al., 2016a) e de outros erros presentes, além da vegetação (YAMAZAKI et al., 2017).

2.2.8 Novos satélites

Como mostrando, diferentes sensores e técnicas de sensoriamento remoto foram utilizados para estimar variáveis hidrológicas na bacia Amazônica. Existe a expectativa em futuros satélites que ampliarão oportunidades para a geração de novos dados e técnicas em pesquisas hidrológicas, como o satélite *Surface Water and Ocean Topography* (SWOT). Esse satélite será lançado em 2021 para estudo de rios e lagos e será utilizado também para estimativa da vazão (BIANCAMARIA; LETTENMAIER; PAVELSKY, 2016; DURAND et al., 2010; PAVELSKY et al., 2014). Além do SWOT, os radares NISAR (banda L e S; VILLANO et al., 2018) e Tandem-L serão lançados em 2020 e em 2022, respectivamente. Recentemente também foram lançados os seguintes satélites: (i) o altímetro ICESat-2 em setembro de 2018, (ii) O GRACE-FO em maio de 2018 que é continuação da missão GRACE, (iii) O altímetro Sentinel-3A em fevereiro de 2016 e (vi) o Sentinel-3B em abril de 2018, que fazem parte da constelação Sentinel-3.

2.3 Modelagem hidráulica

2.3.1 Fundamentos

A representação do escoamento da água, como a propagação de um pulso de cheia no rio e a inundação da planície, pode ser feita a partir de modelos hidráulicos. Esses também fornecem estimativas de áreas de inundação, profundidade da água, direção e velocidade da água, dentre outras variáveis hidrológicas. As simulações são utilizadas para auxiliar ações de gestão, como o planejamento de contingência para inundação, avaliação de inundações em barragens, simulação do transporte de sedimentos, dentre outras aplicações, como auxiliar a compreensão de sistemas naturais.

Os modelos hidráulicos podem ser diferenciados pelas equações que representam o escoamento da água, sendo que a escolha do modelo depende dos objetivos e da escala do estudo (BATES et al., 2005). Por sua vez, tais equações são caracterizadas pela dimensionalidade na representação do domínio espacial e do fluxo da água. Modelos 0D não envolvem a representação de dimensão espacial (e.g. reservatório concentrado), enquanto os modelos unidimensionais (1D) e bidimensionais (2D) são derivados das equações de Navier-Stokes (3D). A descrição de modelos classificados segundo essa abordagem é feita a seguir e resumida na Tabela 2.1 (Modificada de Néelz, Pender e Britain, 2009 e Pender, 2006).

Tabela 2.1 Modelos hidráulicos de acordo com a dimensionalidade e equações (Modificada de Néelz, Pender e Britain, 2009 e Pender, 2006)

Modelo	Descrição	Exemplos
1D	Equações unidimensionais de Saint-Venant	Mike 11, HEC-RAS, MGB-IPH TELEMAC-MASCARET 1**,** SOBEK
1D+	1D e armazenamento na planície de inundação	Mike 11, HEC-RAS, MGB-IPH TELEMAC-MASCARET 1, SOBEK
2D-	2D com simplificações na equação de conservação de momento	HEC-RAS, LISFLOOD-FP, JFLOW
2D	Equações de águas rasas (ou 2D Saint-Venant)	HEC-RAS, Mike 21, SOBEK, TELEMAC-2D
2D+	2D com velocidades verticais usando eq. da continuidade	TELEMAC-3D
3D	Equações de Navier Stokes	IPH-ECO, Mike 3, Delft3D FM

2.3.1.1 Modelos unidimensionais

Modelos 1D estão embasados nas equações unidimensionais de Saint-Venant, que são obtidas integrando as equações de Navier-Stokes sobre a seção transversal do fluxo. Para isso, assume-se que (i) o escoamento é unidimensional, (ii) a velocidade é constante na seção transversal, (iii) o nível da água ao longo da seção é horizontal, (iv) a curvatura da linha d'água e as acelerações são pequenas, (v) a pressão é hidrostática, (vi) a declividade do fundo do canal é pequena, (vii) os efeitos de forças de atrito com o fundo e a viscosidade turbulenta são estimados através de leis semelhantes ao do escoamento permanente (CUNGE; HOLLY JR; VERWEY, 1980).

As equações de Saint-Venant são formadas pela equação da continuidade (eq. 2.1) que representa a conservação de massa e pela equação da quantidade de movimento (eq. 2.2) que representa as forças que agem sobre o escoamento (CUNGE; HOLLY JR; VERWEY, 1980; TUCCI, 2005). O lado esquerdo da equação da quantidade de movimento (eq. 2.2) se refere aos termos da inércia local (1) e da inércia advectiva (2). O lado direito representa as forças externas e internas agindo no fluído: pressão (3), gravidade (4) e atrito (5).

$$\frac{\partial A}{\partial t} + \frac{\partial Q}{\partial x} = q \tag{2.1}$$

$$\underbrace{\frac{\partial Q}{\partial t}}_{1} + \underbrace{\frac{\partial \left(Q^2/A\right)}{\partial x}}_{2} = \underbrace{-gA\frac{\partial h}{\partial x}}_{3} + \underbrace{gAS_0}_{4} - \underbrace{gAS_f}_{5} \tag{2.2}$$

Sendo Q a vazão, h a profundidade, t o tempo, B a largura da seção transversal, x a distância no sentido longitudinal, g a aceleração da gravidade, A a área da seção transversal, q o fluxo lateral de entrada e saída por unidade de comprimento, S_0 a

declividade do fundo; S_f a perda de energia por atrito com o fundo, as margens e efeitos turbulentos.

Alguns termos da equação da quantidade de movimento (eq. 2.2) podem ser desconsiderados resultando na simplificação dos modelos, com códigos de programação mais acessíveis e ganho na eficiência computacional. Um exemplo dessa simplificação são os modelos onda cinemática, Muskingum e Muskingum-Cunge (CHANSON, 2004; CUNGE, 1969; FREAD, 1993) que consideram apenas os termos da gravidade (4) e atrito (5). Outra simplificação, considerada um pouco mais completa, é a resultante do uso dos termos de pressão (3), gravidade (4) e atrito (5), resultando no modelo não inercial. Por último, o modelo conhecido como inercial, ou inercial local, desconsidera apenas o termo da inércia advectiva (2) da equação da quantidade de movimento (BATES; HORRITT; FEWTRELL, 2010). Esses modelos são comumente utilizados como módulo de propagação de vazão em modelos hidrológicos.

Modelos 1D supõem que o fluxo da água está alinhado com a linha central do canal do rio e dessa forma, o fluxo na planície de inundação, considerado paralelo ao canal, pode não ser adequadamente representado. Por outro lado, a abordagem 1D+, também referida como quasi-2D, considerada o rio 1D e a planície como um reservatório ou como células de armazenamento. Assim, é considerado o efeito de atenuação na onda de cheia do rio provocado pelo armazenamento de água na planície.

2.3.1.2 Modelos bidimensionais

As equações 2D de águas rasas (ou equações bidimensionais de Saint-Venant) podem ser obtidas similarmente as equações 1D, ou seja, pela integração vertical das equações de Navier-Stokes entre o fundo e a superfície considerando as direções cartesianas x e y (eqs. 2.3, 2.4 e 2.5). Nessa situação, o fluxo é horizontal com valores médios na vertical. Os termos das equações 2.4 e 2.5 representam as seguintes forças: inércia (1 e 2), pressão e gravidade (3), atrito do fundo (4), força de Coriolis (5), efeitos de turbulência (6) e tensão de cisalhamento do vento (7).

$$\frac{\partial h}{\partial t} + \frac{\partial uh}{\partial x} + \frac{\partial vh}{\partial y} = 0 \tag{2.3}$$

$$\underbrace{\frac{\partial uh}{\partial t}}_{1} + \underbrace{u\frac{\partial uh}{\partial x} + v\frac{\partial uh}{\partial y}}_{2} = \underbrace{-gh\frac{\partial H}{\partial x}}_{3} - \underbrace{\frac{gn^2}{h^{\frac{7}{3}}}|u|u}_{4} + \underbrace{2\omega sen\varphi\, h\, v}_{5} + \underbrace{A_t\nabla^2 hu}_{6} + \underbrace{\tau_x}_{7} \tag{2.4}$$

$$\underbrace{\frac{\partial vh}{\partial t}}_{1} + \underbrace{u\frac{\partial vh}{\partial x} + v\frac{\partial vh}{\partial y}}_{2} = \underbrace{-gh\frac{\partial H}{\partial x}}_{3} - \underbrace{\frac{gn^2}{h^{\frac{7}{3}}}|v|v}_{4} + \underbrace{2\omega sen\varphi\, h\, u}_{5} + \underbrace{A_t\nabla^2 hv}_{6} + \underbrace{\tau_y}_{7} \qquad (2.5)$$

Sendo $u\ e\ v$ as velocidades médias na direção de x e y, respectivamente, H a elevação da água, ω a velocidade angular da terra, φ a latitude, A_t o coeficiente de viscosidade turbulenta, τ_y é a tensão de cisalhamento do vento.

As equações 2.3, 2.4 e 2.5 também podem ser obtidas considerando a variação vertical da velocidade, i.e., nas direções cartesianas x e z, no entanto, essa abordagem não é considerada na revisão dos modelos apresentados na Tabela 2.1. De modo similar à formulação unidimensional, é possível desconsiderar os termos de inercia (1 e 2) resultando no modelo não inercial, e negligenciar os termos de inércia e pressão (1, 2 e 3), resultando no modelo onda cinemática. Os modelos 2D com formulações simplificadas são classificados como abordagem 2D-, e na abordagem 2D+ o fluxo tridimensional é obtido a partir da resolução 2D em planos horizontais em que a velocidade vertical é obtida pela equação da continuidade.

É comum o acoplamento de modelos 1D-2D, onde o rio e a planície são representados de forma unidimensional e bidimensional, respectivamente. A vantagem dessa abordagem é a eficiência computacional já que a geometria do canal não é representada por uma grade detalhada. Por outro lado, esses modelos não consideram a transferência de forças do rio para a planície.

2.3.1.3 Modelos tridimensionais

As equações de Navier-Stokes (eqs. 2.6, 2.7 e 2.8) representam o escoamento nas três dimensões ($x,\ y$ e z), caracterizando a abordagem 3D. Normalmente as equações assumem uma superfície livre e pressão hidrostática. Os termos das equações 2.7 e 2.8 representam as seguintes forças: inércia (1 e 2), gravidade (3), difusão turbulenta (4), Coriolis (5).

$$\frac{\partial u}{\partial x} + \frac{\partial v}{\partial y} + \frac{\partial w}{\partial z} = 0 \qquad (2.6)$$

$$\underbrace{\frac{\partial u}{\partial t}}_{1} + \underbrace{u\frac{\partial u}{\partial x} + v\frac{\partial u}{\partial y} + w\frac{\partial u}{\partial z}}_{2} = \underbrace{-g\frac{\partial H}{\partial x}}_{3} + \underbrace{\mu\left(\frac{\partial^2 u}{\partial x^2} + \frac{\partial^2 u}{\partial y^2}\right) + \frac{\partial}{\partial z}\left(\upsilon\frac{\partial u}{\partial z}\right)}_{4} + \underbrace{2\omega sen\varphi\, v}_{5} \qquad (2.7)$$

$$\underbrace{\frac{\partial v}{\partial t}}_{1} + \underbrace{u\frac{\partial v}{\partial x} + v\frac{\partial v}{\partial y} + w\frac{\partial v}{\partial z}}_{2} = \underbrace{-g\frac{\partial H}{\partial y}}_{3} + \underbrace{\mu\left(\frac{\partial^2 v}{\partial x^2} + \frac{\partial^2 v}{\partial y^2}\right) + \frac{\partial}{\partial z}\left(\upsilon\frac{\partial v}{\partial z}\right)}_{4} - \underbrace{2\omega sen\varphi\, u}_{5} \qquad (2.8)$$

O nível é calculado assumindo a pressão hidrostática:

$$\frac{\partial z}{\partial t} + \frac{\partial}{\partial x}\int_{Z0}^{Z} u dz + \frac{\partial}{\partial y}\int_{Z0}^{Z} v dz = 0 \quad (2.9)$$

Sendo w a velocidades média na direção de z, μ e υ os coeficientes de difusão turbulenta horizontal e vertical, respectivamente.

A tensão de cisalhamento do vento e o atrito do fundo são considerados como condições de contorno na superfície livre e no fundo, respectivamente. Nessas condições, $\upsilon \frac{\partial u}{\partial z} = \tau_x$ e $\upsilon \frac{\partial v}{\partial z} = \tau_y$ na superfície livre, e no fundo $\upsilon \frac{\partial u}{\partial z} = \gamma u$ e $\upsilon \frac{\partial v}{\partial z} = \gamma v$, onde γ é o coeficiente de fricção junto ao fundo.

2.3.1.4 Discretização e condições de contorno

As soluções para as equações apresentadas (1D, 2D e 3D) podem ser obtidas utilizando métodos numéricos, como diferença finita, elementos finitos e volumes finitos. Esses métodos são implementados em uma representação discreta no espaço chamada malha ou grade computacional. As variáveis que definem a condição de fluxo, como a velocidade, a profundidade e o nível, são calculadas nos vértices, centro e/ou face de cada célula computacional. Além disso, a grade pode ser estruturada em matriz retangular ou não estruturada, permitindo uma resolução não uniforme e contornos em áreas de variação topográfica (BATES et al., 2005).

Na resolução das equações é necessário definir as condições de contorno no sistema e as condições iniciais. As condições de contorno são definidas na fronteira à montante e à jusante da malha computacional, como um fluxo de entrada/saída ou uma série temporal de níveis. As condições iniciais consistem em valores das variáveis na grade computacional no início da simulação, como o nível da água.

2.3.2 Modelo hidráulico HEC-RAS

O *Hydrologic Engineering Centre's River Analysis System* (HEC-RAS) é um software de domínio público desenvolvido pelo Centro de Engenharia Hidrológica do corpo de engenheiros americanos (*Hydrologic Enginnering Center for the U.S.Army Corps of Engineers*, www.hec.usace.army.mil). O HEC-RAS (versão 5.0.7) permite a simulação da propagação do escoamento unidimensional e bidimensional. A seguir são

apresentados apenas os modelos bidimensionais: modelo hidrodinâmico (2D) e modelo não inercial (2D-).

2.3.2.1 Modelo hidrodinâmico e modelo não inercial

O modelo hidrodinâmico considera as equações completas de Saint-Venant (eqs. 2.10 e 2.11 expressas na forma vetorial bidimensional):

Equação de conservação da massa:

$$\frac{\partial H}{\partial t} + \vec{\nabla} \bullet h\vec{V} + q = 0 \tag{2.10}$$

Equação da quantidade de movimento:

$$\frac{\partial \vec{V}}{\partial t} + \vec{V} \bullet \vec{\nabla}\vec{V} = -g\vec{\nabla}H + v_t \nabla^2 \vec{V} - \frac{n^2 g|\vec{V}|}{R^{4/3}}\vec{V} + (2\omega sen\varphi)\vec{k} \times \vec{V} \tag{2.11}$$

Sendo $\vec{V} = (u, v)$ o vetor velocidade nas direções x e y; H a elevação da superfície da água; h a profundidade; q o fluxo de entrada/saída; g a aceleração da gravidade, calculada como função da latitude (φ); v_t o coeficiente de viscosidade turbulenta horizontal; n o coeficiente de rugosidade de Manning; R o raio hidráulico; e ω a velocidade angular de rotação da terra.

O fluxo turbulento ($v_t \nabla^2 \vec{V}$) é modelado de forma análoga ao processo de difusão. Para o cálculo do coeficiente de viscosidade turbulenta (v_t, eq. 2.12) considera-se um coeficiente D, adimensional e empírico, que varia com a geometria e as superfícies laterais/inferiores. Os valores de D são recomendados entre pouca mistura (0,11 a 0,26 – canal direto), mistura moderada (0,30 a 0,77 – poucos meandros) e muita mistura (2 a 5 – muitos meandros) (BRUNNER, 2016a).

$$v_t = Dh\frac{n\sqrt{g}}{R^{1/6}}\left|\vec{V}\right|) \tag{2.12}$$

No modelo não inercial, a velocidade é determinada pelo balanço entre o gradiente de pressão, efeitos gravitacionais e o atrito. Os termos de inercia, turbulência e Coriolis da equação de quantidade de movimento são desconsiderados, sendo que esses termos podem ser desconsiderados na maioria das situações com ganho na eficiência computacional e redução no tempo de processamento. O resultado dessa simplificação é

a equação 2.13. A divisão de ambos os lados pela raiz quadrada da sua normal, resulta na equação 2.14.

$$\frac{n^2|\vec{V}|\vec{V}}{R^{4/3}} = -\vec{\nabla}H \tag{2.13}$$

$$\vec{V} = \frac{-R^{2/3}}{n}\frac{\vec{\nabla}H}{|\vec{\nabla}H|^{1/2}} \tag{2.14}$$

Sendo $\vec{V} = (u, v)$ o vetor velocidade, $\vec{\nabla}H$ o gradiente de elevação da superfície da água e n o coeficiente de Manning.

A substituição da equação 2.14 na equação de conservação de massa (eq. 2.10), resulta na aproximação da equação do modelo não inercial, dada pela equação 2.15.

$$\frac{\partial H}{\partial t} - \vec{\nabla} \bullet \beta\vec{\nabla}H + q = 0 \text{ , em que } \beta = \frac{(R(H))^{5/3}}{n|\vec{\nabla}H|^{1/2}} \tag{2.15}$$

2.3.2.2 Dados, condições iniciais e de contorno

A simulação da propagação do escoamento da água pelos modelos descritos acima demanda informações de entrada, como a informação topográfica. Além disso, são necessários valores do coeficiente de rugosidade de Manning, que podem ser estipulados com base em referências na literatura (ex.: ARCEMENT JR; SCHNEIDER, 1989; CHOW, 1959). A cada intervalo de tempo da simulação, condições de contorno devem ser adotadas nas bordas do domínio ou no meio do domínio. As três opções de condições de contorno disponíveis no HEC-RAS são: (i) série temporal da elevação do nível da água; (ii) gradiente da superfície da água; e (iii) série temporal da vazão.

2.3.2.3 Malha computacional

O HEC-RAS permite a utilização de malhas computacionais onde a célula computacional não é fixa à célula topográfica, ou seja, o tamanho da célula não é limitado à resolução espacial do modelo topográfico. Assim, células maiores que as células topográficas podem ser utilizadas permitindo um processamento mais rápido. Um tamanho de célula computacional superior a resolução espacial pode reduzir a precisão da informação topográfica. No entanto, o HEC-RAS utiliza a abordagem de batimetria sub-grid (CASULLI, 2008), em que a informação detalhada da batimetria em cada célula é utilizada para criar tabelas de propriedades hidráulicas antes da simulação. Essas tabelas

relacionam a elevação da água com o volume da célula, a área da seção transversal, o perímetro molhado, o coeficiente de Manning e o perfil da cota de fundo (Figura 2.3). Essas informações são amostradas nas faces da célula (área, perímetro, perfil, Manning) e no centro da célula (volume) e são utilizadas durante a simulação.

Essa abordagem utiliza a informação detalhada da batimetria no contorno da célula, mas não representa exatamente a variação topográfica no interior da célula. Por essa razão, o HEC-RAS permite a utilização de uma malha computacional não estruturada em que cada célula pode ter até oito faces. Dessa forma, para maior precisão na amostragem dos parâmetros, as faces devem estar alinhadas à variação do terreno, como exemplificado na Figura 2.3 para regiões com variação topográfica no canal. Além disso, células maiores e regulares podem ser utilizadas onde o terreno e a declividade da superfície da água não variam rapidamente, como no rio.

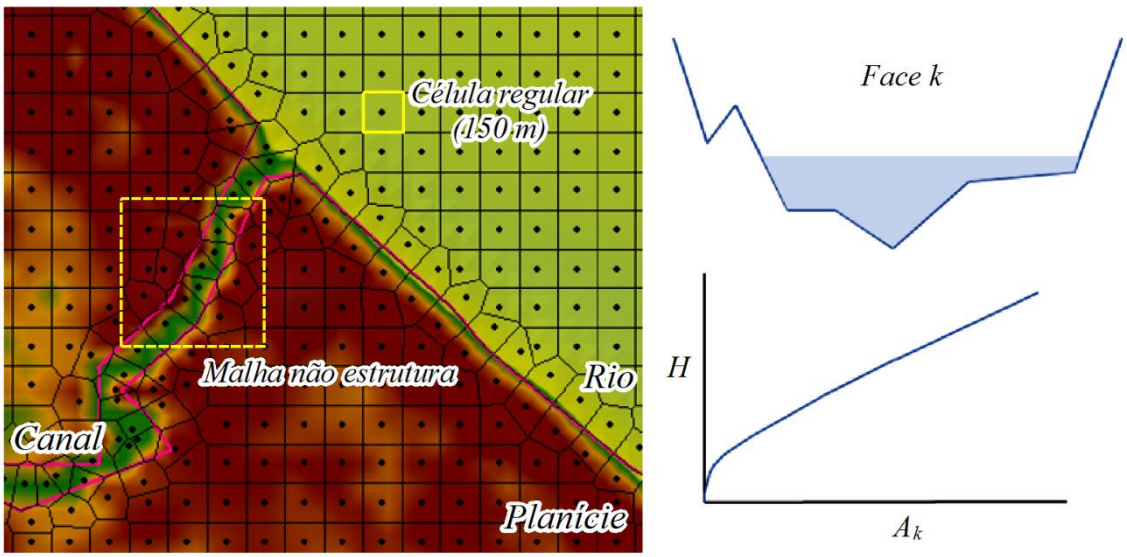

Figura 2.3 Exemplo de uma malha computacional não estruturada com tamanho de célula superior a resolução topográfica do MDE (adaptado de BRUNNER, 2016a).

2.3.2.4 Métodos numéricos

A utilização de uma malha não estruturada produz células ortogonais e não ortogonais, as quais implicam no método numérico utilizado para resolver as equações diferenciais dos modelos. O método de diferenças finitas é utilizado quando as células são ortogonais e o método de volumes finitos quando não são ortogonais. Por exemplo, dada duas células adjacentes com elevação da água H_1 e H_2, a derivada direcional na direção n', determinada pelo centro da célula, é aproximada pela equação 2.16 utilizando

o método de diferenças finitas (Figura 2.4). Nesse caso, se a direção n' é ortogonal à face entre as células, então a equação é suficiente para computar a derivada, caso contrário, o método de volume finito deve ser utilizado. Nesse método, o gradiente ∇H é determinando pelo teorema de divergência de Gauss (detalhes das formulações em BRUNNER, 2016a). Como consequência dos diferentes métodos, uma rotina de pré-processamento é utilizada para avaliar a ortogonalidade das faces e informar o tipo de discretização a ser utilizado.

$$\nabla \mathrm{H} \bullet n' = \frac{\partial H}{\partial n'} \approx \frac{H_1 - H_2}{\Delta n'} \tag{2.16}$$

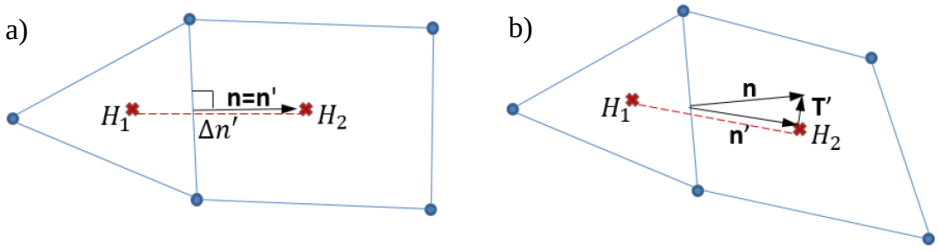

Figura 2.4 a) Células ortogonais: derivada aproximada por diferenças finitas, b) Células não ortogonais: derivada aproximada por volume finito (adaptado de BRUNNER, 2016a).

O HEC-RAS também resolve de forma diferente as equações dos modelos não inercial e hidrodinâmico. No primeiro (eq. 2.15), a abordagem de diferenças finitas (método de Crank-Nicolson) é usada para discretizar derivadas no tempo. A aproximação hibrida, que depende da ortogonalidade das células, é utilizada para discretizar as derivadas espaciais. No modelo hidrodinâmico, a equação da continuidade (eq. 2.10) é discretizada usando o método do volume finito, e cada termo da equação de conservação de quantidade de movimento (eq. 2.11) é discretizada de uma forma. Os termos de aceleração (termo 1) utilizam uma abordagem semi-lagrangiana; a discretização do gradiente de pressão (termo 2) depende da ortogonalidade das células sendo utilizado a aproximação hibrida; e o laplaciano (∇^2) do fluxo turbulento (termo 3) é calculado pela abordagem do volume finito.

Os dois modelos estão sujeitos às condições de estabilidade. O método de Crank-Nicolson, utilizado no modelo não inercial, requer que a razão entre o passo de tempo e o quadrado do passo de espaço ($\frac{\Delta T}{\Delta x^2}$) seja menor do que $\frac{1}{2-4\theta}$ quando $\theta < \frac{1}{2}$, sendo que

para valores $\frac{1}{2} \leq \theta \leq 1$ o esquema é incondicionalmente estável. O termo θ é um ponderador utilizado na discretização da derivada que varia entre 0 e 1. A solução da abordagem semi-lagrangiana para discretização do termo da aceleração na equação de quantidade de movimento do modelo hidrodinâmico, exige que o passo de tempo (ΔT) seja menor do que a razão entre o quadrado do passo de espaço e duas vezes a velocidade ($\frac{\Delta x^2}{2v}$).

Na prática, o manual do HEC-RAS sugere a condição de estabilidade de Courant-Friedrichs-Levy para definir o passo de tempo na simulação. Nessa condição, o número de Courant ($C = \frac{v\Delta T}{\Delta x}$) deve ser menor que 1 para o modelo hidrodinâmico (no máximo 3) e menor que 2 para o modelo não inercial (no máximo 5; BRUNNER, 2016b). Em algumas situações o número de Courant deve ser inferior a 1 para o modelo não inercial, como uma cheia com ascensão rápida ou se a área 2D estiver no início da simulação completamente seca.

Na versão 5.0.7 do HEC-RAS, o passo de tempo pode ser fixo ao longo da simulação ou variar de duas formas. Na primeira, o passo de tempo é ajustado monitorando o número de Courant dentro de um intervalo limitado, e na segunda forma, é possível definir valores para datas específicas. Essas opções melhoram a estabilidade do modelo e podem reduzir o tempo computacional da simulação.

2.3.3 Aplicações da modelagem na Amazônia central

A hidrologia da planície de inundação da região central da bacia Amazônica tem sido estudada a partir de medições em campo e de modelos hidráulicos em escala local e regional focados no escoamento da água.

Os estudos do balanço hídrico de três lagos na planície de inundação (resumidos na Tabela 1) mostraram diferentes contribuições na entrada de água. No Lago Calado, localizado próximo a Manaus, a fonte dominante é o escoamento local representando 57%. Nas planícies do Lago Grande de Curuai (BONNET et al., 2008), localizado no trecho baixo do rio Amazonas, e do Lago Janauacá (BONNET et al., 2017), próximo a Manacapuru, a principal entrada de água é proveniente do rio principal, com 77% e 93%, respectivamente. As diferenças entre os lagos Calado e Curuai em relação a contribuição da água do rio estão relacionadas, entre outros fatores, a morfologia da bacia. Por exemplo, a razão entre a área de drenagem da bacia local e a área superficial do lago

(Ad/As) é maior no lago Calado (Ad/As = sete, LESACK; MELACK, 1995) em relação ao lago Curuai (Ad/As = dois, BONNET et al., 2017). Esses lagos ilustram a heterogeneidade na hidrodinâmica rio-planície nos sistemas de planície da Amazônia.

Tabela 1. Contribuição de entrada de água (%) nos lagos Calado, Curuai e Janauacá

	Rio principal	Escoamento local	Precipitação direta	Infiltração
Lago Calado (LESACK; MELACK, 1995)	21	57	11	4
Lago Grande de Curuai (BONNET et al., 2008)	77	10	9	4
Lago Janauacá (BONNET et al., 2017)	93	10	<5	<1

O Lago Calado foi o primeiro lago da Amazônia estudado em relação a troca de água com o rio (LESACK; MELACK, 1995; LESACK, 1993, 1995). Lesack e Melack (1995) mostraram, com observações em campo, que o escoamento superficial e a chuva local são suficientes para evitar a entrada de água do rio durante a cheia. Os autores observaram um fluxo do rio para o lago no início da cheia, mas o fluxo era revertido do lago para o rio no meio da cheia entre março/abril de 1983 e novembro de 1984. Posteriormente Ji et al. (2019) simularam os fluxos de água nesse lago usando um modelo hidrológico e confirmaram que o volume máximo de água do rio no lago ocorre antes da cheia do rio devido as contribuições locais da bacia. No entanto, os autores ressaltam que o lago é muito dinâmico e condicionado ao nível do rio e configurações climáticas. Por exemplo, os picos interanuais do conteúdo de água do rio no lago variaram de 73 a 23% da água no lago nos 7 anos simulados.

Além do balanço hídrico do Lago Grande de Curuai realizado por Bonnet *et al.* (2008), essa planície foi estudada com mais detalhes por Barbosa (2005) e Rudorff et al., (2014a, 2014b). Barbosa (2005) fez o levantamento batimétrico da planície e quantificou o armazenamento de água nos lagos, enquanto Rudorff et al., (2014a, 2014b) simularam a troca de água rio-planície utilizando o modelo LISFLOOD-FP. Os autores mostraram que a água do rio Amazonas domina a entrada de água na planície representando 0,75% da vazão do rio em Óbidos (RUDORFF; MELACK; BATES, 2014a). Além disso, o escoamento difuso representa 93% do fluxo no sentido rio-planície e 54% do fluxo no

sentido contrário, da planície para o rio, sendo o restante fluxo canalizado (RUDORFF; MELACK; BATES, 2014b).

Posterior ao trabalho de Bonnet et al. (2017), que computaram os fluxos de água entre o rio e a planície do Lago Janauacá, Pinel *et al.* (2019) aplicaram o modelo TELEMAC-2D nessa planície validando e analisando, pela primeira vez, os padrões espaço-temporais da velocidade em uma planície de inundação do rio Amazonas. A circulação da água e a duração da inundação também foram analisadas. Os autores mostraram que entre o período de água baixa até o início da enchente do rio, o escoamento local na planície restringe a entrada de água do rio na planície, enquanto a enchente e a vazante do rio controlam a duração da inundação na planície. Poucas diferenças foram encontradas na distribuição da velocidade nos 9 anos avaliados, mas a duração da inundação foi altamente variável nesses anos.

Além desses estudos locais, foram realizados estudos regionais na planície de inundação do rio Solimões-Amazonas. Wilson et al. (2007) aplicaram o modelo LISFLOOD-FP na planície de inundação adjacente ao rio Solimões, correspondendo a um trecho de rio de 240 km. O modelo teve boa precisão em águas-altas com 72% de ajuste espacial – razão entre a intersecção e união das áreas observadas e modeladas e RMSE = 0,99 m do nível da água. Contudo, devido aos erros nos dados topográficos e omissão de processos hidrológicos, o modelo superestimou a inundação em água-baixa, apresentando 23% de ajuste espacial e RMSE = 3,17 m. Os autores concluíram que a planície foi insuficientemente drenada devido a não representação de canais com resolução inferior ao dado topográfico. Posteriormente, Baugh et al. (2013) removeram o viés devido à altura da vegetação do dado topográfico (SRTM3 DEM) e mostraram que a simulação hidrodinâmica do mesmo trecho teve maior acurácia em relação ao nível da água e a extensão de área inunda. Yamazaki et al. (2012) também simularam esse trecho corrigindo o erro do SRTM3 DEM conhecido como "*pit*", que é caracterizado por pixels cercado por altas elevações. Com a melhor representação dos canais pequenos conectados a planície de inundação, o modelo teve melhor acurácia. Trigg et al. (2009) caracterizaram a onda de inundação do rio também nesse trecho utilizando os modelos LISFLOOD-FP e HEC-RAS comparando diferentes simplificações das equações de Saint-Venant, e mostraram que, no mínimo, o termo de difusão deve ser incluído na simulação para a representação correta do escoamento.

Por último, ressalta-se que com auxílio da modelagem, Bourgoin et al. (2007) e Rudorff, Dunne e Melack (2017) estudaram a troca de sedimentos entre o rio e a planície

do Lago Grande de Curuai e mostraram que o balanço de sedimentos na planície é positivo, ou seja, a planície retém sedimentos. Com exceção dessa planície, não há estudos detalhados para compreender a troca de sedimentos entre rio-planície. Em escala regional, Dunne et al. (1998), Filizola e Guyot (2009), Mangiarotti et al. (2012), Mertes (1994) e Park (2017) também mostraram que a planície de inundação ao longo do rio Amazonas funciona como sumidouro de sedimentos.

CAPÍTULO 3. Mapping spatial-temporal sediment dynamics of river-floodplains in the Amazon

A pesquisa desenvolvida nesta tese inicia-se com um mapeamento e análise da dinâmica de sedimentos em suspensão nos rios e grandes lagos da região central da Amazônia. Esse mapeamento é feito pela primeira vez considerando rios e lagos com baixas concentrações de sedimentos. Estudos anteriores consideraram apenas rios com alta concentração de sedimentos. Além da grande abrangência espacial do mapeamento, são utilizadas séries longas de dados de satélite e da concentração de sedimentos (2003 a 2017). As imagens das faixas do vermelho e do infravermelho, sensíveis a concentração de sedimentos em suspensão na superfície, são temporalmente filtradas para recuperar dados incompletos e de baixa qualidade. Essas imagens são avaliadas como um proxy da concentração de sedimentos em suspensão e mapas da variação espaço-temporal dos sedimentos são criados. Uma metodologia é desenvolvida para sintetizar visualmente essa variação espaço-temporal em um único mapa (ver Graphical abstract abaixo). A mistura das cores azul, verde e vermelho representa quanto tempo em 15 anos cada ponto é mapeado em uma classe de concentração de sedimentos: alta (vermelha), moderada (verde) ou baixa (azul). Se um ponto é amarelo, que é a mistura da cor vermelha e verde, então esse ponto permanece aproximadamente 50% do tempo na classe alta e 50% do tempo na classe moderada. O mapa facilita a interpretação da variação de sedimentos e foi validado com acurácia global de 71%. O funcionamento da bacia Amazônica também é explorado nesse estudo documentando alguns sistemas rio-lago em termos de seu padrão espaço-temporal de sedimentos e fluxos de água. Os mapas produzidos são disponibilizados para usuários que queiram entender como a variação de sedimentos afeta processos ecológicos, hidrológicos e geomorfológicos nos rios e grandes lagos da Amazônia central. Podem ser utilizados, por exemplo, para avaliar a riqueza de espécies de peixes, de frutos e de vegetação na bacia, uma vez que a concentração de sedimentos na água é um fator relacionado ao desenvolvimento de diversas espécies.

This chapter is based on the following paper published at Remote Sensing of Environment: FASSONI-ANDRADE, Alice César; DE PAIVA, Rodrigo Cauduro Dias. **Mapping spatial- temporal sediment dynamics of river-floodplains in the Amazon**. v. 221, p. 94-107, 2019. https://doi.org/10.1016/j.rse.2018.10.038

Graphical abstract

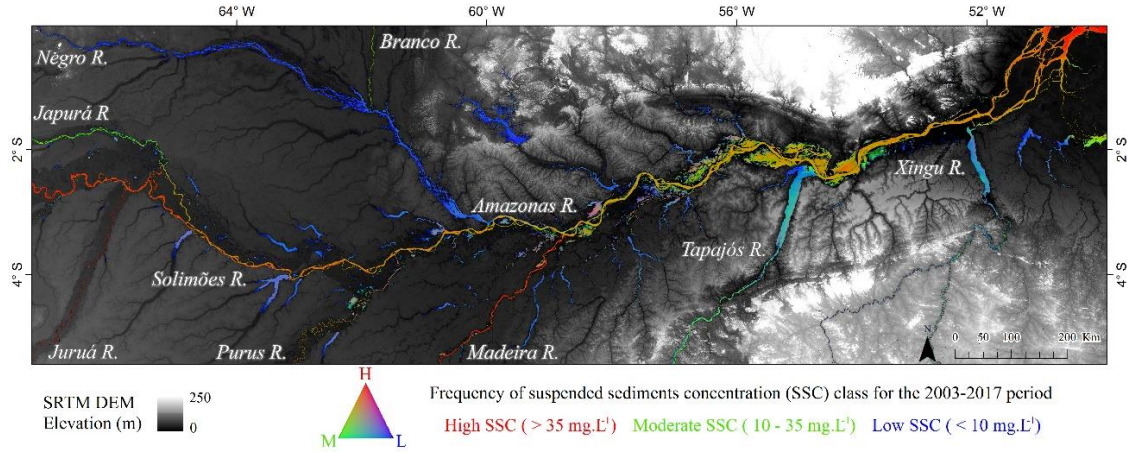

Abstract

Water composition in floodplains plays a key role in ecological processes and is affected by both local water sources and flooding from the main river. Despite local studies, still lacks a complete understanding on the relationship between hydrological processes and sediment distribution in the river-floodplain system of the Amazon basin. This paper presents the first mapping of the dynamics of suspended sediments in rivers and lakes (> 0.25 km^2) of central Amazon, considering different water types. Previous studies have considered only white-water rivers with high sediment concentration. This study also describes some river-lake systems in terms of their spatial-temporal pattern of sediments and water flows. Time series between 2003 and 2017 of red and infrared reflectance of Moderate Resolution Imaging Spectroradiometer (MODIS) images were temporally filtered to retrieve incomplete and low-quality data. These images were assessed as a proxy of the surface suspended sediments concentration; and maps of the spatial-temporal variation of sediments were created, such as the class frequency map. This map represents a 15-year frequency at which each pixel remains in one of the surface suspended sediments concentration classes: high, moderate, and low, with an overall accuracy of 71%. Our findings allowed to observe the variation of sediment concentration along the Solimões-Amazonas River, such as, for instance, its increase from the confluence with the Tapajós River to the mouth. Some hydrological processes were also observed in lakes of the middle reach, such as overbank flow and resuspension of sediments in depression lakes. In some ria lakes, the main water source comes from local basin with the backwater promoting sediment input in these lakes during the low-water period. The maps produced by this study are available and useful for supporting biogeochemical studies.

3.1 Introduction

The Amazon River basin is the largest hydrological system in the world with an annual monomodal flood cycle (JUNK; BAYLEY; SPARKS, 1989). This flood pulse is the main factor controlling the dynamic exchange of water and materials between the channel and the floodplain, which in turn plays an important role in ecological and biogeochemical processes in the floodplain, as well as in methane and CO_2 production (ABRIL et al., 2013; MELACK et al., 2004; RICHEY et al., 2002). Furthermore, the flow affects the floodplain's geomorphology (DUNNE et al., 1998; MERTES; DUNNE; MARTINELLI, 1996), sediment transport (BOURGOIN et al., 2007; DUNNE et al., 1998; MANGIAROTTI et al., 2012; RUDORFF; DUNNE; MELACK, 2017), vegetation diversity (FERREIRA-FERREIRA et al., 2014; JUNK et al., 2015), and water storage, affecting rivers' hydrodynamics (PAIVA et al., 2013).

The floodplain is covered by different vegetation types such as herbaceous, shrub, woodland, and forest (MELACK; HESS, 2010a; SILVERTOWN et al., 1999; WITTMANN et al., 2017), numerous channels and lakes with various shapes and depths, which are directly or indirectly connected to the main river or isolated (BONNET et al., 2008; CONSTANTINE et al., 2014; LATRUBESSE; FRANZINELLI, 2002; TORRES; JOSHUA WEST; CLARK, 2015; TRIGG et al., 2012). For this reason, the water flows through the floodplain are complex and vary in space and time, as shown by Alsdorf et al. (2007). Alsdorf (2003) also showed that variations on water level in the floodplain are related to different sources of the water. In addition to receiving water from the main river, the floodplain receives water from *terra firme* (dry land), direct precipitation and groundwater, all influencing the mixture of different water types (MERTES, 1997; MERTES et al., 1995). Mertes (1997) defines areas of river and local water mixing as "perirheic zone".

Another important source of variation for water mixture on the floodplain is the river's water composition. Amazonian rivers' water types are classified according to physicochemical parameters (SIOLI, 1984). White-water rivers (e.g. Madeira River and Solimões), which originate in the Andes, transport large amounts of sediments and nutrients, while black-water rivers (e.g. Negro River) are sediment- and nutrient-poor but rich in humic substances. Lastly, clear-water rivers (e.g. Tapajós River) are transparent and poor in sediment and dissolved solids. Therefore, the nutrient levels of water types affect floodplain's ecological response. For example, plants' composition, richness, and growth rates are higher in white-water river floodplains, *várzeas*, when compared to the

black-water river floodplains, *igapós* (JUNK et al., 2015; RODRIGUES, 2007, PARK & LATRUBESSE, 2015). Moreover, the primary and secondary productivity is much lower in igapós than in várzeas, so fish richness and fishing potential in igapós are reduced (JUNK et al., 2011, 2015).

Local floodplain studies have shown how water sources affect connectivity and water composition in river-floodplain systems. Some lakes of the Lago Grande de Curuai floodplain may decrease or lose connectivity during the dry season and as water levels decrease, sediment concentration increases due to resuspension of sediments (BONNET et al., 2008; BOURGOIN et al., 2007). During the flood, this floodplain receives water and sediment through overbank diffuse flow and channelized flows (RUDORFF; MELACK; BATES, 2014a). This floodplain has a small local drainage area, and therefore local water sources have little contribution. On the other hand, lakes with higher ratio of catchment area to water surface area receive greater contributions from local sources and during a certain period they experience flow reversal, receiving sediments from the river ((LESACK; MELACK, 1995). Despite different local studies on the Amazon floodplain hydrology, information is still insufficient for a more thorough understanding and characterization of this system.

Therefore, this discussion leads to the following research questions: Is it possible to identify the water sources and river-floodplain hydrodynamics based on the spatial-temporal dynamics of sediment concentration? What is the spatial-temporal dynamics of sediment concentration in floodplain lakes? Given that the distribution of sediment depend on the river's flood and local sources, these questions can be answered with spatial-temporal mapping of sediment using images with a temporal frequency suitable for tracking surface suspended sediments concentration (SSSC) in river and floodplain lakes during the Amazonas flood pulse and for detecting moderate-sized lakes (> 0.25 km^2), predominant in the central Amazon.

Remote sensing images have been used to assess the distribution of components that affect water color, such as chlorophyll (LOBO et al., 2012; NOVO et al., 2006) and SSSC (MANGIAROTTI et al., 2012; MARTINEZ et al., 2009, 2015; MONTANHER et al., 2014; PARK; LATRUBESSE, 2014; VILLAR et al., 2017, 2013) in the Amazon basin. Estimates of sediments by remote sensing are based on the statistical relationship between observed concentration and spectral band of reflectance. This relationship is possible because suspended particles cause an increase in reflectance, that is, the backscatter radiation increases as the concentration increases (KIRK, 2011). In addition,

particles' maximum reflectance occurs in the near infrared and red bands (JENSEN, 2009), as shown by Lobo et al. (2012) and Martinez et al. (2015) for waters with high sediment concentration in Amazon basin. Red band (R_{red}) and NIR band (R_{nir}) reflectance has been frequently applied for estimating SSSC in white-water rivers (MONTANHER et al., 2014; PARK; LATRUBESSE, 2014; VILLAR et al., 2012, 2013) and can also be used as proxies of SSSC so as to observe the spatial and temporal dynamics of suspended sediment. Some factors may hinder SSSC estimations, such as the type of sediment, the presence of other components (NOVO et al., 2006), and the contribution of bottom signal in clear waters (GAO, 2009).

It is still a challenge to create calibrated empirical models with suitable accuracy and large temporal and spatial coverage in the Amazon basin, including the rivers and the floodplain lakes. Previous studies have made accurate local SSSC estimates through field calibrations or by monitoring station data in white-water rivers (MANGIAROTTI et al., 2012; MONTANHER et al., 2014; PARK; LATRUBESSE, 2014; VILLAR et al., 2017, 2013). Furthermore, Montanher et al. (2014) and Park and Latrubesse (2014) showed that regional models would be required for greater accuracy (the root mean square error of Park's regional models range from 6.2 $mg.L^{-1}$ to 35.5 $mg.L^{-1}$). Despite their accuracy, these studies are space and time limited, what prevents their application for a full assessment of sediment dynamics. Moreover, they do not take full advantage of the large data set provided by the Moderate Resolution Imaging Spectroradiometer sensor – MODIS – database, a time series available since 2000 (Aqua and Terra satellites). In addition, a map for a qualitative analysis of sediment dynamic in the Amazon basin considering different water types in rivers and floodplain lakes may dispense accurate estimates of sediment concentration for providing meaningful information for hydrological applications. Such characterization would be useful, for example, for mapping floodplain overbank flows, and for understanding how river-floodplain sediment exchange occurs.

Studies showing patterns of floodplain lakes recharge and water sources based on sediment dynamic maps (PAVELSKY; SMITH, 2009) are not common and were not carried out for the river-floodplain systems of the Amazon. This gap is possibly due to the prioritization of SSSC estimation accuracy or to difficulty of obtaining cloudless images of the Amazon. MODIS images have data gaps and low-quality data caused by glint effect, cloud contamination or algorithm limitations (VERMOTE; VERMEULEN, 1999), thus the affected pixels are usually not included in the analysis. These data can be

replaced by temporally adjusted values, as the sediment dynamics often takes place at longer time scales than its temporal resolution of eight days (RUDORFF; DUNNE; MELACK, 2017). However, there still remain as a challenge on how to use and process a large number of images with clouds and how to use the data with for SSSC estimates to study hydrodynamic and sedimentary processes.

In this paper, a method to overcome data paucity caused by incomplete/low-quality of MODIS data, and to increase the number of observations in the time series is proposed. In addition, a new approach to create maps of the sediment dynamics considering different water types is presented, as well as several case studies on data application to describe river-lake systems in terms of the spatial-temporal pattern of sediments and water flows.

3.2 Rivers and Lakes in the central Amazon basin

This paper presents analyses of sediment dynamics in open water areas of rivers and floodplain lakes (> 0.25 km^2, black and blue in Figure 3.1) in the central Amazon basin (0.025ºS 67.28ºW to -5.42ºS 50.08ºW) by using remote sensing images. The study area was limited to a one-kilometer buffer in the Amazon wetland class in the Hess' map (HESS et al., 2015), elaborated with SAR images (downloaded from <https://daac.ornl.gov/cgi-bin/dsviewer.pl?ds_id=1284>). As this map does not cover the Amazon delta, the region was manually selected and included in the processed area - shown in gray in Figure 3.1.

Wetland areas in the Amazon basin occupy 14% of the watershed area (5.83×10^6 km^2), with 9% of open water, 14% of aquatic macrophytes, and 77% of woody vegetation during high-water season (HESS et al., 2015). According to Sippel et al. (1992), the Amazon main stem (from -70.5ºW to -52.5ºW) contains about 6,500 lakes and associated floodplains.

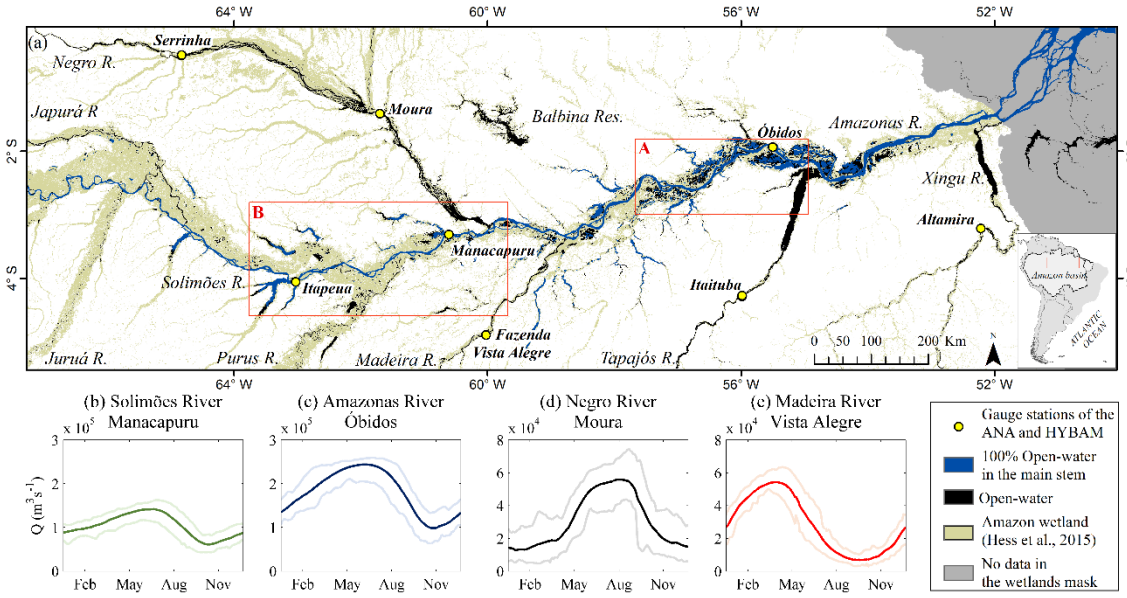

Figure 3.1. (a) Central Amazon basin with main stem open-water areas, tributaries, and the location of gauge stations of the ANA and HYBAM program. A: Middle reach of the Amazonas River. B: Middle-lower reach of the Solimões River. Climatology series of the (b) Solimões River (Manacapuru); (c) Amazonas River (Óbidos); (d) Negro River (Moura – SSSC data from this gauge station was not used); and (e) Madeira River (Fazenda Vista Alegre) discharge (Q, $m^3.s^{-1}$).

This region presents striking differences with the upstream, middle, and downstream reaches of the Solimões-Amazonas River (Solimões and Amazonas rivers). From upstream to downstream, both river sinuosity and migration rates decrease (MERTES; DUNNE; MARTINELLI, 1996). The area of flooded forest decreases from upstream to downstream, while both the number and size (area) of open water lakes increases (HESS et al., 2015; MERTES; DUNNE; MARTINELLI, 1996). Note that the blue area increases downstream on the flooded vegetation in Figure 3.1. The lake type also varies along the Solimões-Amazonas River. Small lakes formed between scroll bars, *scroll lakes* (Junk et al., 2012), and lakes in abandoned river meanders are dominant in the upper reach, *oxbow lakes*, also common in the Juruá River (Junk et al., 2012). *Ria* and *depression* lakes are large and predominate in the central region. *Ria lakes* are formed in drowned valleys of tributaries with a dendritic shape, greater depth, reduced circulation due the protection against wind-induced turbulences, and it receives water from tributaries (Junk et al., 2012; Latrubesse, 2012). *Depression lakes* are formed by the overbank deposition of fine sediments in floodplain depressions and are large and shallow, with a round to oval form (DUNNE et al., 1998; JUNK et al., 2012; MERTES;

DUNNE; MARTINELLI, 1996). The overbank flow during the flood plays an important role in sediment transport in depression lakes and, during the low-water period, large parts of these lakes become dry. Furthermore, due to the size and fetch of these lakes their water circulation is also influenced by wind (MELACK, 1984).

In large tropical watersheds, such as the Amazon basin, hydrographs typically display only one flood peak per year (Junk et al., 1989, Figure 3.1). This flood pulse play an important role in floodplain biota (Junk et al., 2011). In the low-water period (Oct/Nov in the Solimões-Amazonas River) lakes may decrease or lose their connection to the river, while during the flood, the floodplain receives sediments and nutrients from the river altering its biogeochemical cycle and resulting in areas of high productivity (JUNK; BAYLEY; SPARKS, 1989). The high-water period in the Solimões-Amazonas River occurs in May/June (Figure 3.1c), while the flood peak occurs in June and April in the Negro (Figure 3.1d) and Madeira (Figure 3.1e) tributaries, respectively.

3.3 Data and Methods

3.3.1 MODIS data and smoothing filter

Analyses were made using the MOD09Q1 v.6 (Terra) and MYD09Q1 v.6 (Aqua) products derived from the MODIS on the NASA Earth Observing System (EOS) Terra and Aqua platforms (NASA LP DAAC, 2015a, 2015b). The data uses daily images to provide the best possible observation during an eight-day period of the surface reflectance of band 1 (Red, 620-670 nm) and band 2 (Near Infrared - NIR, 841-876 nm) at 250 m spatial resolution (HUETE et al., 2002). Furthermore, the images are provided with corrections of atmospheric gases effects, aerosols, and thin cirrus clouds performed by MODIS aerosol algorithms (VERMOTE; VERMEULEN, 1999). A total of 1,380 images corresponding to tiles h11v09 and h12v09 from 2003 to 2017 were extracted, mosaicked, and re-projected into Geographic/WGS 84 using the MODIS Reprojection Tool package (DWYER & SCHMIDT, 2006). Images were resampled to 250 m through the nearest neighbor method. The area covered by the images is shown in Figure 3.1.

Data gaps and low-quality data in reflectance time series can be replaced by temporally adjusted values. Thus, the time series from each pixel in the MODIS images were filtered by fitting a double logistic model to the data. The flowchart shown in Figure 3.2 exemplifies this process performed in TIMESAT 3.2 software package (available at http://web.nateko.lu.se/timesat/timesat.asp, JÖNSSON; EKLUNDH, 2002, 2004).

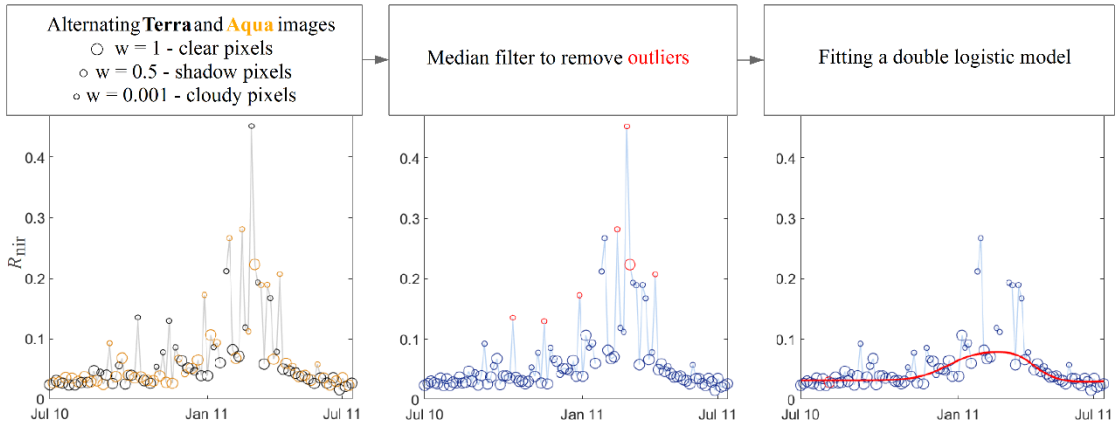

Figure 3.2. Flowchart of the filtering process. The exemplified time series represents the near-infrared reflectance (R_{nir}) of a pixel of the MODIS image, located in the Amazon River (Óbidos) for the period between July 2010 and July 2011. Black, yellow and red dots represent Terra, Aqua and outliers data respectively.

Terra and Aqua images represent the same eight-day period with 46 images per year. In addition, each pixel has a qualitative information, such as cloud state (clear, mixed, cloudy or no set – assumed clear) and cloud shadow (yes or no), coming from the MODIS product's quality band (band stage, VERMOTE; ROGER; RAY, 2015). In the filtering process, Terra and Aqua images were organized alternately and to each pixel value it was given a different weight factor (w) according to the band stage, as follows: w = 1 for pixels classified as clear, no-set or mixed at the same time as no-cloud shadow; w = 0.5 for pixels classified as clear, no-set or mixed at the same time as cloud shadow; and w = 0.001 for cloudy pixels (Figure 3.2b). These weights are used in the adjustment of the double logistic model in a way that the weighted-model allows better adjustment of incomplete and low-quality data.

A median filter to remove outliers was used before fitting the function, where they were assigned w = 0 according to the following criteria (EKLUNDH; JÖNSSON, 2015): i) reflectance values greater than the median in a moving window of 13 immediate neighbors (fixed parameter defined by TIMESAT as half window width equals the ratio of the number of data per year by seven); ii) reflectance values lewer than the mean value of its immediate neighbors minus the standard deviation (σ) of the entire time-series ($y(t) < \text{mean}(y(t-1), y(t+1)) - \sigma$); and the reflectance values greater than the maximum value of its immediate neighbors plus the standard deviation of the entire time-series ($y(t) > \max(y(t-1), y(t+1)) + \sigma$). Finally, the double logistic model function was adjusted to

the time series (Figure 3.2c; See supplementary information Table S3.1 for mathematical formulation details). After filtering, each filtered image was considered representative of four-day periods, totaling 92 images per year.

Regions of open-water (rivers, lakes and reservoirs) in the images were selected after the filtering process, and areas such as bare soil, vegetation and aquatic macrophyte were excluded from the analyses. A water mask was created for each image using two criteria based on the reflectance spectra of water, vegetation, and bare soil - supplementary information Figure S3.1 shows R_{red} and R_{nir} scatter plot with some pixels of these classes and the reflectance thresholds. First, pixels showing high NIR reflectance were excluded ($R_{nir} \geq 0.20$). A second criteria was used, where pixels with $R_{red}/R_{nir} \leq 0.6$ and $R_{nir} \geq 0.075$ were excluded. Other authors applied similar threshold to isolate the water class in MODIS images ($R_{nir} \geq 0.15$ by CHEN et al., 2009b; $R_{nir} \geq 0.10$ by PARK; LATRUBESSE, 2017; $R_{red} \geq 0.20$ by TARPANELLI et al., 2017).

3.3.2 Assessment of the filtered data

In situ data of suspended sediment concentration in rivers were used to evaluate the relationship between R_{red}, R_{nir} filtered and SSSC in white-, black- and clear-water rivers (see supplementary information Table S3.1), since the smoothing changes the original reflectance values. These data were obtained from 10 gauge stations (located in Figure 3.1) of the Brazilian National Water Agency (ANA, <http://hidroweb.ana.gov.br/>) and the Biogeochemistry and Geodynamic of the Amazon Basin (HYBAM) program (<http://www.ore-hybam.org/>). ANA's data are obtained by the average concentration in the vertical column (FILIZOLA; GUYOT, 2009) and the HYBAM's data by surface measurements (VILLAR et al., 2012), but both are determined by the same method (filtering using 0.45 µm cellulose acetate filter). Despite the differences in sampling, linear relationships between SSSC on the surface and integrated in depth were found for the Amazonian rivers (LARAQUE; FILIZOLA; GUYOT, 2005; MARTINEZ et al., 2009; VILLAR et al., 2012). Furthermore, there is no systematic bias between ANA and HYBAM data given that the mean SSSC and standard deviation of both databases for each station are very similar (See Table S3.1).

Pearson correlation coefficient (r) and the Spearman rank correlation (p) between observed SSSC (or natural logarithm of observed SSSC, logSSSC) and reflectance values (R_{red}, R_{nir}) were computed for each gauge station and for the whole data. The reflectance

values in the gauge station corresponded to the average of nine pixels located in the center of the river (3x3 window). In the correlation process, the reflectance was related to SSSC data up to four days later the reflectance image's date, considering this date as the first day of the period.

3.3.3 Maps processing

The following maps were produced with the filtered images: open-water frequency, time-series of reflectance for each band (Red and NIR), and frequency of SSSC classes. A description of the steps involved in the process is given below.

The open-water frequency map was processed as follows: first, all images were converted into binary images (water/no-water). Then, the open-water frequency for each four-day period was calculated by summing the water detected in same four-day period, that is, water detected on 1-4 January 2003 is added to water detected on 1-4 January 2004 and so on, and dividing by the number of years (15), resulting in 92 images with pixel values ranging from 0 to 15. Frequency values below one were considered no-water and excluded. This criterion was adopted by analyzing several images with residual no-water pixels. Finally, the frequency of open-water for the whole period was calculated by summing all four-day periods' frequencies and dividing by the total number of images (1380). This map indicates for how long, during the 15 years, each pixel remained as open-water at every four days.

The time-series reflectance map was calculated averaging the reflectance of every four-day period over 15 years of data, resulting in 92 images. The calculated reflectance image for 1-4 January, for example, represents the image average for 1-4 January 2003, 2004, and so on. The pixels classified as no-water in the open-water frequency map were excluded from this map.

The class frequency map represents the frequency between 2003 and 2017 at which each pixel remains in one of the SSSC classes: low, medium, and high. The flowchart in Figure 3.3 shows the procedures performed. To elaborate this map, a regression model with all SSSC data and filtered reflectance were adjusted. The stepwise regression method (DRAPER; SMITH, 1998) was used to find the best-fit model with the variables: R_{red}, R_{nir}, and R_{red}/R_{nir}. After applying the regression in the images, a concentration threshold was used to classify each image. The 10th percentile of SSSC data of white-water stations was considered as the lower limit for high SSSC class (34.57 $mg.L^{-1}$, rounded to 35 $mg.L^{-1}$), and the 90th percentile of SSSC data of the black-water

stations was considered as the upper limit for low SSSC class (10.20 mg.L^{-1}, rounded to 10 mg.L^{-1}). The remainder, between 10 mg.L^{-1} and 35 mg.L^{-1}, was classified as moderate SSSC class. Although SSSC model was just adjusted with data from the rivers, the high SSSC is wide enough to encompass higher concentrations episodically occurring in shallow lakes mainly in the low water season due to suspended sediment resuspension (BONNET et al., 2008; BOURGOIN et al., 2007). Finally, the occurrence for each class in relation to the total images was calculated, i.e. the ratio between the number of images classified in SSSC classes low, medium or high and the total number of images (1380). The map is presented as an RGB bands composition in which each band is a class: red for high, green for moderate, and blue for low. This relative frequency means that all pixels were considered, even those classified as no-water, and so open-water frequency must be considered to interpret the sediments temporal dynamics in the class frequency map. For example, a pixel in the floodplain lake with frequency of 10, 30, and 20% in SSSC classes low, medium and high respectively, remains 40% of the time as no open-water. The map can be categorized according to the open water frequency map for specific analyzes.

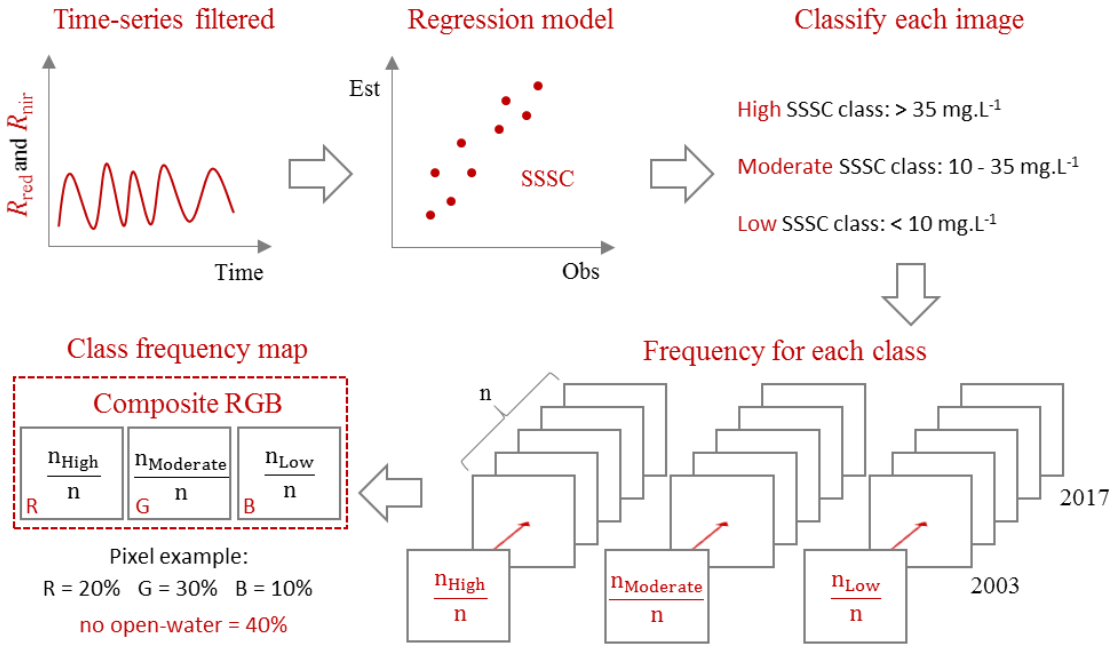

Figure 3.3. Flowchart of class frequency map procedures.

The class frequency map was validated using the k-folds cross-validation technique. The data were divided into ten subsets, each subset with data from ten-gauge stations (Table S3.1). In the validation process, data from one subset is kept recursively

set apart for testing and the remaining subsets used to run the regression model. The amount of data in each subset varies according number of measurements at a given station, with the largest subset –occurring at Faz. Vista Alegre HYBAM, which represents 24% of the data. The root mean square error (RMSE in mg L^{-1}), and coefficient of determination (R^2) between observed and estimated values were calculated. The overall accuracy of the classification was evaluated considering all data – observed and estimated - as well as for each water type – white, black, and clear.

3.4 Results and Discussion

3.4.1 Reflectance as a proxy for suspended sediment concentration

The comparison between raw MODIS images and filtered images in the NIR band shows that the smoothing filter modified the noisy and cloudy pixels. Figure 3.4a and Figure 3.4b shows the raw MODIS image and filtered image in the near-infrared band bounded by the one-kilometer buffer around the open-water class in the Hess' map (HESS et al., 2015), both February 2014. Figure 3.4c and 3. 4d shows an example of R_{red} calculated for 4-7 May 2013 and 1-4 November 2013, where larger values in red represent higher SSSC (the complete time series is presented in supplementary data Movie S1 and Movie S2). It is possible to observe the variation of the SSSC throughout the year and the lower values in rivers of black- and clear-water (e.g. Negro and Tapajos) in relation to the white-water rivers (e.g. Solimões, Madeira and Amazonas). The SSSC temporal variation in lakes adjacent to the Solimões-Amazonas River can also be observed. Large lakes in the upper reach have lower values than those in the middle reach.

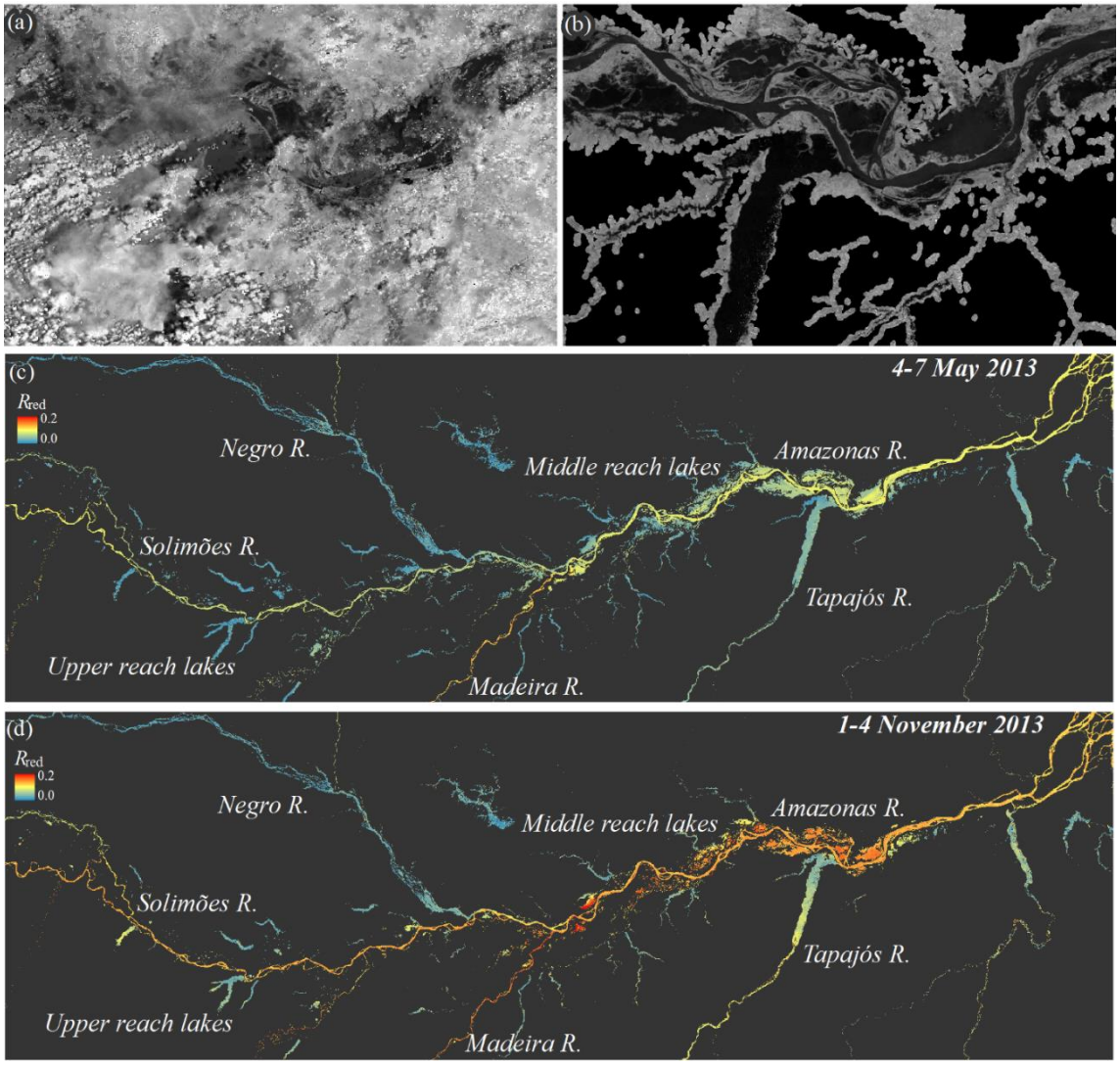

Figure 3.4. (a) raw MODIS image; (b) and filtered image in the near-infrared band bounded by the one-kilometer buffer around the open-water class in the Hess' map (HESS et al., 2015), both February 2014; Example of R_{red} calculated for the following four-day periods: (c) May 4-7, 2013; and (d) November 1-4, 2013.

Figure 3.5a and 3.5b summarizes the data obtained from ten gauge stations (location is shown in Figure 3.1) and the correlation between observed SSSC and filtered reflectance (R_{red} and R_{nir}). The Madeira River presented higher concentration of sediments with high variability (μ=186.9 mg.L^{-1} and σ =161.5 mg.L^{-1} for station 1, Table S3.1). This river and the Amazonas and Solimões rivers (white-water rivers) carry large sediment loads from the Andes (SIOLI, 1984). The observed SSSC (or logSSSC) of these rivers showed high, and significant correlation (p-value $\leq$ 0.05) with R_{red} and R_{nir} (stations 1 to 6 in Figure 3.5b and Table S3.1). On the other hand, the Tapajós River (clear-water) has low concentration of sediments and dissolved solids (JUNK et al., 2011). For this river,

the correlation was low, and significant only for R_{red} (stations 7 and 8). Finally, the Negro River (black-water river) has the lowest sediment concentration (μ = 5.9 mg.L^{-1} and σ = 2.6 mg.L^{-1} for station 9) and a dark color due to humic substances leached from podzolic soils (JUNK et al., 2015). The correlation was not statistically significant for this river (stations 9 and 10). In some stations, the Spearman rank correlation values were higher than the Pearson correlation coefficient values (Figure 3.5b), indicating that the correlation between the data may not be linear or that some extreme values impaired the correlation. To show the benefit of data filtering, correlations between SSSC and reflectance without filtering (raw reflectance) are presented in Table S3.1, and discussed in Text S3.2 (see supplementary information).

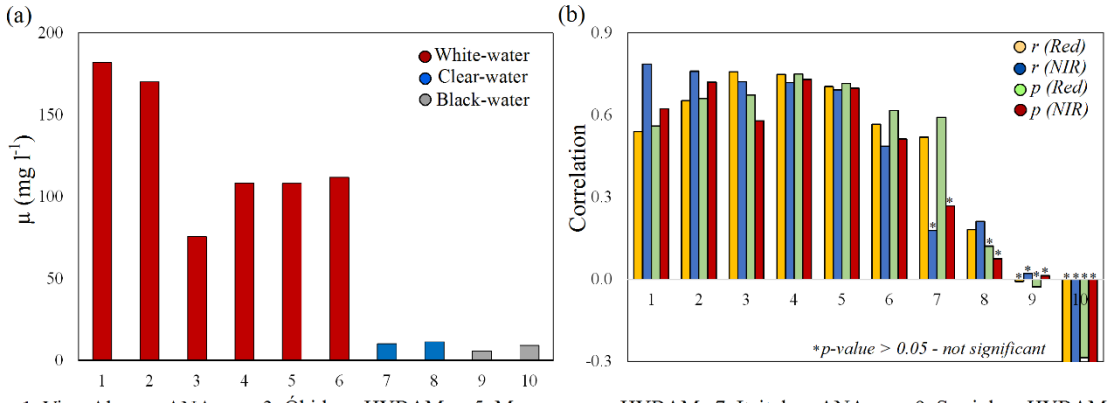

Figure 3.5. (a) Mean SSSC (μ, mg.L^{-1}) for each station. (b) Correlation between observed SSSC and R_{red} and R_{nir} for each station (*r*, Pearson coefficient; *p*, Spearman rank correlation).

The use of reflectance (R_{red} and R_{nir}) as a proxy to display temporal and spatial patterns of SSSC for all stations can be indicated, respectively, by the mean of correlation coefficient of the ten stations and by the correlation of the mean reflectance with the mean SSSC of each station. In this way, the reflectance was enough to display temporal patterns given that the mean and median of Pearson correlation coefficient presented, respectively, values of 0.43 and 0.55 for the R_{red}, and 0.41 and 0.59 for the R_{nir} (Table S3.1). These values are not high due to the existence of stations with low and negative correlation (e.g. Serrinha), what reduces both, the mean and the median correlation coefficient. On the other hand, the ability to observe the spatial pattern was better when mean reflectance was correlated with mean logSSSC was much higher: R_{red}: r = 0.67 and p = 0.68; R_{nir}: r

= 0.83 and p = 0.82 (n = 10; p-value ≤ 0.05). Therefore, the filtering process does not corrupt the spatial patterns.

The high correlation between the natural logarithm and the reflectance for all data (n = 1588) indicates reflectance as a good proxy to represent the spatial-temporal pattern of SSSC. The correlation was significant (p-value ≤ 0.05) for R_{red} (r = 0.83 and p = 0.84) and for R_{nir} (r = 0.68, p = 0.73). It is possible to observe the linear relationship between the logSSSC and R_{red} and R_{nir} in Figure 3.6a and 3.6b.

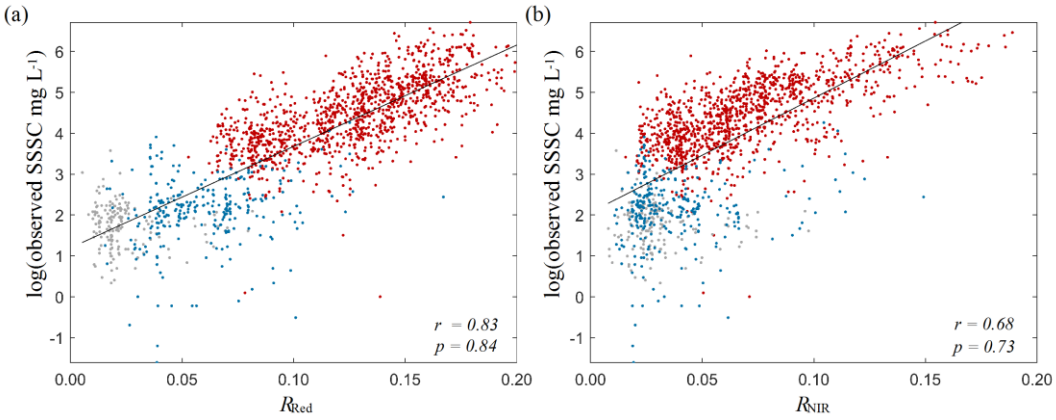

Figure 3.6. (a) Linear relation between the logSSSC with R_{red} (b) and R_{nir}. Red, blue and gray dots represent the data of the white-, clear- and black-water stations respectively.

The correlation of individual stations shows that the relationship between reflectance and SSSC concentration at clear- and black-water rivers, in general, is not significant. Sources of uncertainty for these stations are related to SSSC measurements, reduced sensor sensitivity to low reflectance, bottom reflectance in shallow lakes bottom sign, and the presence of other components. However, the correlation using all data is high and significant, indicating that for large scale patterns the low reflectance of these rivers may represent lower concentrations in relation to all rivers analyzed together. Thus, the reflectance as an SSSC proxy is sufficient for a space-time analysis of sediment dynamics in all Amazonian rivers, but the individual analysis of clear- and black-water rivers should be done with added caution.

3.4.2 Accuracy of the class frequency map

Classes of sediment concentration were defined based on estimates from an empirical model relating MODIS reflectance to SSSC, given by Equation 3.1 (number of data, n = 1588; R^2 = 0.7; RMSE = 75.6 mg.L^{-1}).

$$SSSC(mg.L^{-1}) = exp^{20 \cdot R_{red} + 7.68 \cdot R_{nir} + 0.31 \cdot \frac{R_{red}}{R_{nir}}} \quad (3.1)$$

with R_{red} and R_{red} values ranging between 0 and 1.

Cross-validation statistics showed RMSE = 98.15 mg.L^{-1} and R^2 = 0.65. Despite the high RMSE, the approach of separating SSSC classes (high SSSC -greater than 35 mg.L^{-1}, moderate SSSC -between 10 mg.L^{-1} and 35 mg.L^{-1}, and low SSSC less than 10 mg.L^{-1}) was sufficient to overcome accuracy issues in the class frequency map. The classification using all data was valid with an overall accuracy of 71% and the highest errors were the omission error (exclusion) of the moderate SSSC Class (User's accuracy was 33% - Confusion matrix in Tabela S1). The accuracy was high for both white- and black-water (Negro River) with an overall accuracy of 78.5 and 83% (n=1134 and n=161), respectively. Thus, although the black-water stations' SSSC data do not show significant correlations with reflectance when analyzed individually, the classification of this water type was consistent because a class threshold was considered. On the other hand, the moderate accuracy in the Tapajos River (clear-water, overall accuracy = 34%, n=293) suggests higher classification errors in this river.

3.4.3 Sediment dynamics along Solimões-Amazonas River and floodplains

Figure 3.7 shows the class frequency map (also in supplementary data graphical abstract) and the open-water map for the 2003-2017 period. The high SSSC class frequency (H-SSSC) in red indicates that this class is predominant during the 15 years (e.g. Madeira River). Similarly, the moderate SSSC class frequency (M-SSSC) is shown in green (e.g. Japurá) and the low SSSC class frequency (L-SSSC) in blue (e.g. Negro). The interpretation of the map helps to understand the variability of sediments. The Japurá River, for example, is green (M-SSSC) upstream from the confluence of a channel connected to the Solimões River, but it becomes yellow (M- and H-SSSC) beyond the confluence. This suggests the increases in the H-SSSC class frequency of the Japurá River is possibly due to sediment input from the Solimões River through that channel.

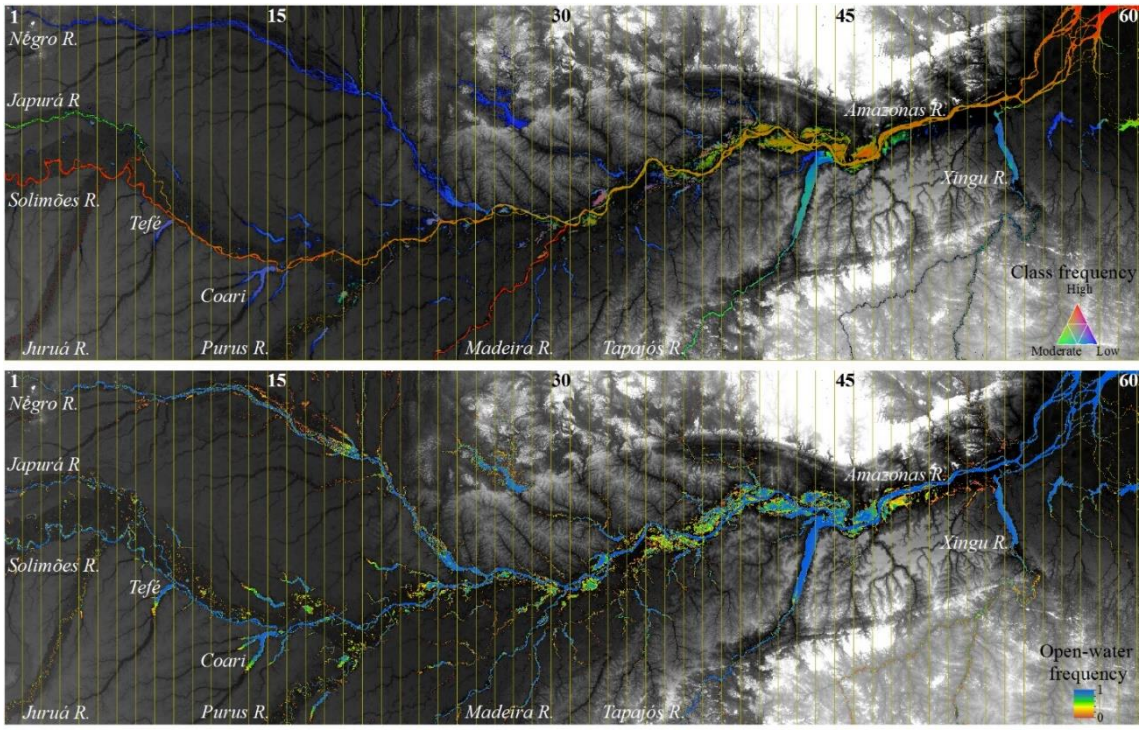

Figure 3.7. (a) Frequency of SSSC class, and (b) open-water frequency between 2003 and 2017 in the central Amazon basin: Low (<10 mg.L^{-1}), Moderate (10-35 mg.L^{-1}), and High (>30 mg. L^{-1}). Relief from SRTM DEM. Yellow lines indicate the 60 longitudinal sections with emphasis on sections 1, 15, 30, 45, and 60.

The frequency of each class was analyzed in 60 longitudinal sections along the Solimões-Amazonas River and in the floodplain (blue area in Figure 3.1) during the periods of Jan/Feb/Mar, Apr/May/Jun, Jul/Aug/Sep and Oct/Nov/Dec (Figure 3.8a to 3.8h). Each section has 32 x 601 km^2 and is indicated by the yellow lines in Figure 3.7. This analysis was performed considering only the area with 90% to 100% of frequency in the open-water frequency map (Figure 3.7b). The open-water frequency in floodplain was also analyzed in three classes: 25% to 50% of the time classified as open-water (orange), 50% to 75% (yellow), and greater than 75% (blue, Figure 3.8i to 3. 8l).

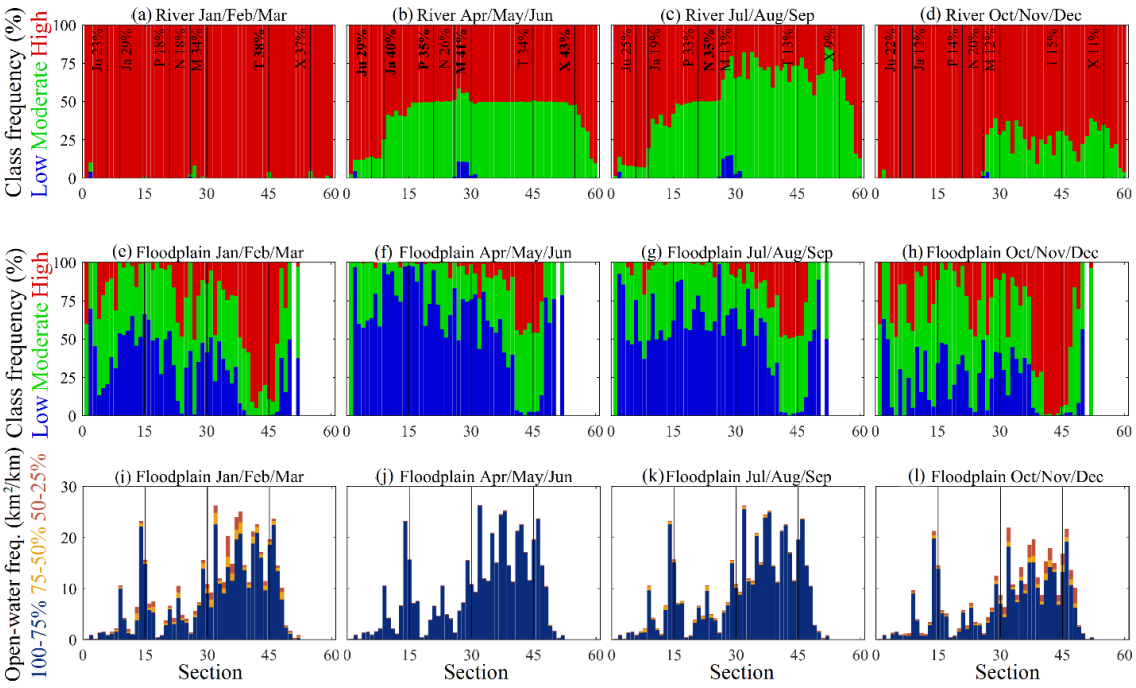

Figure 3.8. Class frequency along Solimões-Amazonas River sections for (a) January to March; (b) April to June; (c) July to September, and (d) October to December. The bars indicate the section at river's confluences (Ju-Juruá, Ja-Japurá, P-Purus, N-Negro, M-Madeira, T-Tapajós, X-Xingu) with the mean annual flow contribution (data from the hydrological model MGB-IPH, PAIVA et al., 2013). Class frequency along the sections in the floodplain for (e) January to March; (f) Abril to June; (g) July to September; and (h) October to December. Open-water frequency along the sections in the floodplain for (i) January to March; (j) April to June; (k) July to September; and (l) October to December.

Along Solimões-Amazonas River, the H-SSSC (red) is predominant during the year, mainly from October to March (Figure 3.8b, 3. 8e), i.e. low- to rising-water period. Between April and September (Figure 3.8c, 3. 8d), i.e. high- and falling-water period, this class decreases from upstream to the Xingú River confluence (sections between 1 and 55) and increases from this reach to the mouth. This increase was not observed by previous studies due to the lack of monitoring stations in this section, and may be related to the impact of tidal variations on grain-size segregation and sediment concentration in the water column due to resuspension and deposition (Jaeger and Nittrouer, 1995; Kosuth et al., 2009; Uncles et al., 2002).

Tributaries' effect on sediment variation along the river was also observed. In the section between the Japurá River and the Purus River (sections 9 to 21), the H-SSSC

reduction is well marked in sections 9 and 15 between April and September (Figure 3.8c and 3. 8d). This reduction may be related to Japurá River's flood (between April and June, contribution of 40% of the annual flow) and the water export from large lakes, such as the Tefé River (or Lago Tefé) in section 9 and the Coari Grande River (or Lago Coari) in section 15 (located in Figure 3.7). Between the confluence of rivers Negro and Madeira (sections between 26 and 30), the M-SSSC (green) and L-SSSC (blue) increase when the Negro River's flow is high, such as from July to September (Figure 3.8c). The H-SSSC increases in sections after the confluence of the Madeira River, mainly between April and June (Figure 3.8c), which is the period with the highest contribution to the annual flow (41%). These patterns of sediment variations along the river have biogeochemical implications and affect the river's morphodynamics, as showed by PARK; LATRUBESSE, 2015).

In the floodplain, the H-SSSC (red in Figure 3.8f - 3.8i) and the total open-water area (Figure 3.8j - 3.8m) generally increase from upstream to downstream. This variation may be related to floodplain's geomorphology, among other factors (LATRUBESSE; FRANZINELLI, 2002). In the upper reach (sections between 1-15), the H-SSSC is low throughout the year, though it is the predominant class in the river (Figure 3.8a - 3.8e). Furthermore, the flooded vegetated area is larger (Figure 3.1) and the open-water area is smaller in relation to the other regions (Figure 3.8j - 3.8m). This indicates that the lakes of the region are likely to receive water flowing throughout flooded vegetation where sediments tend settling down.

Scroll and ria lakes are mixed with rounder, larger lakes, which compose the transition from upstream to downstream features in the middle region (sections between 15 and 30, MERTES et al., 1996). In turn, from the Madeira River to the Tapajós River (sections between 30 and 45), hundreds of shallow and irregular lakes cover the floodplain (Mertes et al., 1996). In both sections (15 to 30 and 30 to 45), the L-SSSC (H-SSSC) decreases (increases) from upstream to downstream during the flood and falling-water (April to September), while the H-SSSC decreases in the river (for instance, note the difference between Figure 3.8d and 3.8h). Thus, it is probable that the sediment load coming from the river increases or that the contribution from local sources (water with low SSSC) decreases in these lakes from upstream to downstream. On the other hand, during the low-water and rising-water (October to March), the H-SSSC increase for almost 100% of the time in sections 30 to 45 due to the sediment resuspension in shallow lakes.

In relation to open-water frequency in the floodplain, some large lakes such as Tefé and Coari are highlighted in sections 9 and 15, respectively, in a region with few open-water lakes. The open-water area is strongly reduced mainly between sections 30 and 45 during the low-water period (Figure 3.8m) because the shallow lakes reduce in size. Finally, downstream of the Tapajós River confluence (sections between 45 and 60), the open-water area decreases. According to Mertes et al. (1996), lakes and floodplain channels in this region were possibly filled by sedimentation from overbank flows.

3.4.4 Case studies of sediment dynamics in river-floodplains

In this section, some case studies are presented as examples of data application for describing river-lake systems functioning in relation to the spatial-temporal pattern of sediments and water flows. For this, maps and time series of reflectance were used as a proxy of SSSC. The analyzed reflectance corresponds to the average of nine pixels located in the lake where the open-water frequency is at least 90%.

Figure 3.9 shows the Class SSSC frequency, the high- and low-water period for the middle reach of the Amazonas River. In the class frequency map, the Lago Grande Urucurituba floodplain is predominantly magenta in areas with high open-water frequency (H-SSSC = 45%, M-SSSC: 14%, L-SSSC: 36% and no open-water: 5% - H(45)M(14)L(36), no OW(5)), and blue in areas with open-water only in the flood (H(2)M(13)L(36); no OW (49)). In the Lago Madabá Grande floodplain, the moderate class (green) dominates in areas that are flooded only in the high-water (H(14)M(48)L(0); no OW(38)), and moderate and high classes (yellow) where the open-water frequency is high (H(48)M(48)L(0); no OW(4)). That is, there is prevalence of low and moderate class, respectively in the floodplains of the Lago Urucurituba and Lago Madabá during the flood, and the high class in both floodplains in the low-water period. This can be explained by the different processes of flooding, it is possible that Lago Urucurituba receives water with less sediments from the local sources while Lago Madabá, like Lago Grande de Curuai, receives more sediments from the river or other tributaries. This implies greater transport of sediment during the flood to these lakes.

During the flood, the flow from the river to these lakes happens mostly by overbank flow when the water elevation exceeds the banks height. This process contributes to sediment transport into the floodplain (DUNNE et al., 1998) and it is observed in the high-water figure for lakes shown in a yellow shade similar to the river's one (red arrows in Figure 3.9b, 3.9d, see also in supplementary data Movie S1 and Movie

S2). Note in this figure that the Lago Grande de Urucurituba floodplain receives water with less sediment than the Lago Madabá Grande floodplain.

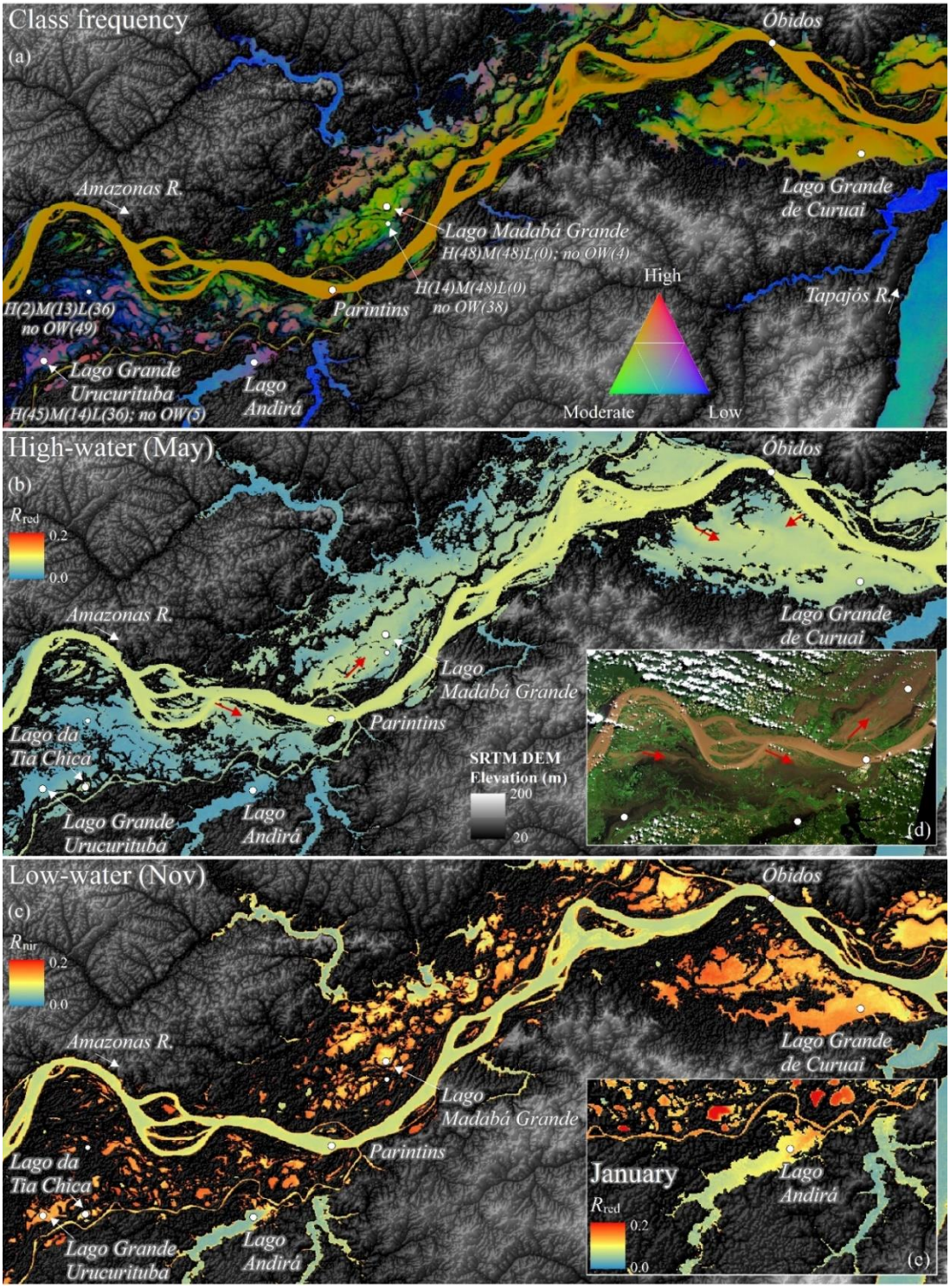

Figure 3.9. Middle reach of the Amazonas River near Parintins (box A in Figure 3.1), relief from SRTM DEM. (a) Class frequency map: Low (<10 mg.L^{-1}), Moderate (10-35 mg.L^{-1}), and High (>30 mg. L^{-1}). (b) R_{red} in high-water period (May). (c) R_{nir} in low-water

period (November). (d) Composite R(3)G(2)B(1) of the Landsat 8 image on June 24, 2015 (path 229 and row 62). (e) R_{red} in January.

The H-SSSC class dominates in the low-water period in these lakes and in the Lago Grande de Curuai as suggested by the high SSSC (or reflectance, note the highest values in lakes in relation to the river in Figure 3.9c). In fact, due to the circulation features of these shallow lakes, the lakes' stage reduction in the falling-water and the effect of winds enable the resuspension of sediments (ALCÂNTARA et al., 2010; BOURGOIN et al., 2007; JUNK et al., 2011). Bourgoin et al. (2007) observed values up to 1,600 $mg.L^{-1}$ in Lago Grande de Curuai in October, which correspond to a concentration six times higher than the maximum concentration observed in the Amazonas River for the same period. This increase is graphically observed when plotting stage versus R_{nir} for Lago Grande de Curuai, Lago Madabá Grande and Lago Grande de Urucurituba (Figure 3.10a, 3.10b, 3.10c). Note the rapid increase in reflectance with stage reduction from July to November and the different pattern in the Amazon River (Óbidos, Figure 3.10d). During the rising-water period, from November to March, as the lakes' water level increases, the resuspension is limited and the sediment concentration (or R_{nir}) is reduced.

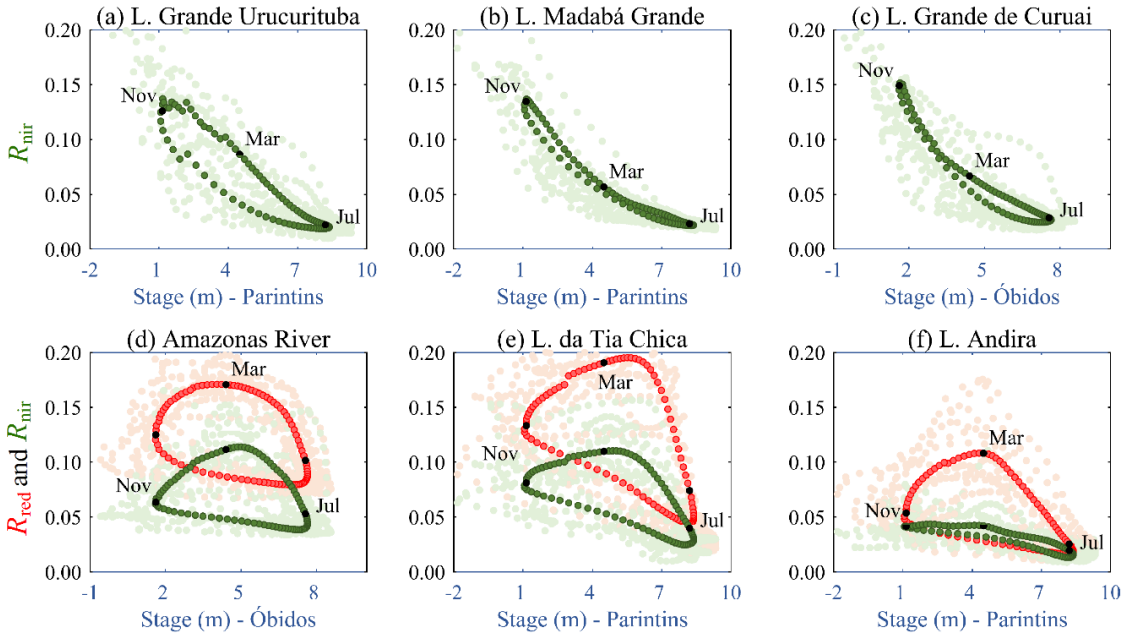

Figure 3.10. Stage-reflectance relationship (R_{red} in red and R_{nir} in green) for (a) Lago Grande Urucurituba. (b) Lago Madabá Grande. (c) Lago Grande de Curuai. (d) Amazonas River (Óbidos). (e) Lago da Tia Chica and (f) Lago Andirá. Climatology series in darker

and temporal series in lighter. Stage data from the ANA (Óbidos and Parintins, located in Figure 3.9).

The clockwise hysteresis loop of the Amazonas River (Óbidos) was observed by Bourgoin et al. (2007) for discharge-SSSC relationship with a pattern similar to Figure 3.10d (stage-reflectance). From November to March, the SSSC (or reflectance) increases with the rising water due to sediment contribution from white-water rivers (Madeira and Solimões). During the flood, from March to June, the SSSC decreases probably due to depletion of these rivers' sediment concentration. In the falling-water period, from June to November, the reflectance increases slightly as the river stage goes down.

The pattern of Lago Tia Chica's R_{nir} is more similar to that of the Amazon River's pattern (Figure 3.10e) and the annual open-water variation is small (Figure 3.9). This indicates that sediment resuspension may not occur and that the lake receives more sediments from the river, probably through a near channel (Paraná de Ramos).

Another lake with a different pattern is the Lago Andirá, a ria lake (Figure 3.9). In general, the R_{nir} is very low throughout the year and the R_{red} increase from November to March (Figure 3.10f). Furthermore, Figure 3.9a shows that part of this lake remains on H-SSSC for a longer period (in magenta, H(40)M(16)L(41); no OW(3)) and this class occurs only in the region near the channel (Paraná de Ramos). This indicates that the lake receives sediments during the low-water and beginning of the rising-water (Figure 3.9e shows the sediments input in January). However, the low reflectance during high-water and falling-water does not suggest sediment input in this period, but it is likely that the lake receives water from the local basin during the flood blocking the input of rich sediment water.

Lesack and Melack (1995) established the water balance at Lake Calado (a lake with similar features, connected to the Solimões River) and showed that the surface runoff and local rainfall are large enough to prevent the river water input into the lake during the flood. In this lake, the ratio of the local drainage basin area to water surface area is seven (in Lago Grande de Curuai it is two, Bonnet et al., 2008). The local runoff was responsible for 57% of the water input, while the Solimões River contributed with 21% and rainfall, with 11%. They observed a steady flow from the lake to the river from mid-March until November (1983 and 1984). It is likely that the hydrological processes of the Lago Andirá are similar to Lago Calado, where runoff and local rainfall are sufficient to block water input during the flood.

The backwater effect and the sediments input in low water season also seems to happen in other ria lakes in the middle-lower reach of the Solimões River, as in Lago Grande de Manacapuru and Lago Coari (Figure 3.11). In these lakes, the reflectance (or SSSC) during the year is smaller than that of Lago Andirá and its peak occurs in November (low-water season), as shown in Figure 3.11c - 3.11d and 3.11f - 3.11g. This probably indicates water input from the sediment-rich Solimões River (or another sediment source) during that period. The results of the hydrological model MGB-IPH (PAIVA et al., 2013, available at <https://www.ufrgs.br/hge/modelos-e-outros-produtos/amazon-basin-simulated-discharge-dataset/>) corroborate this hypothesis. In Figure 3.11f and 3.11g, the negative simulated flow in November indicates the backwater effect in these lakes. Note also that the flow is maximum between March and September, when a reduction of the L-SSSC class in the Solimões River from the confluence of Lago Coari was observed (section 3.4.3 in Figure 3.8c and 3.8d). In addition, it is likely that the greatest increase in reflectance (or SSSC) in Lago Coari in relation to Lago Grande de Manacupu is related to greater connectivity with the Solimões River (distance from the lake mouth to the river in Figure 3.11a).

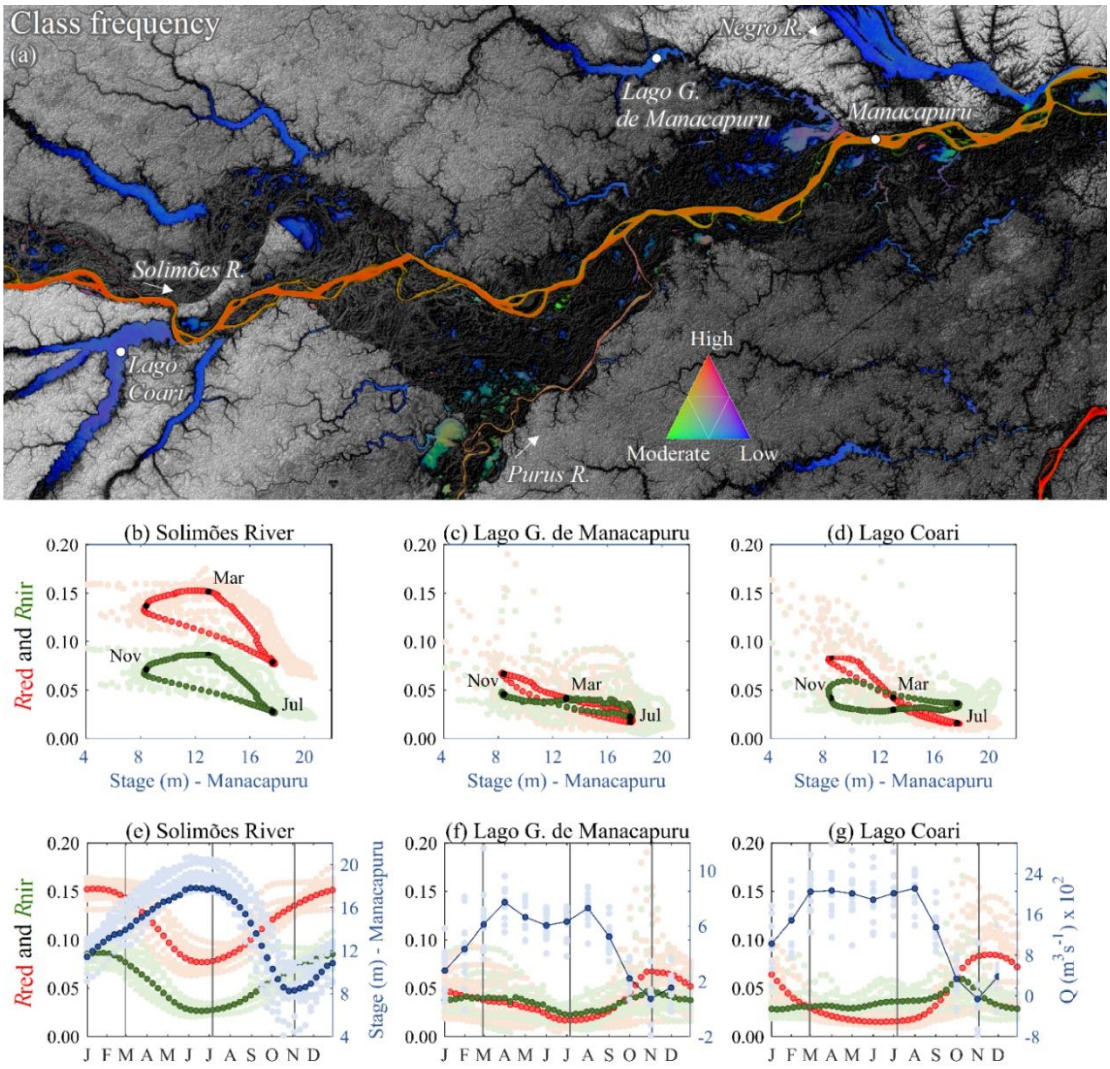

Figure 3.11. Middle reach of the Solimões River near Manacapuru (box B in Figure 3.1), relief from SRTM DEM. (a) Class frequency map. (b) to (d) Clockwise hysteresis loop. R_{red} (red), R_{nir} (green) and river water stage (Manacapuru) in Solimões River, Lago Grande de Manacapuru and Lago Coari. Climatology series (darker) and temporal series (lighter) of reflectance and (e) river water stage (blue) in Solimões River, (f) and (g) flow for 1988 to 2009 from MGB-IPH. Local drainage basin area considered in the hydrological model MGB-IPH (PAIVA et al., 2013): Manacapuru = 12 km^2 and Coari = 36 km^2.

3.5 Implications of resulting dataset

The mapping of sediment dynamics considering different water types for the first time in the central Amazon basin has important implications for hydrology, geomorphology and biogeochemical studies. The distribution and frequency of sediment occurrence, which depends on the river and local sources, are important for analyzing the

nutrient cycle and productivity (MELACK; FORSBERG, 2001). In addition, maps can bring insight about the richness of species such as fish, birds, and plants, since the concentration of sediments in lakes affects these factors (JUNK et al., 2011, 2015; Rodrigues, 2007, PARK & LATRUBESSE, 2015). For example, it has been shown that the Lago Andirá receives more sediments from the river in the stretch near the mouth. Thus, the diversity of plants around this lake may be related to how far sediment-rich waters advance into the lake, as shown by Rodrigues (2007) to Lake Amanã. Mapping can also aid the characterization and classification of rivers and lakes, such as Sioli's classification for rivers types (white, clear and black water, SIOLI, 1984). Furthemore, the mapping of sediment resuspension and the transport of sediment by overbank flow may be useful for studies on sediment accumulation/erosion and river-lake sediment exchange.

Reflectance analysis can also improve the understanding of water exchange between river-floodplain in more detailed local studies, since the simple approach allowed to infer hydraulic/hydrodynamic processes, such as the backwater effect in ria lakes and the resuspension of sediments in some shallow lakes. Thus, the data set, if used properly, can help to understand the system compared to physical modeling, which is often complex and requires considerable input data. In relation to the sediment exchange between river and floodplain, the extensive time series (2003-2017) allows to evaluate extreme conditions of droughts (e.g. 2005) and floods (e.g. 2009), and to deduce over the effect of climate changes. For example, high levels during flood foster greater sediment input in lakes of the middle reach of the Amazon River (RUDORFF; DUNNE; MELACK, 2017), while low average levels seems to promote sediment input into ria lakes. Finally, reflectance can be used to create accurate local empirical models as well as to estimate rates and sediment exchanges in river-floodplains.

3.6 Conclusions

The distribution of sediments in large lakes and rivers of the central Amazon remain little known due to the lack of data. This paper brings for the first time a mapping and investigation of the sediment dynamics in these environments considering different water types (white-, clear- and black-water) using remote sensing images, i.e. MODIS data. Furthermore, flow patterns and variations in water sources in the floodplain were shown.

In the analysis of sediments by remote sensing, images with low quality data are usually discarded. Correlations between reflectance and SSSC suggest that the methodology to replace gaps and low-quality data from images by temporally filtered presented in this paper was adequate if the goal is the use of reflectance as a SSSC proxy for studying large scale spatial-temporal dynamics. Furthermore, the class frequency map is a good tool for summarizing large-scale sediment dynamics with a simple approach for application in other areas. The overall accuracy of the mapping was adequate for white-water and black-water rivers and reasonable for clear-water rivers.

Our analysis allowed to evaluate the sediment variation in confluence stretches along the Solimões-Amazonas River, such as the increase in the confluence with the Madeira River and the reduction in the confluence with the Negro River. We also observed reduction of sediments during the flood of large lakes, such as Coari and Tefé, and sediment input of the Solimões River in the Japurá River. In addition, for the first time, an increase of the sediments from the confluence with the Tapajós River to the mouth was observed, which may be related to the tide effecton sediment concentration in the water column.

Some lakes patterns observed by local studies have been confirmed. It was observed that Lago Grande de Curuai receives sediments-rich water by overbank flow at the beginning and during the flood, and resuspension of sediments occurs in the low water period, as previously documented. These processes were identified in some lakes of the middle reach of the Amazon River and it was observed that during the flood the Lago Madabá Grande floodplain receives more sediments than the Lago Grande Urucurituba floodplain.

The main source of water in some ria lakes comes from local basin (surface runoff and local rainfall) and the stored water is sufficient to block the input of river water during the flood, as already documented for Lake Calado. In addition, the mapping allowed to compare these lakes in relation to the water input rich in sediments in low-water periods. Lago Andirá, for example, seems to receive more sediments than Lago Grande de Mancapuru.

Finally, the new Sentinel-2A and Sentinel-2B satellites, launched respectively in June 2015 and March 2017, offer new opportunities with images every five days (from both satellites) and 10 m spatial resolution. It seems interesting to apply the methodology for noise removal from the time series of these satellites data to get more detailed local studies. Likewise, in situ level and river discharge data complement to reflectance data in

order to understand the system (e.g., stage vs. reflectance). Thus, the maps can be integrated with data such as altimetry satellites (e.g. ENVISAT, and JASON) or from the forthcoming Surface Water and Ocean Topography (SWOT) satellite mission (DURAND et al., 2010).

The maps developed in this study in GeoTIFF format can be found at http://dx.doi.org/10.17632/wy2mz3nm7p.1 or with request to the first author. Supplementary data associated with this article can be found in the online version, at https://doi.org/10.1016/j.rse.2018.10.

CAPÍTULO 4. Lake topography and active storage from satellite observations of flood frequency

Esse capítulo avança no desenvolvimento de técnicas por sensoriamento remoto para estudo de corpos d'água. Uma nova abordagem para a estimativa da topografia em áreas temporariamente inundadas de lagos naturais e artificiais é proposta utilizando imagens de satélites e dados de nível da água. Essa informação é crucial para diversas aplicações hidrológicas, como simulações hidrodinâmicas e gerenciamento de recursos hídricos. No geral, os métodos para estimativa da topografia baseados em sensoriamento remoto consideram a interpolação de isóbatas de lagos individuais, que são linhas que representam profundidades iguais. Essas são estimadas a partir da delimitação da área inundada em imagens de satélites, gerando linhas que representam o contorno da área inundada e atribuindo o nível da água às linhas. Assim, essas abordagens são trabalhosas e dependem de dados da mesma data (imagens e nível da água). A abordagem apresentada nesse capítulo é inovadora pois não necessita desse processamento para cada lago. A topografia é estimada ponto por ponto a partir de um mapa de frequência de inundação, em que o valor de cada ponto representa a frequência em que o ponto ficou inundado em um período. Assim, assume-se a equivalência entre a frequência de inundação no ponto e a probabilidade de o nível da água ser excedido nesse ponto. O processamento é feito para cada ponto transformando um mapa de frequência de inundação em um mapa de elevação do terreno utilizando pelo menos uma série temporal do nível da água do corpo d'água. A validação da nova abordagem foi feita em dois lagos e 12 reservatórios usando o aplicativo Flood2Topo, desenvolvido e documentado nesse estudo. Esse aplicativo fornece um mapa de topografia e uma curva cota-área-volume ativo do corpo d'água. Os resultados mostram valores da raiz do desvio médio quadrático (RDMQ) de 18,50 cm e 1,4 m para os lagos Poopó (Bolívia) e Curuai (bacia Amazônica), respectivamente. Para o armazenamento ativo de reservatórios, os valores normalizados de RDMQ variaram de 2% a 11,09% para 11 reservatórios (média de 6,39%). O método apresentado representa um avanço para representação da topografia por sensoriamento remoto e é promissor para obter dados de monitoramento de corpos d'água não medidos.

This chapter is based on the following paper submitted to Water Resources Research (September of 2019): FASSONI-ANDRADE, Alice César; PAIVA, Rodrigo Cauduro Dias; FLEISCHMANN, Ayan Santos. **Lake topography and active storage from satellite observations of flood frequency**.

Abstract

Topography is critical information for water resources management in lakes, and remote sensing provides a unique opportunity to estimate it in ungauged regions. We introduce here a new method which estimates near shore topography of water bodies based on a flood frequency map and time series of water levels by assuming the equivalence between flood frequency and water level exceedance probability at a given area. Test cases are performed for two lakes and 12 hydropower reservoirs in Brazil using the proposed Flood2Topo app. This new application generates the bottom level pixel by pixel and a level-area-active storage relationships directly from the topography map, without the need to fit functions. Flood extent estimates from the Landsat based JRC Global Surface Water (GSW) dataset, current state-of-the-art, were used to run Flood2Topo, together with water levels from satellite altimetry and in-situ gauges. Results show bottom level root mean square deviation (RMSD) values of 18.5 cm and 146 cm for Lake Poopó (Bolivia) and Lake Curuai (Amazon basin), respectively. For reservoir active storage, RMSD normalized values ranged from 2% to 11.09% for 11 reservoirs (average NRMSD of 6.39 %). The method can be applied to any area seasonally flooded, for instance, it is applicable in 35.8 % (86%) of the global water surface area mapped by occurrence map from GSW dataset, when considering the number of pixels with occurrence between 0 and 95% (99%) over 35 years. This is a promising tool for obtaining data for hydrodynamic simulations and monitoring of ungauged water bodies.

4.1 Introduction

The bathymetry of natural and artificial lakes is critical information for navigation, hydrological, ecological and geomorphological studies (DÖRNHÖFER; OPPELT, 2016; GAO, 2009). At local scales, it has been estimated through methods such as echo sounding, multi-beam SONAR and LiDAR (ABDALLAH et al., 2013; GAO, 2009), while at larger scales recently released global databases (DOWNING et al., 2006; LEHNER et al., 2011b; LEHNER; DÖLL, 2004; MESSAGER et al., 2016; VERPOORTER et al., 2014) have improved the understanding of lakes and reservoirs and their impacts on global hydrology and biogeochemical cycles (BASTVIKEN et al., 2004; DÖLL; FIEDLER; ZHANG, 2009; GRILL et al., 2019; HANASAKI; KANAE; OKI, 2006; SHIN; POKHREL; MIGUEZ-MACHO, 2019; ZAJAC et al., 2017; ZHOU et al., 2016). These global databases, however, lack information on topography, which is typically described in terms of level-area-volume relationships or 3D maps of bottom level. Level-area-volume relationships are used to monitor the variations in water storage and are usually necessary to estimate reservoirs inflows using water balance equations (DENG et al., 2015). In hydrodynamic mathematical modeling, bathymetric data are required to estimate storages and flow propagation across lakes. While the level-area-volume relationships are used in lumped, simplified level-pool routing methods, the availability of bathymetric data allows a more complete description of the hydrodynamics of water bodies (DARGAHI; SETEGN, 2011; FREAD, 1993; LI et al., 2014; LOPES et al., 2018; MUNAR et al., 2018; ZHANG et al., 2017). In river modeling systems, channel bathymetry is also required, and remote sensing-based methods have been proposed (BRÊDA et al., 2019; DOMENEGHETTI, 2016; DURAND et al., 2008; MORAMARCO et al., 2019).

Several studies have estimated level-area-volume relationships from remote sensing data as water level and flood extent, for applications in hydrological modeling, water balance calculations, lake volume monitoring, and others (AVISSE et al., 2017; BUSKER et al., 2019; CAI et al., 2016; COLLISCHONN; CLARKE, 2016; CRÉTAUX et al., 2015, 2016; DUAN; BASTIAANSSEN, 2013; GAO; BIRKETT; LETTENMAIER, 2012; HOEK et al., 2019; MA et al., 2019; TONG et al., 2016; ZHANG; GAO; NAZ, 2014). In general, this estimation involves fitting a function to the lake area and water level data and then integrating the resulting curve to obtain a level-storage relationship (BUSKER et al., 2019; GAO; BIRKETT; LETTENMAIER, 2012; ZHANG; GAO; NAZ, 2014). This approach usually requires that the date of the water

level corresponds to the date of the image used to estimate the water surface area. Although, the fitted function is subject to error, the level-area-volume relationship is easier to obtain than 3D topographic mapping because noise and errors are compensated in the calculation of total volume and total area.

In turn, 3D topographic mapping by bathymetric surveys remains a time- and cost-intensive method, requiring extensive fieldwork and data analyses (MESSAGER et al., 2016). Furthermore, the direct retrieval of bathymetry from satellite imagery is limited for situations in clear and shallow water bodies where the remotely detected signal is dominated by bottom reflected radiation (CARBONNEAU; LANE; BERGERON, 2006; DILBONE et al., 2018; GAO, 2009; LEGLEITER; OVERSTREET, 2012; LEGLEITER; ROBERTS; LAWRENCE, 2009; SANDIDGE; HOLYER, 1998). Alternatively, the topography can be estimated between the smallest and largest water surface areas using water level and flood extent data, such as the approaches presented by Arsen et al. (2013), Feng et al. (2011), Getirana et al. (2018) and Tseng et al. (2016). The methods, however, still have limitations. The approaches presented by Feng et al. (2011), Arsen et al. (2013), Tseng et al. (2016), and Getirana et al. (2018), for instance, require delineating the shorelines of the water body in each flood extent image. Therefore, in regions with many lakes, such as in the Amazon floodplain and in delta areas, such methods have high processing costs, in addition to inherent difficulties in determining the shorelines due to complex flow patterns and connections among lakes (ALSDORF et al., 2007; PARK; LATRUBESSE, 2017; TRIGG et al., 2012). Another caveat of these approaches is the need to obtain water level observations and images on the same date. The method proposed by Tseng et al. (2017) only partly resolves these limitations by estimating the bottom levels on a pixel by pixel basis from a flood frequency map computed from multi-temporal satellite images, but this approach does not account for the temporal variation of water surface elevation.

This study presents a flood frequency-based method to estimate 3D topography above the lowest observed water surface elevation and active storage in regions subject to varying flooded areas, using long-term remote sensing-based flood extent maps and water level observations obtained in-situ and/or via satellite altimetry. In addition to obtaining the bottom level for each pixel, the proposed method does not require simultaneous water level data and flood extent image. The method can be applied to any water body (lakes, reservoirs, and intermittent rivers) subject to flooded area variation.

This paper is organized as follows: section 2 introduces the proposed method, available (current and future) datasets to be used with the method, and the developed Flood2Topo app. Section 3 shows the experimental design for validation of the method. Results and discussion are divided into validation for natural lakes and reservoirs (section 4), followed by a discussion on other proposed methods, as well as future developments and major caveats (section 5).

4.2 Flood frequency-based method

4.2.1 Conceptual formulation

A straightforward method to estimate topography above the lowest observed water surface elevation and active storage of lakes and reservoirs is proposed here based on the following steps and assumptions: 1) the water level duration curve is known for at least one site within the study area; and 2) a flood frequency map is available for the region. The water body bottom level map is then obtained through the combination of the water level duration curve and the flood frequency map, with the same spatial resolution as the flood map and the same vertical reference as the water level data (e.g., the Earth Gravitational Model geoid 2008 - EGM08, sea level, or an arbitrary reference).

The proposed approach considers the flooding process in a given area where variations in water surface elevation produce variations in flood extent. Changes in water level along the area can be represented by the water level duration curve, i.e. the water level cumulative probability in decreasing order (the probability that the water level in the area exceeds a certain value in a particular period of time), and the variation in flood extent can be synthesized by the flood frequency at each point (or pixel) in the area, as shown in Figure 4.1.

Thus, given the flood probability map $F(x, y)$, and the water level duration curve $P(h) = Prob\{h' \geq h\}$, the bottom level at a pixel $Z(x, y)$ is defined to be the water level h whose probability of exceedance is equal to the flood frequency, i.e., $Z(x, y) = P^{-1}(F(x, y))$. In other words, the relationships between (1) water level and its exceedance probability, and (2) flood frequency and the associated bottom level, are the same.

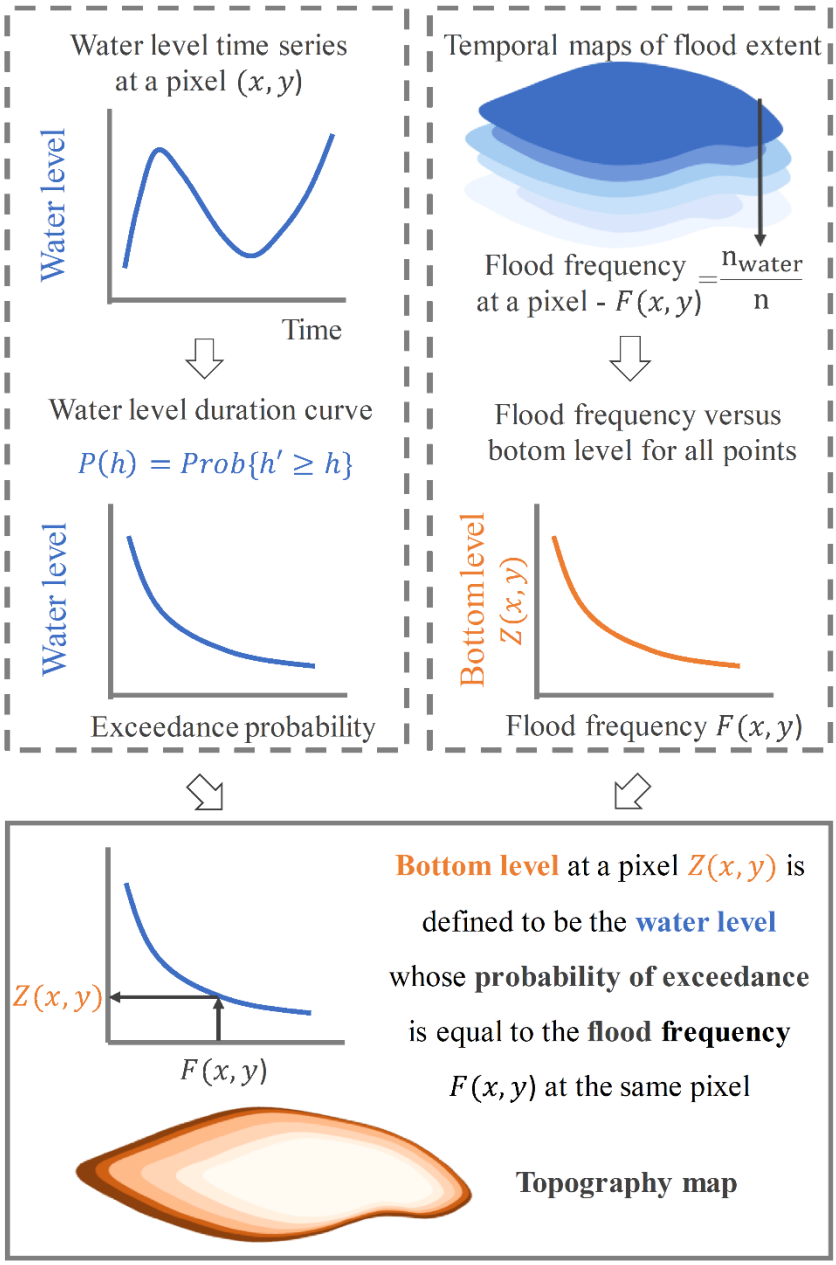

Figure 4.1. Flow chart of the flood frequency-based method to estimate topography.

For any pixel with $F(x, y)$ equal to 100%, $Z(x, y)$ is equal to the lowest water level observed over the period of time, so that the method will be inaccurate to estimate bottom levels for any permanently flooded pixel. In addition, because the calculation is performed pixel by pixel, the water level duration curve and the flood frequency must be known for each pixel (x, y). If only one water level time series is available for the water body, a uniform water level (i.e., a horizontal surface) will be assumed for the whole area ($P(h)$ is defined at a station). For areas with variable water levels, a distributed information of water level gauges (in-situ or virtual stations) are preferable ($P(h)$ is

defined at many stations). In this case, discrete information of water level can be interpolated throughout the extent of the water body to represent the water surface slope.

The method is exemplified in Figure 4.2 by the representation of a digital elevation model (DEM) composed of nine pixels with defined elevations (z_1 to z_4) in which the horizontal water surface increases with each time step (t_1 to t_4). During this period, pixels with bottom level $Z(x,y) = z_3$ have a flood frequency $F(x,y) = 25\%$ (Figure 4.2). Similarly, the water level in the DEM remains above elevation z_3 during 25% of the time (Figure 4.2), i.e., the probability of the water level being greater than z_3 is 25% ($Prob\{h' \geq z_3\} = 25\%$ or $P(h) = 25\%$). This means that the flood probability is equal to the probability that the water level is higher than the bottom level ($F(x,y) = P(h)$).

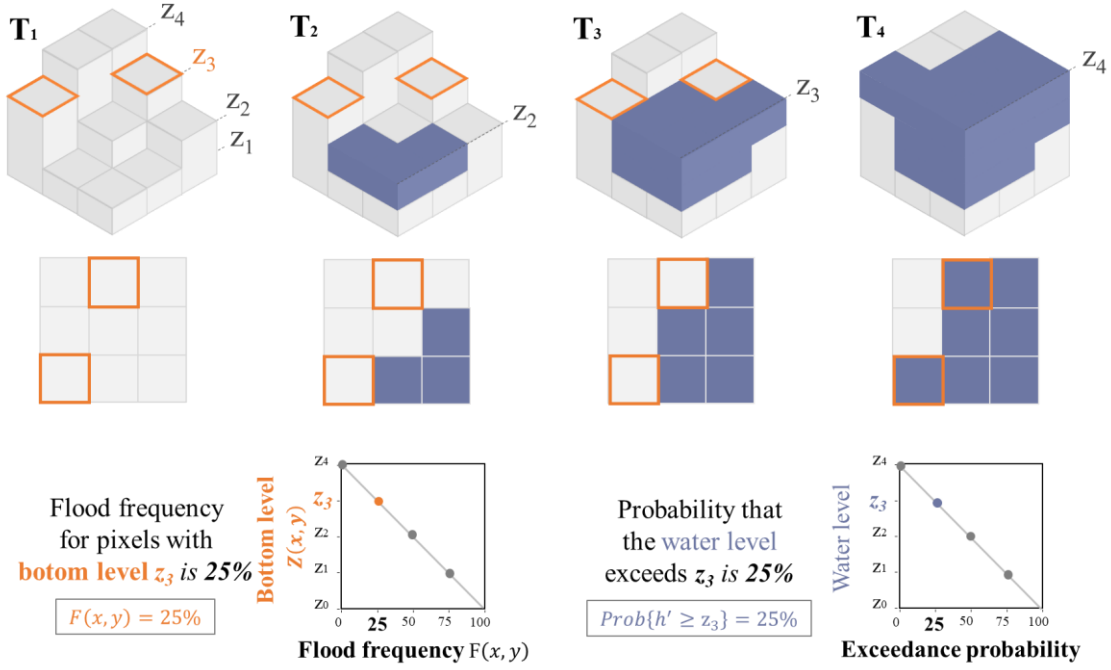

Figure 4.2. Illustration of the flood frequency-based method to estimate topography. Blue pixels are the flooded ones.

4.2.2 Method uncertainties and caveats

The method can be applied in any area that is not permanently flooded, and the size of the estimated area depends on the water level and flood frequency data spatial resolution. These observations should ideally cover the same time period and be representative of the entire range of water levels (i.e., from minimum to maximum water

levels). In other words, more extensive and complete time series data lead to more accurate topography map. In addition, the data temporal resolution must be greater than the water body dynamics, i.e. it must be enough to represent the filling and draining process. Furthermore, the non-stationarity of data must be considered as several processes promote changes in water level and topography over time, such as dams, erosion, deforestation, sediment deposition and climate change.

The method uncertainties depend on the water level and flood frequency data that are used. The water level time series can be derived from in-situ gauge stations or satellite altimeters (i.e., virtual stations). Altimetry levels usually represent the surface averages from multiple tracks and/or footprints, and several altimetry databases also provide level uncertainties. The level accuracy depends on several factors such as the operation and maintenance of in-situ gauge stations and the accuracy of altimeters. However, if the water level error is not systematic, the water level duration curve will not change because the error will cancel itself with many observations.

The accuracy of the flood frequency map depends on the errors of the images used to map the water coverage and the classification accuracy. The images can be derived from optical or radar sensors. Active sensors, such as synthetic aperture radars (SAR), have advantages over optical sensors because they can observe the surface at any weather condition and at any time (day and night), and can map below-canopy inundation (SCHUMANN; MOLLER, 2015). However, long term radar image collections are still scarce, limiting flood frequency mapping. On the other hand, optical images collections have high data availability, such as Landsat missions with data since 1972. Errors in water cover classification using optical images include a possible underestimation of the water coverage extent in canopy inundation areas, such as in lakes that have floating aquatic vegetation or submerged flooded vegetation. Since these areas are classified as flooded only when the water level is equal to or greater than the vegetation height, the flood frequency map represents the flood above the vegetation, and therefore the estimated topography has a vegetation height bias. In addition, the seasonal bias in the flood frequency map can occur due to temporal distribution of the valid observations, that is, cloudy seasons may have fewer valid images than dry seasons. Furthermore, the scan line corrector (SLC) failure in some satellites, such as Landsat-7, introduces a slatted appearance in the images, carrying these artifacts into the flood frequency map (PEKEL et al., 2016). In section 4.2.3, the state-of-the-art of altimeters and flood extension databases is presented.

The number of water level stations used to represent the water surface elevation also affects the accuracy of the bottom level estimation. For instance, distributed information of water level within the water body allows the representation of the water surface slope. However, if only one information is considered (i.e., assumption of a horizontal water surface), the maximum error of the estimate ($Max.Error$) can be calculated considering the slope ($Slope$) and the maximum length ($Max.length$) of the water body by Equation 1.

$$Max.Error = Slope \times Max.length \quad (1)$$

Slope in natural and artificial lakes depends on factors as wind fetch, volume of the inflow hydrograph and length and depth of the lake (FREAD, 1993). In floodplain shallow lakes, additional uncertainties arise due to the terrain heterogeneity and the connectivity with the main river and other floodplain units.

Finally, the method is not able to estimate bottom levels below the lowest observed water surface elevation, i.e. inactive volumes. However, this information can be approximated from 3D topography extrapolations and interpolations considering the edge slope of the water body, as presented by Getirana et al. (2018) and Tseng et al. (2016). Absolute volume can also be estimated by extrapolating the stage-area curve, as presented by Collischonn and Clarke (2016) and Busker et al. (2019).

4.2.3 Data available

In this section, the current and future datasets available for deriving water levels and flood frequency are reviewed, with a focus on remote sensing methods.

4.2.3.1 Water level

The water level duration curve can be calculated from water level time series from in-situ gauge stations or by altimetry data derived from satellite altimeters (virtual stations), such as ICESat-1 and 2 (https://openaltimetry.org), Jason-1, 2 and 3, ENVISAT, and TOPEX/Poseidon. The accuracy of these altimeters ranges from 0.10 m (ICESat-1, URBAN et al., 2008) to 1.07 m (Jason-1, JARIHANI et al., 2013), with a 10 to 91 days repeat cycle. O'Loughlin et al. (2016) present a comparison of this information for the most popular altimetry missions to estimate water level. In addition, there are multi-

mission datasets with time series are available for rivers, lakes, and reservoirs and are listed: 1) Hydroweb-THEIA (CRÉTAUX et al., 2011); 2) Global Reservoir and Lake Elevation Database (G-REALM; BIRKETT et al., 2011); 3) Global Land Surface Altimetry Data (DLAS/ICESat GLA14; ZWALLY et al., (2014); 4) Database for Hydrological Time Series over Inland Waters (DAHITI; SCHWATKE et al., 2015); and 5) Global River Radar Altimetry Time Series (GRRATS; Data are available at DOI 10.5067/PSGRA-SA2V1; COSS et al., 2019). Duan and Bastiaanssen (2013) describe the satellites used in some of these databases, the available data period, and the vertical reference system. In addition to databases, altimetry data can be processed using web applications, such as Altimetry Explorer (AltEx) for JASON-2 and JASON-3 data (MARKERT et al., 2019), or specific software such as MAPS, and Satellite Water Gauging (SWG).

4.2.3.2 Flood frequency

The flood frequency at each pixel in the region of interest can be obtained from temporal maps of surface water cover, e.g., through classification of optical imagery using water indexes and methods as reviewed by Huang et al. (2018). Examples of spaceborne sensors are:1) Landsat (since 1984) with 16-day timescales and spatial resolution of 30 m (DU et al., 2014; FEYISA et al., 2014; FISHER; FLOOD; DANAHER, 2016; JIANG et al., 2014; SHENG et al., 2016; YAMAZAKI; TRIGG; IKESHIMA, 2015); 2) MODerate Resolution Imaging Spectroradiometer (MODIS, since 2000) with daily timescales and spatial resolution of 250–500 m in visible and near- infrared bands (GAO; BIRKETT; LETTENMAIER, 2012; KHANDELWAL et al., 2017; KLEIN et al., 2017; SUN; YU; GOLDBERG, 2011); 3) Sentinel 2A and 2B (since 2015) with 10 m spatial resolution in visible and near- infrared bands at 5–10 day intervals (HUANG et al., 2018b; KORDELAS et al., 2018; SCHWATKE; SCHERER; DETTMERING, 2019); 4) RapidEye constellation (5 satellites, since 2008) with 5 m resolution and temporal resolution of 1-5.5 days (COOLEY et al., 2017, 2019; GAROUSI-NEJAD et al., 2019); and 5) PlanetScope constellation (120CubeSats, since 2014) with daily revisit time globally at 3-5 m spatial resolution (COOLEY et al., 2017, 2019).

Based on the decadal-scale monitoring of Landsat missions, a few global datasets of surface water extent have been developed, such as the JRC Global Surface Water dataset (GSW; PEKEL et al., 2016) available in Google Earth Engine platform (GORELICK et al., 2017), and the recent Landsat Level 3 Dynamic Surface Water Extent

dataset (DSWE; JONES, 2019), with data available for the US. GSW dataset represents a monthly record of water presence on a global scale between March 1984 and October 2015, corresponding to images from the Landsat program classified as water, non-water, and no-data with a spatial resolution of 30 m, and the classification accuracy showed omission errors less than 5% and commission errors less than 1% (PEKEL et al., 2016).

Time series of water surface area of specific lakes and reservoirs that have been corrected for contamination from clouds, cloud shadows, and/or terrain shadows are also available: 1) Surface area time series of 6,817 global reservoirs (Zhao and Gao, 2018; https://ceprofs.civil.tamu.edu/hgao/); 2) Database for Hydrological Time Series of Inland Waters (DAHITI; SCHWATKE; SCHERER; DETTMERING, 2019); and 3) Global lake/reservoir area time series (GLATS; YAO et al., 2019).

Examples of SAR satellites used for water covered mapping are: 1) Sentinel 1 (CAZALS et al., 2016; HUANG et al., 2018b); RADARSAT (BOLANOS et al., 2016); 2) Envisat Advanced Synthetic Aperture Radar (ASAR, SANTORO et al., 2015); 3) JERS-1 (HESS et al., 2003, 2015); and 4) ALOS/PALSAR (ARNESEN et al., 2013; CHAPMAN et al., 2015). New opportunities will emerge with new satellites, such as NASA-ISRO Synthetic Aperture Radar and SWOT (Surface Water and Ocean Topography), which will be launched in 2021. SWOT will allow estimates of both flood extent and distributed information of water levels of inland water bodies (BIANCAMARIA; LETTENMAIER; PAVELSKY, 2016). Bonnema and Hossain (2019) presented a synthetic experiment to investigate the capability of SWOT to estimate reservoir characteristics as the stage-area relationship.

4.2.4 Flood2Topo application

Flood frequency to Topography (Flood2Topo) is a MATLAB application developed to convert a flood frequency map into a topography map (bottom levels), also computing the stage-area-active storage curves. The algorithm takes as input a flood frequency map (GeoTIFF format) and a single water level time series of the water body (txt format), both provided by the user.

Besides flood frequency, water level information is required for each pixel to obtain the bottom level, as described in section 4.2.1. In the Flood2Topo app, the estimation was simplified by choosing a single water level time series for all pixels and assuming that the water surface is horizontal along the region of interest. To use water level time series data for each pixel in the case of a non-horizontal surface, the script must

be modified. The estimated topography is used to infer a stage-area relationship which is then numerically integrated to yield a stage-active storage relationship. The stage-area curve is elaborated considering, for each bottom level value in the topographic map (x), the number of pixels with values less than or equal to x multiplied by the spatial resolution, resulting in the area related to each stage (y). Therefore, it is not necessary to adjust functions from level versus area points, like traditional approaches. This processing is done by considering all pixels in the topography map: if the map contains more than one water body or noise, the area of interest must be delimited before using the Flood2Topo app to yield individual stage-storage curves. Furthermore, since the method does not recover the topography below the lowest observed water surface, the active volume represents the volume above the lowest observed water level. The application with documentation and an example is available at https://data.mendeley.com/datasets/jwxxjc5kyf/draft?a=224b0e01-c4af-4a90-94c2-bd07595b23db.

Flood frequency maps can be obtained from different sources, as described in section 4.2.3.2. As an option for the user, an Earth Engine script is provided (Text S4.1, Supporting Information or code) to calculate the flood frequency map for a defined period from the GSW - JRC Monthly Water History v1.0 dataset (PEKEL et al., 2016), available in Google Earth Engine platform (GORELICK et al., 2017). In the script, the open water cover frequency for each pixel was calculated as the ratio between the number of observations classified as water and the number of valid observations, i.e. with information during the selected period (user defined).

4.3 Validation experiments

In order to evaluate the proposed method, Flood2Topo was used to estimate the topography of two natural lakes, Lake Poopó in the Bolivian Altiplano and Lago Grande de Curuai in the Central Amazon floodplains, and 12 hydropower reservoirs in Brazil (Figure 4.3). The lakes were chosen due to data availability, and the reservoirs were selected to cover a wide variety of reservoir shapes, volumes, and areas, given the limited 30 m spatial resolution of Landsat images. To understand the global representativeness of the assessed lakes, Figure 4.3l and 3m present the distributions of reservoir areas and volumes from global databases on lakes and reservoirs (GRanD and HydroLAKES), and show that the 12 selected reservoirs are representative of the largest 42.6% of dams in the GRanD database in terms of area (smallest value = 5.5 km² for Quebra Queixo dam; ~ 61

pixels), and the largest 34.8% in terms of volume (smallest value=136.6 hm³ for Quebra Queixo dam).

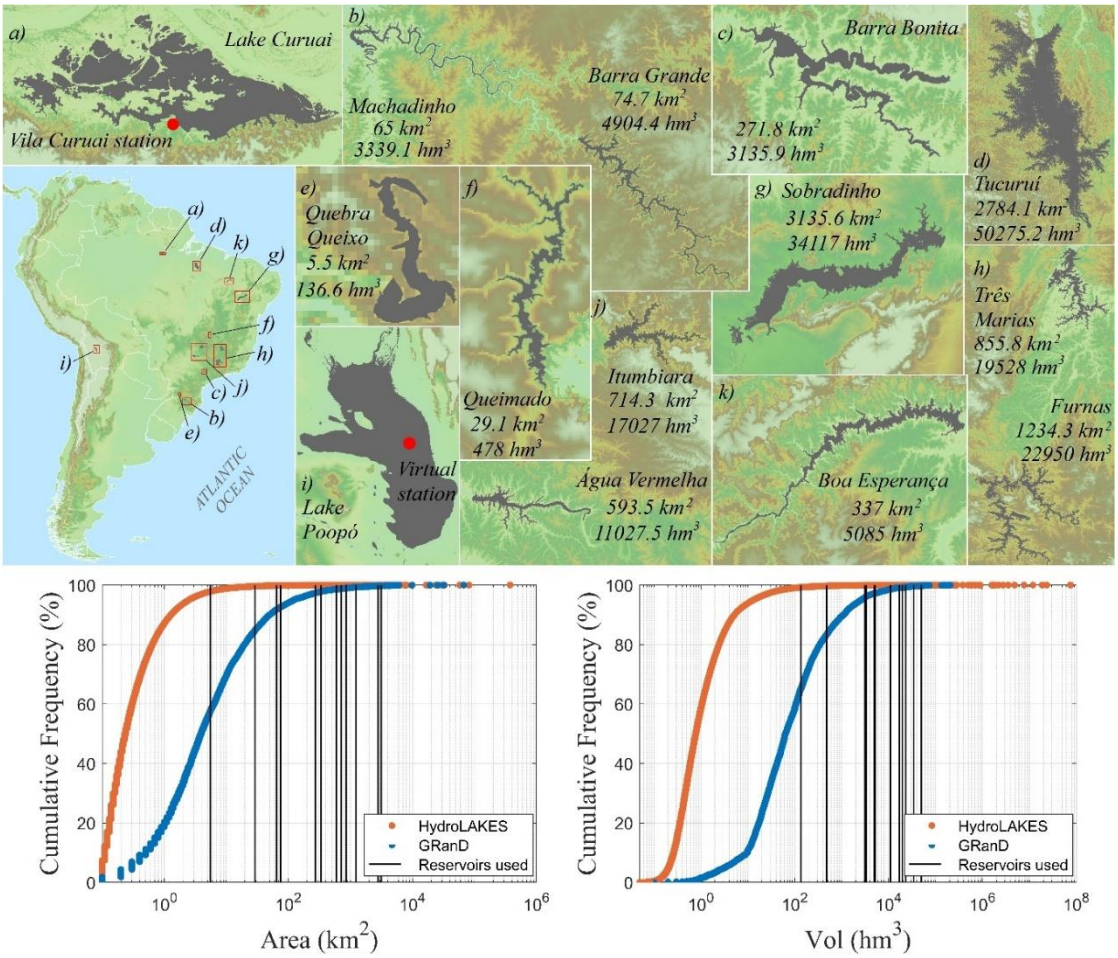

Figure 4.3. a) – k) Location, maximum area, and volume of natural lakes and reservoirs used for validation of the method. Terrain elevation from SRTM DEM (Farr et al., 2007; spatial resolution of 90m). l) and m) Cumulative frequency of area and volume of 1.43 million natural and artificial lakes and 6,862 reservoirs from the HydroLAKES (MESSAGER et al., 2016) and GRanD (LEHNER et al., 2011a) datasets, as well the values related to the 12 analyzed reservoirs.

As described in Section 4.2.4, Flood2Topo requires two information: a water level time series and a flood frequency map. The map was elaborated for each lake from the developed Earth Engine script (Text S4.1, Supporting Information or code), and the assessed period is the same for both GSW Monthly and water level datasets for each lake. The water level was derived from in-situ and virtual stations, as described below.

The topography of Lake Poopó was estimated using 726 water level estimates from a satellite altimetry virtual station (available at the Theia website) for the period from 17-Feb-2000 to 01-Oct-2015, while for the Lago Grande de Curuai 11,628 observations from Vila Curuai in-situ gauge station for the period from 1-Mar-1984 to 31-Dec-2015 were used (see Figure 4.3 for location of the stations). Altimetry data are referenced in relation to geoid EGM08 (Theia dataset), and the Vila Curuai gauge station was referenced in relation to geoid EGM08 according to values recommended by Moreira (2016). Therefore, estimated topographies are also referenced in relation to geoid EGM08. The reservoirs topography was estimated using in-situ water level time series from ONS (Brazilian *Operador Nacional do Sistema Elétrico*; available at <www.ons.org.br>). The assessed period of water level for each reservoir are shown in Table S4.1 (Supporting Information).

Lakes' topographies were validated with the following datasets. Arsen et al. (2013; called hereafter Arsen approach) estimated the Poopó topography interpolating isolines (isobaths) created from Landsat images and altimetry data, which was compared with Flood2Topo estimates. The Curuai bathymetry was obtained in previous studies with an extensive echo-sounding survey (BARBOSA, 2005; BARBOSA et al., 2006; RUDORFF; MELACK; BATES, 2014b). Since reservoir topographies were not available, the method was validated in terms of the stage-active storage relationship i.e., by removing the dead volume from the total reservoir volume.

4.4 Results

4.4.1 Natural lake

Lake Poopó is a shallow lake that can be completely dry at certain years and is situated in the Bolivian Altiplano (Figure 4.3). The lake bottom level was well represented relatively to the Arsen approach (Figure 4.4), with a bias of 5.68 cm and root mean square deviation (RMSD) of 18.50 cm (n = 2,524,605). Topographical variation was also well represented, with a Pearson correlation coefficient of 0.97, an RMSD (bias-corrected) of 17.61 cm, and a coefficient of determination (R^2, bias-corrected) of 0.93. To disregard the bias, RMSD and R^2 values were determined by considering the anomaly of values, i.e., by computing the difference between values and their means.

As the lake was dry in some periods (Max flood frequency < 100%), it was possible to estimate the bottom level in the whole area of Lake Poopó. The satisfactory results also suggest that for this estimation the assumption of a horizontal water surface

was sufficient. In addition, terrain heterogeneities were better estimated with the proposed method than with the Arsen approach, revealing a more detailed topography (see detail in Figure 4.4). This is because Flood2Topo estimation is performed pixel by pixel, avoiding the loss of detail in the isobath interpolation of the Arsen approach.

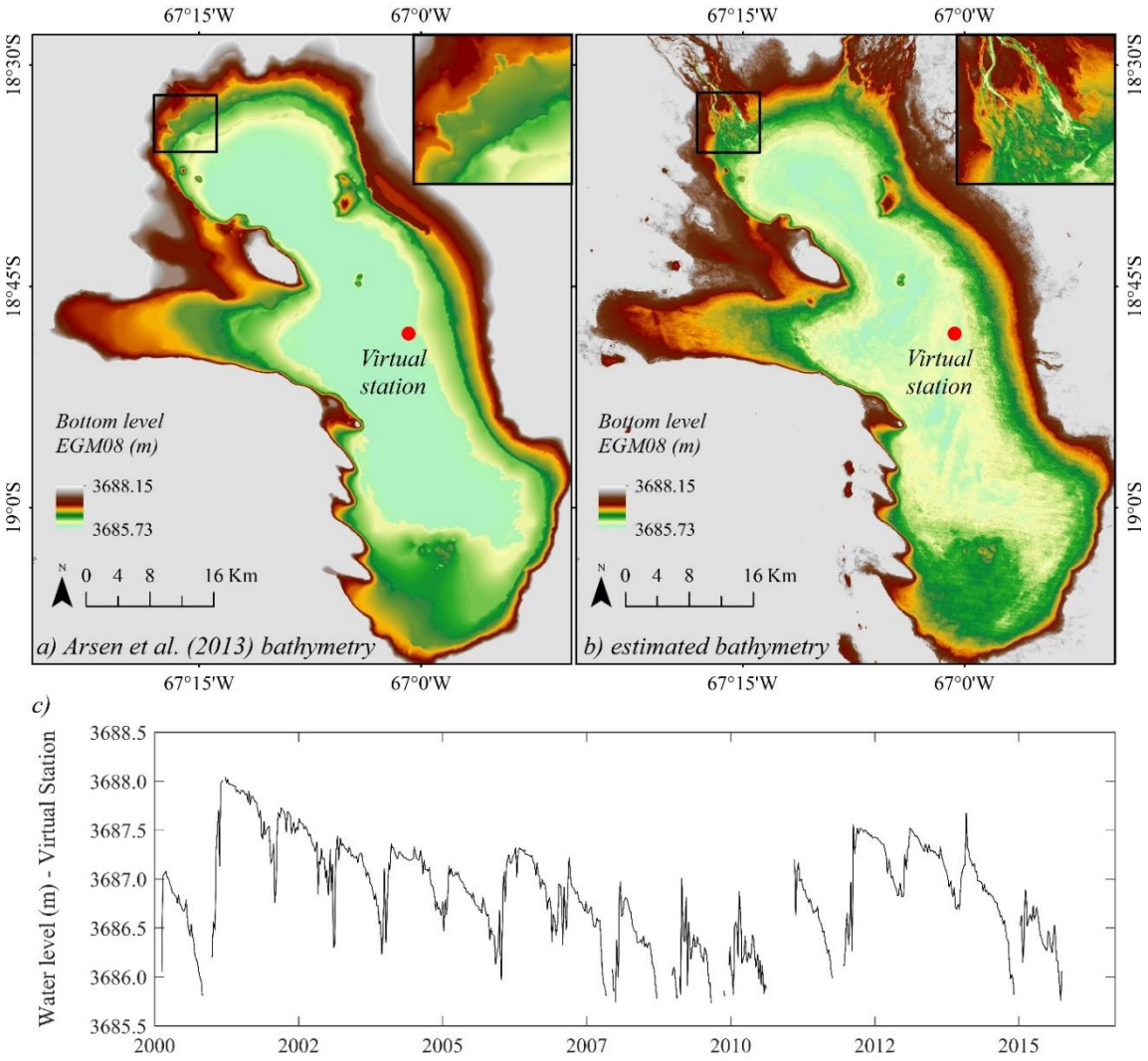

Figure 4.4. a) Locally derived (Arsen et al., 2013) and b) Flood2Topo based topographies for the Lake Poopó. c) Water level (m) time series at the satellite altimetry virtual station.

4.4.2 Floodplain lake

The other evaluated lake is the Lago Grande de Curuai, which is located in the middle-lower reach of the Amazon River and has great variation in flooded areas and water levels associated with flooding from the Amazon mainstem. The floodplain is composed of several lakes that are very shallow in the low water period. The observed (RUDORFF; MELACK; BATES, 2014b) and estimated topographies are presented in

Figure 4.5. Figure 4.5b and d also exemplify the slatted appearance in the estimated topography and flood frequency map due to the Landsat SLC-off (PEKEL et al., 2016).

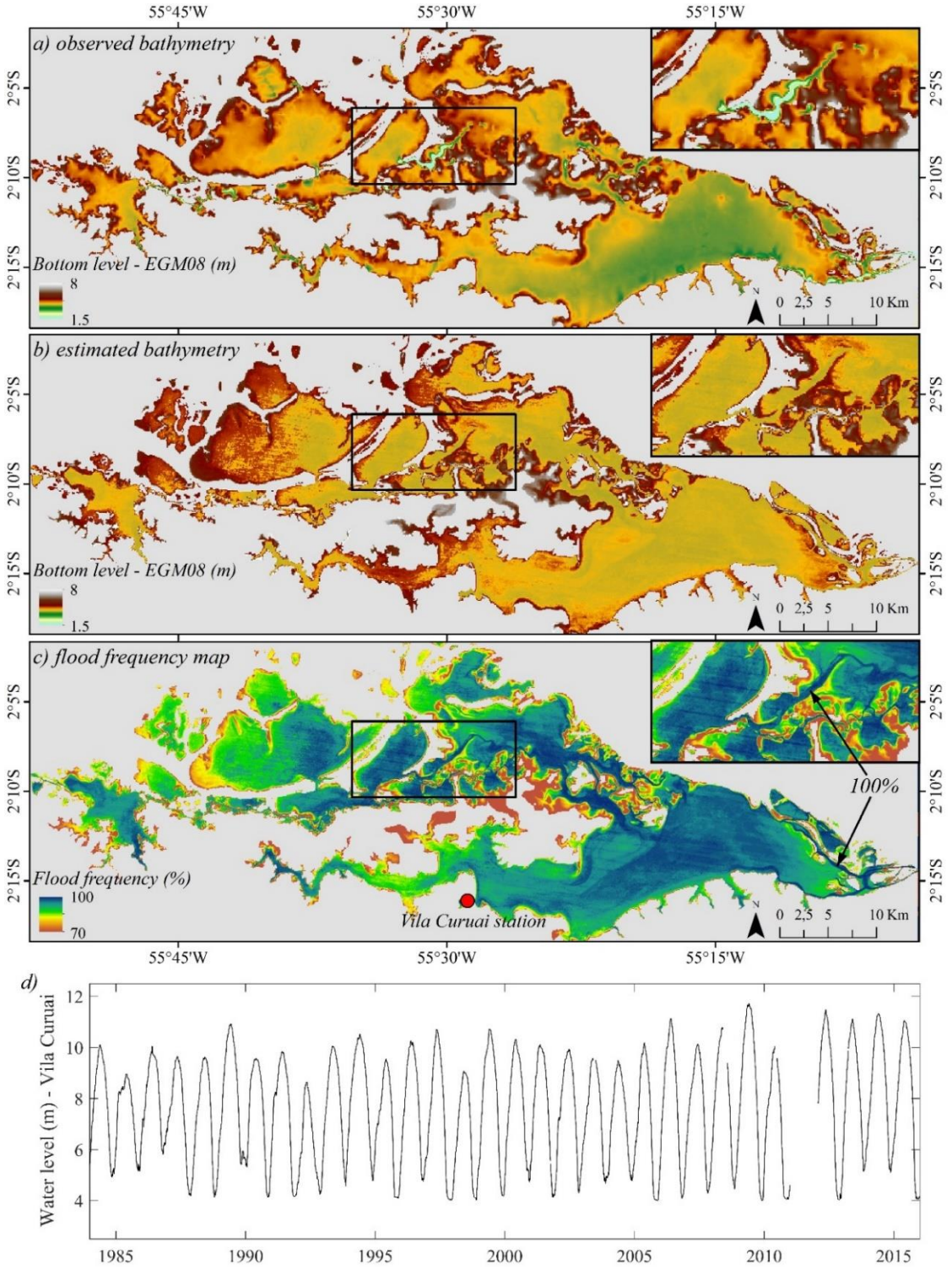

Figure 4.5. Observed (a) and estimated (b) topographies in the Lago Grande de Curuai floodplain; c) Flood frequency map and d) water level at Vila Curuai station.

The bottom level was overestimated with a bias of 0.60 m and an RMSD of 1.46 m (n = 158,387). The estimated minimum value was 4 m, the smallest observed value in the water level time series. Thus, bottom level was overestimated in regions with flood frequencies equal to 100 % (e.g., the channels highlighted in Figure 4.5c). In addition, the lower bottom levels were poorly represented for two reasons. First, while the whole floodplain is subject to the Amazon River flood pulse (RUDORFF; MELACK; BATES, 2014a), the water level measurements were obtained at a single location in the floodplain located on the south edge of the lake (Figure 4.5c); and second, the minimum level in the Vila Curuai station (Figure 4.5d) is affected by the impoundment of water in low-water periods, meaning that the water level at the station may be higher than the river water level and in the lakes that remain connected with the river. Therefore, the water level in Vila Curuai is not fully representative of the water level variation across the floodplain. Despite the underestimation, the topographical variation was reasonably well-represented. Estimations yielded a Pearson correlation coefficient of 0.68, an RMSD (bias-corrected) of 1.33 m, and an R^2 (bias-corrected) of 0.36.

4.4.3 Reservoirs

The observed and estimated stage-active storage relationships of 12 Brazilian reservoirs (location in Figure 4.3), the volume RMSD (hm^3), and the normalized RMSD (NRMSD = RMSD/observed V_{100}) are presented in Figure 4.6. Table S4.1 (Supporting Information) includes, for each reservoir, the percentage of the reservoir area that has a flood frequency equal to 100% ($\frac{FF_{100}}{Area}$) during the assessed period, and the lowest and highest level (L_0 and L_{100}) corresponding respectively to the minimum ($V_0 = 0$) and maximum active storage (V_{100}) for both observation and estimations.

In general, there is a satisfactory agreement between observed and estimated curves, with NRMSD values ranging from 2% to 11.09 % (with the exception of the Barra Bonita reservoir with NRMSD = 27.05%), and average NRMSD of 6.39 %. Other authors found average NRMSD values of 7.4% (n = 18; Busker et al., 2019), 7.2% (n = 5; Gao et al., 2012), and 17.54% (n = 5; Zhang et al., 2014) using optical images and satellite altimetry for reservoirs.

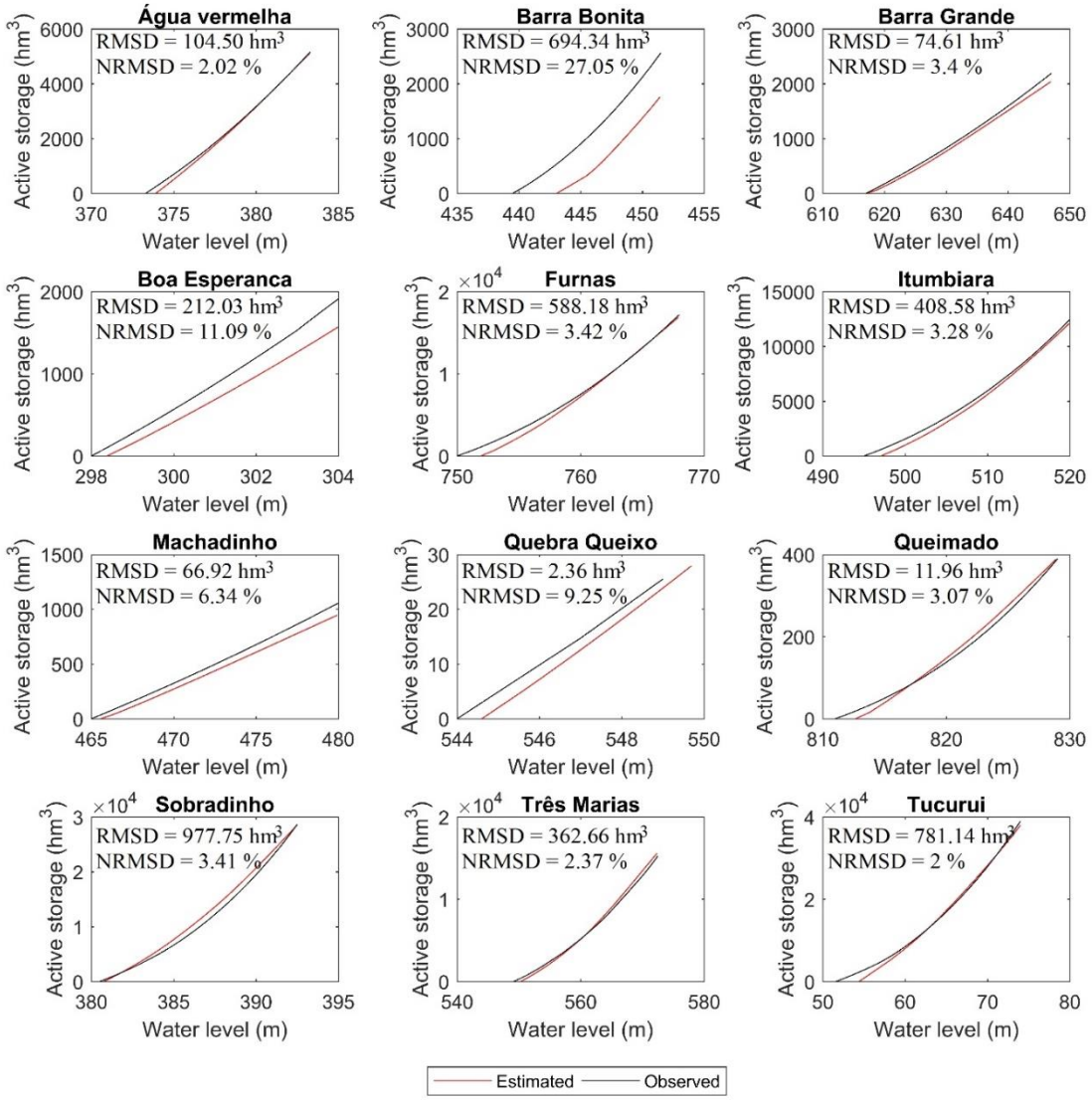

Figure 4.6. Water level versus active storage observed and estimated for 12 artificial reservoirs in Brazil.

Although the method only recovers topography in regions with flooded area variation, it presented satisfactory results to estimate the stage-volume relationship in small lakes with small variation in the flooded area, such as the Quebra Queixo reservoir, where only 14% of the reservoir area (0.77 km^2) has a variable flooding area. In fact, Figure 4.7a shows that there is no clear relation between the reservoirs size and the NRMSD values. The percentage of the reservoir area that is permanently flooded ($\frac{\mathrm{FF}_{100}}{\mathrm{Area}}$) is also not related to NRMSD, as observed in Figure 4.7b. Both reservoirs with areas where flood frequency varies greatly (e.g., Itumbiara with $\frac{\mathrm{FF}_{100}}{\mathrm{Area}}$ = 45.96%) and reservoirs with large permanently flooded areas (e.g., Tucuruí with $\frac{\mathrm{FF}_{100}}{\mathrm{Area}}$ = 85.86%) presented low

NRMSD. Busker et al. (2019) estimated stage-area relationships using Landsat images and satellites altimetry for 135 global lakes and pointed out that low R^2 values were related, among others, to a nearly constant lake area and small lake sizes. Although we did not use satellite altimetry, we did not observe a similar relationship. On the other hand, although the amplitude of level variation (observed L_{100} - L_0) has no clear relationship with NRMSD (Figure 4.7c), two out of the three reservoirs with the highest NRMSD have the smallest variations in level amplitude (Boa Esperança with L_{100} - L_0 = 6 m and Quebra Queixo with L_{100} - L_0 = 5 m). Therefore, the proposed method is satisfactory for small and large reservoirs, and the NRMSD can be related to the amplitude of water level variation (within the range of values tested in this work, with the lower limit tested being 5 m).

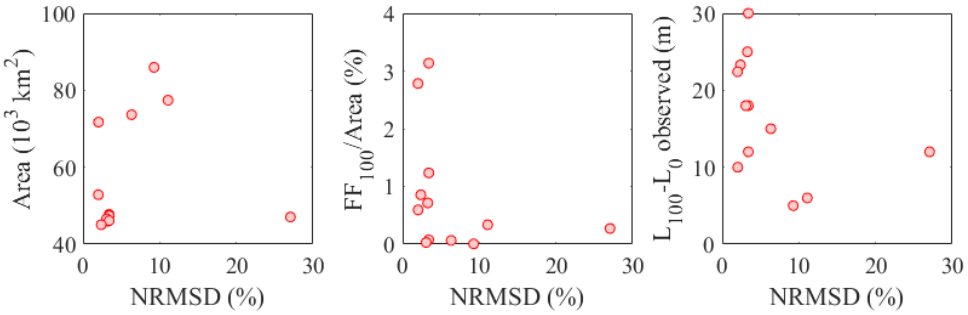

Figure 4.7. NRMSD versus area, the fraction of the reservoir area that has a flood frequency equal to 100% ($\frac{FF_{100}}{Area}$), and amplitude of level variation (observed L_{100} - L_0).

4.5 Discussion

The presented method can be applied to any lake worldwide. Since we use 30 m spatial resolution Landsat images, our ability to resolve small lakes is limited (e.g., the smallest assessed lake is 5.5 km^2, equivalent to ~ 61 pixels). The assessed sample of lakes is not representative of Earth small lakes, since 2.2% and 0.8 % of lakes (n = 1.43 million; HydroLAKES dataset; MESSAGER et al., 2016), or 42.6% and 34.8 % of reservoirs (n = 6,862; GRanD dataset; LEHNER et al., 2011a) are larger than 5.5 km^2 and 136,6 hm^3, respectively (Figure 4.3). Therefore, the method needs to be better evaluated in small lakes using better spatial resolution images. This is possible, for instance, using Sentinel images (5 m) and the PlanetScope constellation (3-5 m). The images from this constellation can be used to depict high-frequency dynamics of flood extent on a daily basis.

Although the analyzed lakes are not representative of global small lakes, the global applicability of the method is promising. Considering the GSW dataset, the most complete dataset currently available, the seasonal water cover in the contemporary timeframe represents 22.5 % (0.81 million km^2) of the water covered mapped from October 2014 to October 2015 (PEKEL et al., 2016). However, as the water coverage is variable in time and space, and the flood frequency map depends on the assessed period, usually longer than one year, the method applicability can be greater. For example, assuming the water level time series data is available, the method is applicable in 35.8 % (86%) of the global water surface area mapped by Pekel et al. (2016; Occurrence map), when considering the number of pixels with occurrence between 0 and 95% (99%) over 35 years. This is an approximate estimate as the coast regions (ocean) are considered in the map.

The method accuracy is related to the input data. Regarding the water level, satellite altimetry virtual station was only used for Lake Poopó with expected accuracy of less than 40 cm, and in situ stations were used in other lakes. The water cover images from GSW dataset has high accuracy in the classification with low errors of omission (<5%) and commission (<1%). However, the estimated topography can have a bias related to the seasonality of valid data and/or the presence of flooded vegetation, as described in section 2.2. To further understand these uncertainties, a detailed analysis is performed for the Curuai floodplain since this region of the Amazon basin has high cloud cover in the austral summer (MARTINS et al., 2018), presence of aquatic macrophytes in lakes (SARTORI et al., 2011), and availability of an in situ surveyed bathymetry.

Figure 4.8 shows the flood frequency versus errors in the bottom level estimation. Note that the vegetation height bias in the Curuai floodplain occurs mainly in regions of lower flood frequency or in higher elevations. This bias could be removed using altimetry data such as ICESat-1 and ICESat-2. For example, by fitting a relationship between flood frequency and the topography error in relation to the altimetry level.

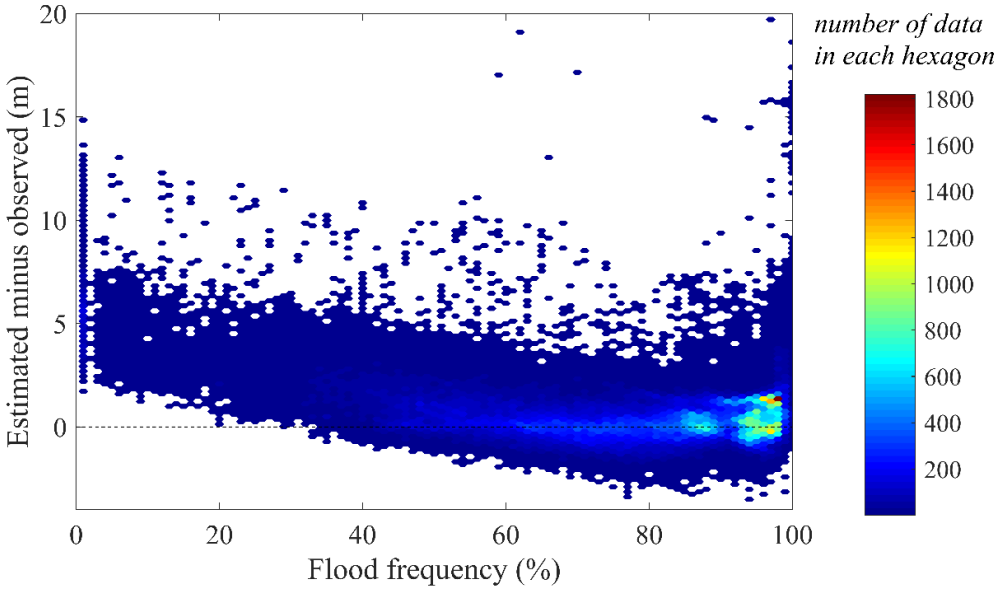

Figure 4.8. Flood frequency versus error in the estimation of the bottom level of the Lago Grande de Curuai floodplain.

The occurrence map developed by Pekel et al. (2016) was used to evaluate the bias related to seasonal variation in the number of valid observations across the year once this map represents the average of all monthly flood frequency, i.e., this map normalizes the occurrences. However, the topography estimate using occurrence map does not improve by comparing the flood frequency computed over the full period: bias increased from 0.60 to 0.72; RMSD increased from 1.46 to 1.57; Pearson's correlation coefficient decreased from 0.68 to 0.63 and R^2 reduced from 0.36 to 0.3. This difference can be related to the high cloud cover in the summer, since the average of all monthly flood frequency is affected if the flood frequency of summer months is very poorly represented. Therefore, normalize the flood frequency did not improve the estimate.

The maximum error due to not considering water surface slope was estimated using Equation 1, and considering the Amazon River water surface slope in this area (1.25 cm/km; average value observed by Birkett et al., 2002 at Óbidos station) and the floodplain longitudinal extent (~ 90 km). It resulted in a maximum error of 1.12 m, which is relatively small if compared to the amplitude of the water surface elevation at Vila Curuai station (5 m; Figure 4.5).

Estimating bathymetry is a major challenge in the remote sensing community due to the time required to obtain and process data. Methods using echo sounders, multi-beam SONAR and LiDAR require time-consuming fieldwork as well as data processing.

Empirical approaches to optical imaging are limited to certain special water conditions (e.g., low sediment load) and still require field data (GAO, 2009; LEGLEITER; ROBERTS; LAWRENCE, 2009). Methods using flood extent require water surface classification and shoreline delineation for each image in a time series (ARSEN et al., 2013; FENG et al., 2011; GETIRANA; CHUL; TSENG, 2018). Besides, none of these studies benefited from using the pre-processed GSW dataset for topography estimation. More recently, Busker et al. (2019) used the GSW database to estimate lake volume, which reduced processing time and storage demands, but they still had to fit functions for the stage-area relationship as in the other, previously developed methods.

The method proposed here distinguishes from others as it uses temporal information (i.e. water level curve duration and flood frequency map), not requiring that data need to be acquired at the same time, and it is performed pixel by pixel. Therefore, it allows topography retrieval for areas connecting large lakes. Similarly, an estimate of the level-active storage relationship can be directly obtained from the topography map, without the need to fit functions or make subjective decisions. The proposed technique is also a straightforward method that can be used with currently available remote sensing datasets.

In addition to lakes, the method can be extended to estimate the bathymetry of intermittent rivers, since they are associated to flood frequencies smaller than 100%. Such rivers are found on all continents, may represent up to 50% of the global river network, and are usually associated with data scarcity (DATRY; LARNED; TOCKNER, 2014; JARIHANI et al., 2015). In this estimation, the bed's slope can be used to consider the inclination of the water surface.

Estimation of wetlands topography is also possible, as in the complex floodplains of the Amazon Basin with multiple lakes (LATRUBESSE, 2012; MELACK; HESS, 2010b; TRIGG et al., 2012). Due to the complexity of these environments, which might include large areas of flooded forest, the flood frequency mapping should be performed using radar or considering only the open water areas using optical images. In addition, the approximation of a horizontal water surface might be inaccurate in floodplains (JUNG et al., 2010). To overcome this problem, the method must be adjusted by accounting for distributed information across the floodplain using different water level gauges (or virtual stations) or estimating the floodplain water level using the mainstem surface water elevation, by interpolation, for example. Currently, the spatial resolution of space altimeters is limited to a few points within the water body, but this could be improved by

adopting distributed information with new swath remote sensing products such as SWOT (BIANCAMARIA; LETTENMAIER; PAVELSKY, 2016).

For the hydrodynamic simulation of flood dynamics in complex river-floodplain systems, the proposed method is also very promising, since current modeling approaches typically neglect the topography or dynamic storage of floodplain lakes due to data unavailability (NEAL; SCHUMANN; BATES, 2012; SCHUMANN et al., 2016; WILSON et al., 2007). Similarly, analyses of the temporal variation of topography could be performed, for example to study lakes with changing patterns, such as the Lake Chad (GAO et al., 2011), Lake Eyre (LEON; COHEN, 2012), and Lake Poyang (FENG et al., 2011) due to dredging or more complex morphodynamics.

4.6 Conclusions

A simple flood frequency-based method was proposed for estimating the topography and active volume of water bodies. The approach requires that the analyzed area is not permanently flooded, in addition to availability of water level data (at least at one station), and a flood frequency information for each pixel, which can be obtained from currently available datasets (e.g., in-situ or satellite altimetry, and GSW dataset). The developed Flood2Topo app provides as outputs the topography map and level-area-active storage relationships.

We validated 3D topography in two natural lakes and 12 artificial reservoirs in Brazil. The estimated bottom level in lakes presented BIAS of 5.68 cm and 60 cm; RMSD of 18.5 cm and 146 cm; and R^2 of 0.93 and 0.36. Test cases in artificial reservoirs showed that the active volume of reservoirs can be estimated from 3D topography and the stage-area-volume relationship with NRMSD values ranging from 2% to 11.09% for 11 reservoirs (average NRMSD of 6.39 %).

The growing number of databases of satellite altimetry and surface water mapping (e.g., 46% of the databases cited in section 2.2 are from 2019), in addition to improved image processing capability (e.g., Google Earth Engine platform), and the perspectives with forthcoming missions (e.g., SWOT to be released in 2021), improve the feasibility of topography estimation by the proposed method. This sets up great opportunities to quickly and simply monitor the volumes of ungauged water bodies (natural lakes, reservoirs, intermittent rivers, and wetlands), as well as using topography for hydrological applications, such as hydrodynamic simulation of flood dynamics. On the other hand, there is still potential for improvements of the method, as well as open major challenges,

such as: 1) application in flooded vegetation areas with radar images; 2) estimation in small lakes using high resolution images; 3) use of distributed water level across the studied region (i.e., considering non-horizontal water surfaces); and 4) estimation of the bottom levels below the lowest observed water surface.

CAPÍTULO 5. High-resolution mapping of floodplain topography from space: a case study in the Amazon

Um método para estimar a topografia de lagos utilizando o sensoriamento remoto foi desenvolvido e validado no estudo anterior (capítulo 4). O capítulo 5 aplica essa técnica em uma área grande e complexa com diversos lagos e canais sujeitos a inundação do rio Amazonas. Essa aplicação considera imagens de extensão de inundação provenientes de uma base de dado global de imagens Landsat e informações do nível da água do rio, que são utilizadas para estimar o nível da água na planície. Assim, a informação distribuída do nível da água na planície é considerada. O viés decorrente da altura da vegetação é removido do modelo topográfico estimado a partir de dados de altimetria por satélite (ICESat-2). A validação apresentou uma raiz do erro médio quadrático de 0,89 m para a elevação da planície de inundação e boa representação de padrões espaciais com coeficiente de correlação de Pearson de 0,77. Assim, o mapeamento topográfico de alta resolução (30 m) em áreas de água aberta pode ser uma alternativa aos modelos globais que representam essas áreas como uma superfície plana. Esse capítulo também avalia a batimetria do rio Amazonas, obtida a partir de cartas náuticas da Marinha do Brasil, e apresenta mapas de profundidade da planície de inundação correspondentes aos períodos de cheia e seca. Os resultados mostram que o volume de armazenamento na planície de inundação em águas abertas varia em média 85,8 km^3 a cada ano, ou seja, vai de 11,9 km^3 em águas baixas até 116,2 km^3 em águas altas. 50% dessa área permanece com profundidade menor que 2 m e 6 m nos períodos de água-baixa e água-alta, respectivamente. O método pode ser aplicado a qualquer área inundada temporariamente e o conjunto de dados disponível fornecerá subsídios para estudos hidrológicos, ecológicos e geomorfológicos na Amazônia.

This chapter is based on the following paper submitted to Remote Sensing of Environment (April of 2020): FASSONI-ANDRADE, Alice C.; PAIVA, Rodrigo C. D. de; RUDORFF, Conrado M.; BARBOSA, Claudio C. F.; NOVO, Evlyn M. L. M. **High-resolution mapping of floodplain topography from space: a case study in the Amazon**

Graphical abstract

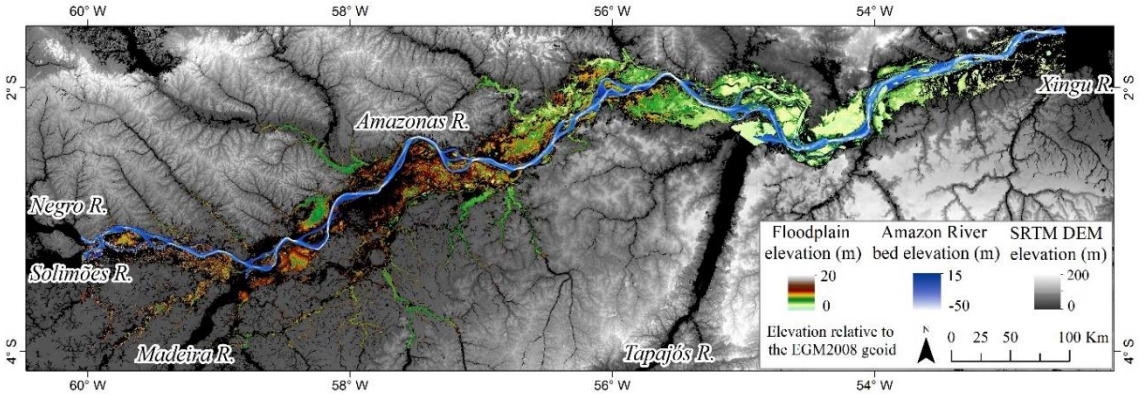

Abstract

Terrain elevation is essential for land management, navigation, and earth science applications. Remote sensing advancements have led to an increase in the availability of a range of digital elevation models with global to quasi-global land coverage. However, the generation of these models in water bodies requires different approaches, such as the delimitation of the shorelines (isobath) of lakes over time. Therefore, the processing costs are high in complex areas with many lakes. Currently, there is no systematic topography mapping of lakes and channels in large and complex floodplains using remote sensing data. We present here the first high-resolution topographic mapping (30 m) of the central Amazon floodplain using a new method based on in-situ Amazon river water levels and a flood-frequency map derived from the Landsat JRC Global Surface Water Dataset. Validation using locally derived bathymetry showed a root mean square error (RMSE) of 0.89 m for floodplain elevation and a good representation of spatial patterns with Pearson's correlation coefficient of 0.77. Our approach for improving topographic representation in open water areas is an alternative to SRTM3 DEM or MERIT DEM, which represent these areas as a flat surface. We also generated the Amazon River bathymetry using nautical charts from the Brazilian Navy (average RMSE of 7.5 m and bias of 5 m), and floodplain depths maps corresponding to the high- and low-water periods of the river flood wave. The results show that the storage volume in the open-water floodplain varies 85.8 km^3 on average each year (from 11.9 km^3 in low-water to 116.2 km^3 in high-water). The method can be applied to any temporarily flooded area to provide the often missing underwater digital topographic data required for hydrological, ecological and geomorphological studies.

5.1 Introduction

Floodplain lakes are important freshwater reservoirs, habitat for aquatic biota and biogeochemical cycling. In this way, lake bathymetry is essential information in the quantification of many processes such as water storage (AVISSE et al., 2017; BUSKER et al., 2019; MESSAGER et al., 2016), sedimentation rate, and many other key variables for understanding floodplain morphology and the hydrodynamic interactions between rivers and lakes (CHEN et al., 2019; HAMILTON; SIPPEL; MELACK, 2004; PAIVA et al., 2013; PARK; LATRUBESSE, 2017; TRIGG et al., 2012). Furthermore, the topography is essential for accurate hydrodynamic simulations, once the error associated with topographic data affects, for example, the representation of water flows, flood extent, and storage volume in numerical simulations (BAUGH et al., 2013; PAIVA et al., 2013; TRIGG et al., 2012; YAMAZAKI et al., 2012).

Digital elevation models (DEMs) can be obtained on global scales, such as WorldDEMTM (KRIEGER et al., 2007), Global Digital Elevation Model – ASTER GDEM (TACHIKAWA et al., 2011), Global Multi-resolution Terrain Elevation Data - GMTED2010 (DANIELSON; GESCH, 2011), and Shuttle Radar Topography Mission – SRTM (FARR et al., 2007a) models. SRTM is the most widely used DEM in hydrodynamic simulations (PAIVA et al., 2013; RUDORFF; MELACK; BATES, 2014b; TRIGG et al., 2009; WILSON et al., 2007; YAMAZAKI et al., 2012). However, these DEMs are affected by vegetation cover or other objects on the surface and are subject to acquisition and processing errors, such as absolute bias, speckle, and stripe noise (RODRÍGUEZ; MORRIS; BELZ, 2006). Besides, topographic information below the water surface observed on the date of the satellite overpass cannot be recovered due to specular reflection of the pulse in the opposite direction of the sensor antenna. Although previous studies have developed global or nearly global DEM with correction of the vegetation bias (LOUGHLIN et al., 2016) and other errors (YAMAZAKI et al., 2017), there is still no database of floodplain topography in regions mapped as open water in the SRTM. In the Amazon floodplain, for example, lake-floodplain topography has been systematically not included in hydraulic simulations due to lack of bathymetric information (e.g. Baugh et al., 2013; Wilson et al., 2007; Yamazaki et al., 2012). Performing bathymetric surveys in large wetland systems as in the Amazon is a difficult task by conventional methods due to its large size and difficulties in accessing remote areas, high cost, and required time for data acquisition and processing. Indeed, few surveys have been performed on floodplains lakes near the Solimões/Amazon rivers

(BARBOSA et al., 2006; PINEL, 2017; TRIGG et al., 2012). Thus, a simple method to characterize the lake and channel topography without field surveys has great relevance to improving the representation of water flow in hydrodynamic simulations. Furthermore, such a product could be used for ecological and geomorphological studies.

Remote sensing data were used to estimate the topography of lakes as an alternative to conventional methods (ARSEN et al., 2013; FENG et al., 2011; GETIRANA; CHUL; TSENG, 2018; TSENG et al., 2016; FASSONI-ANDRADE et al., 2020a). In these studies, temporal water surface extent maps from Landsat images and altimetry data derived from satellite altimeters (e.g. ICESat-1 and 2, Jason-1, 2 and 3 and ENVISAT) were used. Despite these advances, a method that adequately estimates continuous digital terrain elevation over large floodplains with complex topography, such as in the Amazon comprised of lakes with seasonally variable area and intricate network of channels (ALSDORF et al., 2007; TRIGG et al., 2012), has yet to be developed. This gap is possibly due to approaches generally considering individual lakes in the estimate, so the estimate in a region with many lakes is more complex. The flood frequency-based method described by Fassoni-Andrade et al. (2020a) fills this gap of information by estimating topography pixel-by-pixel considering a flood frequency map.

In this context, this paper presents the first remote sensing-based high-resolution mapping (30 m) of the topography of a large floodplain system composed of lakes and channels, located in the central-low reach of the Amazon River. The method applies the Fassoni-Andrade et al. (2020a) approach by using a time series of water level for each floodplain pixel, i.e. the water surface elevation is variable in the area. We also generated the topography for the main channel based on nautical charts from the Brazilian Navy. Finally, we applied the technique to create depth maps corresponding to the high- and low-water periods of the river flood wave and estimate the average range in water storage for the studied reach.

5.2 Study area

The topography was estimated in open water regions of the Amazon River floodplain between the confluence of the Negro and the Xingu rivers (-1.59 ^{o}S -60.48 ^{o}W to -3.98 ^{o}S -52.54 ^{o}W, mask in Figure 5.1). Open water areas correspond to 9% of the Amazon basin wetland areas, a total of 73,458 km^2, and are located mainly in the floodplain associated with the middle-lower Amazon River reach (HESS et al., 2015). The reach from -70.5^{o}W to -52.5^{o}W contains about 6,500 lakes (SIPPEL; HAMILTON;

MELACK, 1992) that vary in shape, depth, and connectivity degree (TRIGG et al., 2012). Along the Amazon mainstem, the variation of open water area in the floodplain increases from the Negro River confluence to the Tapajós River confluence and reduces from that point to the Xingu River confluence (FASSONI-ANDRADE; PAIVA, 2019; HESS et al., 2015; MERTES; DUNNE; MARTINELLI, 1996). The last reach is subject to tidal variation and has few lakes. Therefore, there are more temporally flooded areas in the reach between Parintins and the confluence with Tapajós River (locations are shown in Figure 5.1). This reach has large shallow lakes, which are called depression lakes because they are surrounded by regions of higher overbank deposition of fine sediments (DUNNE et al., 1998; JUNK et al., 2012; MERTES; DUNNE; MARTINELLI, 1996).

The monomodal pulse of the Amazon River, which varies from 10 to 6 m in amplitude from Jatuarana to Óbidos (Figure 5.1), strongly influences the variation in the flooded area of this region, which in turn affects several ecological processes in the floodplain (JUNK et al., 2011). The floodplain receives nutrients and sediments from the river during the flood period (May/June), while in the low-water period (October/November) the lakes decrease in size or connectivity with the river, changing the local ecological conditions (JUNK; BAYLEY; SPARKS, 1989). For example, the seasonality of algal blooms, tree seed dispersal, and fruits are synchronized with the flooding regime; hence, affecting the distributions and feeding habitats of herbivorous and omnivorous fish (MELACK et al., 2009). Furthermore, the growth of aquatic macrophytes in floodplain lakes is related to topography, with a higher concentration occurring towards the littoral zone and a dependence on the lake water level (JUNK; PIEDADE, 1997; SILVA; COSTA; MELACK, 2010).

This study area was chosen because it has a great diversity of lakes and channels of different sizes and shapes, with variation in the flooded area (LATRUBESSE; FRANZINELLI, 2002; MERTES; DUNNE; MARTINELLI, 1996). Besides, this region, except for the Lago Grande de Curuai floodplain (Figure 5.1b), has been poorly studied in terms of floodplain hydrodynamics, with many questions still to be answered concerning water flows, the hydrodynamic interaction of the floodplain with the river, and the effects of these processes on the ecosystem (MELACK et al., 2009).

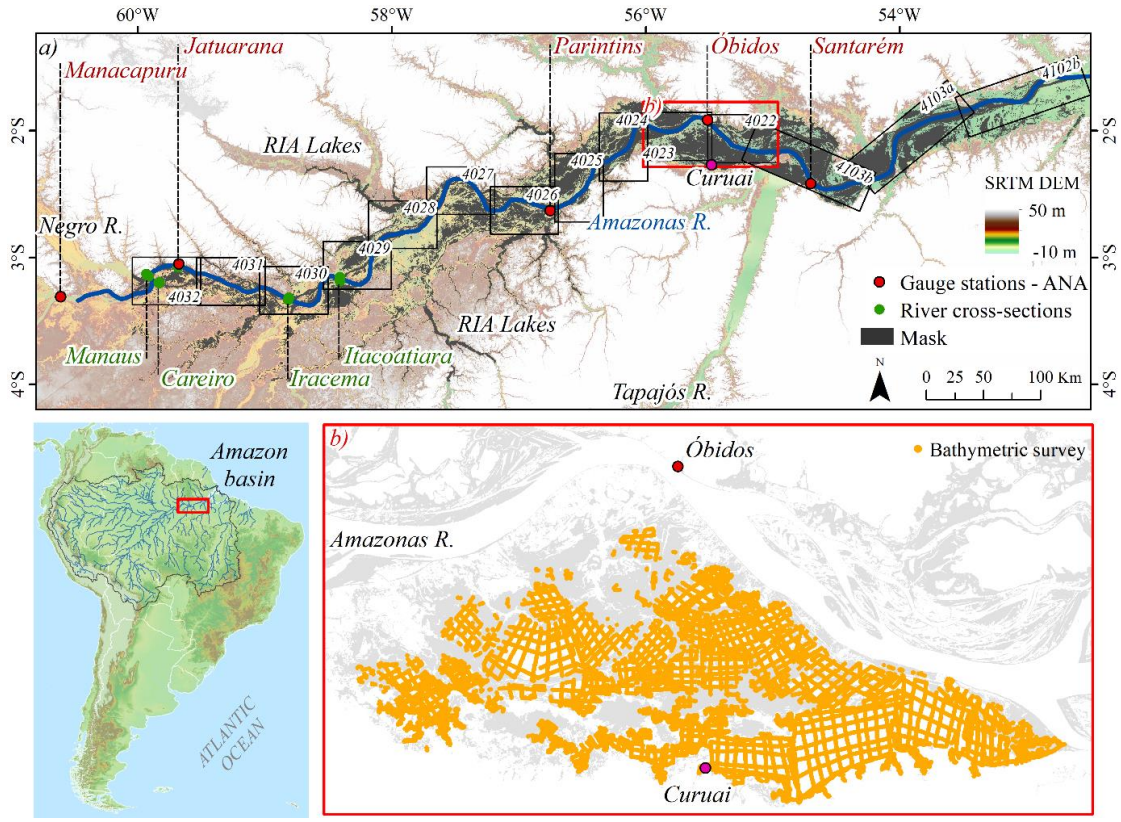

Figure 5.1. a) Amazon floodplain between the confluence of the Rio Negro and the Xingu River showing the locations of gauge stations and cross-section in Amazonas River and the limits and identifications of nautical charts from the Brazilian Navy. b) Bathymetric survey of the Lago Grande de Curuai floodplain.

5.3 Data and Methods

The method to estimate the topography in temporally flooded areas is described in Fassoni-Andrade et al. (2020a) and depends on a flood frequency map and water level duration curve (obtained from water levels time series). In this approach, the bottom level at a pixel is defined to be the water level whose probability of exceedance is equal to the flood frequency at the same pixel (Box A in Figure 5.2). Therefore, it is necessary to know the water level duration curve and the flood frequency for each pixel. If only one water level time series is available for the water body, a horizontal surface will be assumed for the whole area, as assumed in the Flood2Topo application (FASSONI-ANDRADE et al., 2020a). For areas with variable water levels, as in the large floodplain Amazon, distributed information of water level is preferable. However, the water level time series is not available for all floodplain open water areas. Thus, data from gauging stations in the Amazon River were used to estimate the water level in the floodplain.

The flowchart in Figure 5.2 shows the processing steps. The open-water mask in the floodplain was firstly defined, followed by interpolation of the water level along the Amazon River, interpolation of the water level in the floodplain, and estimation of the topography. Finally, bathymetric information of the Amazon River from nautical charts of the Brazilian Navy was included in the mapping.

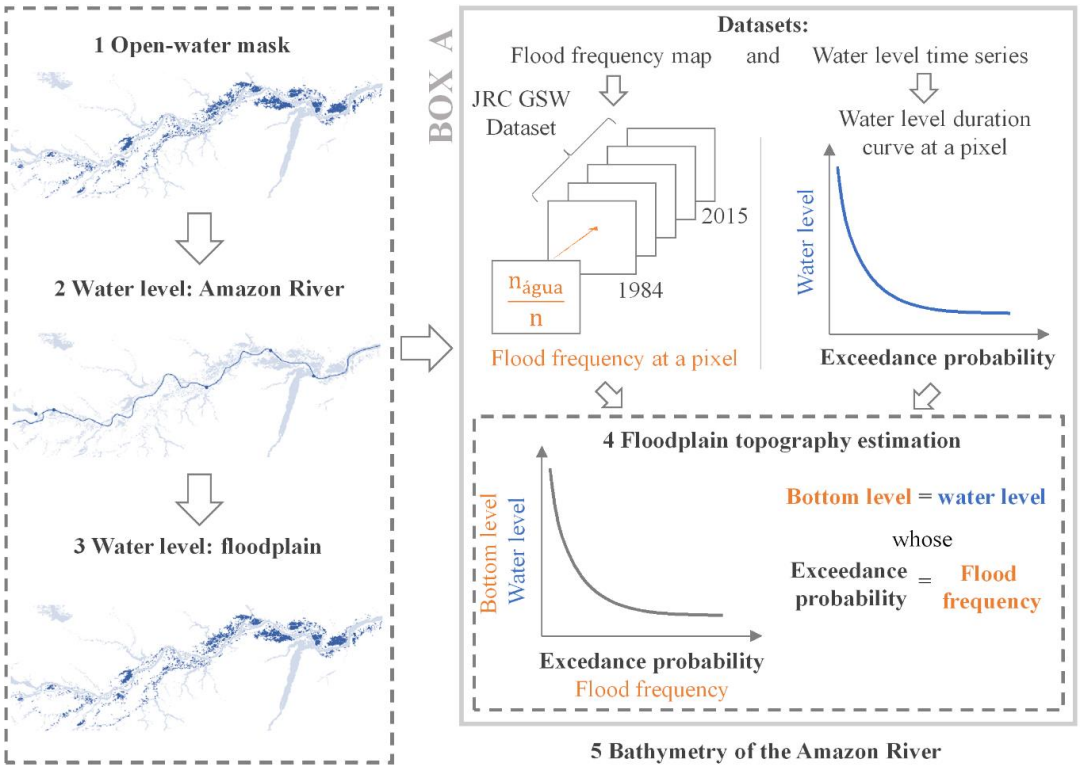

Figure 5.2. Processing flowchart for topography estimation in the Amazon River's floodplain.

5.3.1 Datasets

A flood frequency map (or open water frequency – OWF map) was used to define open water bodies in the study area. It was calculated from the JRC Global Surface Water (JRC GSW) Monthly Water History v1.0 (PEKEL et al., 2016), considering the period from March 1984 to October 2015 (total of 380 months/32 years). This database represents the monthly record of the water presence on a global scale since March 1984, corresponding to the images from the Landsat series classified as water, no-water, and no-data with a spatial resolution of 30 m (Pekel et al., 2016; available at <https://global-surface-water.appspot.com/>). The water cover classification accuracy showed omission errors less than 5% and commission errors less than 1% (PEKEL et al., 2016). Google Earth Engine (GORELICK et al., 2017) was used to create the OWF map, as described

in Fassoni-Andrade et al. (2020a; available at code.earthengine). As Landsat program provides optical images, the number of valid observations is limited in the period in which cloud cover is higher, i.e., during the austral summer for the central Amazon basin (MARTINS et al., 2018), which is the rising period for the Amazon River.

Daily water level data were obtained from 1984 to 2015 for five-gauge stations in the Amazon River provided by the Brazilian National Water Agency (ANA; locations in Figure 5.1). These data were referenced to the 2008 Earth Gravitational Model geoid (EGM08) according to correction values recommended by Calmant et al. (2012). Data gaps were filled as documented in Text S5.1 and Figure S5.1 (Supporting Information). Amazon River bathymetry was obtained by digitizing 14 nautical charts from the Brazilian Navy, which are identified in Figure 5.1a (available at marinha.mil.br). Bathymetric surveys between Manaus and Óbidos (nautical charts from 4032 to 4022) were carried out between 2010 and 2017, and bathymetric surveys of the nautical charts downstream from Óbidos (4103b, 4103a, 4102b) are older, varying between the years 1997 and 2014.

5.3.2 Floodplain topography

The open-water mask in the floodplain was defined using the OWF map, i.e., the area delimited by flood frequency greater than 0% during 1984 and 2015. Since this dataset has a spatial resolution of 30 m, several floodplain channels were mapped. Main tributaries (Madeira, Tapajós, and Trombetas rivers) and the Balbina reservoir were excluded since only water level information from the Amazon River was used. The mask is presented by the black region in Figure 5.1a.

Amazon river daily water levels (five stations) were interpolated along the river channel. In order to overcome the channel sinuosity effect on distance calculation between river sections, equidistant points (30 m) were distributed along its centerline in the flow direction (blue line in Figure 5.1a; total length of ~ 1100 km) and used for the linear interpolation procedure. In the reach downstream of Santarém (~349 km in length), the interpolation considered the water level in Santarém (distance to the ocean is 768 km, Kosuth et al., 2009) and the water level equal to zero in Ponta do Céu (distance to the ocean of 75 km, Kosuth et al., 2009), which can be referred to as the local average sea level (KOSUTH et al., 2009). This reach is subject to maximum tidal wave amplitude variation of 1.5 m at the most downstream evaluated point, located 419 km away from the ocean (KOSUTH et al., 2009).

As suggested by Alsdorf et al. (2010) local runoff originates only 10% to 20% of the Central Amazon floodplain water volume. Thus, it is reasonable to assume that the Amazon River water level is sufficient for estimating the floodplain water level. Thus, daily water level time series from 1984 to 2015 at each pixel in the floodplain were estimated by interpolating the water level along the river using the Nearest Neighbor method. Water level duration curves were then obtained for each pixel by sorting the water level time series data in decreasing order and calculating the exceedance frequency. Finally, the bottom level at a pixel was considered equal to the water level whose exceedance frequency is equal to the flood frequency at the same pixel (Fassoni-Andrade et al., 2020a). The adopted elevation vertical reference is the Earth Gravitational Model 2008 geoid.

Daily water level data and the Nearest Neighbor method were chosen for the floodplain topography estimation because this approach showed better results than six exploratory experiments performed and described in the Supporting information (Text S5.2 and Table S5.1).

5.3.3 Amazon River bathymetry

The method is not able to estimate bathymetry in permanently flooded regions such as some areas in the Amazon mainstem. Therefore, the bathymetry of the river was obtained from the nautical chart information and included in the mapping procedure. Values in the Amazon nautical charts refer to water depths related to the local water surface elevation that remains 90% of the time. This 90% reference level was estimated for each point considering the period from 1984 to 2015. Then, the water surface reference level was subtracted from the water depth resulting in elevation values (EGM08), and the extracted points were interpolated using the topo to raster method (HUTCHINSON, 1989) to create an elevation map with 30 m of spatial resolution.

5.3.4 Validation datasets

The estimated water level along the Amazon River and the floodplain was validated using ICESat-1 altimetry data derived from the DLAS/ICESat GLA14 Global Land Surface Altimetry Data (ZWALLY et al., 2014). These data represent the level from 2003 to 2009 of inland water (O'LOUGHLIN et al., 2016b) delimited by a static global water mask, and has a height accuracy of 10 cm (URBAN; SCHUTZ;

NEUENSCHWANDER, 2008). Therefore, some data may represent the emerged lake bottom surface in periods of low-water due to the reduction of the floodplain flooded area (O'LOUGHLIN et al., 2016b). The criterion for eliminating outliers resulting from this problem was based on the Amazon River annual flood date. The data were divided according to hydrograph phase in rising (January, February, and March), flood (April, May, and June), falling (July, August, and September), and low-water (October, November, and December), in such a way that the upper (lower) levels greater than the average plus (minus) two standard deviations of each period were eliminated. GLA14 data useful for the evaluation were converted from the Datum EGM96 to the Datum EGM08 using the Mensuration Services Program - Geographic Translator (MSP GEOTRANS 3.7, available at earth-info.nga.mil). In addition to altimetry data, water level time series from Vila Curuai Station (Figure 5.1b) were used to validate the interpolated level in this floodplain, with absolute EGM08 values estimated according to Moreira (2016).

Bathymetric data for the Lago Grande de Curuai were used to validate the estimated topography, which are the only to the authors' knowledge available data for floodplain lakes in the studied region. This dataset was produced by previous studies (BARBOSA, 2005; BARBOSA et al., 2006; RUDORFF; MELACK; BATES, 2014b) and corresponds to an extensive bathymetric survey by echo sounder (orange dots in Figure 5.1b). The SRTM3 DEM v2.1 (FARR et al., 2007a) and the Multi-Error-Removed Improved-Terrain DEM (MERIT DEM; Yamazaki et al., 2017) were also compared to the Curuai bathymetry data for open water areas. MERIT DEM improved the SRTM3 DEM by filling some observation gaps over water bodies and removing errors such as speckle noise, stripe noise, absolute bias, and tree height bias (YAMAZAKI et al., 2017). However, both models represent open water areas as a flat surface.

In the Amazon mainstem, channel bathymetry was evaluated from river cross-sections surveyed by the Brazilian Geological Survey (CPRM) at Manaus, Careiro, Jatuarana, Iracema, Itacoatiara, and Óbidos gauges (Figure 5.1).

The following metrics were applied for assessing topography error: mean, standard deviation, minimum, maximum, bias (Equation 5.1), Pearson correlation coefficient, Root Mean Square Error (RMSE, Equation 5.2), RMSE of bias-corrected values (RMSE', Equation 5.3), and coefficient of determination of bias-corrected values (R^{2}'), that is, the coefficient of determination for the anomaly of values (value minus sample average).

$$\text{bias} = \frac{1}{n}\sum_{i=1}^{n}\left(x_i^{est} - x_i^{obs}\right) \quad (5.1)$$

$$\text{RMSE} = \sqrt{\frac{1}{n}\sum_{i=1}^{n}\left(x_i^{est} - x_i^{obs}\right)^2} \quad (5.2)$$

$$\text{RMSE}' = \sqrt{\frac{1}{n}\sum_{i=1}^{n}\left(\left(x_i^{est} - x_{mean}^{est}\right) - \left(x_i^{obs} - x_{mean}^{obs}\right)\right)^2} \quad (5.3)$$

5.4 Results and discussion

5.4.1 Validation of interpolated water levels

5.4.1.1 Amazon mainstem

Figure 5.3 shows the differences between interpolated and ICESat water levels along the Amazon mainstem. Note that the error does not have a spatial pattern along the river (bias of 4.24 cm; n = 281). RMSE is low (44.85 cm), as it represents less than 5% variation in the amplitude of the Amazon River water surface elevation (~10 m at Jatuarana station).

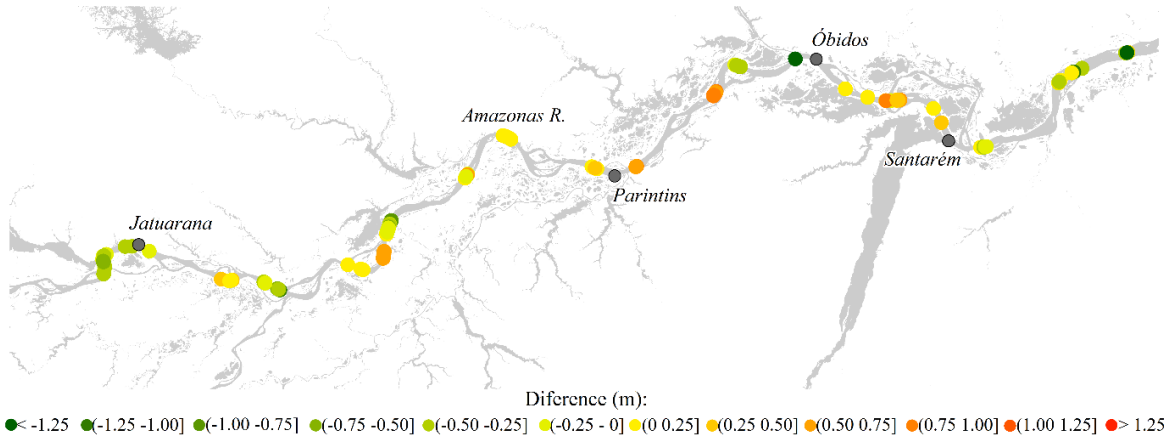

Figure 5.3. Error of interpolated water level along the Amazon River. Green dots indicate underestimation, red dots overestimation, and yellow dots the smallest obtained errors.

5.4.1.2 Floodplain

Figure 5.4 shows the spatial distribution of the errors (interpolated minus ICESat-1 levels) for rising, flood, falling, and low-water periods. The spatial pattern shows that the errors are, in general, random and with no transversal difference to the floodplain.

Also, the interpolated water level was overestimated in the rising, flooding and falling period and underestimated in the low-water period (bias in Figure 5.4). The RMSE ranged from 0.65 (falling) to 1.40 (low water), and Pearson's correlation coefficient was high (>0.8). The overestimations are higher in regions farther from the river, such as the points in the black circles of Figure 5.4. Ria-type lakes that are in these regions receive important streamflow from the local catchment and the backwater from the Amazon River. Overestimations are higher near Parintins in the rising and high-water periods (points in the red box of Figure 5.4a and b). The falling period has low representativeness since few data are available and are located in a single region of the floodplain (n = 160; Figure 5.4c). In the low water period (Figure 5.4d), the spatial pattern is more random, with some values underestimated by up to -15 m and higher RMSE (1.40 m). These underestimates may be related to the observations of ICESat-1 inland regions during this period, that is, the validation data may not be as accurate. Furthermore, with less connectivity among water bodies, water can also be contained in isolated lakes with higher water elevation.

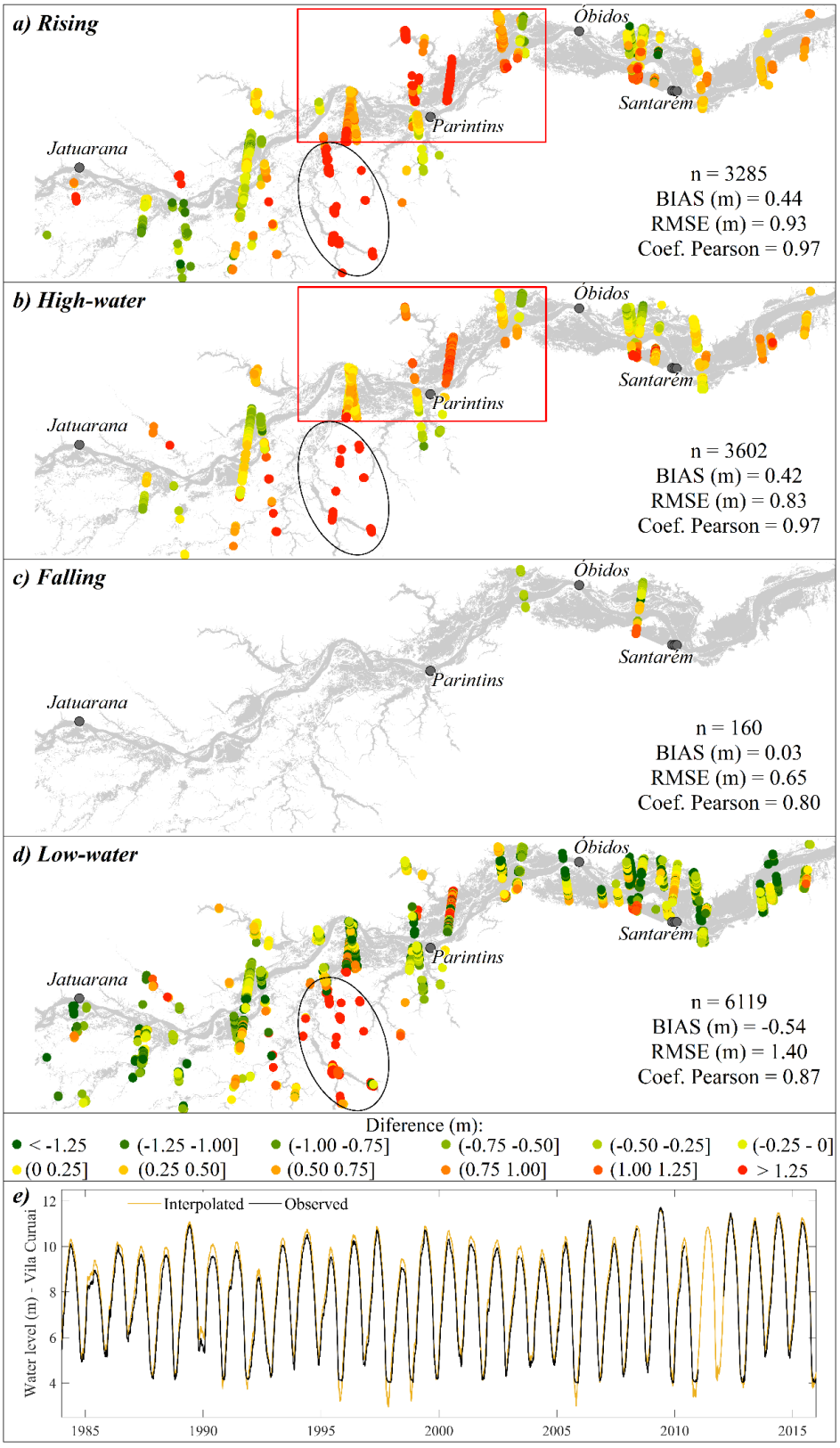

Figure 5.4. Error of the water level in the floodplain estimated by gauge data interpolation for a) rising, b) flood, c) falling, and d) low-water periods. Green dots indicate underestimation, red dots overestimation, and yellow dots the smallest errors; e) Water level at Vila Curuai station.

Comparison of the interpolated level with the observed level at the Vila Curuai station, located in the Amazon river floodplain, shows RMSE of 0.37 m, bias of 0.33, and Pearson's correlation coefficient of 0.98. Throughout the year, the difference between the interpolated and estimated level at the Vila Curuai gauge station is maximal in the high-water period and minimal in the low-water period (Figure 5.4e). Besides, underestimation of the water level was observed in some low water periods, as in November 1995, 1998, 1999, 2005, and 2010 (Figure 5.4e). The loss of connectivity between the gauge station and the main Curuai lake, which remains connected to the Amazon River, may cause this effect. Thus, isolated lakes in the low water period impound water and the water surface elevation can be higher than that of the river and other lakes. Therefore, the estimation of the water level from the interpolation of the river level is subject to underestimation in floodplain areas that lose connection in the low-water period.

The accuracy of the estimated topography is related to uncertainties in the estimation of the floodplain water level. In the approach used here, both floodplain and river water surface elevation are considered to be approximately the same, which is not always true. Alsdorf et al. (2007) and Rudorff et al. (2014b) demonstrated that during the rising and receding limb of the hydrograph differences in water surface elevations between river and floodplain are controlled by the levee topography. During the high water period, widespread overbank flow occurs, and the river-floodplain difference in water surface elevation decreases. Thus, the floodplain water level can be lower than the river water level, overestimating the topography. Moreover, the water can be blocked in some floodplain lakes during the low-water period, such as in the Lago Grande de Curuai (exemplified in Figure 5.4e). In this case, the floodplain water level is higher than the river water level, and the topography is underestimated in regions with high flood frequencies (i.e. areas where the level is low).

5.4.2 Assessment of nautical charts

The Amazon River cross-sections estimated from nautical charts were underestimated with error ranging from 4.3 to 44.5% (average of 20.8%), average RMSE of 7.5 m, and average bias of 5.0 m (Figure 5.5; Location on Figure 5.1). The sections are representative of the reach between Manaus and Santarém. The nautical charts for the reach downstream of Santarém are older (nautical charts 4103B, 4103A, 4102B in Figure

5.1) and have fewer isobaths (lines of equal depth). Therefore, this reach presents greater uncertainty in the river topography relative to the upstream reach.

The comparison of cross-sections in Figure 5.5 considers the coordinates of the bathymetric surveys from CPRM except for the section at Óbidos. Elevations and cross-section distances from this station were obtained from ANA. Cross-section coordinates were missing and were obtained from those reported in Filizola et al. (2014), which can increase the uncertainty of the estimate. For example, the observed section has high elevation points at the river banks that are not observed in the estimated section (red box in Figure 5.5). If these points are disregarded from the analysis, the error in Óbidos cross-sectional area reduces from 27.8% to 2.6%.

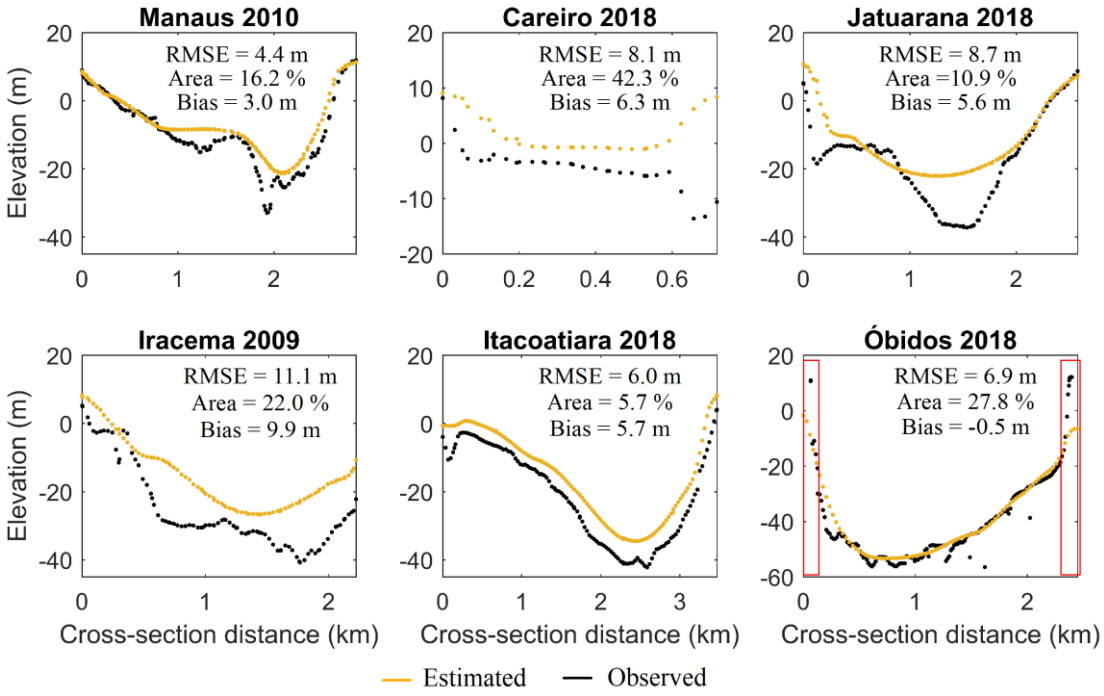

Figure 5.5. Cross-sections transects of the Amazon River (location is shown in Figure 5.1) estimated from nautical charts and observed at CPRM gauges. Elevation relative to the EGM2008 geoid.

5.4.3 Validation of Lake Curuai topography

5.4.3.1 Assessment

Figure 5.6 shows the observed, considering the interpolation of bathymetric survey points (Figure 5.1 for location), and estimated topography in the Lago Grande de Curuai floodplain. In general, there is a spatial-temporal agreement between observed and

estimated values. The deepest floodplain channels were overestimated because the method is limited in permanently flooded regions, however, points with flood frequency equal to 100% represent only 1% of the sampled points. Figure 5.6b also exemplifies the slatted appearance in the estimated topography due to the Landsat scan line corrector failure (PEKEL et al., 2016), carrying these artifacts into the flood frequency and the topographic maps.

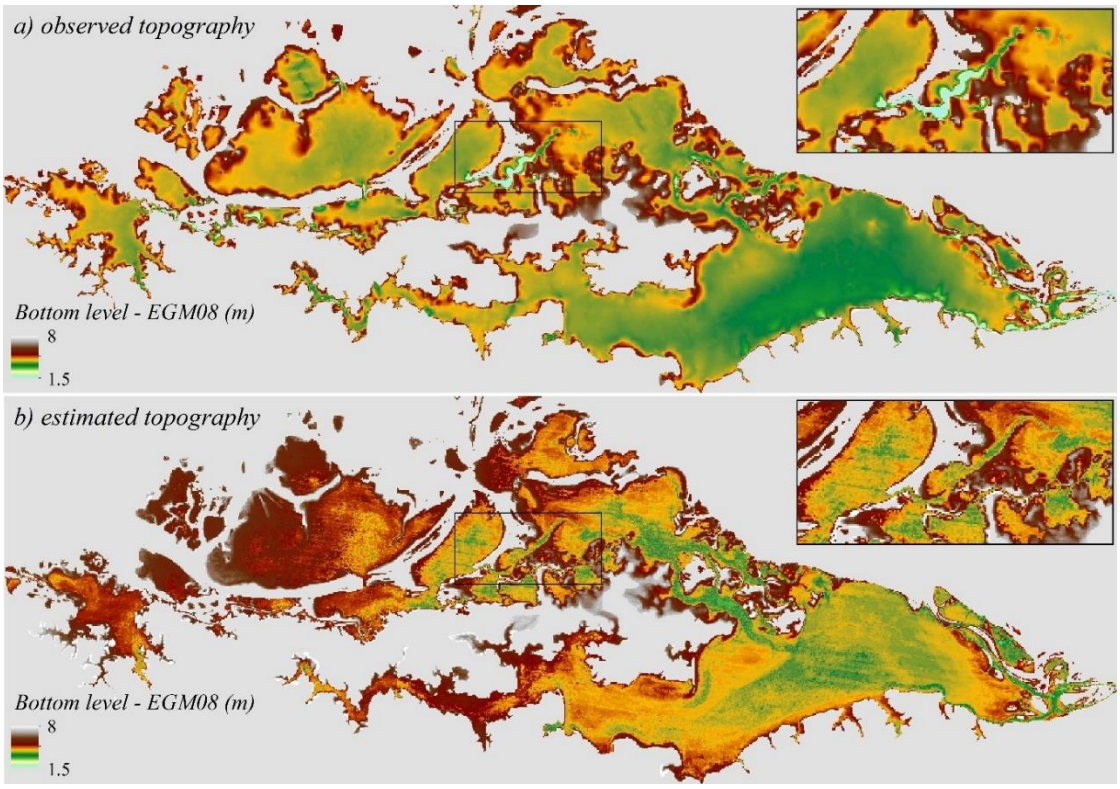

Figure 5.6. Topography of lakes and channels in the Curuai flood basin derived from (a) interpolation of sonar survey data (RUDORFF; MELACK; BATES, 2014b) and (b) the flood-frequency processing of the Landsat JRC Global Surface Water Dataset.

Table 5.1 presents the metrics of estimated topography considering the approach in this study (no-horizontal water surface, called hereafter Estimated), and by other approaches. The table also shows the metrics for SRTM3 DEM v2.1 and for MERIT DEM in open water areas. In addition, Figure 5.7 shows the scatterplots of observed versus estimated bottom level by different approaches. The estimated topography has better metrics than SRTM3 and MERIT metrics. This is especially true for metrics that evaluate the spatial variation of topography, such as Pearson's correlation coefficient, RMSE', and R^{2}' since these models represent the open-water area as a flat surface. Thus,

the proposed method is an alternative to estimate the topography in open water areas and replace those areas in global DEMs.

Table 5.1. Metrics of the observed topography (points in Figure 5.1) compared to SRTM3 DEM, MERIT DEM, and estimated by different methods.

	Mean (m)	**Standard deviation (m)**	**Minimum (m)**	**Maximum (m)**	**Bias (m)**	**RMSE (m)**	**Pearson Coef.**	**RMSE' (m)**	**R^{2}'**
Observed	4.51	1.39	-11.66	9.54	-	-		-	
SRTM3 DEM	1.31	1.03	-5.00	28.00	-3.20	3.55	0.22	1.53	0
MERIT DEM	4.72	1.64	-1.01	27.78	0.21	1.40	0.59	1.38	0
Tseng's approach	4.44	1.38	3.14	12.10	-0.06	1.21	0.62	1.21	0.24
Fassoni-Andrade's approach	5.45	1.40	3.14	11.90	0.94	1.47	0.67	1.13	0.34
Estimated	**5.30**	**1.45**	**2.75**	**12.49**	**0.79**	**1.30**	**0.73**	**1.04**	**0.44**
Estimated with bias removal	**4.51**	**1.02**	**2.39**	**9.17**	**0.00**	**0.89**	**0.77**	**0.89**	**0.59**

The methods proposed by Tseng et al. (2017) and by Fassoni-Andrade et al. (2020a) were also applied to estimate the topography (called hereafter Tseng's and Fassoni-Andrade's approaches; Table 5.1). In the Tseng's approach, the maximum and minimum water level at Óbidos station, located in the Amazon River near Curuai floodplain, were used so that the topography was obtained pixel-by-pixel by multiplying the probability of no-flood by the water level amplitude and adding the minimum level (TSENG et al., 2017). Thus, this method assumes a linear water level duration curve, as exemplified in Figure 5.7f. This figure also showed the observed water level duration curve in Óbidos. Analysis of these curves shows that the Tseng's approach underestimates the bottom level in regions of flood frequency between 20 and 100% and overestimates in regions of flood frequency between 0 and 20%. Also, the accuracy decreases as the distance from Óbidos increases, since the method considers only a single water level time series. Tseng's approach presented lower bias and RMSE and closer mean and standard deviation to the observation reference compared to the Estimated topography (Table 5.1). This is due to the previously discussed sources of the underestimation of the Tseng's approach. In contrast, measures of the spatial variation of the topography (Pearson, R^{2}' and RMSE') are inferior (also in Figure 5.7c).

Fassoni-Andrade's approach is the same as this study but considering a single water level time series, i.e., the authors assumed a flat-water surface without distributed level information on the floodplain. The water level duration curve at Óbidos station used in the Fassoni-Andrade's approach resulted in inferior bias and RMSE than Estimated topography and Tseng's approach. In contrast, it showed a better representation of topographic variation concerning Tseng's approach (Pearson, R^2' and RMSE'; Figure 5.7d). In conclusion, the Estimated topography in the present study provided results that are better than those assuming linear water level duration curve (Tseng's approach) and no-distributed water level in the floodplain (Fassoni-Andrade's approach).

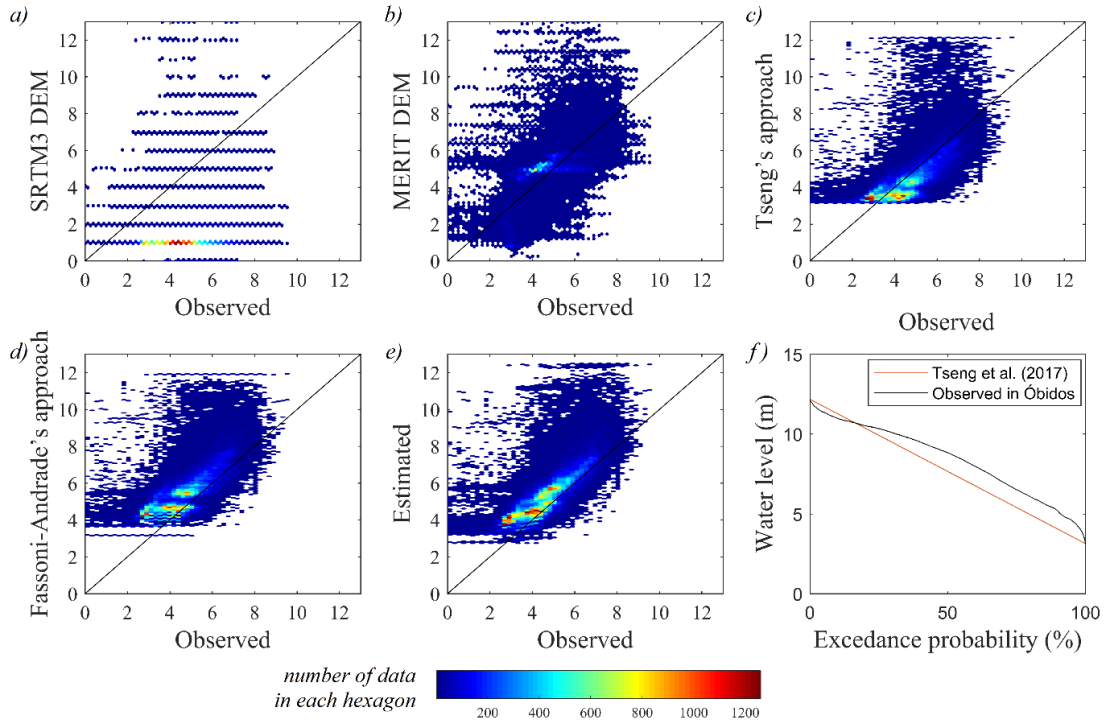

Figure 5.7. Scatterplots of observed versus estimated bottom level in Curuai floodplain. Note the higher (lower) density of spots in red (blue). a) SRTM3 DEM b) MERIT DEM; c) Tseng's approach; d) Fassoni-Andrade's approach; e) Estimated topography; f) Water level duration curve estimated by Tseng's approach, and observed in Óbidos.

5.4.3.2 Removal of vegetation height bias

In addition to having errors associated with the Landsat data, the classification of water-covered surfaces in the JRC Monthly Water History database does not consider the inundated vegetation areas where the vegetation height is greater than the water surface elevation. Since these areas are classified as flooded only when the water level is equal

to or greater than the vegetation height, the flood frequency map represents the flood above the vegetation, and therefore the estimated topography has a vegetation height bias. This systematic bias increases with increasing vegetation height or decreasing flood frequency. Figure 5.8b shows the relationship between flood frequency and the error in the Estimated topography of the Lago Grande de Curuai. As the flood frequency decreases, topography overestimation increases, i.e. larger errors occur in regions of lower flood frequency.

A linear fit of the relationship between flood frequency and bottom level error (Equation 5.4) was used to correct the vegetation height bias in the Central Amazon study area (mask in Figure 5.1). In turn, the bottom level error was calculated from the terrain elevation Estimated and observed by the ICESat-2 altimeter (launched in September 2018; available at openaltimetry.org). Only land data were selected from the ICESat-2 data between September 2018 and November 2019 in the study area since water elevation can be represented by different data points. The following criteria were used in the selection: 1) data collected in the low-water period (October to December); 2) no-water; 3) cloud free condition; 4) data uncertainty smaller than 0.5 m. The adjusted function (Figure 5.8a) was used to correct the Central Amazon floodplain topography. Figure 5.8c shows the relationship between flood frequency and the Estimated topography error in the Lago Grande de Curuai after removal bias. Note that bottom level bias reduced to zero, RMSE reduced from 1.30 m to 0.89 m, and Pearson's correlation coefficient increased from 0.73 to 0.77 in this floodplain (Table 5.1; Estimated enhanced).

$$\text{Bottom level corrected} = \text{Bottom level} - (3.3619 - 0.0301 \cdot FF) \quad (5.4)$$

Where the bottom level is in meters and the flood frequency (FF) is in %.

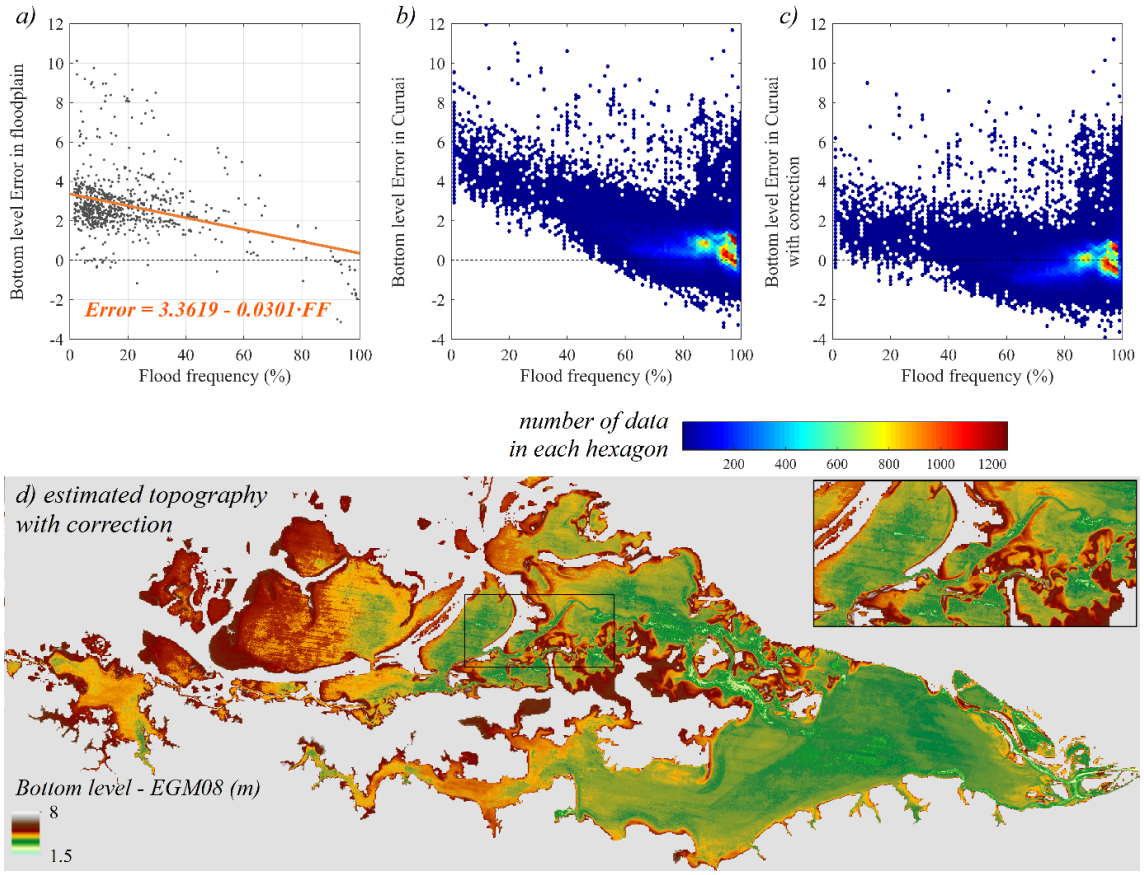

Figure 5.8. a) Linear fit of the bottom level error (Estimated minus observed from ICESat-2) and the flood frequency in the Central Amazon study area; b) Flood frequency versus bottom level error before and c) after vegetation height bias removal; d) Estimated topography with bias removal in the Lago Grande de Curuai.

5.5 Central Amazon floodplain topography and water depth maps

The estimated topography mapping of lakes and channels in the Amazon floodplain, as well as the Amazon River bathymetry, is presented in Figure 5.9 and for a region in the Amazon floodplain in Figure 5.10. MERIT DEM does not represent the topographic variation in water bodies (Figure 5.10a). In contrast, the estimated topography represents many topographic details, such as the complex network of interconnected channels (Figure 5.10b). Therefore, the proposed method is promising for estimating topography in temporarily flooded areas. In addition, the estimated floodplain topography is representative of the period from 1984 to 2015, thus, geomorphological changes in the fluvial channel and in the floodplain during that period were considered. The application of the method considering different periods is a potential impactful application to assess geomorphology changes in a dynamic environment.

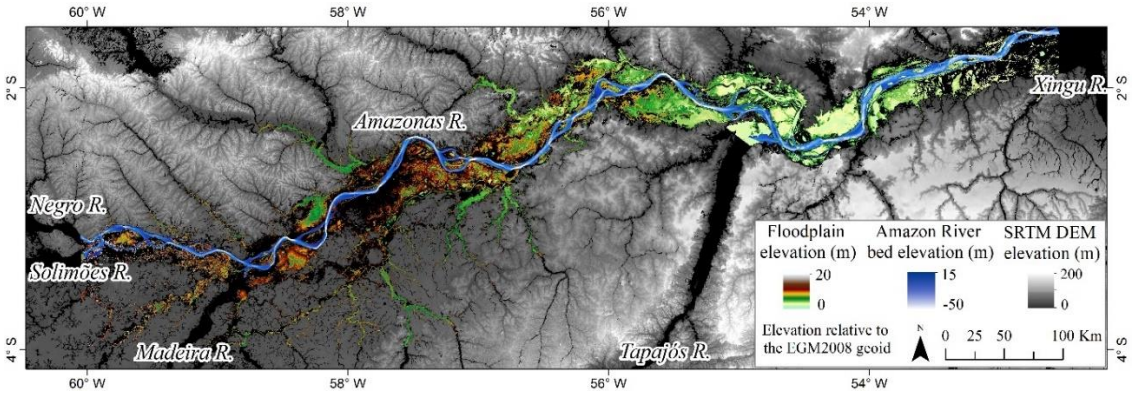

Figure 5.9. Estimated topography mapping of lakes and channels in the Amazon floodplain and Amazon River bed elevation.

Landsat flood frequency-based method does not estimate topographic information in permanently flooded regions, therefore, all regions in the topography mapping that have flood frequency equal to or close to 100% are represented by the lowest water level observed in the period (1984 to 2015), as shown in Figure 5.10c. This occurs, for example, in ria-type lakes (exemplified in Figure 5.1). These lakes with dendritic shapes are deeper, have flood frequency close to 100% (JUNK et al., 2012; LATRUBESSE, 2012), and receive water from both the local basin and the main river (JI et al., 2019; LESACK; MELACK, 1995). Thus, the evaluation of the flood frequency is necessary before using the topography map.

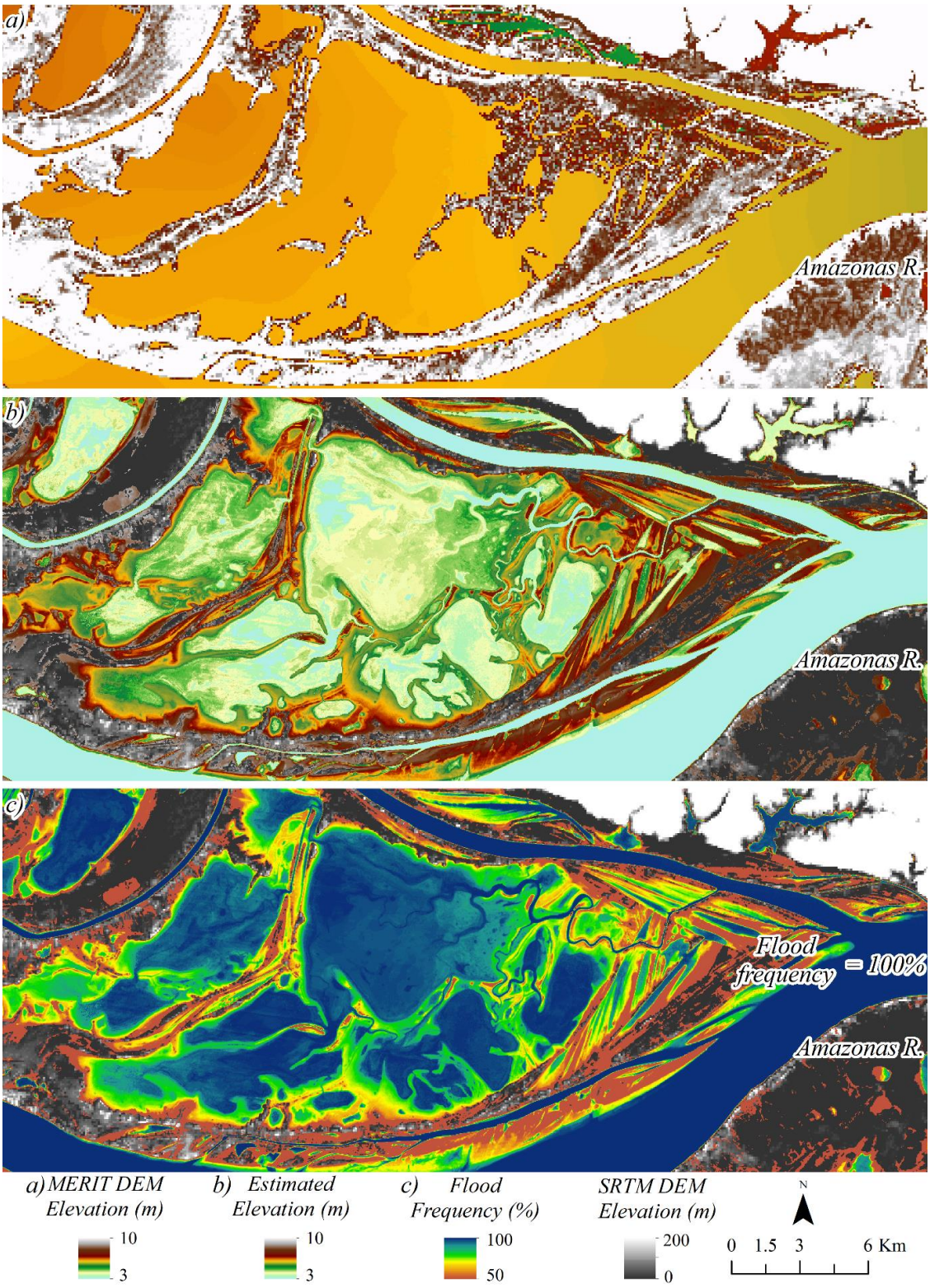

Figure 5.10. a) SRTM3 DEM elevation with flat water surface; b) Estimated topography and c) Flood frequency in an Amazon floodplain. Elevation in relation to the EGM2008 geoid.

Water depth maps in the floodplain open-water areas for the high-water and low-water periods were created considering the maximum and minimum levels corresponding to the average annual level between 1984 and 2015 calculated for each pixel (Figure 5.11a, b, and c). For example, these reference levels in Jatuarana and Óbidos are, respectively, 20.6 and 10.9 m for high-water, and 10.6 and 4.9 for low-water (Figure 5.11a). The cumulative water depth frequency in the floodplain (shown in Figure 5.11d) can be used to estimate the percentage of the area with a depth less than or equal to a reference depth. For example, 75% of the open-water area during the low-water period (total area of 8,159 km^2) has a depth of less than or equal to 2 m. In contrast, 75% of the open-water area has a depth of less than or equal to 8 m in the high-water period (total area of 19,177 km^2). Figure 5.11e shows the active storage volume in the open-water floodplain for both periods.

The maximum depth in temporarily flooded areas (Flood frequency <100%) is given by the range of water level variation over the considered period (i.e., the range from maximum to minimum water level). In the case of the Amazonian floodplain lakes that are subjected mainly to the monomodal Amazon River flood pulse, the method assumes that the variation of the lake water level amplitude is equal to the river amplitude. In other words, the maximum water depth in temporarily flooded areas is always smaller than the water level amplitude of the Amazon River. Therefore, as the river water level amplitude decreases from upstream to downstream (Figure 5.11a), the lake depth also decreases, therefore, upstream lakes are deeper than downstream lakes (Figure 5.11b e c). Trigg et al. (2012) also observed a relationship between the Solimões River water level amplitude and the floodplain channels depth subject only to the river flood wave. The authors showed that the average depth of these channels, obtained in field survey during the high-water period (2009), has values close to the river average amplitude. Results also agree with Alsdorf et al. (2010), who indicated that the water depths follow an upstream-to-downstream trend in the Amazon floodplain using gravimetric and imaging satellite methods.

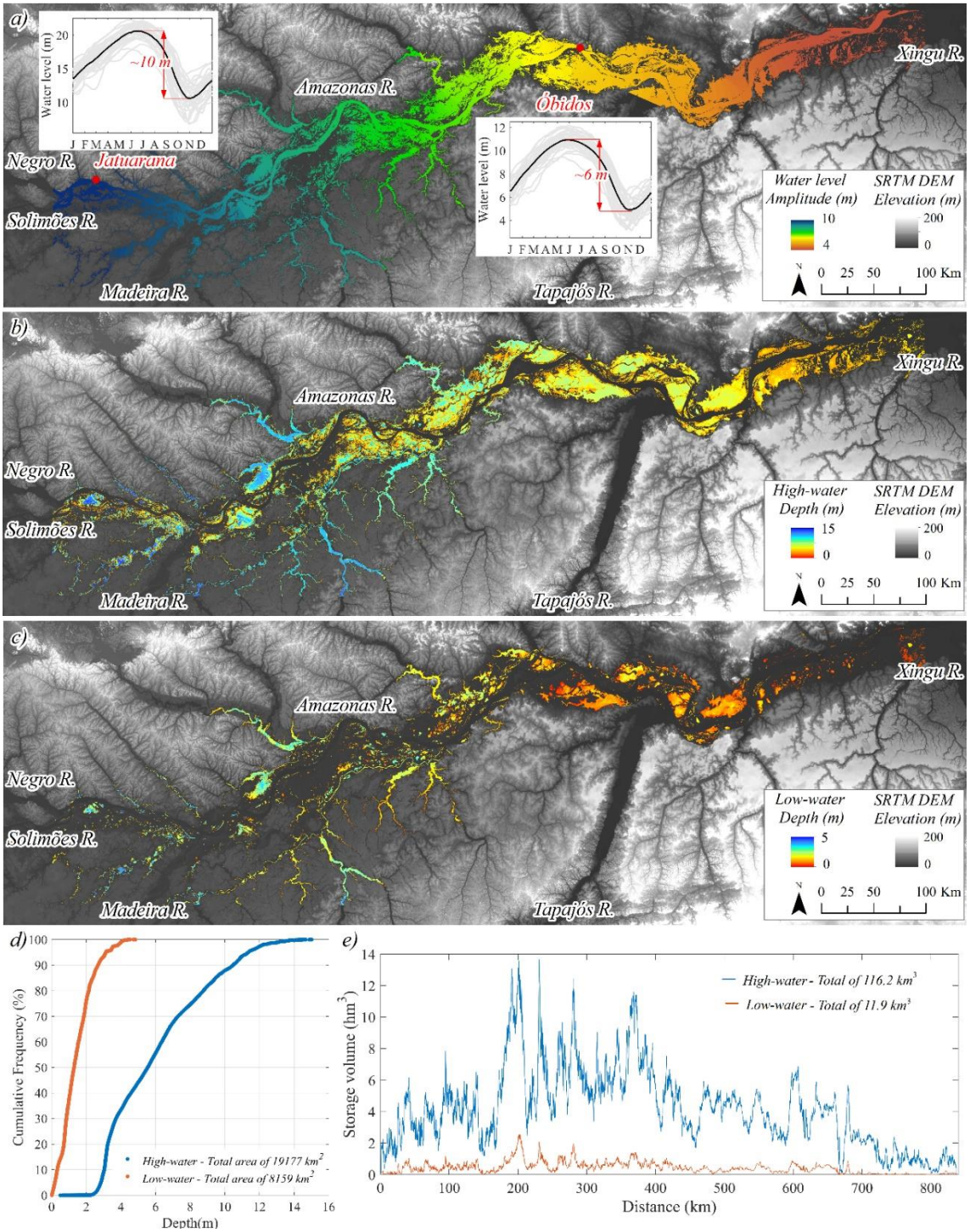

Figure 5.11. a) Amplitude of the water level; Water depths maps for the period of b) high-water and c) low-water; d) Cumulative frequency of water depth in the floodplain open-water areas; e) Storage volume in the open-water floodplain.

Average active volume on the floodplain, i.e., the amount of water varying in the high-water and low-water periods, represents a total of 104.3 km^3 each year (the range from 116.2 km^3 to 11.9 km^3). The topography is not estimated in the whole flooded

vegetation area, so this is an underestimated value, but it represents a considerable volume. Frappart et al. (2019) showed that storage variation in this region of the Amazon basin has a more significant contribution of surface water than soil moisture and groundwater (>50%). Alsdorf et al. (2010) found storage amplitude of Amazon floodplain values of 50 km^3 and 60 km^3 for two square regions (330 km x 330 km) located near Óbidos and Manaus, respectively. Although the range of areas is different, our estimate seems reasonable, representing 95% of the total estimated by Alsdorf which included all flooded vegetation areas. In the Curuai floodplain (Figure 5.6 for location), the storage amplitude was 8.4 km^3, which is slightly more than the 7.9 km^3 estimate by Rudorff et al. (2014b).

5.6 Summary and conclusions

We presented the first high-resolution bathymetric mapping (30 m) of the Central Amazon floodplains using a method based on flood-frequency map derived from Landsat images, which can be applied to any temporarily flooded area (lakes, reservoirs, wetlands, and rives intermittent). We also created a bathymetric data for the Amazon River (~ 1,100 km extension) using Brazilian nautical charts, and floodplain depths maps for high- and low-water periods of the flood wave in the central Amazon River (average RMSE and Error area of 7.5 m and 20.8%).

We showed that our approach using the distributed water level across the floodplain provides better topography estimation than previous approaches. We also corrected the vegetation height bias using ICESat-2 data, a recent and promising satellite for this application. Validation using locally derived bathymetry showed an RMSE of 0.9 m for the floodplain bottom level. Topographic floodplain mapping should be used with caution in the following regions: 1) areas where the flood frequency is equal to or close to 100%; 2) distant areas of the Amazon River; and 3) floodplain areas where the water level is very different from the river level, such as in the low-period, when the water is blocked along the floodplain. Regarding the estimated high- and low-water depth maps, we observed that the depths have upstream to downstream tend in temporally flooded areas, agreeing with other authors. The annual storage volume on the open-water floodplain is large (104.3 km^3) and varies on average each year from 11.9 km^3 in low-water to 116.2 km^3 in the high-water period.

It should be noted that the SRTM3 DEM and MERIT DEM are topographic models that do not represent topography in water bodies, and correcting this error is often

not possible because of the absence of bathymetric surveying. The approach presented here allowed the topography estimation of these areas, i.e. temporarily flooded areas, without the need for bathymetric surveying, but using water level data, and the state-of-the-art of water cover mapping (JRC GSW database). In this way, the approach opens unprecedented opportunities for better topographic representation in open water areas in any region of the globe mainly with the opportunity to use new altimetry data (as ICESat-2 and SWOT) and images (as Sentinel data). Furthermore, sediment deposition and erosion promote dynamic changes in surface morphology in the fluvial channel and in the floodplain. This evolution can be assessed using satellite images, but changes in the surface height are not estimated. Our method can be applied for different periods, for example, every 5 years, allowing to assess geomorphology changes in a dynamic environment and quantify the depositional and erosional history in an unprecedented way.

The datasets we developed can be used for different applications in hydrology, geomorphology, and ecology studies. Our analysis can help to assess the areas occupied by species that are limited by the water depth, such as aquatic macrophytes. Depth mapping in open water areas can also help map these species and estimate the carbon balance and primary productivity. In addition, topographic maps can provide insight into the floodplain geomorphology, the complex network of channels and the direction of channeled flows. Finally, it is expected that the elaborated database can be used in hydrodynamic simulations of the region, helping to understand water flows, inundated area patterns, and the water volume stored in the Amazon river-floodplain system.

CAPÍTULO 6. Caracterização dos fluxos de água entre o rio e a planície de inundação da Amazônia central

Simulações hidráulicas permitem a representação do escoamento da água e a obtenção de diversas variáveis hidrológicas, como área inundada, volume armazenado, fluxos de água e campos de velocidade. No entanto, dados topográficos de boa qualidade são requisitos para a boa acurácia dessas representações. Nesse capítulo, o dado topográfico elaborado no capítulo anterior (Capítulo 5) é utilizado para a simulação do escoamento da água no rio e na planície de inundação da região central da Amazônia em três anos hidrológicos: 2008, 2009 e 2010. A validação do modelo mostra boa representação do nível da água no rio e da área inundada na planície durante a cheia, em contraste com alta subestimativa da área inundada na água baixa. O volume armazenado e área inunda na planície varia anualmente 162,27 km^3 e 7,56 mil km^2 entre a seca e a cheia. A elevação da superfície da água na planície, com regiões heterogêneas, é superior à do rio no período de água-baixa. Com a enchente, a elevação da água se torna mais similar em ambas regiões, com uniformidade durante a cheia. Os fluxos de troca de água rio-planície são expressivos durante a cheia. Em 2009, caracterizado por um ano de cheia acima da média, os fluxos totais de entrada e saída foram 189,6 mil $m^3.s^{-1}$ e 206 mil $m^3.s^{-1}$, respectivamente, armazenando um volume de 238 km^3. Já na cheia de 2010, ano com uma cheia abaixo da média, os fluxos foram 60 e 62% menores que os fluxos de 2009, com um armazenamento de 204 km^3. Em agosto/setembro, período da vazante, predomina os fluxos da planície para o rio, e em fevereiro, período de baixa conectividade com o rio, pode ocorrer entrada de água na planície de jusante para montante. A caracterização desse sistema é importante para avaliar possíveis impactos das alterações hidrológicos no ambiente. Além disso, os resultados desse estudo podem ser utilizados como suporte para ações de gestão e em estudos ecológicos.

6.1 Introdução

O pulso monomodal do rio Amazonas, o maior rio do mundo em descarga anual, provoca uma grande variação no nível da água na planície de inundação e na área inundada. Por exemplo, a amplitude da variação do nível do rio pode chegar até 13 m (BIRKETT et al., 2002) e as áreas úmidas da bacia variam entre 288,9 mil km^2 e 78,2 mil km^2 nos períodos de cheia e água baixa (HESS et al., 2003). Além disso, os fluxos bidirecionais e o tempo de residência da água na planície de inundação são dinâmicos no espaço e no tempo e os padrões de variação do nível da água são complexos (ALSDORF; RODRIGUEZ; LETTENMAIER, 2007; CAO et al., 2018). A inundação anual do rio Amazonas exerce grande influência no armazenamento de água do rio (PAIVA et al., 2013), no transporte de sedimentos (DUNNE et al., 1998), na definição da geomorfologia local (LATRUBESSE; FRANZINELLI, 2002), na distribuição de espécies vegetais (FERREIRA-FERREIRA et al., 2014), na dispersão de sementes (MELACK et al., 2009), na emissão de dióxido de carbono (RICHEY et al., 2002) e de metano (MELACK et al., 2004), e na pesca de subsistência de comunidades ribeirinhas (JUNK et al., 2012; MELACK et al., 2009). Portanto, compreender o fluxo da água entre o rio Amazonas e a planície é de grande importância para entender esses processos.

Modelos hidrológicos foram aplicadas à bacia Amazônica para melhorar a compreensão dos processos hidrológicos (BEIGHLEY et al., 2009; COE; COSTA; HOWARD, 2008; CORREA et al., 2017; GETIRANA et al., 2012; LUO et al., 2017; PAIVA et al., 2013; SORRIBAS, 2016; YAMAZAKI et al., 2011). Apesar desses modelos representarem todos os componentes hidrológicos, os processos na planície foram simplificados. Por exemplo, a planície foi considerada como uma região de armazenamento, não sendo possível avaliar a direção e a velocidade da água na planície. Já os modelos bidimensionais de alcance médio, como de Wilson et al. (2007), avaliaram a troca de água do rio e da planície (240 km de extensão de rio). No entanto, o processo de drenagem na planície foi mal representado devido aos erros dos dados topográficos do SRTM3 DEM (WILSON et al., 2007). Posteriormente, Yamazaki et al. (2012) e Baugh et al. (2013) mostraram que a simulação do mesmo trecho teve maior acurácia com a correção de erros do SRTM3 DEM. Apesar da melhora, esses estudos consideraram a informação do SRTM3 DEM nas áreas de água aberta, em que os lagos são representados por uma superfície plana. É difícil a representação da topografia da planície de inundação da Amazônia central por modelos de elevações globais uma vez que essa é complexa e compostas por diversos lagos e canais interconectados (TRIGG et al., 2012) e tipos de

vegetação. Baugh et al. (2013), Paiva et al. (2013) e Yamazaki et al. (2012) ressaltam que a correta representação da topografia é fundamental para a correta simulação do escoamento da água, ao mesmo tempo que é um dado difícil de ser obtido. A batimetria dos lagos Calado (LESACK; MELACK, 1995), Curuai (BARBOSA et al., 2006) e Janauacá (PINEL et al., 2015) foram estimadas localmente, permitindo a aplicação de modelos locais e ampliando o conhecimento em relação a hidrologia do sistema rio-planície da Amazônia (BONNET et al., 2008, 2017; JI et al., 2019; LESACK; MELACK, 1995; PINEL et al., 2019; RUDORFF; MELACK; BATES, 2014b, 2014a). No entanto, as áreas de aplicação dos modelos são pequenas (73, 2440 e 786 km^2 para o Lago Calado, Curuai e Janauacá, respectivamente) e podem não ser representativos de toda a complexidade da planície de inundação da Amazônia. Além disso, os fluxos de troca de água rio-planície foram descritos em poucos desses estudos (RUDORFF; MELACK; BATES, 2014a). A primeira (e única) validação da velocidade da água na Amazônia foi feita por Pinel et al. (2019) para o Lago Janauacá. Portanto, muito ainda pode ser feito para melhorar o entendimento dessa complexa e importante área.

Fassoni-Andrade et al. (2020b) estimaram a topografia de áreas temporariamente inundadas na região central da planície de inundação do rio Amazonas com alta resolução espacial, além de obterem a batimetria de um trecho de 1100 km extensão do rio por cartas náuticas. Assim, surge a oportunidade de utilizar esse dado para entendimento mais detalhado dos fluxos de água e a troca de água rio-planície. O modelo bidimensional HEC-RAS permite a documentação desses fluxos e representa o escoamento pelas equações completas de Saint-Venant. Portanto, o objetivo desse estudo é caracterizar a inundação da planície de inundação da região central da bacia Amazônica documentando o volume de água, a área inundada, os fluxos de água e os padrões de variação do nível da água. Além disso, comparou-se três anos hidrológicos caracterizados como condição normal, de cheia e seca histórica.

6.2 Materiais e métodos

6.2.1 Modelo hidráulico

O HEC-RAS é um modelo hidráulico que possibilita a simulação do escoamento bidimensional a partir da solução numérica das equações completas de Saint-Venant (modelo hidrodinâmico), dadas pela equação da continuidade (eq. 6.1) e equação da quantidade de movimento (eq. 6.2). O modelo representa os termos da inércia (1),

gradiente de pressão e efeitos gravitacionais (2), atrito (3), efeitos de turbulência (4) e Coriolis (5). O fluxo turbulento e a força de Coriolis foram desconsideradas nesse estudo pois testes preliminares demostraram que essas forças possuem pequena contribuição na representação do escoamento.

$$\frac{\partial H}{\partial t} + \vec{\nabla} \bullet h\vec{V} + q = 0 \tag{6.1}$$

$$\underbrace{\frac{\partial \vec{V}}{\partial t} + \vec{V} \bullet \vec{\nabla}\vec{V}}_{1} = \underbrace{-g\vec{\nabla}H}_{2} - \underbrace{\frac{n^2 g|\vec{V}|}{R^{4/3}}\vec{V}}_{3} + \underbrace{v_t \nabla^2 \vec{V}}_{4} + \underbrace{(2\omega sen\varphi)\vec{k} \times \vec{V}}_{5} \tag{6.2}$$

Sendo $\vec{V} = (u, v)$ o vetor velocidade nas direções x e y; H elevação da superfície da água; h a profundidade; q o fluxo de entrada/saída; g a aceleração da gravidade, calculada como função da latitude (φ); v_t o coeficiente de viscosidade turbulenta horizontal; n o coeficiente de rugosidade de Manning; R o raio hidráulico; e ω a velocidade angular de rotação da terra. Detalhes das formulações e esquemas numéricos utilizados no modelo podem ser encontrados em Brunner (2016).

6.2.2 Domínio computacional e condições de contorno

O modelo foi aplicado em um trecho de 1100 km do rio Amazonas entre as confluências do rio Negro e do rio Xingu (Figura 6.1). O domínio computacional representa a planície de inundação adjacente ao rio nesse trecho, sendo delimitado a partir de uma margem de 1 km da máscara de áreas úmidas da Amazônia criada por Hess et al. (2015; Figura 6.1). A área total do domínio corresponde à 39.334 km^2.

Como condição de contorno a montante do rio Amazonas, foi utilizada a série temporal de vazões da estação Manacapuru, localizada a ~67 km a montante do domínio computacional e nivelada em relação ao geoide EGM 2008 (CALMANT et al., 2012). A localização da estação é mostrada na Figura 6.1 e as informações complementares dessa e de outras estações operadas pela Agência Nacional de Águas (ANA) são mostradas na Tabela S6.1 no material suplementar. A jusante, foi utilizada uma série de níveis da estação em Porto de Moz (operada pela ANA), que representa o nível da água no rio Xingu na confluência desse rio com o rio Amazonas, localizada a ~77 km do domínio computacional (localização na Figura 6.1). Devido ao efeito de remanso nos tributários do rio Amazonas, a estação pode ser representativa do nível do rio Amazonas. O

nivelamento dessa estação (EGM 2008) foi calculado considerando o nível de altimetria em uma estação virtual próxima (estação amz_amz_s3a_0433_01; http://hydroweb.theia-land.fr/) com viés estimado de 1,108 m (49 dados).

Além dessas forçantes, a vazão resultante da simulação do modelo hidrológico MGB-IPH foi utilizada como condições de contorno para representar as contribuições dos principais tributários no domínio (SIQUEIRA et al., 2018). Para isso, os 24 tributários que fazem intersecção com o domínio computacional foram selecionados. Desses, 13 foram utilizados na simulação por representarem até 99% da vazão média que contribui no domínio computacional (pontos em magenta na Figura 6.1).

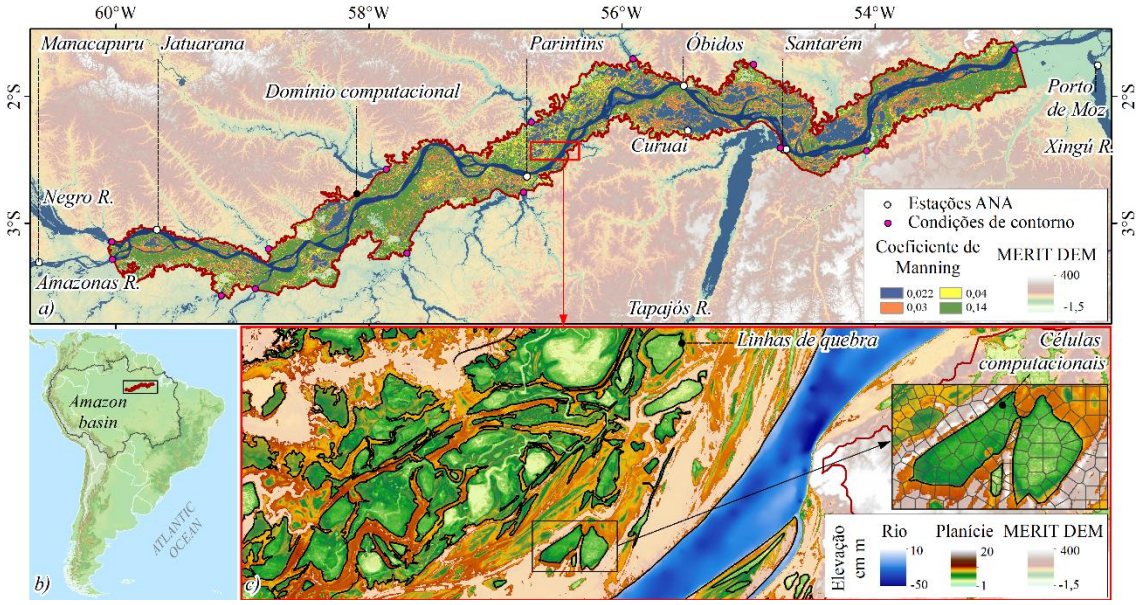

Figura 6.1. a) Localização do domínio computacional (~40 mil km^2), das condições de contorno e das estações de monitoramento da ANA. Mapeamento do coeficiente de Manning e modelo topográfico MERIT DEM. b) Localização da região central da bacia Amazônica. c) Detalhe da planície de inundação com os dados topográficos utilizados, as linhas de quebra e exemplificação da posição de células computacionais.

6.2.3 Topografia e malha computacional

A topografia da área de estudo foi elaborada a partir da junção de algumas bases de dados. No rio Amazonas e na área de água aberta da planície de inundação foi utilizada a topografia estimada por Fassoni-Andrade et al. (2020b) com resolução espacial de 30m (Figura 6.1a). O viés da batimetria do rio, documentado como 5 m, foi descontado nos valores de elevação.

Nas áreas complementares, a topografia foi obtida pelo modelo de elevação do terreno MERIT DEM v1.0.1 (*Multi-Error-Removed Improved-Terrain DEM*; disponível em: http://hydro.iis.u-tokyo.ac.jp/~yamadai/MERIT_DEM/). Este modelo foi escolhido por ter cobertura global em que o viés absoluto, ruídos e a altura da vegetação dos dados SRTM3 DEM e AW3D-30m v1 foram removidos (YAMAZAKI et al., 2017). O datum vertical de referência do modelo (EGM 1996) foi ajustado para o datum EGM 2008 utilizando o MSP GEOTRANS 3.7 (disponível em: <http://earth-info.nga.mil/GandG/geotrans/index.html#zza1).

O HEC-RAS permite a utilização de uma malha computacional não estruturada onde o tamanho da célula pode variar de acordo com a variação topográfica. Em regiões mais planas, podem ser adotas células maiores que a resolução espacial do dado topográfico, reduzindo o número de células computacionais. O requisito para a elaboração de uma boa malha computacional é definir as faces das células computacionais em regiões sem variações topográficas (BRUNNER, 2016b). No modelo HEC-RAS, linhas de quebra são manualmente incluídas no processo de construção da malha computacional para definição das faces (Figura 6.1d). Assim, essas linhas foram adicionadas considerando uma digitalização manual dos contornos topográficos das margens do rio e na planície com base nas isolinhas formadas pela frequência de inundação de 90% e 60% do mapa de frequência de inundação produzido por Fassoni-Andrade et al. (2020b). A malha computacional gerada com células de tamanho nominal de 400 m resultou em ~250 mil células com tamanho de célula médio de 398 m (mínimo de 48 m e máximo de 740 m).

6.2.4 Coeficiente de rugosidade de Manning

O mapa de coeficiente de rugosidade de Manning na planície de inundação foi elaborado com base no mapeamento da cobertura da terra em áreas úmidas da Amazônia (HESS et al., 2015). Foram atribuídos coeficientes de rugosidade de Manning para cada classe com base nos valores recomendados por Arcement Jr.; Schneider (1989) e Chow (1959), segundo a Tabela 6.1. A tabela também apresenta a proporção espacial que cada classe ocupa no domínio.

Outros trabalhos também se basearam nesse mapeamento atribuindo valores do coeficiente de Manning similares para cada classe. Rudorff et al. (2014a) atribuíram 0,14 e 0,10 para as classes de floresta e vegetação arbustiva. Pinel et al. (2019) atribuíram

0,032 para água permanente, 0,042 para vegetação arbustiva, 0,14 para floresta inundada e 0,18 para zonas de floresta.

Tabela 6.1. Coeficientes de rugosidade de Manning adotados em cada classe do mapeamento elaborado por Hess et al. (2015) e proporção da área ocupada no domínio computacional

Classe	Descrição*	Código do mapeamento (HESS et al., 2015)	Coeficientes de rugosidade de Manning	Proporção espacial no domínio**
Open water	Lago, paraná, igarapé, furo	11 13	igual ao do rio	17%
Bare soil or herbaceous	Terreno aberto, campo, macrófitas aquáticas	21 23 33	0,03	18%
Shrub	Vegetação arbustiva, campina	41 44 45 51 55	0,04	11%
Woodland	Chavascal, pântano, savanas inundadas	66 67 77	0,14	27,3%
Forest	Floresta, mata	88 89 99	0,14	4,4%
Terra firme	Fora da planície de inundação	-	0,18	9,1%

* Tabela 3 em Hess et al. (2003).**13,2% da área representa o rio Amazonas.

No rio Amazonas, o coeficiente de Manning foi calibrado para o período de 1 de setembro de 2006 até 31 de agosto de 2007 (1 ano). O menor RMSE (*Root mean square error*) do nível da água observado nas estações em Jatuarana (0,19 m), Parintins (0,13 m) e Santarém (0,21 m; Estações operadas pela ANA; Localização na Figura 6.1) resultou em um coeficiente de Manning de 0,022. Lefavour e Alsdorf (2005) assumiram um coeficiente de Manning de 0,025 com erro de 12% para estimativa da vazão no rio Solimões considerando um canal de areia sem vegetação. Wilson et al., (2007) calibraram um modelo hidráulico regional do trecho do baixo rio Solimões utilizando os valores na faixa entre 0,022 e 0,028 com base na estimativa de Lefavour e Alsdorf (2005). Portanto, apesar do valor encontrado ser baixo comparado com as simulações para o rio Solimões-Amazonas de Rudorff; Melack; Bates (2014a; 0,031) e Trigg et al. (2009; 0,032), está dentro da incerteza considerada por Lefavour e Alsdorf (2005).

6.2.5 Período da simulação e métricas avaliadas

A simulação considerou um passo de tempo de 15 minutos e 3 anos hidrológicos: novembro de 2007 a outubro de 2010. Esses anos foram escolhidos por representarem anos de condição normal (2008), cheia (2009) e seca (2010). Uma elevação da superfície da água de 2 metros foi considerada como condição inicial no domínio computacional e

um período inicial de 5 meses foi considerado como inicialização do modelo, permitindo o enchimento e drenagem da planície antes do início do período avaliado. Isso resultou em um processamento de 23 horas em um computador com 8 núcleos e 16 threads rodando em uma frequência média de 4.3 GHz.

O nível da água nas estações em Óbidos e Curuai foram considerados para validação do modelo (Estações operadas pela ANA; Localização na Figura 6.1). Também foram considerados dados de altimetria de satélite ao longo do rio proveniente dos satélites JASON2/JASON3 e ENVISAT. Esses dados representam estações virtuais extraídas a partir da intersecção do traço do altímetro com o rio e estão disponíveis em http://hydroweb.theia-land.fr (SANTOS DA SILVA et al., 2010). As informações dessas estações encontram-se na Tabela S6.1 no material suplementar. As métricas avaliadas foram: i) RMSE, ii) Viés, iii) coeficiente de correção de Pearson (*r*) e vi) coeficiente de eficiência de Nash–Sutcliffe (NSE *Nash–Sutcliffe efficiency*).

A extensão da inundação simulada foi avaliada através do fator F (eq. 6.3), que determina a acurácia do modelo (HORRITT e BATES, 2001). Para isso, o mapeamento de áreas úmidas da Amazônia com resolução espacial de 100 m (HESS et al., 2015) nos períodos de cheia (maio de 1996) e água-baixa (outubro de 1995) foram comparados à extensão de área inundada simuladas nos dias 1 de maio de 2008 e 1 de outubro de 2008.

$$F = \left(1 - \frac{b+c}{a}\right) 100 \tag{6.3}$$

Em que a representa a área total inundada, mapeada pelo modelo corretamente, b é a área inundada não mapeada pelo modelo (subestimativa), e c é a área não inundada e mapeada pelo modelo (superestimativa).

6.3 Resultados e Discussão

6.3.1 Validação

A área inundada no período de água-alta e água-baixa apresentou um fator F de 76,6% e 12,4%, respectivamente (Figura 6.2). Os erros de superestimativa do modelo (áreas verdes na Figura 6.2) correspondem as mesmas áreas nos dois períodos avaliados e são áreas de floresta segundo o mapeamento de Hess et al. (2015; classe mapeada com acurácia de 95%). Isso indica uma possível subestimativa da elevação do terreno no dado topográfico, causando uma superestimativa da área inundada. Já o erro de subestimativa

do modelo no período de água-baixa (áreas em vermelho na Figura 6.2c) foi muito alto, representando 34% da área inundada mapeada por Hess et al. (2015). Além da subestimativa da área inundada pelo modelo, a baixa acurácia no período de água-baixa pode ter ocorrido por dois motivos: i) o nível da água na planície de inundação no período do mapeamento de Hess et al. (2015; outubro de 1995) estava mais alto que no período considerado na avaliação da simulação (outubro de 2008); ii) o mapeamento de Hess et al. (2015) pode não ser tão preciso na representação da extensão da inundação nas áreas mapeadas como macrófitas aquáticas inundadas. Essa classe apresentou acurácia de apenas 50% (HESS et al., 2015) e é expressiva na área subestimada pelo modelo no período de água-baixa.

O nível da água no rio foi bem representado nas 23 estações avaliadas apresentando um viés médio de -0,45 m, RMSE de 0,77 m, NSE de 0,87 e r = 0.98. Esses erros são pequenos em relação a amplitude de variação do nível da água do rio (10 a 4 m; Estação 0063_01 e 0263_01 na Figura 6.2a). O viés e o RMSE para cada estação são apresentados na Figura 6.2. Somente as estações monitoradas pela ANA apresentaram viés positivo (Óbidos e Curuai), enquanto as estações de altimetria apresentaram viés negativo. O maior RMSE (1,55 m) ocorreu em uma estação localizada em um canal com subestimativa no período de água baixa, como apresentado na Figura 6.2b (Estação 0392_01).

Tanto a validação da área inundada quanto o do nível da água no rio apresentaram resultados melhores que o modelo de Wilson et al. (2007) para o rio Solimões. O fator F encontrado pelos autores foi 72% e 23% para a cheia e água baixa, respectivamente, com superestimativa da área inundada na água baixa devido à má drenagem da água na planície. Para o nível da água, os autores obtiveram um RMSE de 0,99 m na cheia e 3,17 m na água baixa.

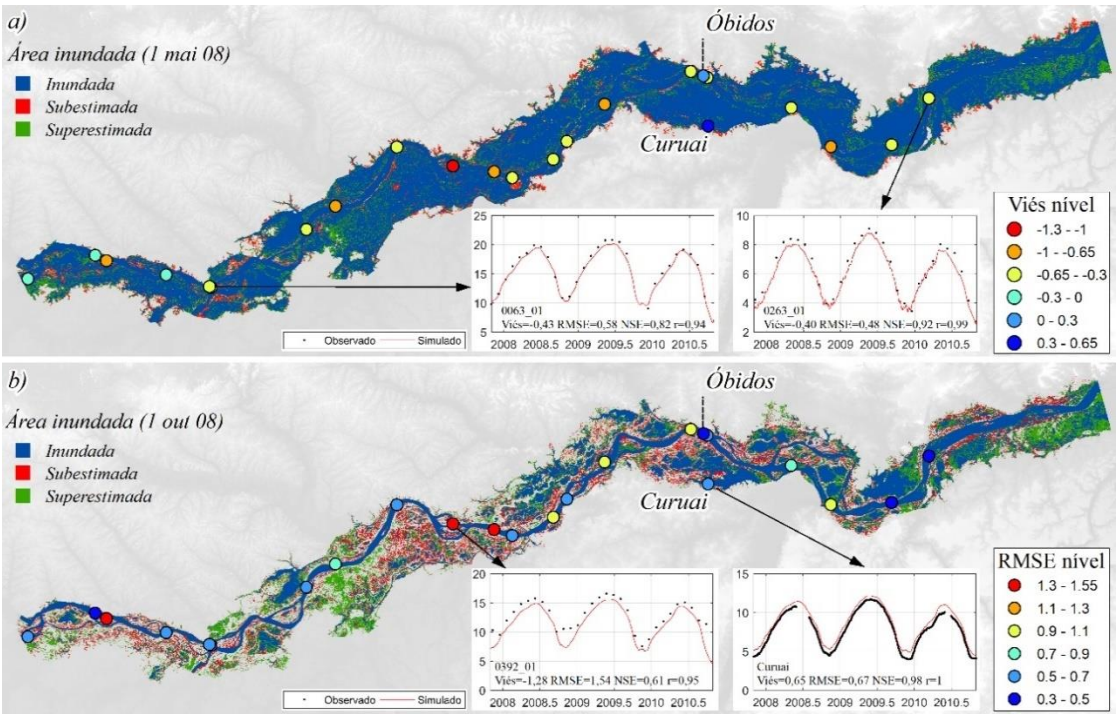

Figura 6.2. Validação da área inundada simulada no período de a) água-alta e b) água baixa. Viés (a) e RMSE (a) do nível da água no rio.

6.3.2 Variação do volume, profundidade da água e área inundada na planície

O volume armazenado na planície ao longo do período analisado é apresentado na Figura 6.3a. No período de água baixa (novembro) o volume armazenado variou de 55,3 km^3 em 2010 a 59,68 km^3 em 2009, enquanto no período de água alta (junho) o volume armazenado foi 216,8 km^3 em 2007, 238 km^3 em 2009 e 204 km^3 em 2010. Portanto, a diferença do volume armazenado na planície no pico da cheia entre um ano caracterizado por uma cheia história (2009) e um ano de seca (2010) foi de 34 km^3. Esse volume é expressivo e representa ~60% do volume médio armazenado na planície no período de água-baixa. A planície possui uma variação média de volume de 162,27 km^3, ou seja, anualmente esse volume é armazenado e drenado na planície de inundação entre o período de água baixa e a cheia. A profundidade média da água na planície apresenta um padrão similar ao volume armazenado ao longo do tempo. Na Figura 6.3b é apresentado o valor médio (± o desvio padrão). A amplitude média de variação da profundidade é 4,62 m (± 3m), ou seja, a profundidade média varia de 2,5 m a 7,12 m entre o período de água baixa e água alta.

Diferente da forte variação do volume armazenado, a área inundada no período de água alta apresentou um patamar com pouca variação, e valor médio de 31,5 mil km^2. Já

no período de água baixa, a área inundada apresentou um valor médio de 23,94 mil km^2. Esses valores representam, respectivamente, 11% e 31% das áreas úmidas mapeadas na bacia Amazônica nos períodos de cheia e água baixa (HESS et al., 2015).

A relação volume e área inundada na planície apresenta histerese, sendo que para o mesmo volume armazenado, a área inundada é maior na vazante do que na enchente. Por exemplo, para um volume armazenado de 73 km^3, a área inundada foi 28 mil m^2 na vazante e 26 mil m^2 na enchente.

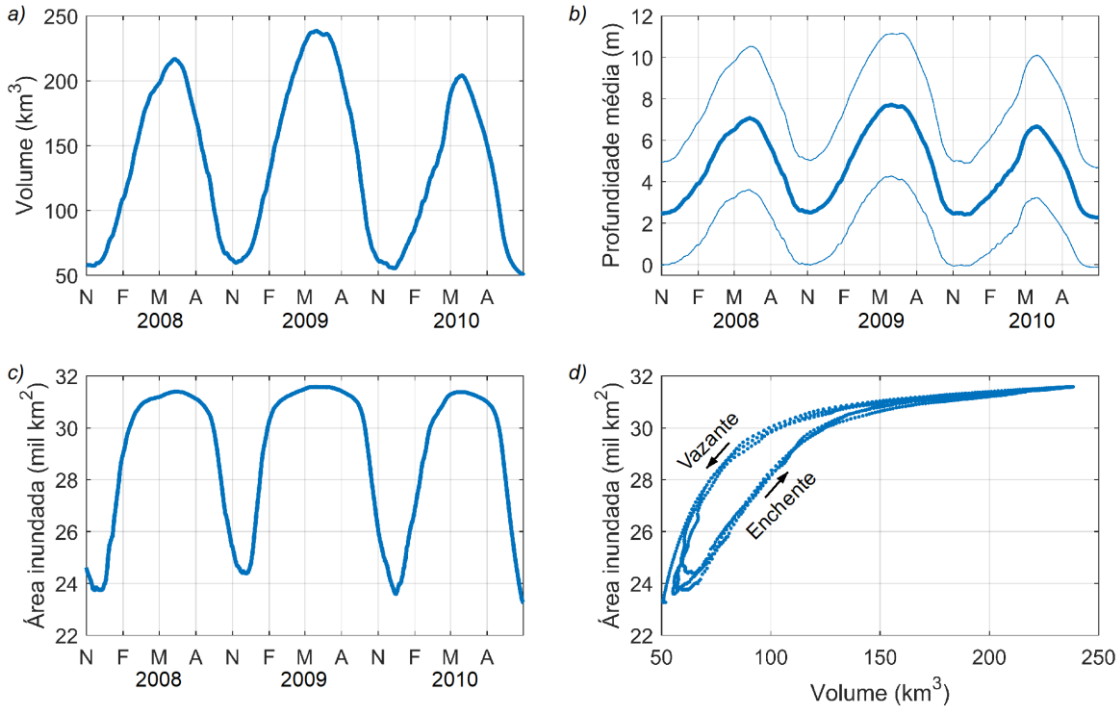

Figura 6.3. a) Volume armazenado na planície, b) profundidade média ± o desvio padrão e c) área inundada ao longo do período analisado. d) relação entre o volume e a área inundada na planície.

6.3.3 Elevação da superfície da água e conectividade

A elevação da superfície da água (*Elev*) para o ano hidrológico 2007/2008 e a variação do nível da água em 10 dias (*dh/dt*) é apresentado na Figura 6.4 para o período de água baixa (1 de novembro de 2007; a), enchente (1 de fevereiro de 2008; b), água-alta (1 de maio de 2008; c) e vazante (1 de agosto de 2008; d).

A heterogeneidade da elevação da superfície da água na planície é maior no período de água-baixa devido a menor conectividade com o rio. De forma geral, o nível da água é mais elevado na planície em relação ao rio, mas a variação do nível é positiva

no rio e negativa na planície. Ou seja, enquanto o nível da planície está reduzindo gradativamente (< 0,09 m a cada 10 dias), o nível no rio está aumentando (> 0,1 m). Algumas áreas da planície possuem variação do nível nula e outras possuem variação parecida com a do rio devido a maior conectividade. Na enchente, o nível da água na planície torna-se mais parecido com o nível do rio e a variação do nível aumenta à uma taxa maior que 0,2 m a cada 10 dias. O nível da água nos períodos de água-alta (maio) e vazante (agosto) são similares, com regiões homogêneas no rio e na planície. No entanto, enquanto o nível em maio continua a aumentar a uma taxa menor que 0,25 m a cada 10 dias, o nível em agosto reduz rapidamente a uma taxa maior que 0,35 m a cada 10 dias. Portanto, a enchente é mais lenta que a vazante (Figura 6.4b e c).

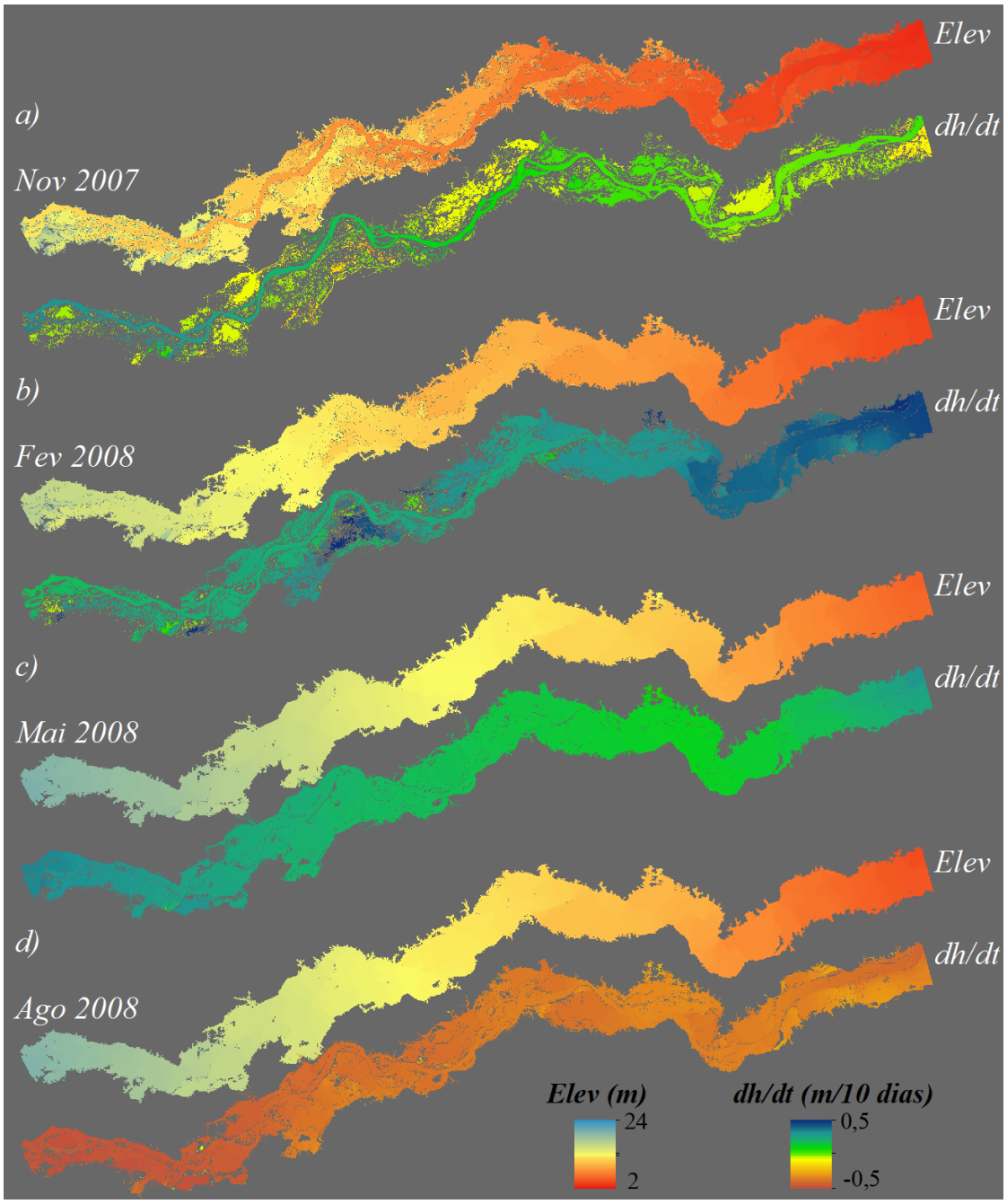

Figura 6.4. Elevação da superfície da água (*Elev*) e variação do nível da água em 10 dias para os períodos de a) água baixa (novembro), b) enchente (fevereiro), c) água alta (maio) e d) vazante (agosto).

6.3.4 Troca de água rio-planície e padrões de circulação da água

A troca de água entre o rio Amazonas e a planície de inundação foi avaliada em oito regiões a partir da estimativa da vazão em transectos paralelos às margens do rio. Em cada região foram definidos dois transectos de comprimentos (L) iguais: um a montante e outro a jusante. Os fluxos ao longo do tempo nos dois transectos (azul e amarelo) e o

fluxo resultante (linha vermelha) em cada região e em toda a planície são apresentados na Figura 6.5. Valores positivos indicam que a planície está recebendo água e valores negativos que está saindo água da planície.

Em todas as regiões, a entrada (saída) de água da planície predomina no transecto a montante (a jusante) da área avaliada, ou seja, pode ocorrer a entrada ou a saída de água nos dois transecto, mas o saldo é positivo (negativo) para o transecto a montante (jusante). De forma geral, o saldo positivo de entrada de água na planície inicia-se com a enchente do rio e predomina até o pico da cheia do rio (junho/julho). A partir da vazante, a saída de água se torna predominante com um máximo em agosto/setembro, quando a entrada de água na planície é muito pequena ou nula. O saldo negativo (fluxo da planície para o rio) continua ocorrendo nas regiões analisadas com valores pequenos até o início da inundação. No entanto, nas regiões 2 e 4 esse fluxo planície-rio é maior no período de água baixa pois há maior contribuição de tributários.

O fluxo total de água que entra em todas as regiões é máximo na cheia de 2009 com uma vazão de 189,6 mil $m^3.s^{-1}$, sendo maior que a vazão máxima do rio Solimões na cheia de 2009 (~160 mil $m^3.s^{-1}$). Por outro lado, o fluxo da planície para o rio é 206 mil $m^3.s^{-1}$ em 2009. Esses valores são bem menores na cheia de 2010, um ano caracterizado como seco. A vazão máxima que entra na planície é 114,5 mil $m^3.s^{-1}$ e que saí da planície é 128 mil $m^3.s^{-1}$, correspondendo a 60% e 62% dos fluxos de entrada e saída em 2009.

Além do maior fluxo de água, a cheia prolonga o período de troca de água entre o rio e a planície em algumas regiões. Nas regiões 1, 3, 5 e 6 a enchente começa entre fevereiro e abril, dependendo do ano: em 2007/2008 começa em março, em 2008/2009 em fevereiro e em 2009/2010 em abril. Ou seja, um ano seco (úmido) parece promover um atraso (adiantamento) da entrada de água na planície em aproximadamente um mês nessas regiões. O início da enchente nas regiões 2, 4, 7 e 8 ocorre em dezembro/janeiro, independente do ano, e, portanto, essas áreas parecem ter maior conexão com o rio a partir de fluxos canalizados. Apesar do saldo positivo iniciar em meses diferentes nas regiões, o fluxo máximo de entrada e saída de água da planície ocorre na cheia do rio (junho/julho), uma vez que o fluxo difuso na planície predomina.

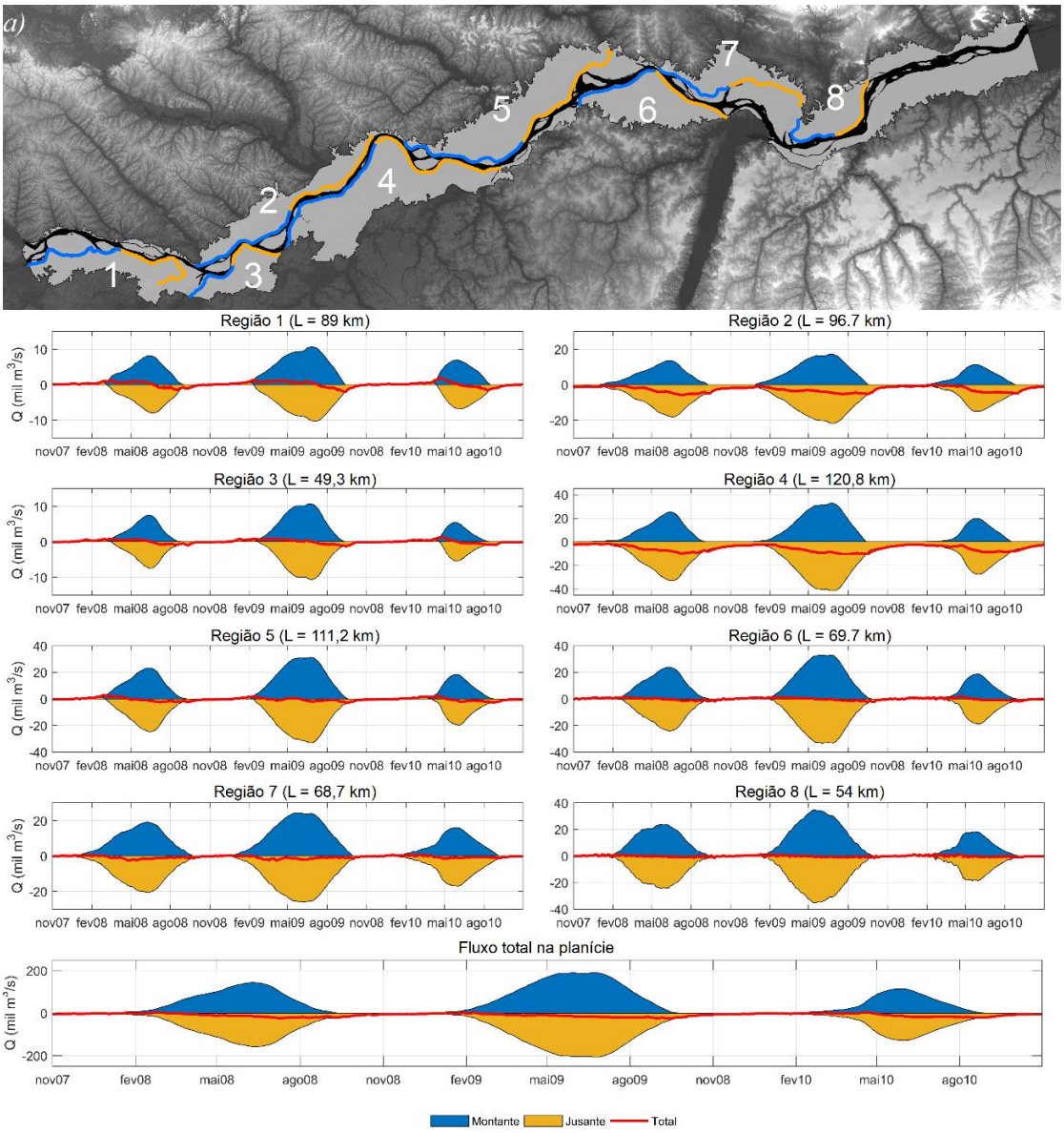

Figura 6.5. Fluxos de água em transectos de comprimento L em oito regiões da planície de inundação. Transectos em azul (amarelo) representam a região montante (jusante) de cada região.

O fluxo total (> 125 mil $m^3.s^{-1}$ na cheia) é muito expressivo, mas representa a entrada e saída de água nas regiões que ocorrem praticamente ao mesmo tempo. Assim, ocorre fluxos paralelos aos rios na planície durante a cheia, como documentado Rudorff et al, (2014a). Para avaliar esses fluxos, os campos de velocidade na cheia de 2009 foram avaliados, bem como o fluxo transversal na planície.

A Figura 6.6 mostra o fluxo transversal na planície nas oito regiões analisadas (em roxo) e os campos de velocidade nas regiões 2, 4, 5 e 6 para o dia 15 de junho de 2009. A direção do escoamento mostra a entrada e saída de água na planície durante a cheia na

direção de montante para jusante. O fluxo que passa pelos transectos é praticamente igual ao fluxo dos transectos paralelos ao rio à jusante (linhas amarelas da Figura 6.5a), indicados pela linha preta nos gráficos. No período de água baixa, o fluxo nos transectos transversais é baixo e pode ocorrer na direção oposta, de jusante para montante. Esses fluxos reversos em fevereiro de 2009, por exemplo, variaram de 76,13 $m^3.s^{-1}$ (região 3) a 389,1 $m^3.s^{-1}$ (região 6). Isso também é observado nos fluxos dos transectos a jusante onde ocorre valores negativos, ou seja, há entrada de água na planície na região a jusante no período de água-baixa, predominante em fevereiro.

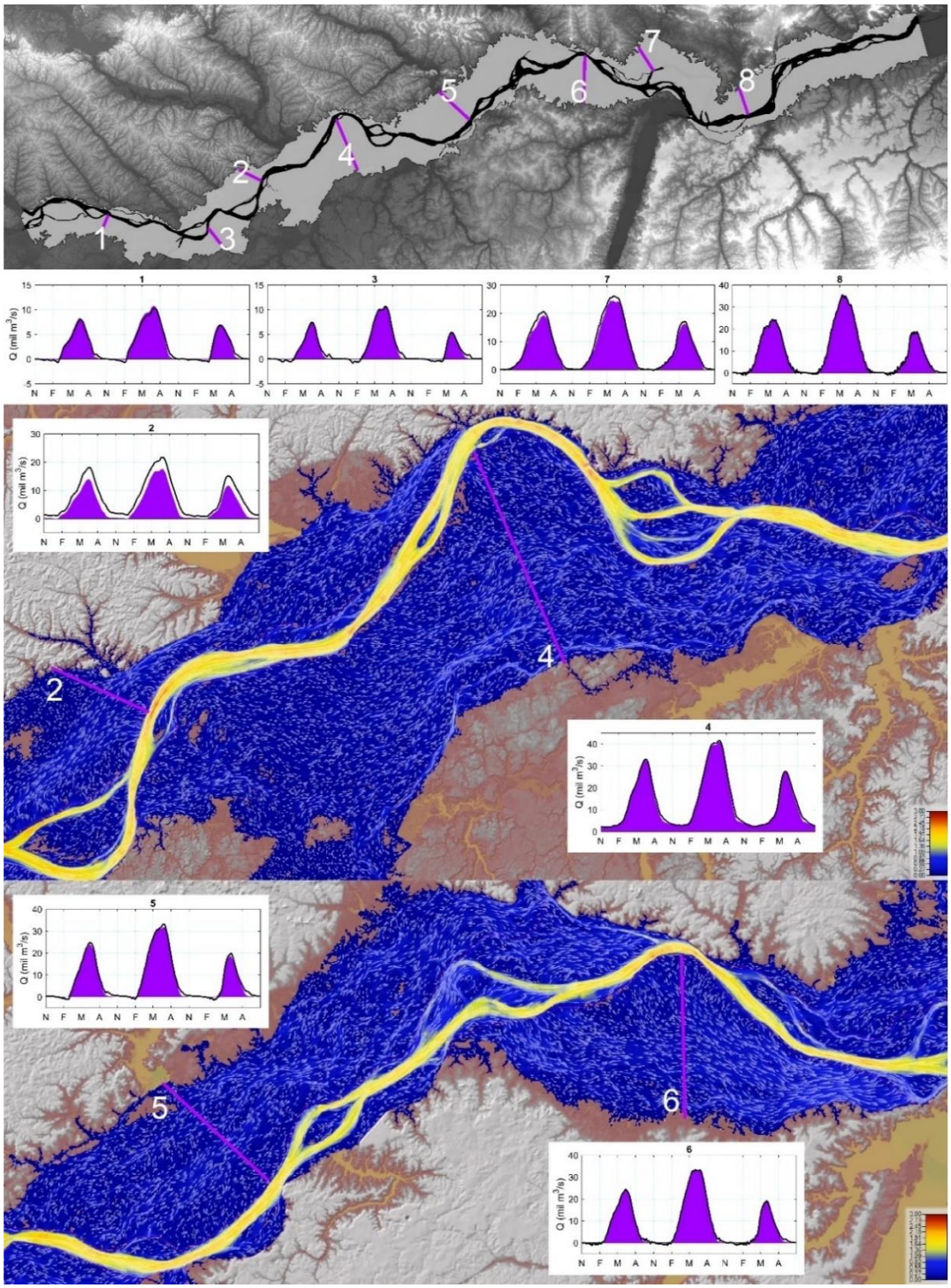

Figura 6.6. Fluxos de água transversais a planície em oito regiões analisadas e campos de velocidade da água em 15 de junho de 2009.

6.4 Sumário e Conclusões

A simulação hidráulica do escoamento da água na planície de inundação da região central do rio Amazonas foi realizada de forma pioneira ao considerar um modelo hidrodinâmico bidimensional em uma extensa planície de inundação (40 mil km^2) com

informações topográficas detalhadas. A variação do volume, da profundidade e da área inundada foram avaliadas, bem como os fluxos de água na planície e a conectividade com o rio.

O volume estocado, a profundidade e a área inundada na planície variaram em média 162,27 km^3, 4,62 m e 7,56 mil km^2 entre o período de água baixa e água alta. A elevação da superfície da água no rio e na planície é heterogênea (homogênea) no período de água-baixa (água-alta). O nível da água na planície reduz no período de água-baixa enquanto o nível do rio aumenta, apesar do nível na planície permanecer mais alto que o nível do rio. Na enchente (vazante), o nível aumenta (reduz) em ambas regiões a uma taxa maior que 0,2 m (0,35 m) a cada 10 dias. Portanto a enchente é mais lenta que a vazante. Já na cheia, o nível aumenta gradativamente a uma taxa de 0,25 m a cada 10 dias.

Os fluxos de entrada (saída) de água na planície são expressivos e ocorrem predominantemente na região a montante (jusante) de unidades da planície limitadas pelo rio. O fluxo do rio para a planície (da planície para o rio) é predominante no início da enchente do rio (agosto/setembro), e durante a cheia os fluxos ocorrem ao mesmo tempo com altos valores. No pico da cheia de 2009, um ano caracterizado por uma cheia acima da média, o fluxo total de entrada e saída correspondeu a 189,6 mil $m^3.s^{-1}$ e 206 mil $m^3.s^{-1}$, respectivamente, armazenando um volume de 238 km^3. Já na cheia de 2010, um ano caracterizado como seco, os fluxos corresponderam a 60 e 62% dos fluxos de entrada e saída em 2009, com um armazenamento de 204 km^3. Além das diferenças expressivas de fluxos em 2009 e 2010, um ano seco (úmido) parece promover um atraso (adiantamento) da entrada de água na planície em aproximadamente um mês. No período de baixa conectividade com o rio, principalmente em fevereiro, o fluxo de água na planície pode ocorrer na direção de jusante para montante com valores poucos expressivos em relação a cheia, na ordem de centenas de $m^3.s^{-1}$.

Esse estudo contribui para a caracterização de um sistema complexo com fluxos de água dinâmicos no espaço e no tempo, e é importante para avaliar possíveis impactos das alterações hidrológicos no ambiente. Os resultados podem ser utilizados, por exemplo, para entender a dispersão de sementes nas planícies bem como as variações de nutrientes e sedimentos. As estimativas de áreas inundadas e volume armazenado podem auxiliar ações de gestão e na estimativa do balanço de carbono na planície.

CAPÍTULO 7. Conclusões gerais

Essa tese procurou avançar i) no desenvolvimento de técnicas de sensoriamento remoto e base de dados para aplicações em estudos de rios e lagos, e ii) na compreensão da hidrologia superficial do sistema rio-planície da Amazônia central.

7.1 Desenvolvimento de técnicas e base de dados

O estudo realizou pela primeira vez um mapeamento da dinâmica de sedimentos em suspensão nos rios e lagos da Amazônia considerando diferentes tipologias de águas (branca, clara e preta). Esse mapeamento considerou imagens óticas de satélites que são afetadas pela cobertura de nuvens, e, portanto, uma metodologia de filtragem temporal das imagens foi utilizada para substituir dados com baixa qualidade. Para estudar padrões espaços temporais da concentração de sedimentos, essa metodologia foi adequada. Além de ser inovador em relação a cobertura espacial do mapeamento, o estudo inovou ao criar uma metodologia para resumir a variação temporal da concentração de sedimentos nos rios e lagos da Amazônia a partir de um único mapa. Esse mapa representa a frequência de três classes de concentração de sedimentos nesse ambiente em 15 anos: alta, moderada e baixa concentração. A acurácia global do mapeamento foi adequada para rios de água branca (78.5%) e preta (83%) e razoável par rios de água clara (34%). A metodologia pode ser aplicada em qualquer corpo d'água com variação na concentração de sedimentos em suspensão. Os mapeamentos produzidos, com resolução espacial de 250 m, estão disponíveis em http://dx.doi.org/10.17632/wy2mz3nm7p.1.

Um método utilizando dados de sensoriamento remoto para a estimativa da topografia em áreas temporariamente inundadas e do volume ativo de corpos d'água também foi desenvolvido e validado nessa tese. A abordagem requer um mapa de frequência de inundação e pelo menos uma série temporal do nível da água no corpo d'água. A topografia é estimada considerando uma superfície da água plana se apenas uma série temporal for utilizada, e, nesse caso, o aplicativo desenvolvido Flood2Topo pode ser usado para a estimativa (disponível em https://data.mendeley.com/datasets/jwxxjc5kyf/draft?a=224b0e01-c4af-4a90-94c2-bd07595b23db). A topografia estimada pelo Flood2Topo app apresentou uma raiz do erro médio quadrático (REMQ) de 18,50 cm e 146 cm para a elevação do terreno de dois lagos naturais e o erro no volume ativo para 11 reservatórios analisados variou em média 6,39%. Para considerar a declividade da água no corpo d'água, deve-se utilizar uma

informação distribuída do nível d'água na área. Essa abordagem também foi validada para a área de água aberta da planície de inundação do rio Amazonas, que apresenta diversos canais e lagos interconectados (REMQ = 90 cm). Nesse caso, o nível na planície foi estimado considerando o nível observado em estações de monitoramento no rio. A metodologia pode ser aplicada em qualquer área temporariamente inundada (lagos, reservatórios, áreas úmidas e rios intermitentes), e tem grande potencial para substituir a informação em áreas de água aberta de modelos topográficos globais, como o SRTM3 DEM e o MERIT DEM. A base de dado com a i) batimetria do rio Amazonas, digitalizada de cartas náuticas (RMSE e erro na área de 7,5m e 20,8%), ii) topografia estimada da planície de inundação do rio Amazonas, e iii) mapas de profundidade da água na planície para o período de água baixa e água alta estão disponíveis em XX com resolução espacial de 30 m. A partir dessa base de dados, foi desenvolvida a primeira modelagem bidimensional do rio Amazonas com alta resolução e usando informação batimétrica do rio e da planície, representando um avanço em relação aos modelos aplicados anteriormente.

7.2 Hidrologia do sistema rio-planície

O sistema rio-planície foi investigado em relação a variação de sedimentos e fluxos de água utilizando o mapeamento da dinâmica de sedimentos. Observou-se, por exemplo, a entrada de água/sedimentos do rio Solimões para o rio Japurá e um aumento na concentração de sedimentos da confluência com o rio Tapajós até a foz do rio Amazonas. Alguns padrões de variação de sedimentos em lagos observados por estudos locais foram confirmados e generalizados para lagos não estudados. Lagos do trecho médio-baixo do rio Amazonas recebem sedimentos por fluxo difuso, que ocorre quando o nível da água do rio extravasa pela margem durante a inundação, e a ressuspensão de sedimentos ocorre no período de água baixa quando os lagos estão rasos. O mapeamento também permitiu comparar a entrada de água com sedimentos em lagos do tipo ria no período de água baixa.

A variação do volume de água nas áreas de água aberta da planície de inundação da região central da Amazônia entre o período de água baixa e o período de água corresponde a 104,3 km^3. Esse volume é inferior à variação média do volume armazenado considerando também as áreas de vegetação inundada da planície de inundação (162,27 km^3), estimado a partir da simulação hidráulica do escoamento da água nessa região. A área inundada na planície de inundação dessa região representa 11% e 31% das áreas

úmidas mapeadas na Amazônia (HESS et al., 2015) no período de água alta e água baixa, respectivamente. A variação média da área inunda entre os dois períodos foi 7,56 mil km^2.

A simulação hidráulica também permitiu avaliar a elevação da superfície da água e os fluxos de água trocados entre o rio e a planície de inundação. Antes da enchente, a planície possui um nível mais elevado que o rio e pequena conectividade. A partir da enchente do rio, as duas regiões se tornam mais homogêneas em termos de elevação da superfície da água, com valores similares na cheia. A enchente é mais lenta que a vazante com o nível variando a taxas de +0,2 m e -0,35 m a cada 10 dias, respectivamente. Na cheia, o nível aumenta a uma taxa de 0,25 m a cada 10 dias.

O fluxo de água do rio para a planície torna-se predominante no início da enchente do rio com data variável. Nos anos hidrológicos de 2009 e 2010, caracterizados por cheias acima e abaixo da média, a enchente na planície começou, respectivamente, um mês antes e um mês depois da enchente de 2008. Durante a cheia, os fluxos de entrada e saída de água da planície são expressivos, ocorrem ao mesmo tempo e na direção de montante para jusante da planície. Em 2009, os fluxos totais de entrada e saída foram 189,6 mil $m^3.s^{-1}$ e 206 mil $m^3.s^{-1}$, respectivamente, armazenando um volume de 238 km^3. Já na cheia de 2010, os fluxos foram 60 e 62% menores que os fluxos de 2009, com um armazenamento de 204 km^3. Em agosto/setembro, predomina os fluxos da planície para o rio, e em fevereiro, período de baixa conectividade com o rio, pode ocorrer entrada de água na planície pela região a jusante.

7.3 Perspectivas

Os estudos dessa tese apontam para diversas perspectivas de pesquisa relacionadas às aplicações das técnicas desenvolvidas e a compreensão da hidrologia e ecologia da planície de inundação do rio Amazonas na região central.

A metodologia para mapeamento da dinâmica de sedimentos nos lagos foi aplicada para um estudo regional. No entanto, essa pode ser aplicada para estudos locais utilizando imagens com melhor resolução espacial, como o Landsat (30 m) e o Sentinel-2 (10 m). As imagens do programa Landsat estão disponíveis desde 1984 permitindo uma avaliação da tendência temporal das alterações da concentração de sedimentos, enquanto as imagens satélites Sentinel-2A e Sentinel-2B estão disponíveis a cada 5 dias desde 2017. Além disso, as séries temporais de reflectância desenvolvidas podem ser utilizadas para avaliar tendências de aumento ou redução da concentração de sedimentos em suspensão

na superfície nos rios e lagos da bacia. Assim, pode-se avaliar essas tendências com o uso e ocupação do solo, uma vez que diversas atividades na bacia, como garimpo e desmatamento, alteram a produção de sedimentos na bacia. De forma semelhante, as tendências podem ser avaliadas com parâmetros hidrológicos, como a precipitação.

A metodologia para estimativa da topografia de lagos tem grande potencial para ser aplicada globalmente uma vez que ainda não existe uma base de dados desse tipo. Além disso, com o lançamento do satélite SWOT, que fornecerá informações distribuídas de nível e extensão de áreas inundadas, a abordagem pode ser aprimorada para considerar a declividade da superfície da água no corpo d'água. A metodologia também pode ser aplicada em planícies de inundação com vegetação inundada utilizando imagens de radar, que permitem a estimativa da extensão de área inundada nessas áreas. Assim, a topografia de grandes áreas úmidas poderia ser estimada. Além da topografia, a partir de um modelo digital de elevação e a informação do nível da água na planície, a frequência de inundação nessas áreas poderia ser estimada. Além disso, as alterações geomorfológicas na planície, ou seja, alterações horizontais e verticais da topografia, podem ser avaliadas de forma pioneira a partir da aplicação da metodologia em diferentes períodos do tempo.

Diversos trabalhos ressaltam a importância de um modelo topográfico consistente para simulações hidrodinâmicas. Portanto, a abordagem desenvolvida nessa tese tem grande potencial para melhorar os dados topográficos globais e utilização em simulações. Os resultados da simulação hidráulica da planície de inundação central da Amazônia são promissores para dar suporte a estudos de ecologia na região. Mapas de áreas inundada e frequência de inundação podem ser utilizados, por exemplo, para estudar espécies vegetais dependentes do pulso de inundação, estimar a emissão de metano na planície e avaliar processos relacionados a distribuição de animais. Junto com a simulação, o mapeamento da dinâmica de sedimentos pode ser utilizado para melhorar a compreensão da variação e dispersão de sedimentos e nutrientes nesse sistema rio-planície.

Referências

ABDALLAH, H. et al. Potential of Space-Borne LiDAR Sensors for Global Bathymetry in Coastal and Inland Waters. **IEEE Journal of Selected Topics in Applied Earth Observations and Remote Sensing**, [s. l.], v. 6, n. 1, p. 202–216, 2013.

ABRIL, Gwenaël et al. Amazon River carbon dioxide outgassing fuelled by wetlands. **Nature**, [s. l.], v. 505, n. 7483, p. 395–398, 2013. Disponível em: <http://www.nature.com/doifinder/10.1038/nature12797>

ALCÂNTARA, E. et al. A contribution to understanding the turbidity behaviour in an Amazon floodplain. **Hydrology and Earth System Sciences**, [s. l.], v. 14, n. 2, p. 351–364, 2010.

ALSDORF, D. E.; RODRIGUEZ, E.; LETTENMAIER, Dennis P. Measuring surface water from space. **Reviews of Geophysics**, [s. l.], v. 45, n. 2, p. 1–24, 2007. Disponível em: <http://www.agu.org/pubs/crossref/2007/2006RG000197.shtml>

ALSDORF, Doug et al. Spatial and temporal complexity of the Amazon flood measured from space. **Geophysical Research Letters**, [s. l.], v. 34, n. 8, p. 1–5, 2007.

ALSDORF, Douglas et al. Diffusion modeling of recessional flow on central Amazonian floodplains. **Geophysical Research Letters**, [s. l.], v. 32, n. 21, p. 1–4, 2005.

ALSDORF, Douglas et al. Seasonal water storage on the Amazon floodplain measured from satellites. **Remote Sensing of Environment**, [s. l.], v. 114, n. 11, p. 2448–2456, 2010. Disponível em: <http://dx.doi.org/10.1016/j.rse.2010.05.020>

ALSDORF, Douglas E. et al. Interferometric radar measurements of water level changes on the Amazon flood plain. **Nature**, [s. l.], v. 404, n. March, p. 174–177, 2000.

ALSDORF, Douglas E. Water Storage of the Central Amazon Floodplain Measured with GIS and Remote Sensing Imagery. **Main**, [s. l.], v. 93, n. 1, p. 55–66, 2003.

AMIDROR, Isaac. Scattered data interpolation methods for electronic imaging systems: a survey. **Journal of Electronic Imaging**, [s. l.], v. 11, n. 2, p. 157, 2002. Disponível em: <http://electronicimaging.spiedigitallibrary.org/article.aspx?doi=10.1117/1.1455013>

ARCEMENT JR, G. J.; SCHNEIDER, V. R. Guide for Selecting Manning's Roughness Coefficients for Natural Channels and Flood Plains. **Technical Report, Geological Survey Water-Supply, United States Government Printing Office, Washington, U.S.A**, [s. l.], p. 38, 1989. Disponível em: <http://mosfet.isu.edu/classes/Sato/ENVE615/S13/Manning n.pdf>

ARNESEN, Allan S. et al. Monitoring flood extent in the lower Amazon River floodplain using ALOS/PALSAR ScanSAR images. **Remote Sensing of Environment**, [s. l.], v. 130, p. 51–61, 2013. Disponível em: <http://dx.doi.org/10.1016/j.rse.2012.10.035>

ARSEN, Adalbert et al. Remote sensing-derived bathymetry of Lake Poopó. **Remote Sensing**, [s. l.], v. 6, n. 1, p. 407–420, 2013.

AVISSE, Nicolas et al. Monitoring small reservoirs' storage with satellite remote sensing in inaccessible areas. **Hydrology and Earth System Sciences**, [s. l.], v. 21, n. 12, p. 6445–6459, 2017.

BARBOSA, Claudio Clemente. **Sensoriamento Remoto da dinâmica da circulaçnao da água do sistema planície de Curuai/ Rio Amazonas**. 2005. Instituto de Pesquisas Espacia, [s. l.], 2005.

BARBOSA, Cláudio Clemente Faria et al. A methodology for analysis of volume and flooded area dynamics: Lago Grande de Curuai várzea as an example. **Revista Brasileira de Cartografia**, [s. l.], v. 58, n. 3, p. 201–210, 2006.

BARBOSA, Cláudio Clemente Faria et al. Geospatial analysis of spatiotemporal patterns of pH, total suspended sediment and chlorophyll-a on the Amazon floodplain. **Limnology**, [s. l.], v. 11, n. 2, p. 155–166, 2009. Disponível em: <http://link.springer.com/10.1007/s10201-009-0305-5>

BASTVIKEN, David et al. Methane emissions from lakes: Dependence of lake characteristics, two regional assessments, and a global estimate. **Global Biogeochemical Cycles**, [s. l.], 2004.

BATES, Paul D. et al. **Numerical Modelling of Floodplain Flow**. [s.l: s.n.]. v. 4

BATES, Paul D.; HORRITT, Matthew S.; FEWTRELL, Timothy J. A simple inertial formulation of the shallow water equations for efficient two-dimensional flood inundation modelling. **Journal of Hydrology**, [s. l.], v. 387, n. 1–2, p. 33–45, 2010.

BAUGH, Calum A. et al. SRTM vegetation removal and hydrodynamic modeling accuracy. **Water Resources Research**, [s. l.], v. 49, n. 9, p. 5276–5289, 2013.

BEIGHLEY, R. E. et al. Simulating hydrologic and hydraulic processes throughout the Amazon River Basin. **Hydrological Processes**, [s. l.], v. 23, p. 1221–1235, 2009. Disponível em: <http://jamsb.austms.org.au/courses/CSC2408/semester3/resources/ldp/abs-guide.pdf>

BIANCAMARIA, Sylvain; LETTENMAIER, Dennis P.; PAVELSKY, Tamlin M. **The SWOT Mission and Its Capabilities for Land HydrologySurveys in Geophysics**, 2016.

BIRKETT, C. et al. From research to operations: The USDA global reservoir and lake monitor. In: **Coastal Altimetry**. [s.l: s.n.]. p. 19–50.

BIRKETT, C. M. et al. Surface water dynamics in the Amazon Basin: Application of satellite radar altimetry. **Journal of Geophysical Research D: Atmospheres**, [s. l.], v. 107, n. 20, 2002.

BOLANOS, Sandra et al. Operational surface water detection and monitoring using Radarsat 2. **Remote Sensing**, [s. l.], v. 8, n. 4, 2016.

BONNEMA, Matthew; HOSSAIN, Faisal. Assessing the Potential of the Surface Water and Ocean Topography Mission for Reservoir Monitoring in the Mekong River Basin. **Water Resources Research**, [s. l.], v. 55, n. 1, p. 444–461, 2019.

BONNET, Marie Paule et al. Floodplain hydrology in an Amazon floodplain lake (Lago Grande de Curuaí). **Journal of Hydrology**, [s. l.], v. 349, n. 1–2, p. 18–30, 2008.

BONNET, Marie Paule et al. Amazonian floodplain water balance based on modelling and analyses of hydrologic and electrical conductivity data. **Hydrological Processes**, [s. l.], v. 31, n. 9, p. 1702–1718, 2017.

BOURGOIN, Laurence Maurice et al. Temporal dynamics of water and sediment

exchanges between the Curuaí floodplain and the Amazon River, Brazil. **Journal of Hydrology**, [s. l.], v. 335, n. 1–2, p. 140–156, 2007. Disponível em: <http://linkinghub.elsevier.com/retrieve/pii/S0022169406005932>

BRÊDA, J. P. L. F. et al. Assimilation of Satellite Altimetry Data for Effective River Bathymetry. **Water Resources Research**, [s. l.], 2019.

BRUNNER, Gary. HEC-RAS river analysis system, Hydraulic reference manual, Version 5.0. **US Army Corps of Engineers Hydrologic Engineering Center, Davis CA**, [s. l.], n. February, p. 1–962, 2016. a.

BRUNNER, Gary W. HEC-RAS river analysis system, User's Manual, Version 5.0. **US Army Corps of Engineers Hydrologic Engineering Center, Davis CA**, [s. l.], n. February, p. 960, 2016. b.

BUSKER, Tim et al. A global lake and reservoir volume analysis using a surface water dataset and satellite altimetry. **Hydrology and Earth System Sciences**, [s. l.], v. 23, n. 2, p. 669–690, 2019.

CAI, Xiaobin et al. Remote Sensing of the Water Storage Dynamics of Large Lakes and Reservoirs in the Yangtze River Basin from 2000 to 2014. **Scientific Reports**, [s. l.], v. 6, n. October, p. 1–9, 2016. Disponível em: <http://dx.doi.org/10.1038/srep36405>

CALMANT, Stéphane et al. Detection of Envisat RA2/ICE-1 retracked radar altimetry bias over the Amazon basin rivers using GPS. **Advances in Space Research**, [s. l.], v. 51, n. 8, p. 1551–1564, 2012.

CAO, Ning et al. Estimation of Water Level Changes of Large-Scale Amazon Wetlands Using ALOS2 ScanSAR Differential Interferometry. [s. l.], v. 10, n. 966, 2018.

CARBONNEAU, Patrice E.; LANE, Stuart N.; BERGERON, Normand. Feature based image processing methods applied to bathymetric measurements from airborne remote sensing in fluvial environments. **Earth Surface Processes and Landforms**, [s. l.], v. 31, n. 11, p. 1413–1423, 2006.

CASULLI, Vincenzo. A high-resolution wetting and drying algorithm for free-surface hydrodynamics. **International Journal for Numerical Methods in Fluids**, [s. l.], v. 60, n. 4, p. 391–408, 2008.

CAZALS, Cécile et al. Mapping and characterization of hydrological dynamics in a coastal marsh using high temporal resolution Sentinel-1A images. **Remote Sensing**, [s. l.], v. 8, n. 7, 2016.

CHANSON, Hubert. **The Hydraulics of Open Channel Flow: An Introduction**. [s.l.] : Oxford: Butterworth-Heinemann, 2004.

CHAPMAN, Bruce et al. Mapping Regional Inundation with Spaceborne L-Band SAR. **Remote Sensing**, [s. l.], v. 7, n. 5, p. 5440–5470, 2015. Disponível em: <http://www.mdpi.com/2072-4292/7/5/5440/>

CHEN, J. L. et al. 2005 drought event in the Amazon River basin as measured by GRACE and estimated by climate models. **Journal of Geophysical Research: Solid Earth**, [s. l.], v. 114, n. 5, p. 1–9, 2009. a.

CHEN, J. L.; WILSON, C. R.; TAPLEY, B. D. The 2009 exceptional Amazon flood and interannual terrestrial water storage change observed by GRACE. **Water**

Resources Research, [s. l.], v. 46, n. 12, p. 1–10, 2010.

CHEN, S. et al. Aridity is expressed in river topography globally. **Nature**, [s. l.], 2019. Disponível em: <http://dx.doi.org/10.1038/s41586-019-1558-8>

CHEN, Shuisen et al. Remote sensing assessment of sediment re-suspension during Hurricane Frances in Apalachicola Bay, USA. **Remote Sensing of Environment**, [s. l.], v. 113, n. 12, p. 2670–2681, 2009. b. Disponível em: <http://dx.doi.org/10.1016/j.rse.2009.08.005>

CHOW, Ven Te. Open-channel hydraulics. **McGraw-Hill Book Company**, [s. l.], p. 728, 1959.

COE, Michael T.; COSTA, Marcos H.; HOWARD, Erica A. Simulating the surface waters of the Amazon River basin: Impacts of new river geomorphic and flow parameterizations. **Hydrological Processes**, [s. l.], v. 22, n. 14, p. 2542–2553, 2008.

COE, Michael T.; COSTA, Marcos H.; SOARES-FILHO, Britaldo S. The influence of historical and potential future deforestation on the stream flow of the Amazon River - Land surface processes and atmospheric feedbacks. **Journal of Hydrology**, [s. l.], 2009.

COLLISCHONN, Bruno; CLARKE, Robin Thomas. Estimation and uncertainty of remote-sensing-based Depth-Area-Volume (DAV) relationships. **Brazilian Journal of Water Resources**, [s. l.], v. 21, n. 4, 2016.

CONSTANTINE, José Antonio et al. Sediment supply as a driver of river meandering and floodplain evolution in the Amazon Basin. **Nature Geoscience**, [s. l.], v. 7, n. 12, p. 899–903, 2014.

COOLEY, Sarah W. et al. Tracking dynamic northern surface water changes with high-frequency planet CubeSat imagery. **Remote Sensing**, [s. l.], v. 9, n. 12, p. 1–21, 2017.

COOLEY, Sarah W. et al. Arctic-Boreal Lake Dynamics Revealed Using CubeSat Imagery. **Geophysical Research Letters**, [s. l.], v. 46, n. 4, p. 2111–2120, 2019.

CORREA, Sly Wongchuig et al. Multi-decadal Hydrological Retrospective: Case study of Amazon floods and droughts. **Journal of Hydrology**, [s. l.], v. 549, p. 667–684, 2017.

COSS, Stephen et al. Global River Radar Altimetry Time Series (GRRATS): New River Elevation Earth Science Data Records for the Hydrologic Community. **Earth System Science Data Discussions**, [s. l.], p. 137–150, 2019.

COSTA, M. Estimate of net primary productivity of aquatic vegetation of the Amazon floodplain using Radarsat and JERS-1. **International Journal of Remote Sensing**, [s. l.], v. 26, n. 20, p. 4527–4536, 2005.

COSTA, M. P. F. Use of SAR satellites for mapping zonation of vegetation communities in the Amazon floodplain. **International Journal of Remote Sensing**, [s. l.], v. 25, n. 10, p. 1817–1835, 2004.

CRÉTAUX, J. F. et al. SOLS: A lake database to monitor in the Near Real Time water level and storage variations from remote sensing data. **Advances in Space Research**, [s. l.], v. 47, n. 9, p. 1497–1507, 2011.

CRÉTAUX, Jean-François et al. Global surveys of reservoirs and lakes from satellites and regional application to the Syrdarya river basin. **Environmental Research Letters**,

[s. l.], v. 10, n. 1, 2015.

CRÉTAUX, Jean-François et al. Lake Volume Monitoring from Space. **Surveys in Geophysics**, [s. l.], v. 37, n. 2, p. 269–305, 2016.

CUNGE, J. A. On the subject of a flood propagation computation method (musklngum method). **Journal of Hydraulic Research**, [s. l.], v. 7, n. 2, p. 205–230, 1969.

CUNGE, J. A.; HOLLY JR, F. M.; VERWEY, A. **Practical Aspects of Computational River Hydraulics**. [s.l: s.n.]. Disponível em: <http://openlibrary.org/b/OL4421427M/Practical_aspects_of_computational_river_hydraulics>

DA ROCHA, Maíra et al. Thirty years after Balbina Dam: Diversity and floristic composition of the downstream floodplain forest, Central Amazon, Brazil. **Ecohydrology**, [s. l.], v. 12, n. 8, 2019.

DANIELSON, JJ.; GESCH, DB. Global Multi-resolution Terrain Elevation Data 2010(GMTED2010). **U.S. Geological Survey Open-File Report 2011–1073**, [s. l.], v. 2010, p. 26, 2011.

DARGAHI, Bijan; SETEGN, Shimelis Gebriye. Combined 3D hydrodynamic and watershed modelling of Lake Tana, Ethiopia. **Journal of Hydrology**, [s. l.], v. 398, n. 1–2, p. 44–64, 2011.

DATRY, Thibault; LARNED, Scott T.; TOCKNER, Klement. **Intermittent rivers: A challenge for freshwater ecologyBioScience**, 2014.

DENG, Chao et al. Estimation of nonfluctuating reservoir inflow from water level observations using methods based on flow continuity. **Journal of Hydrology**, [s. l.], v. 529, p. 1198–1210, 2015.

DILBONE, E. et al. Spectrally based bathymetric mapping of a dynamic, sand- bedded channel: Niobrara River, Nebraska, USA. **River Research and Applications**, [s. l.], n. January, p. 1–12, 2018.

DÖLL, P.; FIEDLER, K.; ZHANG, J. Global-scale analysis of river flow alterations due to water withdrawals and reservoirs. **Hydrology and Earth System Sciences**, [s. l.], 2009.

DOMENEGHETTI, Alessio. On the use of SRTM and altimetry data for flood modeling in data-sparse regions. **Water Resources Research**, [s. l.], 2016.

DÖRNHÖFER, Katja; OPPELT, Natascha. Remote sensing for lake research and monitoring – Recent advances. **Ecological Indicators**, [s. l.], v. 64, p. 105–122, 2016.

DOWNING, J. A. et al. The global abundance and size distribution of lakes, ponds, and impoundments. **Limnology and Oceanography**, [s. l.], v. 51, n. 5, p. 2388–2397, 2006.

DRAPER, Norman R.; SMITH, Harry. **Applied Regression Analysis**. Hoboken, NJ: Wiley-Interscience, 1998. Disponível em: <http://books.google.com/books?id=CJi2QgAACAAJ>

DU, Zhiqiang et al. Analysis of Landsat-8 OLI imagery for land surface water mapping. **Remote Sensing Letters**, [s. l.], v. 5, n. 7, p. 672–681, 2014.

DUAN, Zheng; BASTIAANSSEN, W. G. M. Estimating water volume variations in

lakes and reservoirs from four operational satellite altimetry databases and satellite imagery data. **Remote Sensing of Environment**, [s. l.], v. 134, p. 403–416, 2013. Disponível em: <http://dx.doi.org/10.1016/j.rse.2013.03.010>

DUNNE, T. et al. Exchanges of sediment between the flood plain and chennel of the Amazon River in Brazil. **Geological Society of America Bulletin**, [s. l.], v. 110, n. December 1997, p. 450–467, 1998.

DURAND, Michael et al. Estimation of bathymetric depth and slope from data assimilation of swath altimetry into a hydrodynamic model. **Geophysical Research Letters**, [s. l.], v. 35, n. 20, p. 1–5, 2008.

DURAND, Michael et al. The surface water and ocean topography mission: Observing terrestrial surface water and oceanic submesoscale eddies. **Proceedings of the IEEE**, [s. l.], v. 98, n. 5, p. 766–779, 2010.

EKLUNDH, Lars; JÖNSSON, Per. TIMESAT 3.2 with parallel processing Software Manual. [s. l.], p. 1–88, 2015.

FARR, T. et al. The shuttle radar topography mission. **Reviews of Geophysics**, [s. l.], v. 45, n. 2005, p. 1–33, 2007. a.

FARR, Tom G. et al. The shuttle radar topography mission. **Reviews of Geophysics**, [s. l.], v. 45, p. 1–33, 2007. b.

FASSONI-ANDRADE, Alice César; PAIVA, Rodrigo Cauduro Dias De. Mapping spatial-temporal sediment dynamics of river-floodplains in the Amazon. **Remote Sensing of Environment**, [s. l.], v. 221, p. 94–107, 2019. Disponível em: <https://doi.org/10.1016/j.rse.2018.10.038>

FASSONI-ANDRADE, Alice C., PAIVA, Rodrigo C., FLEISCHMANN, Ayan S., 2020a. Lake topography and active storage from satellite observations of flood frequency. **Submitted to Water Resources Research in September of 2019**. (2020a).

FASSONI-ANDRADE, Alice et al. High-resolution mapping of floodplain topography from space: a case study in the Amazon. **Submitted to Remote Sensing of Environment in February of 2020**. (2020b).

FENG, Lian et al. MODIS observations of the bottom topography and its inter-annual variability of Poyang Lake. **Remote Sensing of Environment**, [s. l.], v. 115, n. 10, p. 2729–2741, 2011. Disponível em: <http://dx.doi.org/10.1016/j.rse.2011.06.013>

FERREIRA-FERREIRA, Jefferson et al. Combining ALOS/PALSAR derived vegetation structure and inundation patterns to characterize major vegetation types in the Mamirauá Sustainable Development Reserve, Central Amazon floodplain, Brazil. **Wetlands Ecology and Management**, [s. l.], v. 23, n. 1, p. 41–59, 2014.

FEYISA, Gudina L. et al. Automated Water Extraction Index: A new technique for surface water mapping using Landsat imagery. **Remote Sensing of Environment**, [s. l.], v. 140, p. 23–35, 2014.

FILIZOLA, Naziano et al. Was the 2009 flood the most hazardous or the largest ever recorded in the Amazon? **Geomorphology**, [s. l.], v. 215, p. 99–105, 2014. Disponível em: <http://dx.doi.org/10.1016/j.geomorph.2013.05.028>

FILIZOLA, Naziano; GUYOT, Jean-loup. Suspended sediment yields in the Amazon

basin: an assessment using the Brazilian national data set. **Hydrological Processes**, [s. l.], v. 23, p. 3207–3215, 2009.

FISHER, Adrian; FLOOD, Neil; DANAHER, Tim. Comparing Landsat water index methods for automated water classification in eastern Australia. **Remote Sensing of Environment**, [s. l.], v. 175, p. 167–182, 2016.

FORSBERG, Bruce R. et al. The potential impact of new Andean dams on Amazon fluvial ecosystems. **PLoS ONE**, [s. l.], v. 12, n. 8, 2017.

FRAPPART, F. et al. The spatio-temporal variability of groundwater storage in the Amazon River Basin. **Advances in Water Resources**, [s. l.], v. 124, n. October 2016, p. 41–52, 2019. Disponível em: <https://doi.org/10.1016/j.advwatres.2018.12.005>

FRAPPART, Frédéric et al. Floodplain water storage in the Negro River basin estimated from microwave remote sensing of inundation area and water levels. **Remote Sensing of Environment**, [s. l.], v. 99, n. 4, p. 387–399, 2005.

FRAPPART, Frédéric et al. Satellite-based estimates of groundwater storage variations in large drainage basins with extensive floodplains. **Remote Sensing of Environment**, [s. l.], v. 115, n. 6, p. 1588–1594, 2011. Disponível em: <http://dx.doi.org/10.1016/j.rse.2011.02.003>

FRAPPART, Frédéric et al. Surface freshwater storage and dynamics in the Amazon basin during the 2005 exceptional drought. **Environmental Research Letters**, [s. l.], v. 7, n. 4, 2012.

FREAD, Danny. Flow Routing. In: MAIDMENT, David R. (Ed.). **Handbook of Hidrology**. New York: McGraw-Hill Inc, 1993. p. 10.1-10.36.

FURTADO, Luiz Felipe de Almeida; SILVA, Thiago Sanna Freire; NOVO, Evlyn Márcia Leão de Moraes. Dual-season and full-polarimetric C band SAR assessment for vegetation mapping in the Amazon várzea wetlands. **Remote Sensing of Environment**, [s. l.], v. 174, p. 212–222, 2016. Disponível em: <http://dx.doi.org/10.1016/j.rse.2015.12.013>

GAO, H. et al. On the causes of the shrinking of Lake Chad. **Environmental Research Letters**, [s. l.], v. 6, n. 3, 2011.

GAO, Huilin; BIRKETT, Charon; LETTENMAIER, Dennis P. Global monitoring of large reservoir storage from satellite remote sensing data. **Water Resources Research**, [s. l.], v. 48, n. September, p. 1–12, 2012.

GAO, Jay. Bathymetric mapping by means of remote sensing: Methods, accuracy and limitations. **Progress in Physical Geography**, [s. l.], v. 33, n. 1, p. 103–116, 2009.

GAROUSI-NEJAD, I. et al. **Terrain Analysis Enhancements to the Height Above Nearest Drainage Flood Inundation Mapping Method**. [s.l: s.n.]. Disponível em: <https://onlinelibrary.wiley.com/doi/abs/10.1029/2019WR024837>

GETIRANA, Augusto et al. The Hydrological Modeling and Analysis Platform (HyMAP): evaluation in the Amazon basin. **Journal of Hydrometeorology**, [s. l.], v. 13, p. 1641–1665, 2012.

GETIRANA, Augusto; CHUL, Hahn; TSENG, Kuo-hsin. Deriving three dimensional reservoir bathymetry from multi-satellite datasets. **Remote Sensing of Environment**,

[s. l.], v. 217, n. May, p. 366–374, 2018. Disponível em: <https://doi.org/10.1016/j.rse.2018.08.030>

GORELICK, Noel et al. Google Earth Engine: Planetary-scale geospatial analysis for everyone. **Remote Sensing of Environment**, [s. l.], v. 202, p. 18–27, 2017.

GRILL, G. et al. Mapping the world's free-flowing rivers. **Nature**, [s. l.], v. 569, n. 7755, p. 215–221, 2019.

HALL, Amanda C. et al. Geodetic corrections to Amazon River water level gauges using ICESat altimetry. [s. l.], v. 48, p. 1–6, 2012.

HAMILTON, Stephen K.; SIPPEL, Suzanne J.; MELACK, John M. Comparison of inundation patterns among major South American floodplains. **Journal of Geophysical Research Atmospheres**, [s. l.], v. 107, n. 20, p. 1–14, 2002.

HAMILTON, Stephen K.; SIPPEL, Suzanne J.; MELACK, John M. Seasonal inundation patterns in two large savanna floodplains of South America: The Llanos de Moxos (Bolivia) and the Llanos del Orinoco (Venezuela and Colombia). **Hydrological Processes**, [s. l.], v. 18, n. 11, p. 2103–2116, 2004.

HANASAKI, Naota; KANAE, Shinjiro; OKI, Taikan. A reservoir operation scheme for global river routing models. **Journal of Hydrology**, [s. l.], v. 327, n. 1–2, p. 22–41, 2006.

HESS, Laura L. et al. Dual-season mapping of wetland inundation and vegetation for the central Amazon basin. **Remote Sensing of Environment**, [s. l.], v. 87, n. 4, p. 404–428, 2003.

HESS, Laura L. et al. Wetlands of the Lowland Amazon Basin: Extent, Vegetative Cover, and Dual-season Inundated Area as Mapped with JERS-1 Synthetic Aperture Radar. **Wetlands**, [s. l.], v. 35, n. 4, p. 745–756, 2015.

HOEK, Jamon Van Den et al. Monitoring reservoir drought dynamics with landsat and radar/lidar altimetry time series in persistently cloudy eastern Brazil. **Remote Sensing**, [s. l.], v. 11, n. 7, 2019.

HUANG, Chang et al. Detecting, Extracting, and Monitoring Surface Water From Space Using Optical Sensors: A Review. **Reviews of Geophysics**, [s. l.], v. 56, n. 2, p. 333–360, 2018. a.

HUANG, Wenli et al. Automated extraction of surface water extent from Sentinel-1 data. **Remote Sensing**, [s. l.], v. 10, n. 5, 2018. b.

HUETE, A. et al. Overview of the radiometric and biophysical performance of the MODIS vegetation indices. **Remote Sensing of Environment**, [s. l.], v. 83, n. 1–2, p. 195–213, 2002.

HUTCHINSON, M. F. A new procedure for gridding elevation and stream line data with automatic removal of spurious pits. **Journal of Hydrology**, [s. l.], v. 106, n. 3–4, p. 211–232, 1989.

JARIHANI, Abdollah A. et al. Satellite-derived Digital Elevation Model (DEM) selection, preparation and correction for hydrodynamic modelling in large, low-gradient and data-sparse catchments. **Journal of Hydrology**, [s. l.], v. 524, p. 489–506, 2015.

JARIHANI, Abdollah Asadzadeh et al. Evaluation of multiple satellite altimetry data

for studying inland water bodies and river floods. **Journal of Hydrology**, [s. l.], v. 505, p. 78–90, 2013.

JENSEN, John R. **Sensoriamento remoto do ambiente: uma perspectiva em recursos terrestres**. [s.l: s.n.]. v. 21 Disponível em: <http://www.parentese.com.br/pdf/jensen.pdf>

JI, Xinye et al. Seasonal and inter-annual patterns and controls of hydrological fluxes in an Amazon floodplain lake with a surface-subsurface processes model. **Water Resources Research**, [s. l.], v. 55, n. 4, p. 3056–3075, 2019. Disponível em: <https://onlinelibrary.wiley.com/doi/abs/10.1029/2018WR023897>

JIANG, Hao et al. An automated method for extracting rivers and lakes from Landsat imagery. **Remote Sensing**, [s. l.], v. 6, n. 6, p. 5067–5089, 2014.

JONES, John W. Improved Automated Detection of Subpixel-Scale Inundation — Revised Dynamic Surface Water Extent (DSWE) Partial Surface Water Tests. **Remote Sensing**, [s. l.], v. 11, n. 4, p. 374, 2019. Disponível em: <https://www.mdpi.com/2072-4292/11/4/374>

JÖNSSON, Per; EKLUNDH, Lars. Seasonality extraction by function fitting to time-series of satellite sensor data. **IEEE Transactions on Geoscience and Remote Sensing**, [s. l.], 2002.

JÖNSSON, Per; EKLUNDH, Lars. TIMESAT - A program for analyzing time-series of satellite sensor data. **Computers and Geosciences**, [s. l.], 2004.

JUNG, Hahn Chul et al. Characterization of complex fluvial systems using remote sensing of spatial and temporal water level variations in the Amazon, Congo, and Brahmaputra rivers. **Earth Surface Processes and Landforms**, [s. l.], v. 35, n. 3, p. 294–304, 2010.

JUNK, W.; BAYLEY, P. B.; SPARKS, R. E. The flood pulse concept in river-floodplain-systems. **Canadian Journal of Fisheries and Aquatic Sciences**, [s. l.], v. 106, p. 110–127, 1989.

JUNK, Wolfgang J. et al. A classification of major naturally-occurring amazonian lowland wetlands. **Wetlands**, [s. l.], v. 31, n. 4, p. 623–640, 2011.

JUNK, Wolfgang J. et al. A classification of major natural habitats of Amazonian white-water river floodplains (várzeas). **Wetlands Ecology and Management**, [s. l.], v. 20, n. 6, p. 461–475, 2012.

JUNK, Wolfgang J. et al. A classification of the major habitats of Amazonian black-water river floodplains and a comparison with their white-water counterparts. **Wetlands Ecology and Management**, [s. l.], v. 23, n. 4, p. 677–693, 2015.

JUNK, Wolfgang J.; PIEDADE, Maria Teresa F. Plant Life in the Floodplain with Special Reference to Herbaceous Plants. In: **The central Amazon floodplain**. Berlin: Springer, 1997. p. 147–185.

KHANDELWAL, Ankush et al. An approach for global monitoring of surface water extent variations in reservoirs using MODIS data. **Remote Sensing of Environment**, [s. l.], v. 202, p. 113–128, 2017.

KIRK, John TO. **Light and Photosynthesis in Aquatic Ecosystems**. Third edit ed.

[s.l.] : Cambridge university press, 2011.

KLEIN, Igor et al. Global WaterPack – A 250 m resolution dataset revealing the daily dynamics of global inland water bodies. **Remote Sensing of Environment**, [s. l.], v. 198, p. 345–362, 2017. Disponível em: <http://linkinghub.elsevier.com/retrieve/pii/S003442571730305X>

KORDELAS, Georgios A. et al. Fast and automatic data-driven thresholding for inundation mapping with Sentinel-2 data. **Remote Sensing**, [s. l.], v. 10, n. 6, 2018.

KOSUTH, Pascal et al. Sea-tide effects on flows in the lower reaches of the Amazon River. **Hydrological Processes**, [s. l.], v. 23, n. November 2008, p. 3141–3150, 2009. Disponível em: <http://jamsb.austms.org.au/courses/CSC2408/semester3/resources/ldp/abs-guide.pdf>

KRIEGER, Gerhard et al. TanDEM-X: A satellite formation for high-resolution SAR interferometry. In: IEEE TRANSACTIONS ON GEOSCIENCE AND REMOTE SENSING 2007, **Anais**... [s.l: s.n.]

LARAQUE, Alain; FILIZOLA, Naziano; GUYOT, Jean Loup. Variations spatio-temporelles du bilan sédimentaire dans le bassin Amazonien Brésilien , à partir d ' un échantillonnage décadaire. [s. l.], v. 1, n. April, p. 250–258, 2005.

LATRUBESSE, Edgardo M. Amazon lakes. In: BENGTSSON, Lars; HERSCHY, Reginald W.; FAIRBRIDGE, Rhodes W. (Eds.). **Encyclopedia of Lakes and Reservoirs**. [s.l.] : Springer Verlag, 2012. p. 13–26.

LATRUBESSE, Edgardo M. et al. Damming the rivers of the Amazon basin. **Nature Publishing Group**, [s. l.], v. 546, n. 7658, p. 363–369, 2017. Disponível em: <http://dx.doi.org/10.1038/nature22333>

LATRUBESSE, Edgardo M.; FRANZINELLI, Elena. The Holocene alluvial plain of the middle Amazon River, Brazil. **Geomorphology**, [s. l.], v. 44, n. 3–4, p. 241–257, 2002.

LEFAVOUR, Gina; ALSDORF, Doug. Water slope and discharge in the Amazon River estimated using the shuttle radar topography mission digital elevation model. **Geophysical Research Letters**, [s. l.], v. 32, n. 17, p. 1–5, 2005.

LEGLEITER, C. J.; OVERSTREET, B. T. Mapping gravel bed river bathymetry from space. **Journal of Geophysical Research F: Earth Surface**, [s. l.], v. 117, n. 4, p. 1–24, 2012.

LEGLEITER, Carl J.; ROBERTS, Dar A.; LAWRENCE, Rick L. Spectrally based remote sensing of river bathymetry. **Earth Surface Processes and Landforms**, [s. l.], v. 34, n. March, p. 155–161, 2009.

LEHNER, B. et al. **Global Reservoir and Dam Database, Version 1 (GRanDv1): Dams, Revision 01**. Palisades, NY: NASA Socioeconomic Data and Applications Center (SEDAC), 2011. a. Disponível em: <https://doi.org/10.7927/H4N877QK>.

LEHNER, Bernhard et al. High-resolution mapping of the world's reservoirs and dams for sustainable river-flow management. **Frontiers in Ecology and the Environment**, [s. l.], v. 9, n. 9, p. 494–502, 2011. b.

LEHNER, Bernhard; DÖLL, Petra. Development and validation of a global database of

lakes, reservoirs and wetlands. **Journal of Hydrology**, [s. l.], v. 296, n. 1–4, p. 1–22, 2004.

LEITE, Christiane Cavalcante et al. Historical land use change and associated carbon emissions in Brazil from 1940 to 1995. **Global Biogeochemical Cycles**, [s. l.], v. 26, n. 2, 2012.

LEON, J. G. et al. Rating curves and estimation of average water depth at the upper Negro River based on satellite altimeter data and modeled discharges. **Journal of Hydrology**, [s. l.], v. 328, n. 3–4, p. 481–496, 2006.

LEON, J. X.; COHEN, T. J. An improved bathymetric model for the modern and palaeo Lake Eyre. **Geomorphology**, [s. l.], v. 173–174, p. 69–79, 2012.

LESACK, F. W.; MELACK, John M. Flooding hydrology and mixture dynamics of lakewater derived from multiple sources in an Amazon floodplain lake. **Water Resources Research**, [s. l.], v. 31, n. 2, p. 329–345, 1995.

LESACK, Lance F. W. Water Balance and Hydrologic Characteristics of a Rain Forest Catchment in the Central Amazon Basin. [s. l.], v. 29, n. 3, p. 759–773, 1993.

LESACK, Lance F. W. Seepage exchange in an Amazon floodplain lake. **Limnology and Oceanography**, [s. l.], v. 40, n. 3, p. 598–609, 1995.

LI, Yunliang et al. Hydrodynamic and Hydrological Modeling of the Poyang Lake Catchment System in China. **Journal of Hydrologic Engineering**, [s. l.], v. 19, n. 3, p. 607–616, 2014.

LOBO, Felipe de Lucia et al. Reference spectra to classify Amazon water types. **International Journal of Remote Sensing**, [s. l.], v. 33, n. 11, p. 3422–3442, 2012.

LOBO, Felipe L.; COSTA, Maycira P. F.; NOVO, Evlyn M. L. M. Time-series analysis of Landsat-MSS / TM / OLI images over Amazonian waters impacted by gold mining activities. **Remote Sensing of Environment**, [s. l.], v. 157, p. 170–184, 2015. Disponível em: <http://dx.doi.org/10.1016/j.rse.2014.04.030>

LOPES, Vitória Ache Rocha et al. A first integrated modelling of a river-lagoon large-scale hydrological system for forecasting purposes. **Journal of Hydrology**, [s. l.], v. 565, n. August, p. 177–196, 2018.

LOUGHLIN, F. E. O. et al. Remote Sensing of Environment A multi-sensor approach towards a global vegetation corrected SRTM DEM product. **Remote Sensing of Environment**, [s. l.], v. 182, p. 49–59, 2016. Disponível em: <http://dx.doi.org/10.1016/j.rse.2016.04.018>

LUO, Xiangyu et al. Modeling surface water dynamics in the Amazon Basin using MOSART-Inundation v1.0: Impacts of geomorphological parameters and river flow representation. **Geoscientific Model Development**, [s. l.], v. 10, n. 3, p. 1233–1259, 2017.

MA, Yue et al. Estimating water levels and volumes of lakes dated back to the 1980s using Landsat imagery and photon-counting lidar datasets. **Remote Sensing of Environment**, [s. l.], v. 232, n. November 2018, p. 111287, 2019. Disponível em: <https://doi.org/10.1016/j.rse.2019.111287>

MANGIAROTTI, S. et al. Discharge and suspended sediment flux estimated along the

mainstream of the Amazon and the Madeira rivers (from in situ and MODIS Satellite Data). **International Journal of Applied Earth Observation and Geoinformation**, [s. l.], v. 21, n. 1, p. 341–355, 2012. Disponível em: <http://dx.doi.org/10.1016/j.jag.2012.07.015>

MARKERT, Kel N. et al. AltEx: An open source web application and toolkit for accessing and exploring altimetry datasets. **Environmental Modelling and Software**, [s. l.], v. 117, n. February, p. 164–175, 2019. Disponível em: <https://doi.org/10.1016/j.envsoft.2019.03.021>

MARTINEZ, J. M. et al. Increase in suspended sediment discharge of the Amazon River assessed by monitoring network and satellite data. **Catena**, [s. l.], 2009.

MARTINEZ, Jean-michel et al. The optical properties of river and floodplain waters in the Amazon River Basin: Implications for satellite-based measurements of suspended particulate matter. **Journal of Geophysical Research : Earth Surface**, [s. l.], v. 1, n. 860, p. 1–11, 2015.

MARTINEZ, Jean Michel; LE TOAN, Thuy. Mapping of flood dynamics and spatial distribution of vegetation in the Amazon floodplain using multitemporal SAR data. **Remote Sensing of Environment**, [s. l.], v. 108, n. 3, p. 209–223, 2007.

MARTINS, Vitor S. et al. Seasonal and interannual assessment of cloud cover and atmospheric constituents across the Amazon (2000–2015): Insights for remote sensing and climate analysis. **ISPRS Journal of Photogrammetry and Remote Sensing**, [s. l.], n. October 2017, p. 0–1, 2018. Disponível em: <https://doi.org/10.1016/j.isprsjprs.2018.05.013>

MEADE, R. H. et al. **Storage and remobilization of suspended sediment in the lower Amazon river of Brazil.Science (New York, N.Y.)**, 1985.

MELACK, J. M.; HESS, L. L. Remote sensing of the distribution and extend of wetlands in the Amazon Basin. In: W;, Junk et al. (Eds.). **Amazonian Floodplain Forests. Ecological Studies (Analysis and Synthesis)**. Dordrecht: Springer, 2010. a. v. 210p. 43–59.

MELACK, John M. et al. Regionalization of methane emissions in the Amazon Basin with microwave remote sensing. **Global Change Biology**, [s. l.], v. 10, p. 530–544, 2004. Disponível em: <http://onlinelibrary.wiley.com/doi/10.1111/j.1365-2486.2004.00763.x/full>

MELACK, John M. et al. Floodplain Ecosystem Processes. In: **Amazonia and Global Change**. [s.l: s.n.].

MELACK, John M.; FORSBERG, Bruce R. **Biogeochemistry of the Amazon Floodplain Lakes and Associated WetlandsThe Biogeochemistry of the Amazon Basin and its Role in a Changing World**, 2001.

MELACK, John M.; HESS, Laura L. Remote Sensing of the Distribution and Extent of Wetlands in the Amazon Basin. In: **Amazonian Floodplain Forests**. [s.l: s.n.]. p. 43–59.

MELACK, John Michael. Amazon floodplain lakes: shape, fetch and stratification. **Verh. Internat. Verein. Limnol.**, [s. l.], v. 22, p. 1278–1282, 1984.

MERTES, L. A. K. Rates of flood-plain sedimentation on the central Amazon River.

Geology, [s. l.], v. 22, n. 2, p. 171–174, 1994.

MERTES, Leal a. K. Documentation and significance of the perirheic zone on inundated floodplains. **Water Resources Research**, [s. l.], v. 33, n. 7, p. 1749, 1997. Disponível em: <http://onlinelibrary.wiley.com/doi/10.1029/97WR00658/abstract>

MERTES, Leal A. K. et al. Spatial patterns of hydrology, geomorphology, and vegetation on the floodplain of the Amazon river in Brazil from a remote sensing perspective. **Geomorphology**, [s. l.], v. 13, n. 1–4, p. 215–232, 1995.

MERTES, Leal a K.; DUNNE, Thomas; MARTINELLI, Luiz a. Channel-floodplain geomorphology along the Solimoes-Amazon River, Brazil. **Bulletin of the Geological Society of America**, [s. l.], v. 108, n. 9, p. 1089–1107, 1996.

MESSAGER, Mathis Loıc et al. Estimating the volume and age of water stored in global lakes using a geo-statistical approach. **Nature communications**, [s. l.], p. 1–11, 2016.

MONTANHER, Otávio C. et al. Empirical models for estimating the suspended sediment concentration in Amazonian white water rivers using Landsat 5/TM. **International Journal of Applied Earth Observation and Geoinformation**, [s. l.], v. 29, n. 1, p. 67–77, 2014. Disponível em: <http://dx.doi.org/10.1016/j.jag.2014.01.001>

MORAMARCO, Tommaso et al. River Bathymetry Estimate and Discharge Assessment from Remote Sensing. **Water Resources Research**, [s. l.], 2019. Disponível em: <https://onlinelibrary.wiley.com/doi/abs/10.1029/2018WR024220>

MOREIRA, Daniel Medeiros. Doctorat de l'université de toulouse. [s. l.], n. Umr 5563, p. 118, 2016.

MUNAR, Andrés Mauricio et al. Coupling large-scale hydrological and hydrodynamic modeling: Toward a better comprehension of watershed-shallow lake processes. **Journal of Hydrology**, [s. l.], v. 564, n. March, p. 424–441, 2018.

NEAL, Jeffrey; SCHUMANN, Guy; BATES, Paul. A subgrid channel model for simulating river hydraulics and floodplain inundation over large and data sparse areas. **Water Resources Research**, [s. l.], v. 48, n. 11, 2012.

NÉELZ, S.; PENDER, G.; BRITAIN, G. **Desktop review of 2D hydraulic modelling packages**. [s.l: s.n.]. Disponível em: <http://scholar.google.com/scholar?hl=en&btnG=Search&q=intitle:Desktop+review+of+2D+hydraulic+modelling+packages#0>

NOVO, Evlyn Marcia Leao de Moraes et al. Seasonal changes in chlorophyll distributions in Amazon floodplain lakes derived from MODIS images. **Limnology**, [s. l.], v. 7, n. 3, p. 153–161, 2006.

O'LOUGHLIN, F. E. et al. A multi-sensor approach towards a global vegetation corrected SRTM DEM product. **Remote Sensing of Environment**, [s. l.], v. 182, p. 49–59, 2016. a.

O'LOUGHLIN, Fiachra E. et al. ICESat-derived inland water surface spot heights. **Water Resources Research**, [s. l.], v. 52, n. 4, p. 3276–3284, 2016. b.

OVANDO, A. et al. Multi-temporal flood mapping and satellite altimetry used to evaluate the flood dynamics of the Bolivian Amazon wetlands. **International Journal**

of Applied Earth Observation and Geoinformation, [s. l.], v. 69, n. January, p. 27–40, 2018. Disponível em: <https://doi.org/10.1016/j.jag.2018.02.013>

PAIVA, Rodrigo Cauduro Dias De et al. Large-scale hydrologic and hydrodynamic modeling of the Amazon River basin. **Water Resources Research**, [s. l.], v. 49, n. 3, p. 1226–1243, 2013.

PARIS, Adrien et al. Stage-discharge rating curves based on satellite altimetry andmodeled discharge in the Amazon basin. **Water Resources Research**, [s. l.], v. 52, p. 3787–3814, 2016.

PARK, Edward. **TRIBUTARY IMPACTS, HYDROLOGICAL CONNECTIVITY AND DISTRIBUTION OF SEDIMENT SINKS ALONG THE MIDDLE-LOWER AMAZON RIVER**. 2017. The University of Texas at Austin, [s. l.], 2017.

PARK, Edward; LATRUBESSE, Edgardo M. Modeling suspended sediment distribution patterns of the Amazon River using MODIS data. **Remote Sensing of Environment**, [s. l.], v. 147, p. 232–242, 2014. Disponível em: <http://dx.doi.org/10.1016/j.rse.2014.03.013>

PARK, Edward; LATRUBESSE, Edgardo M. Surface water types and sediment distribution patterns at the confluence of mega rivers: The Solimões-Amazon and Negro Rivers junction. **Water Resources Research**, [s. l.], v. 51, n. 8, p. 6197–6213, 2015.

PARK, Edward; LATRUBESSE, Edgardo M. The hydro-geomorphologic complexity of the lower Amazon River floodplain and hydrological connectivity assessed by remote sensing and field control. **Remote Sensing of Environment**, [s. l.], v. 198, p. 321–332, 2017. Disponível em: <http://dx.doi.org/10.1016/j.rse.2017.06.021>

PAVELSKY, Tamlin M. et al. Assessing the potential global extent of SWOT river discharge observations. **Journal of Hydrology**, [s. l.], v. 519, n. PB, p. 1516–1525, 2014. Disponível em: <http://dx.doi.org/10.1016/j.jhydrol.2014.08.044>

PAVELSKY, Tamlin M.; SMITH, Laurence C. Remote sensing of suspended sediment concentration, flow velocity, and lake recharge in the Peace-Athabasca Delta, Canada. **Water Resources Research**, [s. l.], v. 45, n. 11, p. 1–16, 2009.

PEKEL, Jean-François et al. High-resolution mapping of global surface water and its long-term changes. **Nature**, [s. l.], v. 540, n. 7633, p. 418–422, 2016. Disponível em: <http://www.nature.com/doifinder/10.1038/nature20584>

PENDER, G. Briefing: Introducing the Flood Risk Management Research Consortium. **Proceedings of the Institution of Civil Engineers - Water Management**, [s. l.], v. 159, n. 1, p. 3–8, 2006. Disponível em: <http://www.icevirtuallibrary.com/doi/10.1680/wama.2006.159.1.3>

PFEFFER, Julia et al. Low-water maps of the groundwater table in the central Amazon by satellite altimetry. **Geophysical Research Letters**, [s. l.], v. 41, n. 6, p. 1981–1987, 2014.

PINEL, Sebastien et al. Correction of Interferometric and Vegetation Biases in the SRTMGL1 Spaceborne DEM with Hydrological Conditioning towards Improved Hydrodynamics Modeling in the Amazon Basin. **Remote Sensing**, [s. l.], v. 7, n. 12, p. 16108–16130, 2015. Disponível em: <http://www.mdpi.com/2072-4292/7/12/15822>

PINEL, Sebastien et al. Flooding dynamics within a Amazonian floodplain : 2 . Water

circulation patterns and inundation duration. **Water Resources Research**, [s. l.], v. 56, n. 1, 2019. Disponível em: <https://doi.org/10.1029/2019WR026081>

PINEL, Sebastien Stefan Laurent. **Amazonian floodplain hydrodynamics: Characterization and local modeling with in situ and remotely sensed data**. 2017. Universidade do estado do Amazonas, [s. l.], 2017.

RESENDE, Angélica Faria De et al. Massive tree mortality from flood pulse disturbances in Amazonian floodplain forests: The collateral effects of hydropower production. **Science of the Total Environment**, [s. l.], v. 659, p. 587–598, 2019. Disponível em: <https://doi.org/10.1016/j.scitotenv.2018.12.208>

RICHEY, Jeffrey E. et al. Sources and routing of the Amazon River flood wave. [s. l.], v. 3, n. 3, p. 191–204, 1989.

RICHEY, Jeffrey E. et al. Outgassing from Amazonian rivers and wetlands as a large tropical source of atmospheric CO2. **Nature**, [s. l.], v. 416, n. 6881, p. 617–620, 2002. Disponível em: <http://www.nature.com/doifinder/10.1038/416617a>

RICHEY, Jeffrey E. et al. The Role of Rivers in the Regional Carbon Balance. In: **Amazonia and Global Change**. [s.l: s.n.]. p. 489–504.

RÍOS-VILLAMIZAR, Eduardo A. et al. Physicochemical features of Amazonian water typologies for water resources management. **IOP Conference Series: Earth and Environmental Science**, [s. l.], v. 427, 2020.

RODRÍGUEZ, Ernesto; MORRIS, Charles S.; BELZ, J. Eric. A Global Assessment of the SRTM Performance. [s. l.], v. 72, n. 3, p. 249–260, 2006.

RUDORFF, Conrado M.; DUNNE, Thomas; MELACK, John M. Recent increase of river-floodplain suspended sediment exchange in a reach of the lower Amazon River. **Earth Surface Processes and Landforms**, [s. l.], 2017. Disponível em: <http://doi.wiley.com/10.1002/esp.4247>

RUDORFF, Conrado M.; MELACK, John M.; BATES, Paul D. Flooding dynamics on the lower Amazon floodplain: 2. Seasonal and interannual hydrological variability. **Water Resources Research**, [s. l.], v. 50, n. 1, p. 635–649, 2014. a.

RUDORFF, Conrado M.; MELACK, John M.; BATES, Paul D. Flooding dynamics on the lower Amazon floodplain: 1. Hydraulic controls on water elevation, inundation extent, and river-floodplain discharge. **Water Resources Research**, [s. l.], v. 50, n. 1, p. 619–634, 2014. b.

SANDIDGE, Juanita C.; HOLYER, Ronald J. Coastal bathymetry from hyperspectral observations of water radiance. **Remote Sensing of Environment**, [s. l.], v. 65, n. 3, p. 341–352, 1998.

SANTORO, Maurizio et al. Strengths and weaknesses of multi-year Envisat ASAR backscatter measurements to map permanent open water bodies at global scale. **Remote Sensing of Environment**, [s. l.], v. 171, p. 185–201, 2015.

SANTOS DA SILVA, Joecila et al. Water levels in the Amazon basin derived from the ERS 2 and ENVISAT radar altimetry missions. **Remote Sensing of Environment**, [s. l.], p. 2160–2181, 2010.

SANTOS DA SILVA, Joecila et al. Water level dynamics of Amazon wetlands at the

watershed scale by satellite altimetry. **International Journal of Remote Sensing**, [s. l.], v. 33, n. 11, p. 3323–3353, 2012.

SARTORI, Lauriana Rúbio et al. Mapping macrophyte species in the amazon floodplain wetlands using fully polarimetric ALOS/PALSAR data. **IEEE Transactions on Geoscience and Remote Sensing**, [s. l.], v. 49, n. 12, p. 4717–4728, 2011.

SCHUMANN, Guy J. P. et al. Rethinking flood hazard at the global scale. **Geophysical Research Letters**, [s. l.], v. 43, n. 19, p. 10,249-10,256, 2016.

SCHUMANN, Guy J. P.; MOLLER, Delwyn K. Microwave remote sensing of flood inundation. **Physics and Chemistry of the Earth, Parts A/B/C**, [s. l.], v. 83–84, p. 84–95, 2015. Disponível em: <http://www.sciencedirect.com/science/article/pii/S1474706515000406>

SCHWATKE, C. et al. DAHITI - An innovative approach for estimating water level time series over inland waters using multi-mission satellite altimetry. **Hydrology and Earth System Sciences**, [s. l.], v. 19, n. 10, p. 4345–4364, 2015.

SCHWATKE, Christian; SCHERER, Daniel; DETTMERING, Denise. **Automated Extraction of Consistent Time-Variable Water Surfaces of Lakes and Reservoirs Based on Landsat and Sentinel-2**. [s.l: s.n.]. v. 11 Disponível em: <https://www.mdpi.com/2072-4292/11/9/1010>

SHENG, Yongwei et al. Representative lake water extent mapping at continental scales using multi-temporal Landsat-8 imagery. **Remote Sensing of Environment**, [s. l.], v. 185, p. 129–141, 2016.

SHIN, Sanghoon; POKHREL, Yadu; MIGUEZ-MACHO, Gonzalo. High-Resolution Modeling of Reservoir Release and Storage Dynamics at the Continental Scale. **Water Resources Research**, [s. l.], v. 55, n. 1, p. 787–810, 2019.

SILVA, Thiago S. F.; COSTA, Maycira P. F.; MELACK, John M. Annual net primary production of macrophytes in the eastern Amazon floodplain. **Wetlands**, [s. l.], v. 29, n. 2, p. 747–758, 2009. Disponível em: <http://link.springer.com/10.1672/08-107.1>

SILVA, Thiago S. F.; MELACK, John M.; NOVO, Evlyn M. L. M. Responses of aquatic macrophyte cover and productivity to flooding variability on the Amazon floodplain. **Global Change Biology**, [s. l.], v. 19, n. 11, p. 3379–3389, 2013.

SILVA, Thiago Sanna F.; COSTA, Maycira P. F.; MELACK, John M. Spatial and temporal variability of macrophyte cover and productivity in the eastern Amazon floodplain: A remote sensing approach. **Remote Sensing of Environment**, [s. l.], v. 114, n. 9, p. 1998–2010, 2010. Disponível em: <http://dx.doi.org/10.1016/j.rse.2010.04.007>

SILVERTOWN, Jonathan et al. Hydrologically defined niches reveal a basis for species richness in plant communities. **Nature**, [s. l.], v. 400, n. 6739, p. 61–63, 1999.

SIOLI, Harald. Über natur und mensch im brasilianischen Amazonasgebiet. **Erdkunde**, [s. l.], p. 89–109, 1956. Disponível em: <http://www.jstor.org/stable/23218158>

SIPPEL, S. J.; HAMILTON, S. K.; MELACK, J. M. Inundation Area and Morphometry of Lakes on the Amazon River Floodplain, Brazil. **Archiv Fur Hydrobiologie**, [s. l.], v. 123, n. 4, p. 385–400, 1992.

SIQUEIRA, Vinicius A. et al. Toward continental hydrologic-hydrodynamic modeling in South America. **Hydrology and Earth System Sciences**, [s. l.], v. 22, n. 9, p. 4815–4842, 2018.

SORRIBAS, Mino Viana et al. Projections of climate change effects on discharge and inundation in the Amazon basin. **Climatic Change**, [s. l.], v. 136, n. 3–4, p. 555–570, 2016.

SORRIBAS, Mino Viana. **Modelo de rastreamento hidrológico: um estudo das águas da bacia amazônica**. 2016. Universidade Federal do Rio Grande do Sul, [s. l.], 2016.

SUN, Donglian; YU, Yunyue; GOLDBERG, Mitchell D. Deriving Water Fraction and Flood Maps From MODIS Images Using a Decision Tree Approach. **IEEE Journal of Selected Topics in Applied Earth Observations and Remote Sensing**, [s. l.], v. 4, n. 4, p. 814–825, 2011.

TACHIKAWA, T. et al. **ASTER Global Digital Elevation Model Version 2 – Summary of Validation ResultsASTER GDEM Validation Team**. [s.l: s.n.]. Disponível em: <http://www.jspacesystems.or.jp/ersdac/GDEM/ver2Validation/Summary_GDEM2_validation_report_final.pdf>.

TARPANELLI, Angelica et al. Discharge estimation and forecasting by MODIS and altimetry data in Niger-Benue River. **Remote Sensing of Environment**, [s. l.], v. 195, p. 96–106, 2017. Disponível em: <http://dx.doi.org/10.1016/j.rse.2017.04.015>

TONG, Xiaohua et al. Estimating water volume variations in Lake Victoria over the past 22 years using multi-mission altimetry and remotely sensed images. **Remote Sensing of Environment**, [s. l.], v. 187, p. 400–413, 2016. Disponível em: <http://dx.doi.org/10.1016/j.rse.2016.10.012>

TORRES, Mark; JOSHUA WEST, A.; CLARK, Kathryn E. Geomorphic regime modulates hydrologic control of chemical weathering in the Andes-Amazon. **Geochimica et Cosmochimica Acta**, [s. l.], v. 166, p. 105–128, 2015.

TOURIAN, M. J.; REAGER, J. T.; SNEEUW, N. The Total Drainable Water Storage of the Amazon River Basin: A First Estimate Using GRACE. **Water Resources Research**, [s. l.], v. 54, n. 5, p. 1–27, 2018.

TRIGG, Mark A. et al. Amazon flood wave hydraulics. **Journal of Hydrology**, [s. l.], v. 374, n. 1–2, p. 92–105, 2009. Disponível em: <http://dx.doi.org/10.1016/j.jhydrol.2009.06.004>

TRIGG, Mark A. et al. Floodplain channel morphology and networks of the middle Amazon River. **Water Resources Research**, [s. l.], v. 48, n. 10, p. 1–17, 2012.

TSENG, Kuo Hsin et al. Integrating Landsat Imageries and Digital Elevation Models to Infer Water Level Change in Hoover Dam. **IEEE Journal of Selected Topics in Applied Earth Observations and Remote Sensing**, [s. l.], v. 9, n. 4, p. 1696–1709, 2016.

TSENG, Kuo Hsin et al. Reconstruction of time-varying tidal flat topography using optical remote sensing imageries. **ISPRS Journal of Photogrammetry and Remote Sensing**, [s. l.], v. 131, p. 92–103, 2017. Disponível em:

<http://dx.doi.org/10.1016/j.isprsjprs.2017.07.008>

TUCCI, C. E. M. **Modelos hidrológicos**. 2. ed. Porto Alegre: Editora da UFRGS, 2005.

URBAN, Timothy J.; SCHUTZ, Bob E.; NEUENSCHWANDER, Amy L. A survey of ICESat coastal altimetry applications: Continental Coast, Open Ocean Island, and Inland River. In: TERRESTRIAL, ATMOSPHERIC AND OCEANIC SCIENCES 2008, **Anais**... [s.l: s.n.]

VAUCHEL, Philippe et al. A reassessment of the suspended sediment load in the Madeira River basin from the Andes of Peru and Bolivia to the Amazon River in Brazil, based on 10 years of data from the HYBAM monitoring programme. **Journal of Hydrology**, [s. l.], v. 553, p. 35–48, 2017. Disponível em: <http://dx.doi.org/10.1016/j.jhydrol.2017.07.018>

VERMOTE, E. F.; ROGER, J. C.; RAY, J. P. MODIS Surface Reflectance User's Guide: Collection 6. **User Guide**, [s. l.], p. 1–40, 2015.

VERMOTE, E. F.; VERMEULEN, A. Algorithm Technical Background Document ATMOSPHERIC CORRECTION ALGORITHM : SPECTRAL REFLECTANCES (MOD09) NASA contract NAS5-96062. [s. l.], n. April, p. 1–107, 1999.

VERPOORTER, Charles et al. A global inventory of lakes based on high-resolution satellite imagery. **Geophysical Research Letters**, [s. l.], v. 41, n. 18, p. 6396–6402, 2014.

VILLANO, Michelangelo et al. Gapless imaging with the NASA-ISRO SAR (NISAR) Mission: Challenges and opportunities of staggered SAR. In: PROCEEDINGS OF THE EUROPEAN CONFERENCE ON SYNTHETIC APERTURE RADAR, EUSAR 2018, **Anais**... [s.l: s.n.]

VILLAR, Raul Espinoza et al. Spatio-temporal monitoring of suspended sediments in the Solimões River (2000–2014). **Comptes Rendus Geoscience**, [s. l.], p. 1–9, 2017. Disponível em: <http://linkinghub.elsevier.com/retrieve/pii/S1631071317300469>

VILLAR, Raúl Espinoza et al. The integration of field measurements and satellite observations to determine river solid loads in poorly monitored basins. **Journal of Hydrology**, [s. l.], v. 444–445, p. 221–228, 2012.

VILLAR, Raúl Espinoza et al. A study of sediment transport in the Madeira River, Brazil, using MODIS remote-sensing images. **Journal of South American Earth Sciences**, [s. l.], v. 44, p. 45–54, 2013. Disponível em: <http://dx.doi.org/10.1016/j.jsames.2012.11.006>

WILSON, Matthew D. et al. Modeling large-scale inundation of Amazonian seasonally flooded wetlands. **Geophysical Research Letters**, [s. l.], v. 34, n. 15, p. 4–9, 2007.

WITTMANN, Florian et al. The Brazilian freshwater wetscape: Changes in tree community diversity and composition on climatic and geographic gradients. **PLoS ONE**, [s. l.], v. 12, n. 4, 2017.

YAMAZAKI, Dai et al. A physically based description of floodplain inundation dynamics in a global river routing model. **Water Resources Research**, [s. l.], v. 47, n. 4, 2011.

YAMAZAKI, Dai et al. Adjustment of a spaceborne DEM for use in floodplain

hydrodynamic modeling. **Journal of Hydrology**, [s. l.], v. 436–437, p. 81–91, 2012. Disponível em: <http://dx.doi.org/10.1016/j.jhydrol.2012.02.045>

YAMAZAKI, Dai et al. A high-accuracy map of global terrain elevations. **Geophysical Research Letters**, [s. l.], v. 44, n. 11, p. 5844–5853, 2017.

YAMAZAKI, Dai; TRIGG, Mark A.; IKESHIMA, Daiki. Development of a global ~90m water body map using multi-temporal Landsat images. **Remote Sensing of Environment**, [s. l.], v. 171, p. 337–351, 2015.

YAO, Fangfang et al. Constructing long-term high-frequency time series of global lake and reservoir areas using Landsat imagery. **Remote Sensing of Environment**, [s. l.], v. 232, n. July, p. 111210, 2019. Disponível em: <https://doi.org/10.1016/j.rse.2019.111210>

ZAJAC, Zuzanna et al. The impact of lake and reservoir parameterization on global streamflow simulation. **Journal of Hydrology**, [s. l.], v. 548, p. 552–568, 2017.

ZAKHAROVA, Elena A. et al. Amazon River discharge estimated from TOPEX/Poseidon altimetry. **Comptes Rendus - Geoscience**, [s. l.], v. 338, n. 3, p. 188–196, 2006.

ZHANG, Ling et al. Stream flow simulation and verification in ungauged zones by coupling hydrological and hydrodynamic models: a case study of the Poyang Lake ungauged zone. **Hydrology and Earth System Sciences**, [s. l.], v. 21, n. 11, p. 5847–5861, 2017.

ZHANG, Shuai; GAO, Huilin; NAZ, Bibi S. Monitoring reservoir storage in South Asia from multi satellite remote sensing. **Water Resources Research**, [s. l.], v. 50, n. 11, p. 8927–8943, 2014.

ZHAO, Gang; GAO, Huilin. Automatic Correction of Contaminated Images for Assessment of Reservoir Surface Area Dynamics. **Geophysical Research Letters**, [s. l.], v. 45, n. 12, p. 6092–6099, 2018.

ZHOU, Tian et al. The Contribution of Reservoirs to Global Land Surface Water Storage Variations. **Journal of Hydrometeorology**, [s. l.], v. 17, n. 1, p. 309–325, 2016.

ZWALLY, H. J. et al. **GLAS/ICESat L1A and 2 Global Land Surface Altimetry Data V028NASA National Snow and Ice Data Center Distributed Active Archive Center**, 2007. Disponível em: <http://nsidc.org/forms/glas_subset_form.html>

Supplementary information S3

Text S3.1. The local model functions implemented in TIMESAT 3.2 software package have the general form:

$$f(t; c_1, c_2, x_1, \dots, x_4) = c_1 + c_1\, g(t; x_1, \dots, x_4) \quad (1)$$

Where $g(t; x_1, \dots, x_4)$ is a double logistic function:

$$g(t; x_1, \dots, x_4) = \frac{1}{1+\exp\left(\frac{x_1 - t}{x_2}\right)} - \frac{1}{1+\exp\left(\frac{x_3 - t}{x_4}\right)} \quad (2)$$

The linear parameters (c_1, c_2) determine the base level and the amplitude, and for double logistic function, x_1 determines the position of the left inflection point while x_2 gives the rate of change. Similarly x_3 determines the position of the right inflection point while x_4 gives the rate of change at this point. These parameters are restricted in overlapping intervals around maxima and minima and are obtained by minimizing a merit function, which is described in Eklundh & Jönsson (2015).

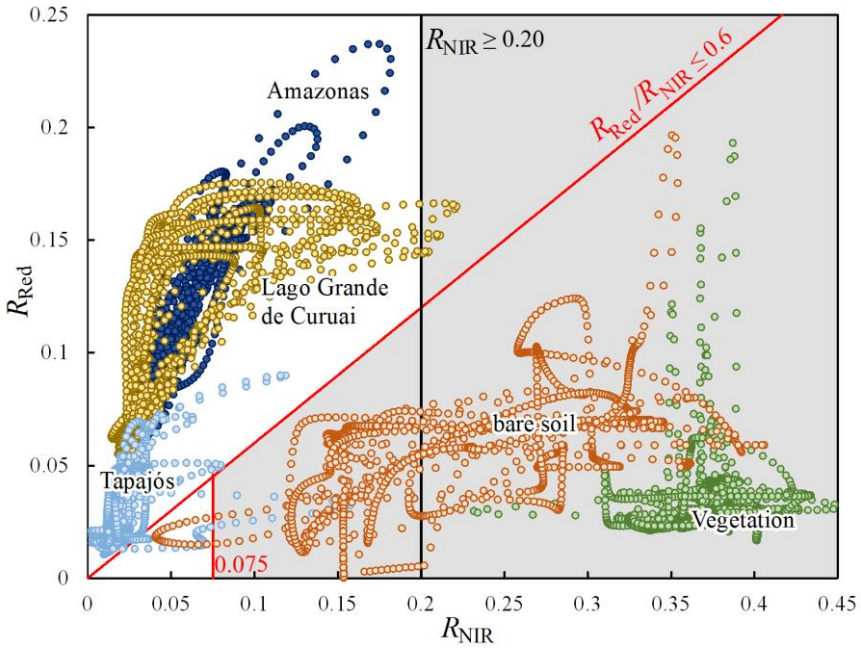

Figure S3.1. Scatter plot of the red and infrared bands with the reflectance thresholds used for image classification in water and no-water (gray area). The black and red lines indicate criterion 1 and 2, respectively.

Table S3.1. In situ data from gauge stations of the Brazilian National Water Agency (ANA) and the Biogeochemistry and Geodynamic of the Amazon Basin (HYBAM) program and correlation with filtered reflectance and raw reflectance.

Station		Source	River	Observed SSSC ($mg.L^{-1}$)		Filtered reflectance					Raw reflectance				
							SSSC x R_{red}		SSSC x R_{nir}			SSSC x R_{red}^r		SSSC x R_{nir}^r	
				μ	σ	n	*r*	*p*	*r*	*p*	n	*r*	*p*	*r*	*p*
1	Vista Alegre	ANA	Madeira	181.9	161.4	46	0.54	0.56	0.79	0.62	11	0.40[a*]	0.32[*]	0.41[*]	0.34[*]
2	Vista Alegre	HYBAM	Madeira	170.2	148.7	380	0.65[a]	0.66	0.76	0.72	102	0.35	0.32	0.43	0.35
3	Óbidos	HYBAM	Amazonas	75.6	55.7	276	0.76	0.67	0.72	0.58	133	0.62	0.53	0.60	0.45
4	Manacapuru	ANA	Solimões	108.4	80.1	44	0.75[a]	0.75	0.72[a]	0.73	24	0.81[a]	0.87	0.55	0.60
5	Manacapuru	HYBAM	Solimões	108.2	65.6	343	0.70[a]	0.71	0.69[a]	0.70	170	0.64	0.68	0.54	0.63
6	Itapeua	ANA	Solimões	111.8	73.5	45	0.57[a]	0.62	0.49	0.51	3	0.92[*]	0.50[*]	1.00[*]	1.00[*]
7	Itaituba	ANA	Tapajós	10.3	6.8	48	0.52[a]	0.59	0.18[a*]	0.27[*]	20	0.48[*]	0.45[*]	0.15[*]	0.21[*]
8	Itaituba	HYBAM	Tapajós	11.4	9.4	245	0.18	0.12[*]	0.21	0.08[*]	115	0.06[a*]	0.08[*]	0.13[a*]	0.10[*]
9	Serrinha	HYBAM	Negro	5.9	2.6	131	-0.01[*]	-0.03[*]	0.02[*]	0.01[*]	64	-0.18[*]	-0.05[*]	-0.04[*]	-0.09[*]
10	Serrinha	ANA	Negro	9.2	6.4	30	-0.31[*]	-0.29[*]	-0.44[*]	-0.34[*]	14	-0.24[*]	0.15[*]	-0.16[*]	0.36[*]
Columm Mean				79.3	61.0		0.43	0.44	0.41	0.39		0.39	0.38	0.36	0.39
Columm Median				91.9	60.6		0.55	0.60	0.59	0.54		0.44	0.39	0.42	0.36

Note: Mean SSC (μ, $mg.L^{-1}$), standard deviation (σ ($mg.L^{-1}$) and number of data (n). Correlation between observed SSSC (or logSSSC, [a]) and R_{red} and R_{nir} (*r*, Pearson coefficient; *p*, Spearman rank correlation; [*], p-value ≥ 0.05, i.e. not significant)

Text S3.2. Correlations between SSSC and reflectance without filtering (raw reflectance, R_{red}^r and R_{nir}^r) showed that the main advantage of filtering was the increase of data in the time series (increased 41%, from 656 to 1588). The only processing on raw data was to eliminate no-water pixels according to the criteria established in section 3.3.1. Individual correlation was significant (p-value ≤ 0.05) for only four stations, and the correlation between the natural logarithm and the raw reflectance for all data was lower for R_{red}^r (r = 0.70 and p = 0.72) and for R_{nir}^r (r = 0.47, p = 0.53) than for the filtered data.

Table S3.2. Confusion matrix with producer's accuracy, and user's accuracy of the suspended sediments concentration (SSSC) class frequency classification.

			Reference				
			Low SSSC	Mod. SSSC	High SSSC	Row total	**User's accuracy**
Classifier	**All data**	Low SSSC	**157**	22	3	182	**86.26**
		Mod. SSSC	150	**166**	188	504	**32.94**
		High SSSC	23	79	**800**	902	**88.69**
		Columm total	330	267	991	**1588**	
		Producer's accuracy	**47.58**	**62.17**	**80.73**		
Classifier	**White-water**	Low SSSC	**0**	0	0	0	**NA**
		Mod. SSSC	2	**93**	185	280	**33.21**
		High SSSC	3	54	**797**	854	**93.33**
		Columm total	5	147	982	**1134**	
		Producer's accuracy	**0.00**	**63.27**	**81.16**		
Classifier	**Clear-water**	Low SSSC	**23**	10	2	35	**65.71**
		Mod. SSSC	134	**73**	3	210	**34.76**
		High SSSC	20	25	**3**	48	**6.25**
		Columm total	177	108	8	**293**	
		Producer's accuracy	**12.99**	**67.59**	**37.50**		
Classifier	**Black-water**	Low SSSC	**134**	12	1	147	**91.16**
		Mod. SSSC	14	**0**	0	14	**0.00**
		High SSSC	0	0	**0**	0	**NA**
		Columm total	148	12	1	**161**	
		Producer's accuracy	**90.54**	**0.00**	**0.00**		

Supplementary information S4

Text S4.1

```
// This script calculates a flood frequency map of a selected region over a defined period.
// update: 2020-04-04

// Reference: FASSONI-ANDRADE, Alice César; PAIVA, Rodrigo Cauduro Dias;
// FLEISCHMANN, Ayan Santos. Lake topography and active storage from satellite observations
// of flood frequency (2020)

// JRC Global Surface Water dataset (Pekel et al, 2016)
var jrcDataset = ee.ImageCollection('JRC/GSW1_0/MonthlyHistory');
var countriesLayer = ee.FeatureCollection('ft:1tdSwUL7MVpOauSgRzqVTOwdfy17KDbw-
1d9omPw');

// Select the area by drawing polygon or indicating the coordinates
ex.: Poopó lake:
var coordinates = [-67.4736,-19.2598, -67.4736,-18.4515, -66.7678,-18.4515, -66.7678,-
19.2598];
//var geometry = ee.Geometry.Polygon(coordinates);
// Define start and end date (year/month/day)
var startDate = '1984-01-01';
var endDate = '2015-01-01';
// Palette
var palette = ['c10000','d742f4','001556','b7d2f7'];
var filteredJRCDataset = jrcDataset.filterBounds(geometry).filterDate(startDate, endDate);

// Calculate flood frequency map
var validFilteredJRCDataset = filteredJRCDataset.map(function (img) {
  var valid = img.gt(0);
  return valid.set('system:time_start', img.get('system:time_start'));
});
var waterJRCDataset = filteredJRCDataset.map(function (img) {
  var waterImage = img.select('water').eq(2);
  return waterImage.set('system:time_start', img.get('system:time_start'));
});
var totalValidJRCDataset = validFilteredJRCDataset.sum().toFloat();
var totalWaterJRCDataset = waterJRCDataset.sum().toFloat();
var totalWaterPercentJRCDataset =
totalWaterJRCDataset.divide(totalValidJRCDataset).multiply(100);
var maskedWaterImage = totalWaterPercentJRCDataset.gt(1);
var waterPercentImage = totalWaterPercentJRCDataset.updateMask(maskedWaterImage);
waterPercentImage = waterPercentImage.clip(geometry);
Map.centerObject(geometry);
Map.addLayer(waterPercentImage, {'min': '0', 'max': '100', 'bands': 'water', 'palette': palette},
'filtered');

// Export flood frequency map to Drive
var geometry2=ee.Image(waterPercentImage).geometry();
Export.image.toDrive({
  image: waterPercentImage,
  description: 'Flood_frequency',
  scale: 30,
  folder: 'MonthlyHistory',
```

```
  fileFormat: 'GeoTIFF',
   region: geometry2,
  maxPixels:1e13,
 // formatOptions: {
  //  cloudOptimized: true
  //}
})
```

Table S4.1. Percentage of the reservoir area that has a flood frequency equal to 100% ($\frac{\mathbf{FF_{100}}}{\mathbf{Area}}$), the assessed period, the lowest and highest level (L_0 and L_{100}) corresponding respectively to the minimum ($V_0 = 0$) and maximum active storage (V_{100}) for 12 regularization reservoirs in Brazil. L_0, L_{100}, and V_{100} are shown for the observed and estimated values.

Reservoir	$\frac{\mathbf{FF_{100}}}{\mathbf{Area}}$	**Assessed period**	**n**	**Observed**			**Estimated**		
				L_0 (m)	**L_{100} (m)**	**V_{100} (hm^3)**	**L_0 (m)**	**L_{100} (m)**	**V_{100} (hm^3)**
Água Vermelha	71.72	1-Jan-1990 to 15-May-2018	2060	373.3	383.3	5169.23	373.9	383.27	5126.24
Barra Bonita	47.06	1-Jan-1993 to 15-May-2018	1077	439.5	451.5	2566.86	443.06	451.43	1758.75
Barra Grande	47.73	4-Nov-2005 to 14-May-2018	1235	617	647	2192.66	617.07	646.92	2040.82
Boa esperança	77.41	1-Jan-1995 to 15-May-2018	979	298	304	1912	298.38	303.99	1569.41
Furnas	47.38	1-Jan-1990 to 21-May-2018	4770	750	768	17217	751.9	767.91	16868.19
Itumbiara	45.96	1-Jan-1993 to 21-May-2018	3207	495	520	12454	497.06	519.89	12055.87
Machadinho	73.64	28-Sep-2001 to 20-May-2018	1511	465	480	1055.81	465.57	479.92	944.99
Quebra queixo	85.95	20-Mar-2003 to 20-May-2018	323	544	549	25.51	544.6	549.69	27.90
Queimado	46.59	25-Mar-2004 to 21-May-2018	1258	811	829	389.46	812.65	828.85	387.70
Sobradinho	46.12	1-Jan-1991 to 21-May-2018	3664	380.5	392.5	28669	380.76	392.51	28585.13
Três Marias	45.06	1-Jan-1998 to 21-May-2018	2971	549.2	572.5	15278	550.29	572.39	15612.73

Tucuruí	85.86	1-Jan-1995 to 20-May-2018	2760	51.6	74	38982.4	54.41	74	37982.8

Supplementary information S5

Text S5.1. Water level gaps from five-gauge stations on the Amazon River were filled as follows: In years with more than 85% of complete data, gaps were corrected from the linear interpolation of the station's time series. In years with less than 85% of the data, such as Parintins and Santarém stations, the correction was made by linearly interpolating data from other stations (see **Figure S5.1**). The Jatuarana and Óbidos stations, upstream and downstream of Parintins, respectively, were used to fill the gaps in Parintins. While for Santarém station, Parintins and Óbidos stations were used, both upstream of Santarém.

Figure S5.1. Percentage of annual data at Manacapuru, Jatuarana, Parintins, Óbidos, Santarém and Curuai stations from 1984 to 2015. Observed (blue) and interpolated (yellow) water levels at Parintins and Santarém (1984 to 2015) river stations.

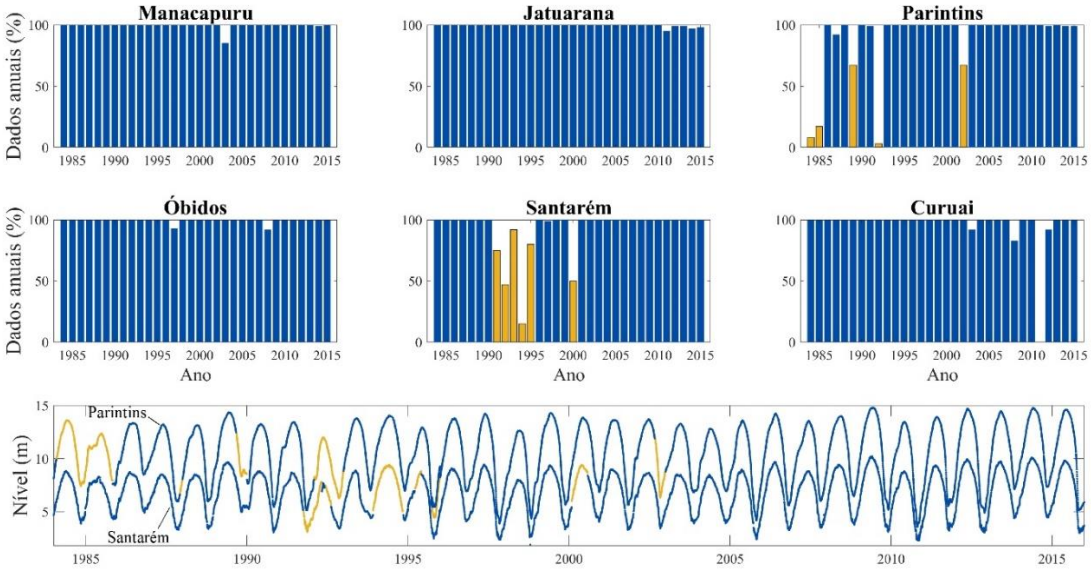

Text S5.2. Six experiments were performed to estimate the floodplain topography considering two interpolation methods used to estimate the floodplain water level and three methods for calculating the water level duration curve. The experiments were evaluated using the Lago Grande de Curuai bathymetric, and the experiment with the best performance (**Table S5.1**) was used to estimate topography in the open water mask of the Amazon floodplain.

The water level time series data in the floodplain was estimated by interpolation of the river water level. To define the best interpolation method, two methods were compared: 1) Linear and 2) Nearest Neighbor. In the linear interpolation, the value is

approximated by the equation of a plane formed by three points defined considering the Delaunay triangulation (AMIDROR, 2002).

The method assumes the equivalence between flood frequency and water level exceedance probability, so the calculation of the water level duration curve for each pixel should ideally be done using only the water levels corresponding to dates with information on the flood frequency at the pixel. That is, the water levels corresponding to dates without information in the flood extension image, due to cloud coverage, gaps or other failures should be excluded. Thus, three approaches to obtaining the water level duration curve were compared: 1) all daily water levels of the floodplain were considered between 1984 and 2015; 2) all monthly water levels between 1984 and 2015 were considered, and 3) the monthly water levels between 1984 and 2015 corresponding to the months with information in the open-water frequency map, i.e., the months with valid information in the flood extension image were evaluated in each pixel to define the monthly levels used. It was necessary to use monthly levels due to the information gap regarding the image date from the JRC Monthly Water History composition.

The different experiments conducted are described below:

Experiment LDA: **Daily** time series data and **linear** interpolation;

Experiment LMA: **Monthly** time series data and **linear** interpolation;

Experiment LMS: **Monthly** time series data **selected** according to valid information in the flood extension, and **linear** interpolation;

Experiment NDA: **Daily** time series data interpolated by the **nearest neighbor** method;

Experiment NMA: **Monthly** time series data interpolated by the **nearest neighbor** method;

Experiment NMS: **Monthly** time series data **selected** according to valid information in the flood extension, and interpolated by the **nearest neighbor** method;

*__L__ – Linear; **N** - N. Neighbor; **D** – Daily; **M** – Monthly; **A** - All; **S** - Selected;

In general, all experiments overestimated the topography (**Table S5.1**). The experiments using nearest-neighbor interpolation performed better than the experiments using linear interpolation. Also, experiments using the daily levels had better performance for the bias and RMSE metrics concerning the experiments using the monthly levels with complete and selected data. On the other hand, experiments using the monthly levels had slightly better performance on metrics that evaluate the spatial variation of the topography (Pearson correlation coefficient, RMSE' and $R^{2'}$) about experiments using daily levels.

There was no improvement in the experiments that used data selected according to information on the flood frequency in comparison with the methods that used all data. Thus, the step for evaluating the months with images with non-valid data and deleting the water levels of respective months in each pixel increased the processing time and did not improve accuracy.

In conclusion, the best performance was the experiment NDA with BIAS of 0.79, Pearson correlation coefficient of 0.73, RSME of 1.30 m, RMSE' of 1.04 and R^2' of 0.44. Although the experiments with monthly levels showed RMSE' and R2' slightly smaller than the experiment NDA (ex. experiment NMA with RMSE' = 1.02 m and R2' = 0.46), the overestimation is greater in these experiments.

Table S5.1. Metrics of the topography observed and estimated by experiments

	Mean (m)	**Standard deviation (m)**	**Minimum (m)**	**Maximum (m)**	**bias (m)**	**RMSE (m)**	**Pearson Coef.**	**RMSE' (m)**	**R^2'**
Observed	4.51	1.39	-11.66	9.54	-	-		-	
Experiment LDA	5.33	1.47	2.74	12.63	0.82	1.33	0.73	1.05	0.43
Experiment NDA	5.30	1.45	2.75	12.49	**0.79**	**1.30**	**0.73**	1.04	0.44
Experiment LMA	5.44	1.43	3.03	12.64	0.93	1.39	0.73	1.03	0.45
Experiment NMA	5.41	1.42	3.03	12.50	0.90	1.36	0.73	1.02	0.46
Experiment LMS	5.44	1.40	3.06	12.76	0.93	1.39	0.72	1.04	0.44
Experiment NMS	5.42	1.39	3.06	12.63	0.91	1.37	0.72	**1.03**	**0.45**

Supplementary information S6

Tabela S6.1 Nome, código e localização das estações utilizadas e operadas pela Agência Nacional de Águas (ANA)

Nome	Código	Fonte	Latitude	Longitude
Manacapuru	14100000	ANA	-3.308	-60.609
Porto de Moz	18950003	ANA	-1.753	-52.241
Moura	14840000	ANA	-1.456	-61.634
Jatuarana	15030000	ANA	-3.052	-59.678
Parintins	16350002	ANA	-2.630	-56.752
Santarém	17900000	ANA	-2.416	-54.716
Curuai	17060000	ANA	-2.268	-55.481
Óbidos	17050001	ANA	-1.947	-55.511
amz_amz_env_	0020_01	Hydroweb	-3.161	-59.465
amz_amz_env_	0063_01	Hydroweb	-3.338	-58.774
amz_amz_env_	0220_01	Hydroweb	-2.391	-54.266
amz_amz_env_	0263_01	Hydroweb	-2.083	-54.02
amz_amz_env_	0306_01	Hydroweb	-1.907	-55.596
amz_amz_env_	0349_01	Hydroweb	-1.946	-55.487
amz_amz_env_	0392_01	Hydroweb	-2.533	-57.171
amz_amz_env_	0435_01	Hydroweb	-2.611	-56.778
amz_amz_env_	0478_02	Hydroweb	-3.331	-58.784
amz_amz_env_	0521_01	Hydroweb	-2.953	-58.14
amz_amz_env_	0607_01	Hydroweb	-3.125	-59.539
amz_amz_env_	0764_01	Hydroweb	-2.146	-54.93
amz_amz_env_	0807_01	Hydroweb	-2.405	-54.668
amz_amz_env_	0850_01	Hydroweb	-2.368	-56.416
amz_amz_env_	0893_01	Hydroweb	-2.123	-56.167
amz_amz_env_	0936_01	Hydroweb	-2.798	-57.948
amz_amz_env_	0979_01	Hydroweb	-2.407	-57.542
R_amz_amz_jas_	0139_01	Hydroweb	-2.5709	-56.897
R_amz_amz_jas_	0152_01	Hydroweb	-3.2539	-59.0681
R_amz_amz_jas_	0228_01	Hydroweb	-2.4879	-56.5076
R_amz_amz_jas_	0063_01	Hydroweb	-3.2809	-59.9848

Tabela S6.2 Métricas do nível da água avaliado no rio Amazonas para cada estação

Estação	Número de dados	Viés	RMSE	NSE	*r*
0020_01	28	-0.86	1.38	0.82	0.94
0063_01	29	-0.43	0.58	0.97	1.00
0220_01	29	-0.42	0.48	0.93	0.99
0263_01	30	-0.40	0.48	0.92	0.99
0306_01	31	-0.60	1.01	0.83	0.95
0349_01	29	-0.47	0.62	0.93	0.99
0392_01	31	-1.28	1.54	0.61	0.95
0435_01	30	-0.47	0.62	0.95	0.99
0478_02	31	-0.36	0.51	0.98	1.00
0521_01	30	-0.48	0.61	0.96	0.99
0607_01	29	-0.13	0.45	0.99	0.99
0764_01	29	-0.59	0.70	0.85	0.98
0807_01	29	-0.82	1.02	0.64	0.96
0850_01	31	-0.59	0.67	0.94	1.00
0893_01	31	-0.83	0.99	0.84	0.98
0936_01	29	-0.75	0.80	0.93	1.00
0979_01	31	-0.47	0.68	0.95	0.99
0139_01	81	-0.68	1.38	0.45	0.95
0152_01	75	0.00	0.61	0.96	0.98
0228_01	82	-0.50	0.94	0.81	0.97
0063_01	74	-0.15	0.64	0.98	0.99
Curuai	1005	0.65	0.67	0.92	1.00
Óbidos	1066	0.30	0.37	0.98	1.00